

# Non-Destructive Bio-Assay of Single Living Cell

Vahé Nerguizian

A Thesis  
In the Department  
of  
Mechanical and Industrial Engineering

Presented in Partial Fulfillment of the Requirements  
For the Degree of Doctor of Philosophy at  
Concordia University  
Montreal, Quebec, Canada

April 2012

© Vahé Nerguizian, 2012

**CONCORDIA UNIVERSITY  
SCHOOL OF GRADUATE STUDIES**

This is to certify that the thesis prepared

By: Vahé Nerguizian

Entitled: Non-Destructive Bio-Assay of Single Living Cell

and submitted in partial fulfillment of the requirements for the degree of

DOCTOR OF PHILOSOPHY (Mechanical Engineering)

complies with the regulations of the University and meets the accepted standards with respect to originality and quality.

Signed by the final examining committee:

Dr. Paula Wood-Adams Chair

Pr. Renato G. Bosisio External Examiner

Dr. Sheldon Williamson External to Program

Dr. Rolf Wultrich Examiner

Dr. Sivakumar Narayanswamy Examiner

Dr. I. Stiharu and Dr. Miguel Burnier Jr. Thesis Supervisor

Approved by

Chair of Department or Graduate Program Director

# Abstract

## **Non-Destructive Bio-Assay of Single Living Cell**

Vahé Nerguizian, Ph.D.

Concordia University, 2012

For more than a decade, researchers are trying to find out practical commercial tool for particle/cell detection and characterization with portable, low cost, specific and sensitive characteristics [1-4]. The advance of Micro Electro Mechanical Systems (MEMS) and microfluidic technologies opened a major challenge for a large number of researchers, industrial health and bio companies to invest their time and budget into the avenue of point of care health instruments or devices helping the early detection of cancer cells within the human blood via circulating malignant cells.

Actual existing commercial flow cytometer that detects and identifies the type and size of cells are costly, time consuming and need the assistance of highly qualified operators. Moreover, in certain research activities, micro cytometers are investigated and assessed with different detection techniques such as optical, impedance spectroscopy, electromagnetic spectroscopy and many other techniques [5-9].

The aim of this research is to investigate an innovative mechanism that enables to characterize, identify and differentiate among various living cells including malignant tumor cells through the use of the electromagnetic energy detection technique. Cells are spatially centered in a microfluidic channel through dielectrophoresis technique then

detected and characterized by measuring and interpreting the RF signal transmission of the cells passing one by one through the interrogation region in the microchannel.

The outcome of this research might help the clinical end user to gain certain important information about the condition of the patient, establish personalized treatment or track the effect of a treatment. Detection and counting of tumor cells may help identification of early stages of illness and help patient with early care that may significantly cut the overall cost of cancer management.

# Acknowledgment

In the first place I would like to express my gratitude and thanks to my supervisors Dr. Ion Stiharu and Dr. Miguel Jr. Burnier in their judicious and professional guidance and assistance throughout my research project.

I address also my special thanks to several persons who strongly helped and supported me technically, namely Anas Alazzam and Jules Gauthier. A special thanks to Sylvain Brisebois mostly for his software programming support and to Emilia Anteckka for her wise and important bio related advices. For professional support I thank Dacian Roman, Silvin Bakalian, Daniel Abourbih, Shawn Maloney, Sebastien Di Cesare, Tiffany Porraccio, Kousseil Ben Ahmed, Steve Dubé, Maxime Thibault, Mustapha Rafaf, Bruno Yango, Aurélie Dominguez and Ron Ettetdgui.

The author would like to thank the CREER (Centre de Recherche En Electronique Radiofréquence) strategic group for providing the fabrication process facility. Canadian Microelectronic Corporation (CMC) provided on lending bases some of the Microwave and RF test equipment and the author would like to express his gratitude for this contribution. Thanks to COMSOL and HF Works for providing software support for some simulations. I would like also to thank the support of École de technologie supérieure and of my colleagues.

For moral support, many thanks to my wife Choghig Piloyan and my children Abraham Paul and Vana Gabriella, to my mom Alice Nerguizian, to my older brother Varouj Nerguizian and his family, to my twin brother Chahé Nerguizian and his family and finally to my bishop his reverend father Georges Zabarian.

This thesis is dedicated to my wonderful wife Choghig Piloyan and my children Abraham Paul and Vana Gabriella. Thanks for your patience, support and encouragements during all these years in preparing my research and writing my thesis.

I thank you all from the bottom of my heart and I love you.

# Table of Contents

Abstract.....	iii
Acknowledgment.....	v
Table of Contents.....	vii
List of Acronyms.....	xi
List of Symbols.....	xv
List of Biological Terms.....	xxi
List of Figures.....	xxii
List of Tables.....	xxvii
<b>CHAPTER 1: RESEARCH INTRODUCTION.....</b>	<b>1</b>
1.1 INTRODUCTION.....	1
1.2 DEFINITION OF THE PROBLEM.....	2
1.3 OBJECTIVES OF THE RESEARCH.....	3
1.4 ORIGINALITY OF THE THESIS.....	5
1.5 CONTRIBUTION.....	7
1.6 MANUSCRIPTS IN THE THESIS.....	8
1.7 MICRODEVICE SYSTEM REQUIREMENTS, RESEARCH METHODOLOGY, PLAN AND IMPLEMENTATION SUMMARY.....	9
1.7.1 Introduction.....	9
1.7.2 Micro devices.....	9
1.7.2.1 Device for RF/Microwave frequency and power level determination.....	10
1.7.2.2 Device for cell dielectric property determination (off line characterization).....	10
1.7.2.3 Device for cell centering, detection and characterization (on line characterization).....	11
1.7.2.4 Device for RF cell detection.....	12
1.8 CHAPTER SUMMARY AND THESIS LAYOUT.....	13
<b>CHAPTER 2: LITERATURE REVIEW AND STATE OF THE ART.....</b>	<b>15</b>
2.1 INTRODUCTION:.....	15
2.2 CELL CENTERING AT THE INTERROGATION POINT.....	19
2.3 CELL DETECTION AND COUNTING.....	22
2.4 CELL CHARACTERIZATION AND IDENTIFICATION.....	24
2.5 CHAPTER SUMMARY.....	28
<b>CHAPTER 3: THEORETICAL ANALYSIS FOR SINGLE CELL MANIPULATION, CENTERING, DETECTION AND CHARACTERIZATION.....</b>	<b>29</b>
3.1 INTRODUCTION.....	29
3.2 DIELECTROPHORESIS.....	30
3.2.1 Principle of Dielectrophoresis (DEP).....	30
3.2.2 Dielectrophoresis theory.....	32
3.2.3 Clausius-Mossotti factor and DEP force.....	35
3.3 RF/MICROWAVE TRANSMISSION LINES.....	38
3.3.1 Coplanar waveguide transmission line theory.....	39
3.3.2 Different CPW line configurations within microfluidic devices.....	42
3.3.2.1 Standard CPW lines electrodes on one substrate.....	42
3.3.2.2 CPW lines electrodes sandwiched between two substrates.....	43
3.3.2.3 CPW lines electrodes sandwiched between two substrates with a gasket layer in between.....	44
3.3.3 Transmission line matrix for CPW lines.....	44
3.3.3.1 Cascaded two ports or transmission lines.....	45
3.3.3.2 S parameters and extraction from ABCD matrix.....	46
3.4 SINGLE CELL MODEL BETWEEN TWO ELECTRODES.....	48
3.4.1 Introduction.....	48
3.4.2 Model of two electrodes without cell or particle.....	49
3.4.3 Model of two electrodes with cell or particle.....	51
3.5 COMPLEX PERMITTIVITY MEASUREMENT THEORY (CAVITY PERTURBATION METHOD).....	53

3.5.1	<i>Introduction of complex permittivity</i> .....	53
3.5.2	<i>Modes in rectangular resonant cavities</i> .....	54
3.5.3	<i>Rectangular cavity perturbation method</i> .....	56
3.5.4	<i>Measurable resonant frequency and quality factor</i> .....	62
3.6	FLUID ANALYSIS IN MICROFLUIDIC CHANNEL .....	62
3.6.1	<i>Navier-Stokes equations for a steady flow and incompressible fluids</i> .....	62
3.6.2	<i>Forces present on an immersed spherical particle in a fluid</i> .....	64
3.6.2.1	Introduction .....	64
3.6.2.2	DEP electrodes effect .....	64
3.6.2.3	Electro- magnetic effect .....	65
3.7	CHAPTER SUMMARY .....	65
<b>CHAPTER 4: THEORETICAL ANALYSIS OF DIELECTROPHORETIC FORCE GENERATED BY PARALLEL FACING ELECTRODES FOR CENTERING THE LIVING CELLS WITHIN THE MICROFLUIDIC CHANNEL</b> .....		<b>67</b>
4.1	INTRODUCTION .....	67
4.2	CELL CENTERING MICRO DEVICE .....	68
4.3	PROBLEM DESCRIPTION FOR DEP PARALLEL FACING ELECTRODES .....	71
4.4	SOLUTION OF THE GOVERNING EQUATIONS BY FOURIER SERIES .....	76
4.4.1	<i>The electric field</i> .....	81
4.4.2	<i>Dielectrophoretic force</i> .....	83
4.5	EXPERIMENTAL RESULTS .....	84
4.5.1	<i>Micro device design and fabrication</i> .....	84
4.5.2	<i>Cell preparation</i> .....	86
4.5.3	<i>Experimental set up and procedure</i> .....	86
4.6	RESULTS AND DISCUSSION .....	87
4.7	CONCLUSIONS .....	92
4.8	CHAPTER SUMMARY .....	93
<b>CHAPTER 5: DESIGNS, SIMULATION AND FABRICATION OF MICRO DEVICE FOR CELL CENTERING AND SINGLE CELL DETECTION/CHARACTERIZATION</b> .....		<b>94</b>
5.1	INTRODUCTION .....	94
5.2	EFFECT OF NON THERMAL RADIO FREQUENCY RADIATION ON UVEAL MELANOMA CELLS .....	96
5.2.1	<i>RF signal exposure on living cells</i> .....	96
5.2.2	<i>Specification of the RF signal frequency and the power level on normal and cancer living cells</i> .....	97
5.2.3	<i>Determination of frequency and power level of RF signal</i> .....	98
5.2.4	<i>RF apparatus and measurement set-up</i> .....	98
5.2.4.1	Methods .....	100
5.2.4.2	Proliferation test .....	101
5.2.4.3	Experimental results and discussions .....	102
5.3	SINGLE CELL CHARACTERIZATION DEVICE .....	106
5.3.1	<i>Materials</i> .....	106
5.3.1.1	Channel substrate material .....	108
5.3.1.2	Electrodes Material (Thin Film) .....	109
5.3.2	<i>Channel fabrication</i> .....	109
5.3.3	<i>Hermetic channel and flexibility of channel re-utilization</i> .....	110
5.3.4	<i>Fabrication procedure</i> .....	111
5.3.4.1	Substrate preparation .....	113
5.3.4.2	Electrodes Deposition (Thin Film Process) .....	113
5.3.4.3	Holes drilling .....	115
5.3.4.4	Channel fabrication process .....	116
5.3.4.5	Channel sealing and structure assembly .....	118
5.3.5	<i>Microfluidic chip integration</i> .....	119
5.3.6	<i>Simulation</i> .....	119

5.3.6.1	Simulation Results .....	123
5.3.7	<i>Experimental Results</i> .....	125
5.3.7.1	Media preparation for polystyrene microspheres .....	125
5.3.7.2	Media preparation for <i>Saccharomyces cerevisiae</i> .....	125
5.3.7.3	Media preparation for different cancer cells .....	126
5.3.7.4	Experiments with polystyrene microspheres and <i>Saccharomyces cerevisiae</i> .....	126
5.4	DISCUSSIONS.....	130
5.5	CONCLUSION.....	131
5.6	CHAPTER SUMMARY .....	132
<b>CHAPTER 6: OFF LINE CHARACTERIZATION OF BIOLOGICAL CELLS.....</b>		<b>134</b>
6.1	INTRODUCTION.....	134
6.2	THEORETICAL BACKGROUND.....	137
6.2.1	<i>Polarization, permittivity, conductivity and dispersion of materials</i> .....	137
6.2.2	<i>Microwave frequency biological material permittivity and conductivity measurement theory</i> 141 .....	141
6.2.3	<i>Complex permittivity of cells at microwave frequencies</i> .....	145
6.3	CAVITY DESIGN AND FABRICATION .....	148
6.3.1	<i>Design of cavities at S-Band</i> .....	148
6.4	SET UP FOR PERMITTIVITY AND CONDUCTIVITY MEASUREMENT .....	152
6.5	SOFTWARE FOR AUTOMATIC MEASUREMENTS.....	155
6.6	PERMITTIVITY AND CONDUCTIVITY MEASUREMENT PROCEDURE .....	155
6.7	MATERIAL PREPARATION AND METHOD .....	158
6.8	TEST RESULTS AND MEASUREMENTS.....	158
6.8.1	<i>Calibration or reference measurement</i> .....	158
6.8.2	<i>Different biological cells (reference, WBC, Hela, prostate, breast and uveal melanoma cancer) measurement</i> .....	161
6.9	DISCUSSIONS.....	165
6.10	CONCLUSIONS .....	167
6.11	CHAPTER SUMMARY .....	168
<b>CHAPTER 7: ON LINE CHARACTERIZATION OF BIOLOGICAL CELLS AND BULK MEASUREMENT OF CELLS</b>		<b>169</b>
7.1	INTRODUCTION.....	169
7.2	CROSS FREQUENCY DETERMINATION OF LIVING CELLS .....	170
7.2.1	<i>Introduction</i> .....	170
7.2.2	<i>Material and media preparation</i> .....	171
7.2.3	<i>Cross frequency measurement and results of RBCs, WBCs and different types of cancer cells</i> 172 .....	172
7.3	CELL DETECTION AND COUNTING .....	174
7.3.1	<i>Introduction</i> .....	174
7.3.2	<i>RF/Microwave detector</i> .....	174
7.3.3	<i>Cell detection and counting</i> .....	175
7.3.4	<i>Discussions</i> .....	176
7.4	ON LINE CHARACTERIZATION AND IDENTIFICATION .....	177
7.4.1	<i>Introduction</i> .....	177
7.4.2	<i>Single cell model in the in the RF/Microwave path</i> .....	178
7.4.2.1	Geometrical dimensions of the electrodes and the microchannel of the two devices .....	178
7.4.2.2	Analytical model of the CPW of the entire microstructure .....	181
7.4.2.3	Simulation of the single living cell in between two parallel facing overlapping electrodes within the micro devices .....	185
7.4.2.4	Analytical model of the single living cell in between two parallel facing overlapping electrodes within the micro devices .....	188
7.4.2.4.1	Analytical model results of cell 92.1 in Glycerol.....	189

7.4.2.4.2	Analytical model results of cell 92.1 in sucrose/dextrose .....	192
7.4.2.4.3	Analytical model results of WBC in Glycerol .....	195
7.4.2.4.4	Analytical model results of WBC in sucrose/dextrose.....	198
7.4.3	<i>Single cell RF/Microwave measurements for cell characterization</i> .....	202
7.4.3.1	Material and media preparation .....	202
7.4.3.2	Single cell RF/Microwave measurement set-up.....	203
7.4.3.3	Cells centering.....	205
7.4.3.4	Single cell RF/Microwave measurements .....	210
7.4.3.5	Discussions and difficulties .....	219
7.5	CHAPTER SUMMARY .....	223
<b>CHAPTER 8: GENERAL CONCLUSIONS, SUMMARY OF CONTRIBUTIONS AND FUTURE WORK .....</b>		<b>224</b>
8.1	GENERAL CONCLUSIONS OF THE RESEARCH STUDY.....	224
8.2	SUMMARY OF CONTRIBUTIONS .....	226
8.3	AREAS OF FUTURE RESEARCH WORK .....	228
	<b>Appendix A</b> .....	231
	<b>Appendix B</b> .....	235
	References: .....	238

## List of Acronyms

2D	Two dimensional
3D	Three dimensional
AC	Alternative Current
ANSYS	Engineering simulation software , Computer Aided Engineering (CAE)
ARclear™ 8154	Adhesive from Adhesives Research, USA
ARROW	Anti-Resonant Reflecting Optical Waveguides
ARVO	Association for Research in Vision and Ophthalmology
AutoCAD	Software application for Computer-Aided Design (CAD), Autodesk CAD
AZ1518	Photoresist from AZ Electronic Materials
Bio MEMS	Bio Micro Electro Mechanical Systems
BNC	Bayonet Neill–Concelman low frequency connector
CAD	Computer Aided Design
CATIA	Dassault Système CAD software
CM	Clausius-Mosotti factor
CO <sub>2</sub>	Carbon Dioxide
COMSOL	Finite Element Analysis Solver and Simulation Software
CP	Complex permittivity
CPW	CoPlanar Waveguide
CMC	Circulating Malignant Cells
CTC	Circulating Tumor Cells

DC	Direct Current
DEP	DiElectroPhoresis or DiElectroPhoretic
DNA	Deoxyribo Nucleic Acid
FACS	Fluorescence Activated Cell Sorters
FEA	Finite element analysis
FEM	Finite Element Method
FTIR-MSP	Fourier Transform Infra-Red-Micro SPectroscopy
GE112A	Silicone rubber from General Electric
GUI	Graphic user interface
HFWorks	High Frequency Design Analysis for SolidWorks Designers
ISM	Industrial Scientific and Medical
ITO	Indium Tin Oxide
Labview	Laboratory Virtual Instrumentation Engineering Workbench
LTTC	Low Temperature Co-fired Ceramic
Matlab <sup>TM</sup>	MATrix LABoratory
MEMS	Micro Electro Mechanical Systems
MMIC	Microwave Monolithic Integrated Circuits
mRNA	Messenger Ribo Nucleic Acid
mS/m	Milli-Siemens per meter
nDEP	Negative DiElectroPhoresis
NIH	National Institute of Health
NIST	National Institute of Standards and Technology

Op-Amp	Operational Amplifier
PCB	Printed Circuit Board
PCR	Polymerase Chain Reaction
pDEP	Positive DiElectroPhoresis
PDMS	PolyDiMethyl Siloxane
PH	Measure of the acidity or basicity of an aqueous solution
PMMA	PolyMethylMethAcrylate
POC	Point Of Care
Q-TEM	Quasi-Transverse Electro Magnetic
RBC	Red Blood Cell
RF	Radio Frequency
RT-PCR	Real Time Polymerase Chain Reaction
S-band	Covering the frequency range from 2 to 4 GHz
SU-8	Negative photoresist
SCM	Schwarz–Christoffel Mapping
SMA	SubMiniature version A RF connector
Sulforhodamine B based (TOX-6)	In vitro toxicology assay kit
UM	Uveal Melanoma
TE	Transverse Electric
TM	Transverse Magnetic
V-groove	V shaped groove
WBC	White Blood Cell

WR284

Waveguide Rigid (Rectangular) for S band

## List of Symbols

$\beta(t)$	Dielectric relaxation
$\beta_{lg}$	Phase constant
$\mu_0$	Air permeability
$\mu_d$	Dynamic viscosity
$\mu_r$	Relative permeability
$A_0$	Fourier series constant
$A_{CSn}$	Area cross section at port n
$a_i, A_i, b_i, B_i, c_i,$ $C_i, C_{ii}, d_i, D_i, F_i,$ $G_i$	Geometric dimensions or constants or parameters
$A_n$	nth Fourier series constant
$A_{RF}$	RF signal amplitude
$B$	Magnetic field flux density
$b$	Magnetic field flux density variation
$B_0$	Magnetic flux density in the unperturbed or empty cavity
$B_0^*$	Conjugate of the magnetic flux density in the unperturbed or empty cavity
$C_j$	Capacitance of jth element
$C_{mem}$	Membrane capacitance
$c_o$	Velocity of the light
$D$	Electric displacement field in the interior of sample
$D_0$	Electric displacement field in the unperturbed or empty cavity
$D_0^*$	Conjugate of the electric displacement field in the unperturbed or empty cavity

$\mathbf{E}$	Electrical field vector
$\mathbf{e}$	Electrical field vector variation
$\mathbf{E}_0$	Electric field in the unperturbed or empty cavity
$\mathbf{E}_0^*$	Conjugate of the electric field in the unperturbed or empty cavity
$\mathbf{E}_{RMS}$	Root Mean Square amplitude of the applied electric field
$\mathbf{F}$	Electrophoretic and polarization forces
$f$	Frequency
$f$	With specimen cavity measurable frequency
$f_{10l}$	Frequency of the dominant mode
$\mathbf{F}_{BUOYANCY}$	Buoyancy force
$f_{CROSS}$	Cross frequency
$\mathbf{F}_{DEP}$	DEP force
$\mathbf{F}_{DEP\text{ RF/MICROWAVE}}$	DEP force from RF/Microwave signal
$\mathbf{F}_{DRAG}$	Drag force
$\phi$	Volume fraction
$\mathbf{F}_{GRAVITY}$	Gravity force
$\mathbf{F}_{LORENTZ}$	Lorentz force
$f_0$	Empty cavity measurable frequency
$f_{RF}$	RF signal frequency
$\mathbf{g}$	Gravity vector
GHz	Giga Hertz

$H$	Magnetic field strength in the interior of sample
$H_0$	Magnetic field in the unperturbed or empty cavity
$H_0^*$	Conjugate of the magnetic field in the unperturbed or empty cavity
$\text{Im}(\beta^*)$	Imaginary part of the Fourier transform of $\beta(t)$
$j$	Complex number
$K$	Complete elliptical integral of the first kind
KHz	Kilo Hertz
$k_i$	Argument of the complete elliptical integral of the first kind
$K_i$	Wall correction factor in the $i$ direction
$K_s, K_g$	Variable or constant
$L, W, h, L_p, W_p, hp$	Dimensions or length or width or height
$m$	Variable or constant
MHz	Mega Hertz
$P$	Particle dipole moment vector
$p$	Pressure
$\mathbf{p}$	Pressure vector
$Q, Q_s$	With specimen cavity measurable quality factor
$Q_c$	Particle charge
$Q_n$	Volume flow rate at port $n$
$Q_o,$	Empty cavity measurable quality factor
$R$	Radius of the particle

$\text{Re}(\beta^*)$	Real part of the Fourier transform of $\beta(t)$
$\text{Re}[f_{CM}]$	Real part of the Clausius-Mossotti factor
$R_i$	Resistance of $i$ th element
$S$	Cavity surface
$S$	Empty cavity surface
$S$ parameters	Scattering parameters
$S_{ii}$	Complex scattering parameters of $i$ th port
$\text{TE}_{101}$	Dominant mode transverse electric
$\text{TM}$	Transverse magnetic
$T_h$	Thickness of the electrodes layer
$V$	Cavity volume or electrical potential
$\mathbf{v}$	Velocity vector
$V_0$	Empty cavity volume or electric potential
$V_i$	Electric potential with respect to $i$ axis
$V_{ii}$	Second partial derivative with respect to $i$
$v_n$	Velocity
$V_p$	Volume of the particle
$V_S$	Volume of the specimen
$W_E$	Electric energy in the cavity
$W_M$	Magnetic energy in the cavity
$W_T$	Total energy in the cavity
$x_i$	$x$ coordinates with respect to the considered domain

$y_i$	y coordinates with respect to the considered domain
$Z_0$	Characteristic impedance
$Z_i$	Impedance of the $i$ th element
$\alpha$	Attenuation
$\alpha$ dispersion	Ionic polarization
$\beta$	Constant or variable
$\beta$ dispersion	Interfacial polarization
$\gamma$	Propagation constant
$\gamma$ dispersion	Atomic and electronic polarizations
$\delta$ dispersion	Orientation polarization
$\varepsilon$	Relative permittivity
$\varepsilon^*$	Complex permittivity
$\varepsilon_m^*, \varepsilon_m^*$	Complex permittivity of the media
$\varepsilon_p^*, \varepsilon_p^*$	Complex permittivity of the particle
$\varepsilon_0$	Air permittivity
$\varepsilon_{eff}$	Effective permittivity
$\varepsilon_m$	Dielectric constant of the media
$\varepsilon'_m$	Dielectric constant of the media
$\varepsilon''_m$	Dielectric loss of the media
$\varepsilon'_p$	Dielectric constant of the particle
$\varepsilon''_p$	Dielectric loss of the particle
$\varepsilon''_{ri}, \varepsilon_{ri}''$	Dielectric loss of the $i$ th material

$\epsilon_{ri}$	Dielectric constant of ith material
$\epsilon'_{ri}, \epsilon''_{ri}$	Dielectric constant of the ith material
$\lambda$	Wavelength
$\rho$	Fluid density
$\rho_c$	Total electric charge density
$\sigma$	Conductivity
$\sigma_m$	Conductivity of the media
$\sigma_p$	Conductivity of the particle
$\omega$	AC signal oscillation frequency or angular frequency
$\omega_0$	Angular frequency of empty cavity

## List of Biological Terms

92.1	Human uveal melanoma cell line
D-PBS	Dulbecco's Phosphate Buffered Saline
EDTA	Ethylene Diamine Tetraacetic Acid widely used in biological applications
FBS	Fetal Bovine Serum rich of proteins and used in cell culturing were cells can grow and divide
Ficoll	Synthetic branched co-polymer of sucrose and epichlorhydrin. The solution has high viscosity and low osmotic pressure. Often used for preparing density gradients for cell separations
Hela	Oldest and most commonly used human cervical cancer cell line
MDA231	Breast cancer cells line MDA231 have been isolated from human breast cancer patients as continuous culture in University of Texas, Medicine Department of Anderson Hospital and Tumor Institute. The cell line is used as in vitro models for breast cancer cells. The MDA231 line consists of identical cells that have been multiplied from the same cells
OCM	Human uveal melanoma cell line
PBS	Phosphate Buffered Saline a buffer solution used in biological applications
PC3	Cell line originally derived from advanced androgen independent bone metastasis/metastasized prostate cancer
RPMI 1640	Cells media used to culture cells was developed at Roswell Park Memorial Institute (RPMI)
Trypsin	Trypsin is a pancreatic serine protease used to detach adherent cells from the cell culture dish wall during the process of harvesting cells to re-suspend them in media
WBC - Jurkat, Clone E6-1	Pseudodiploid human cell line and acute T cell leukemia (T lymphocyte)

# List of Figures

Figure 1.1: Block diagram of microfluidic cell characterization system .....	5
Figure 2.1: Hydro fluidic centering of sample stream. The two input sheath flows push the particle sample flow and keep the particle vertically focused at the vertical center plane. Reprinted with permission from Holmes, Morgan et al. 2006 .....	21
Figure 2.2: Dielectrophoresis centering of sample stream. The electrodes are activated with low frequency voltage to create a negative dielectrophoresis force to repulse the particle flow and confined them at the center line of the microchannel. Reprinted with permission from Holmes, Morgan et al. 2006.....	21
Figure 2.3: Picture of the glass chip impedance spectroscopy flow cytometer. Reprinted with permission from Cheung, Gawad et al. 2005.....	26
Figure 2.4: Cross section of the microfluidic channel with the particle passing between electrodes and its electrical simplified model at the cell detection region. The graph shows the differential impedance versus the time. Reprinted with permission from Cheung, Gawad et al. 2005 .....	26
Figure 2.5: 3D (a) and 2D (b) pictures where Hela cell captured at micro pillar is measured for impedance with impedance spectroscopy system at low frequency. Reprinted with permission from Jang and Wang 2007.....	27
Figure 3.1: The effect of uniform and non-uniform electric fields on a cell or particle. Reprinted with permission from Voldman 2007 .....	31
Figure 3.2: The effect of uniform and non-uniform electric fields on a cell or particle. a) When a particle is more polarized than the media, the particle moves towards the region with high electric-field strength and this is positive DEP. b) When a particle is less polarized than the media, the particle moves towards the region with low electric-field strength and this is negative DEP. Reprinted with permission from Doh et al 2005.....	31
Figure 3.3: Electric field distortions due to interfacial polarization. Adapted from Kua et al 2005.....	32
Figure 3.4: Different polarization mechanisms of a dielectric particle in a solution. The curve shows the frequency dependence of the complex permittivity. The complex permittivity is composed by the dielectric constant $\epsilon'$ and the dielectric loss $\epsilon''$ . Reprinted with permission from Demierre 2008 .....	34
Figure 3.5: Real part of CM versus AC frequency of the applied signal for different living cells in a media with conductivity of 10 mS/m. Reprinted with permission from Alazzam 2011.....	37
Figure 3.6: Real part of CM versus AC frequency of the applied signal for different models of cells. Reprinted with permission from Demierre 2008 .....	38
Figure 3.7: Cross section of general CPW configuration.....	40
Figure 3.8: Cross section of standard CPW line .....	43
Figure 3.9: Cross section of a CPW line sandwiched between two substrates .....	43
Figure 3.10: Cross section of a CPW line sandwiched between two substrates with a gasket layer in between.....	44
Figure 3.11: ABCD Matrix presentation with the input and output ports of the 2 ports device.....	45
Figure 3.12: S parameter presentation with the input and output ports of the 2 ports device.....	47
Figure 3.13: Physical model of a particle between two parallel facing electrodes. The overlapped two plates are considered as the tips of electrodes where the centered particle will be present and be measured at RF/microwave frequencies.....	49
Figure 3.14: Model of the two facing electrodes separated by a media (with fringing effect). The picture shows a cross section of the electrodes with width equals to $W$ .....	50
Figure 3.15: Model of the two facing electrodes separated by a media (with fringing effect) with the presence of the particle. The picture shows a cross section of the electrodes with width equals to $W$ .....	51
Figure 3.16: The final electrical model of the two facing overlapped electrodes with and without the particle.....	53
Figure 3.17: A sketch of a rectangular cavity with the specimen capillary tube introduced at the position of the maximum electric field (at the center of the cavity). Reprinted with permission from Sheen 2009 .....	55
Figure 4.1: (a) Schematic diagram showing the experimental arrangement of the electrodes used for manipulation of cells. Series of electrodes are patterned on the upper and bottom parts of the channel.	

Energizing one pair of electrodes “third from the left” influences the movement of cells toward the electrodes (positive DEP) or far from the electrodes (negative DEP). (b) 2D schematic diagram showing the cells displacement under the influence of moving dielectrophoresis. The circles represent cells. In the first part of figure b, only the third pair of electrodes is actuated while in the second part only the fourth pair electrodes. Sequential energizing of the electrodes causes the cells to move in the microchannel due to the dielectrophoretic phenomenon .....70

Figure 4.2: Illustration of the geometry of the unit segment and the boundary conditions used in the analytical solution. The unit segment consists of finite size pair of electrodes of length  $d/2$  with a potential of  $V_0$  and  $-V_0$ . The Gaussian surface used in the solution is shown as dashed line at the upper right part of the channel. The electrodes are shown with some thickness for better visualization but they are considered thin compared with the height of the channel .....73

Figure 4.3: Schematic diagram includes the upper part of the microchannel showing the energized electrode and the coordinate system used in the solution to indicate the potential distribution at the upper part of microchannel .....77

Figure 4.4: The variation of the constant  $\beta$  as the microchannel height  $H$  changes. The constant  $\beta$  is used to describe the potential function at the upper and the bottom parts of the microchannel between the edge of the electrode and the right end of the unit segment. The value of  $\beta$  was calculated up to three significant digits using Matlab™ based on equation (53) with ( $m=n= 100$  terms) .....83

Figure 4.5: Picture taken of the experimental device lies beside a Canadian twenty five cent coin. The Bio Microchannel is made by blue tape and several electrodes are shown in the picture (DEP, Low frequency and high frequency electrodes). The inlet and outlet holes can be seen on the top glass .....85

Figure 4.6: Comparison of analytical results and numerical simulations for the electric potential (V), magnitude of electric field (V/m) and the gradient of  $\nabla(\mathbf{E}\cdot\mathbf{E})$  ( $V^2/m^3$ ). Numerical simulations were obtained by finite element methods using COMSOL Multiphysics™. The contour plots of the same level in the microchannel are shown for analytical and numerical results respectively. The thick lines at the top and bottom of the figures represent the electrodes and calculation were carried out using (upper electrode voltage of 10 Volts, lower electrode voltage of -10V,  $d=50\mu m$ , and  $H=60\mu m$ ) .....89

Figure 4.7: The error percentage of the electric potential in the microchannel as the parameter  $\frac{L}{H}$  changes. The step size in the x and y direction is selected to be  $\frac{1}{2} \mu m$  and the values of  $d$  and  $H$  were assumed  $20\mu m$  and  $60 \mu m$  respectively .....90

Figure 4.8: Analytical and experimental results (a) Vector plot of the magnitude of  $\nabla(\mathbf{E}\cdot\mathbf{E})$  using the analytical solution (the electrodes are shown as thick lines); (b-d) Microscopic images showing the accumulation of red blood cells under positive DEP force with different applied voltages (b) 2 Volts peak and 1 MHz with round edges electrodes (c) 2 Volts peak, 1 MHz with sharps edges electrodes (d) 10 Volts peak, 1 MHz. Clustering of the cells correspond to the configuration of the electric field .....91

Figure 5.1: The RF electrodes with copper stripes and 3 SMA connectors. The generator is connected to one of the inputs of the RF apparatus for RF radiation exposure. Uveal melanoma cell lines 92.1 and Fibroblast in a media are filled in 96 well plates .....99

Figure 5.2: The generator is connected to one of the inputs of the RF apparatus for RF radiation exposure. Uveal melanoma cell lines 92.1 and Fibroblast in a media are filled in 96 well plates .....100

Figure 5.3: RF radiation proliferation results on 92.1 uveal melanoma cells in a media. F1, F2 and F3 present RF frequency ranges of (1 to 1.6 GHz), (1.7 to 2.3 GHz) and (2.4 to 3 GHz) respectively. The vertical axis presents the proliferation rate compared to the control 92.1 cells that were not subjected to RF radiation .....103

Figure 5.4: RF radiation proliferation results on Fibroblast in a media. F1, F2 and F3 present RF frequency ranges of (1 to 1.6 GHz), (1.7 to 2.3 GHz) and (2.4 to 3 GHz) respectively. The vertical axis presents the proliferation rate compared to the control Fibroblast cells that were not subjected to RF radiation .....103

Figure 5.5: New RF apparatus to inject RF radiation with stronger electrical field. The RF signal can be injected through the SMA connector. Indium Tin Oxide (ITO) films are evaporated on the two glasses acting as the conducting electrodes and permitting visual observation under the microscope .....104

Figure 5.6. The FEA simulation structure of electrode stripe on middle column of wells of the RF apparatus .....	105
Figure 5.7. Return Loss of the input port of the RF apparatus versus the frequency.....	106
Figure 5.8: Assembled structure of the microfluidic device .....	111
Figure 5.9: Cross section view (a) and side cut view (b) of the entire structure .....	112
Figure 5.10: Block diagram of thin film process and channel fabrication .....	115
Figure 5.11: Patterned screen used for screen printing the silicone rubber creating the microchannel - mask 2 (a) and the sealing rings - mask 3 (b) .....	117
Figure 5.12: Sandwiched fused silica substrates showing the channel and the parallel facing electrodes ..	118
Figure 5.13: Integrated microfluidic channel with electronic circuits for system control and measurements .....	119
Figure 5.14: Focusing principle based on negative dielectrophoresis. Particles injected at the input of the channel follow the direction of the arrows and they are focused at the center of the channel. The two different colors on the electrodes represent the applied two electric potentials .....	121
Figure 5.15: Close up picture, through the aluminum blocks' opening, of the microchannel with the focusing and measurement electrodes .....	122
Figure 5.16: 3D structure electric potential distribution in the channel (a) and electric field distribution at the mid plane of the channel (b). Applied voltage is 10 and 0 Volts on the opposite electrodes of the trapezoid electrodes. Applied voltage is 1 and 0 Volt on the stripe electrodes. Scaled values are in Volts for electric potential and in Volts/meter for electric field.....	124
Figure 5.17: The mid plane distribution of gradient of squared electric field distribution at the focused interrogation point for perfect alignment of electrodes (a) and with 10 $\mu$ m x-direction shifted electrodes due to the misalignment of the substrates (b). Applied voltage is 10 and 0 Volts on the opposite electrodes of the trapezoid electrodes. Applied voltage is 1 and 0 Volt on the stripe electrodes. Scaled values are in Volts <sup>2</sup> /meter <sup>3</sup> .....	124
Figure 5.18: Polystyrene beads movement within the center of the microchannel. The polystyrene beads diameter is 15 $\mu$ m and the flow rate is 0.1 $\mu$ l/mn .....	128
Figure 5.19: Bulk stream of yeast cells movement under nDEP within the center of the microchannel between trapezoid and Y electrodes (a and b) and their movement under pDEP (c and d).....	129
Figure 5.20: Bulk yeast cells with bubbles formed due electrolysis with high conductivity of the media and low frequency of the applied voltage on trapezoidal electrodes (a) under nDEP and (b)Y electrodes under pDEP .....	130
Figure 6.1: The Y axis presents the particle dielectric constant when the mixture effective complex permittivity is $\epsilon_{eff}^* = 50 - j15$ and media complex permittivity is $\epsilon_m^* = 70 - j20$ for different values of volume fraction .....	147
Figure 6.2: The Y axis presents the particle dielectric loss when the mixture effective complex permittivity is $\epsilon_{eff}^* = 50 - j15$ and media complex permittivity is $\epsilon_m^* = 70 - j20$ for different values of volume .....	147
Figure 6.3: S-band physical cavity with two real views and a Catia <sup>TM</sup> drawing. The last picture shows the magnetic coupling mechanism at the input and output ports of the cavity connected to an SMA high frequency connector through 0.141 inch cable .....	151
Figure 6.4: S-band cavity resonant frequency peaks observed on the Agilent 8722ES network analyzer. 9 Peaks are observed for the S-band cavity with 35.6 cm of length.....	152
Figure 6.5: Temperature measurement setup on the S-band cavity .....	153
Figure 6.6: Complete measurement setup showing the S-band cavity, the capillary tube in the center of the cavity, the 8722ES network analyzer for insertion loss measurement and the computer for automatic control of the network analyzer giving automatic output results of the complex permittivity of the biological material.....	154
Figure 6.7: An example of Labview calibration image (a) and generated measurement image (b) on the GUI.....	157
Figure 6.8: Relative dielectric constant of distilled water, Acetone, Ethanol 99%, Methanol, Glycerol, Glycerol-distilled water 1:1 and D-PBS at different S-Band frequencies (at temperature of 23 $^{\circ}$ C) .....	159

Figure 6.9: Relative dielectric loss of distilled water, Acetone, Ethanol 99%, Methanol, Glycerol, Glycerol-distilled water 1:1 and D-PBS at different S-Band frequencies (at temperature of 23°C) .....	160
Figure 6.10: Relative dielectric constant of WBC Hela, prostate, breast, uveal melanoma cancer cells with volume fraction of inclusion equal to 0.7 at different S-Band frequencies (at temperature of 23°C) .....	162
Figure 6.11: Relative dielectric loss of WBC, Hela, prostate, breast, uveal melanoma cancer cells with volume fraction of inclusion equal to 0.7 at different S-Band frequencies (at temperature of 23°C) .....	163
Figure 6.12: Uveal melanoma cancer cell line 92.1 dielectric constant reduction ( $\Delta\epsilon'$ ) after 60 minutes of test. Results are shown for each discrete mode frequency .....	164
Figure 6.13: Uveal melanoma cancer cell line 92.1 dielectric loss reduction ( $\Delta\epsilon''$ ) after 60 minutes of test. Results are shown for each discrete mode frequency .....	164
Figure 7.1: Cross frequency measurement chip. The chip consist of several planar electrodes permitting the application of low AC signal .....	172
Figure 7.2: High frequency signal detector circuit containing the RF/Microwave detector, the filtering and amplification components.....	175
Figure 7.3: Simple measurement set-up for high frequency detection of cells.....	176
Figure 7.4: A picture of the detector circuit with the Schottky diode detector at the left and the amplifier circuit at the right.....	176
Figure 7.5: A top view picture of the microchannel and the electrodes of first device for single cell characterization. The height of the channel is 50 $\mu\text{m}$ and all electrodes widths and gaps are 50 $\mu\text{m}$ .....	179
Figure 7.6: The substrate of the second device (ABTECH Scientific, Inc.) fabricated for a height of 40 $\mu\text{m}$ and line widths and gaps of 15 $\mu\text{m}$ .....	180
Figure 7.7: A picture of the second device with the 2 SMA high frequency connectors .....	181
Figure 7.8: Different CPW line segments in the microdevice. The 4 segments on the left of the center overlap section are repeated on the right.....	182
Figure 7.9: Analytical results of the return loss of the RF/Microwave path consisting of CPW lines and with or without a particle between the parallel facing electrodes.....	183
Figure 7.10: Analytical results of the insertion loss of the RF/Microwave path consisting of CPW lines and with or without a particle between the parallel facing electrodes.....	184
Figure 7.11: A picture with two different angles (in HFWorks) of a particle between two facing electrodes. The particle is assumed spherical. The overlapped electrodes are at the tips .....	185
Figure 7.12: Simulation results of the insertion loss and the return loss of the RF/Microwave path with the particle between the overlapped parallel facing electrodes .....	186
Figure 7.13: Simulation results of the insertion losses of the RF/Microwave path with and without the particle between the overlapped parallel facing electrodes .....	187
Figure 7.14: The total impedance of overlapped parallel facing electrodes with (Z1) and without (Z2) the 92.1 cell. The cell is suspended in Glycerol .....	190
Figure 7.15: The difference of the total impedance with and without the 92.1 cell (Glycerol) .....	190
Figure 7.16: The insertion loss of overlapped parallel facing electrodes with and without the 92.1 cell. The cell is suspended in Glycerol .....	191
Figure 7.17: The difference of the insertion loss with and without the 92.1 cell (Glycerol) .....	191
Figure 7.18: Another view of the difference of the insertion loss with and without the 92.1 cell (Glycerol) .....	192
Figure 7.19: The total impedance of overlapped parallel facing electrodes with (Z1) and without (Z2) the 92.1 cell. The cell is suspended in sucrose/dextrose.....	193
Figure 7.20: The difference of the total impedance with and without the 92.1 cell (sucrose/dextrose).....	193
Figure 7.21: The insertion loss of overlapped parallel facing electrodes with and without the 92.1 cell. The cell is suspended in sucrose/dextrose.....	194
Figure 7.22: The difference of the insertion loss with and without the 92.1 cell (sucrose/dextrose).....	194
Figure 7.23: Another view of the difference of the insertion loss with and without the 92.1 cell (sucrose/dextrose).....	195
Figure 7.24: The total impedance of overlapped parallel facing electrodes with (Z1) and without (Z2) the WBC. The cell is suspended in Glycerol.....	196
Figure 7.25: The difference of the total impedance with and without the WBC (Glycerol).....	196

Figure 7.26: The insertion loss of overlapped parallel facing electrodes with and without the WBC. The cell is suspended in Glycerol .....	197
Figure 7.27: The difference of the insertion loss with and without the OCM (Glycerol).....	197
Figure 7.28: Another view of the difference of the insertion loss with and without the WBC (Glycerol) ....	198
Figure 7.29: The total impedance of overlapped parallel facing electrodes with (Z1) and without (Z2) the WBC. The cell is suspended in sucrose/dextrose .....	199
Figure 7.30: The difference of the total impedance with and without the WBC (sucrose/dextrose) .....	199
Figure 7.31: The insertion loss of overlapped parallel facing electrodes with and without the WBC. The cell is suspended in sucrose/dextrose .....	200
Figure 7.32: The difference of the insertion loss with and without the OCM (sucrose/dextrose) .....	200
Figure 7.33: Another view of the difference of the insertion loss with and without the WBC (sucrose/dextrose).....	201
Figure 7.34: The complete RF/Microwave measurement set-up for the first device.....	204
Figure 7.35: The complete RF/Microwave measurement set-up for the second device.....	205
Figure 7.36: pDEP is observed on Bulk WBCs – Jurkat, Clone E6-1 attracted by the 2 types of focusing electrodes (Y shape and trapezoidal shape) within the microchannel. AC signal frequency is 1 MHz with amplitude of 20 Volts peak to peak.....	206
Figure 7.37: With a frequency of 10 KHz the WBCs – Jurkat, Clone E6-1 are still under pDEP but a bubble start to get built between trapezoidal electrodes .....	207
Figure 7.38: When the signal of the generator is OFF, WBCs – Jurkat, Clone E6-1 follow the flow of the media and the effect of pDEP is slowly vanishing. The 2 pictures show the evolution of the vanishing effect .....	207
Figure 7.39: pDEP is observed on uveal melanoma 92.1 cells attracted by the focusing electrodes within the microchannel. AC signal frequency is 1 MHz with amplitude of 20 Volts peak to peak .....	208
Figure 7.40: nDEP is observed on uveal melanoma 92.1 cells repulsed from the focusing electrodes and centered within the microchannel. AC signal frequency is 50 KHz with amplitude of 20 Volts peak to peak. In the four pictures the movement of the 92.1 cell at the center is observed. As seen in these pictures, when the particle gets close to the center of the channel with a smaller electrodes gap, the velocity of the particle is higher and the clarity of the picture of the particle is reduced due to this higher speed effect..	209
Figure 7.41: pDEP is observed on uveal melanoma OCM cells attracted by the focusing electrodes within the microchannel. AC signal frequency is 1 MHz with amplitude of 20 Volts peak to peak .....	210
Figure 7.42: nDEP is observed on uveal melanoma OCM cells repulsed from the focusing electrodes and centered within the microchannel. AC signal frequency is 10 KHz with amplitude of 20 Volts peak to peak .....	210
Figure 7.43: Insertion loss of the channel response filled with air (1 to 12 GHz).....	212
Figure 7.44: Insertion loss of the channel response filled with Glycerol (1 to 12 GHz).....	212
Figure 7.45: Insertion loss of the channel response filled with suspended 92.1 cell (1 to 12 GHz).....	213
Figure 7.46: Insertion loss of the channel response filled with suspended WBC (1 to 12 GHz) .....	213
Figure 7.47: Return loss of the channel response filled with air (1 to 12 GHz) .....	214
Figure 7.48: Return loss of the channel response filled with Glycerol (1 to 12 GHz) .....	214
Figure 7.49: Return loss of the channel response filled with suspended 92.1 cell (1 to 12 GHz).....	215
Figure 7.50: Insertion loss of the channel response filled with air (2 to 4.5 GHz).....	215
Figure 7.51: Insertion loss of the channel response filled with Glycerol (2 to 4.5 GHz).....	216
Figure 7.52: Insertion loss of the channel response filled with suspended 92.1 cell (2 to 4.5 GHz).....	216
Figure 7.53: Insertion loss of the channel response filled with suspended WBC (2 to 4.5 GHz) .....	217
Figure 7.54: Return loss of the channel response filled with air (2 to 4.5 GHz) .....	217
Figure 7.55: Return loss of the channel response filled with Glycerol (2 to 4.5 GHz) .....	218
Figure 7.56: Return loss of the channel response filled with suspended 92.1 cell (2 to 4.5 GHz) .....	218
Figure 7.57: The metallic enclosure for noise reduction over the first device (a) and the second device (b) .....	219
Figure 7.58: Insertion loss difference between media and 92.1 (2 to 4.5 GHz).....	221
Figure 7.59: Insertion loss difference between media and OCM (2 to 4.5 GHz).....	221

## List of Tables

<i>Table 1: The geometrical dimensions of the S band cavity.....</i>	<i>150</i>
<i>Table 2: The <math>TE_{10l}</math> mode frequencies in the S band cavity.....</i>	<i>150</i>
<i>Table 3: The cross frequency of different living cells with different media conductivities. The measurement error for cross frequency is less than 5 % for all living cells and conductivities used during measurement. The max AC signal frequency of the generator is 60 MHz.....</i>	<i>173</i>

# Chapter 1: Research Introduction

## 1.1 Introduction

In the recent years, the aging of the population associated with the increase demand of higher quality of life at old age has set a significant demand for higher quality medical care associated with faster and more accurate and minimal invasive assays [9]. The demand is more significant for systems that could provide early prediction of debilitating medical conditions. Most of the assays used blood, urine, saliva, tissue cells and tissues to detect and screen important clues associated with the medical condition. The outcome of these assays was reflected in the medical data which further emerged in better treatments, more effective drugs. The advancements in the early detection of specific medical conditions are further required to understand or early prevent diseases. Most of the present assays require high qualified personnel to prepare, analyze and perform the interpretation of the results as well as sophisticated and expensive equipment and long period of analysis time.

The emergence of new technologies such as MEMS (Micro Electro Mechanical Systems) in association with microfluidics and Lab-on-a-chip concept brings new type of available tools with the possibility to perform efficient tests and assays with very little help of the human operator and at relatively low associated costs. The introduction of Bio MEMS technology [10-12] and the good review documented by [13] created a synergy between the medical and engineering researchers. The ultimate objective was to reproduce the same laboratory biological assays with miniaturized Bio MEMS devices

associated to acceptable specific and sensitive results. Initial investigations have proved that Bio MEMS will be able to enrich the preventive capability of the laboratory assays through functions that yield more accurate diagnostics, earlier capture or better prognostics of medical conditions. With the commercially successful micro devices, the future of medical systems would be beneficial to the healthcare system as long as the detection and screening is accurate, safe and performed at low cost [14].

As above mentioned, the design of new components and devices using Bio MEMS needs the collaborative and close working environment between research engineers and medical researchers. Engineers bring the design expertise of MEMS components (microfluidics and lab-on-a-chip) while medical researchers contribute in identification and validation of the procedures and medical needs for implementation. This team working environment creates a multidisciplinary approach creating a team synergy for innovation of new components and tools. As a final product, it is desired by all parties to achieve commercially successful, reliable detection and screening noninvasive tools with low cost and minimum external manipulation.

## **1.2 Definition of the problem**

With the increase capability of diagnosing cancer patients, the development of a miniaturized Point Of Care (POC) equipment or devices is desired to detect and screen free Circulating Tumor Cells (CTC) in the blood. It has been demonstrated the presence of CTCs in the blood of patients having uveal melanoma (UM) before and after cancer treatment [15]. The early detection of cancer malignant circulating cells permits the prevention of the disease with early predetermined therapies. In fact, it is highly desired

to detect, characterize and identify cancer cells from a very small blood specimen at the physician office. This information would help the physician to take rapid and preventive action with his or her patient to avoid further progress of the condition which is associated with serious hardship and huge cost. Cells' sensitive and specific detection system requires a simple operation, low cost and maintenance free equipment. Microfluidic devices with incorporated sensitive and accurate detection mechanisms would probably be the appropriate technology and devices to satisfy such needs. Although several authors published different micro systems and micro flow cytometers for detection and sorting cancer cells [12, 16-23], the specific research area about cancer cell detection is in its early phase requiring more effort and focusing on finding new tools, new techniques and new devices for practical applications . Cancer cell detection tests must yield accurate results without false negative or false positive occurrences. According to the National Institute of Health (NIH), false negative test result indicates that a person does not have a disease when the person actually does have it. False positive test result indicates that a person has a specific disease when the person actually does not have it. The reason behind an inaccurate result and the rate at which they happen depend on the test type and the protocol used to double-check test results. Therefore, different tests are used to confirm the exact test results minimizing the false negative and false positive occurrences.

### **1.3 Objectives of the research**

The main objective of this research is to investigate the feasibility of a new approach or a measurement technique and a procedure to detect/count, characterize/

identify specific cells/cancer cells through non-chemical destructive assays. The detection, counting, characterization and identification could require the automatic manipulation of single cell in vitro using microfluidic devices. Although the overall research requires cell separation, detection/counting, characterization and identification, the major contribution of this research emphasizes on the characterization and identification of cancer malignant cells in flowing media or stream. With the Bio MEMS technology, the measurement device will contain microfluidic channel to circulate the sample stream at the convenient flow rate. Therefore the transport mechanism occurs in a microfluidic channel such that cells are surrounded by media. Several characterization and identification techniques with micro devices are investigated by other authors (optical, impedance, capacitance and others) while this thesis presents a technique based on RF/Microwave characterization and identification of cancer circulating malignant cells. Certain type of cells yield a specific absorption signature associated with their cell properties and condition. The block diagram of the microdevice architecture is given at Figure 1.1. Only actions identified by shading are part of this research investigation.

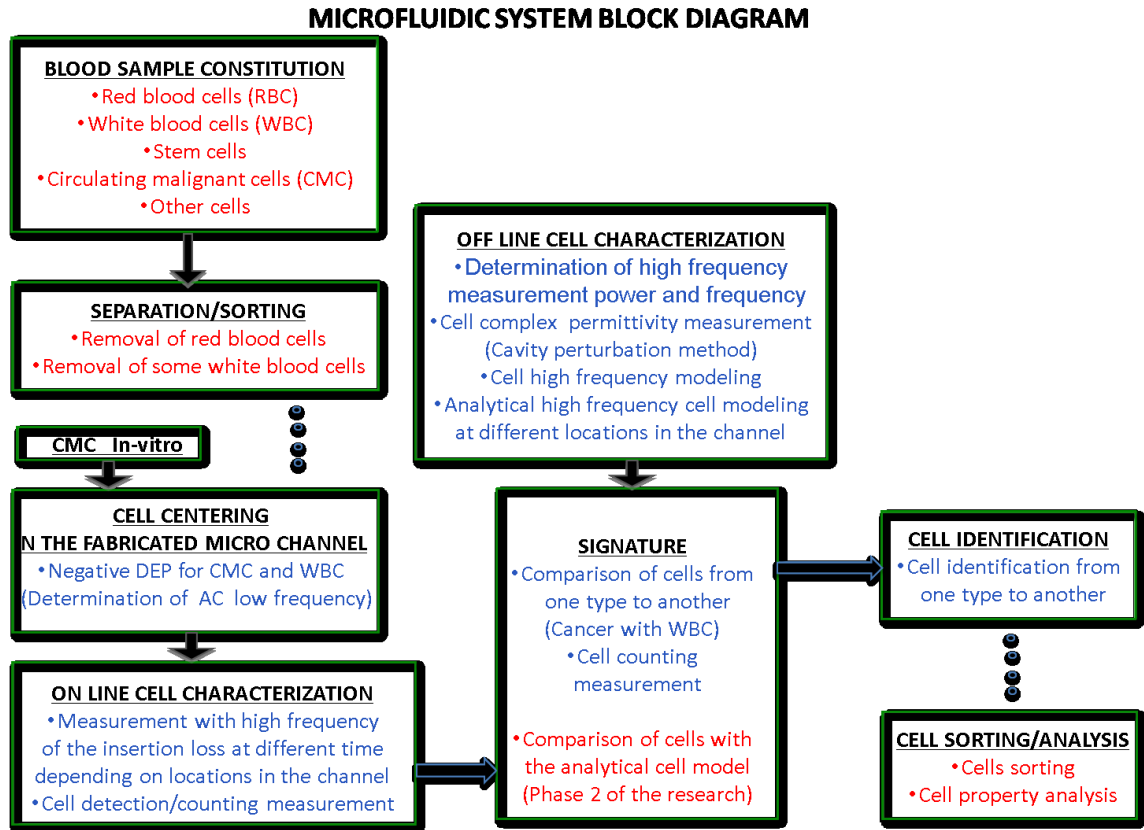


**Figure 1.1: Block diagram of microfluidic cell characterization system**

## 1.4 Originality of the thesis

Several researchers investigated, designed, fabricated and tested microfluidic devices to detect and analyze cancer and other type of cells [4, 24-26]. Most common devices designed by researchers in single cell analysis are microfluidic cytometers using optical and impedance detections to analyze the cells. Low frequency microfluidic detection methods could face measurement interference and large variability due to some low frequency effects such as ionic conduction, electrode polarization, interfacial polarization, high potential gradient at cell membranes/walls. Moreover at these frequencies it is quite difficult to discriminate between different types and sizes of bio

particles and internal cell structures of the same type since the properties of individual cell is masked by population variance (size, shape and dielectric properties or composition) [27-29]. Optical microfluidic detection methods, with very short wavelength, require fluorescent tags and a complicated sample preparation. At these photonic frequencies [30]:

- Scattering related to the size of particles is in the Mie scattering region (particle is about the same size as the light wavelength)
- Cell configuration yields resonant scattering
- Measurement is in scalar nature rather than vector nature
- Frequency dependent dielectric properties are in the resonance form.

With microwave frequencies, the interferences and variability are avoided, sample preparation is simple and physiological insight dielectric characteristic is improved by vector analysis since the scattering is relaxation type and not resonant.

To the knowledge of the candidate and to this date, no researchers or institutions use the RF/Microwave insertion loss measurement technique to detect, characterize and identify cancer cells in a miniaturized microfluidic system. RF/Microwave detection using low power electromagnetic signals (without heating) is an original way to identify the cells due to its simplicity, low manufacturing cost, and ease of sample preparation (fluorescent labeling is not needed as for flow cytometry). This method of characterization and identification based on the cell absorption measurement (amplitude and phase) is selective, specific and sensitive. Moreover, the drawback of optical detection is the difficulty of integrating optical sources and detectors at miniaturized and commercial level compared to microwave sources and detectors. With the advanced

techniques of Microwave Monolithic Integrated Circuits (MMIC) the complete RF/Microwave characterization and identification system can be made simple, accurate and cost effective.

## **1.5 Contribution**

Out of general objectives, the main research objectives require the fabrication of a device to manipulate and measure suspended particles with the desired goals predetermined within this work. Therefore, microfluidic devices were fabricated and completed, where different electrodes were designed within the micro devices. The device with its parallel facing electrodes (of different shapes) is used for Dielectrophoretic manipulation and for high frequency detection/identification of particles. The overall contribution is the attempt to use a technology to separate cells and to differentiate them using signature to RF/Microwave signal. Several considerations were taken into account during the fabrication: the use of biocompatible material, the hermeticity of the microchannel, and the cleaning and sterilizing simplicity of the microfluidic device. The mass production is also considered for future commercial considerations. This microdevice was capable to do on line measurements by centering the bio particles at the middle of the microchannel, detecting, counting and differentiating among particles using RF/Microwave frequencies. For Dielectrophoretic manipulation a low frequency signal is applied to some electrodes. For controlled manipulation of cells, the proper AC signal frequency was determined for each type of cancer cells and white blood cells. This is called the cross frequency.

A measurement methodology is also considered for high frequency identification of bio particles. The success of this method relies on the determination of the appropriate microwave off line measurement power and frequency bandwidth.

With a special fabricated set-up, uveal melanoma (line 92.1) and fibroblast cells were exposed to RF signal at different power levels and the proliferation of cells were observed. This experiment evaluated the effect of RF frequency range and power level on cells.

Another significant contribution is made by off line dielectric characterization of cancer and white blood cells. Different RF and Microwave cavities were fabricated and resonant cavity perturbation method was used to measure and characterize the complex permittivity of different cancer and white blood cells. The measurements were carried out automatically using a software program developed for monitoring at high frequencies the dielectric constant and dielectric loss with time. This information was never published by other authors.

## **1.6 Manuscripts in the thesis**

This thesis is a comprehensive summary of several papers presented in conferences and in scientific journals. License agreements between the author and the editors or authors to use figures in the thesis are found in Appendix A. The summary and the description of all these articles are presented in the Appendix B at the end of the thesis.

## **1.7 Microdevice system requirements, research methodology, plan and implementation summary**

### **1.7.1 Introduction**

The objective of this research can be achieved with the help of several resources and capabilities. The resources and equipment are mainly hardware material (micro devices and measurement equipment), software packages for finite element analysis and specific developed software for automatic testing. Moreover, these requirements will determine the methodology and detailed plan for the execution of the needed tasks in this research.

### **1.7.2 Micro devices**

Micro devices are usually designed using the overall system requirements. Based on the technology, the microdevice is intended to be fabricated. Out of these requirements and the existing technology, several questions are raised initiating appropriate planning for the design of micro devices and measurements of single cell. Some of these questions are the following:

- For single cell measurement and characterization at RF/Microwave frequencies, what will be the RF frequencies and power level without affecting the cells, and getting the maximum sensitivity and specificity?
- For single cell characterization measurement, how would the cells enter into the microfluidic channel, how they will be centered at the interrogation point, how they will be counted, and finally how they will be characterized on line?

- For comparison between on line experimental results and theoretical model, what are the specific cell features or parameters making possible the validation of RF/Microwave theoretical model versus measurement results? This will enable cell dielectric property determination.

### **1.7.2.1 Device for RF/Microwave frequency and power level determination**

RF/Microwave effect on cancer cells is investigated by injecting high frequency energy on cells through a high frequency radiation system. During radiation measurements, defined power levels and frequency ranges are used and, for cell survivability, they are kept in media solution for less than two hours. After radiation cycles, proliferation results enabled the estimation of the appropriate high frequency power level and frequency range necessary for single cell characterization without cell damage. The device fabrication details and measurements results are given in chapter 6.

### **1.7.2.2 Device for cell dielectric property determination (off line characterization)**

High frequency single cell characterization measurement can be validated when compared with the microdevice model containing the single cell. This is achieved by single cell model estimation and microdevice modeling at high frequencies. First single cell model is obtained by measuring its dielectric properties, then analytical solution and finite element analysis yields the microdevice model. For cell modeling, resonant rectangular cavity high precision perturbation method is used to determine and estimate

single cell's complex permittivity from 2 to 4.3 GHz. The microdevice is also modeled using high frequency analytical equations and finite element analysis (FEA) simulation. With this single cell estimated model and associated microdevice model for the transmission lines, the measurement results are compared for validation. The details of the microdevice model are found in chapter 3 and cavity perturbation device fabrication and measurement details are given in chapter 6.

### **1.7.2.3 Device for cell centering, detection and characterization (on line characterization)**

For single cell characterization measurement of biological cells suspended in a media, a microfluidic device is designed and fabricated. The requirements for the device capabilities are:

- Centering cells one by one at the center of the microchannel with DiElectroPhoresis (DEP) electrodes (for negative DEP force creation)
- Detecting/counting cells with low and high frequency electrodes
- Characterizing the cell at the interrogation point with high frequency electrodes (for insertion loss measurement).

All these electrodes need to be built as bio compatible for cells in suspension (gold or platinum electrodes). Moreover, the microchannel should be designed for easy cleaning sterilization and hermetic properties. Several parameters can affect the DEP force for cell centering and they are:

- The shapes and configurations of the DEP electrodes
- The microchannel height

- The initial position and the speed of the cells within the channel
- The electrical voltage applied on the electrodes
- The low frequency dielectric properties of the cell and the suspension media
- The cell or particles size or diameter.

With DEP force, several other forces are also present in the microfluidic channel and contribute to the overall applied forces on cells or particles. They are drag, buoyancy, and gravitational.

The parallel facing RF/Microwave electrodes are designed for minimum gap and minimum stray capacitance with the available fabrication process capabilities. Electronic circuit surrounds also the microchannel to inject DEP voltage inputs, detection input/output and RF input/output connectors. The circuitry can be a major source of measurement noise.

It is important to note at this point that off line measurement provides the complex permittivity estimation of each cell type and on line measurement detects and identifies single cell one by one within the microfluidic channel. This topic is covered in chapter 7.

#### **1.7.2.4 Device for RF cell detection**

A device made of high frequency detector with filtering is used to detect the passage of cells under the RF/Microwave electrodes through an oscilloscope. The low frequency signal is amplified with a low frequency amplifier and the signal is detected with an oscilloscope. The detection can be used to count the cells passing through the microchannel. This device description and measurement details are given in chapter 7.

## 1.8 Chapter summary and thesis layout

In this chapter, the problem definition is described emphasizing the need of Point of Care system to detect the presence of Circulating Tumor Cells (CTC). The objectives of the research are also presented where new approach is investigated for in vitro cancer cell's detection and identification with microfluidic devices through non chemical assays. The originality of the thesis relies on microwave frequency measurements on single living cell with the help of parallel facing electrodes within a microfluidic channel. The main contributions of this thesis are:

- Analytical modeling of dielectrophoretic force in a microfluidic channel with parallel facing electrodes
- RF/Microwave devices fabrication and measurement completion for frequency and power level determination on uveal melanoma cells
- Microchannel devices fabrication with all electrodes needed for cell manipulation and characterization at low and high frequency measurements.
- RF/Microwave dielectric property measurement device fabrication and different cancer cell dielectric constant and dielectric loss characterization.
- RF/Microwave Cell detection/counting device fabrication. Cells are detected and counted at high frequencies
- Single cell characterization and identification of cancer cells and WBC. Differentiating of normal WBCs from cancer cells

The answers to the questions addressed in this chapter initiate the literature review and the state of art followed by the theoretical understanding needs to the related

subjects. Chapter 2 presents the literature review and the state of the art for single cell centering, detection and characterization. Chapter 3 exposes the theoretical subjects needed for the completion of this project. The theory and the principle of Dielectrophoresis are given; the description of RF transmission line is given along with the analysis of cascaded stages followed by modeling the single cell between two parallel facing electrodes. Chapter 4 exposes the analytical analysis of dielectrophoretic force in a microchannel using Fourier series. Chapter 5 describes the fabrication of micro devices for ‘On line’ cell characterization and evaluation of the power and frequency applied during RF measurement. Chapter 6 provides all the details related to RF cavity fabrication and measurements technique for the determination of the dielectric properties (‘off line’ measurement of different living cells. Finally chapter 7 presents measurement details for cross frequency determination of different living cells, RF cell detection and counting and ‘on line’ single cell characterization and identification using microchannel device. The conclusions and the future works are found in chapter 8.

## Chapter 2: Literature Review and State of the Art

### 2.1 Introduction:

Recently, a new approach in the assessment of certain medical conditions is generally performed in vitro by medical assays on living cells. Specific substances are added to the extracted blood of the patient to avoid clumping and clustering of cells. The extracted blood specimen passes through different type of separation process.

The separation of cells is needed since blood is a mix of plasma and many other biological cells such as Red Blood Cells (RBC), White Blood Cells (WBC), platelets, Stem Cells and many others.

Four major methods for living cells separation are used:

- Centrifugation
- Micro-filtration
- Magnetophoresis
- Dielectrophoresis

Once cells are separated, they can be further manipulated for characterization and identification. The manipulation methods are mainly based on immunocytochemical and biomedical microarrays.

Classical centrifugation process separates the blood into layers of different type depending on their mass density. Markers are added to cells for counting and examining

for specific properties through medical bio-assays and cytometry. For example immunocytochemical method based on monoclonal antibodies is used to detect CTCs.

Another immunocytochemical method is the flow cytometry, where single cell stream flows at high speed in front of a laser beam and several optical detectors. The measurement is based on the interaction between single cell and the laser light beam through scattering of light and attached fluorescent probes. Thousands of cells can be analyzed every second by flow cytometer and this technique is sensitive to detect some type of cells. Up to 20 different types of cells can be detected with different optical markers according to cells properties [31].

The flow cytometry compared to Real Time Polymerase Chain Reaction (RT-PCR) is not able to confirm the tumor cells, and this makes the rejection of false positives quite difficult. Nevertheless, this technique has the advantage to enable further characterization at molecular level an action that cannot be carried out with RT-PCR where cells are destroyed for mRNA (messenger Ribo Nucleic Acid) extraction. Moreover, the efficient use of cytometry technique requires an enrichment technique to remove the unwanted cells from CTCs. Immunomagnetic enrichment technique is one of them. In this technique, magnetic beads are linked to antibodies with some affinity to CTCs. Then a powerful magnet is used to separate these specific cells. This technique is used by Veridex in the cell search systems [32]. Filtering enrichment is also used where small cells like leukocytes and erythrocytes pass through the filter leaving behind bigger malignant cells [33].

In microsystems, another separation technique uses Dielectrophoresis method to group cells of same type. During this type of separation care is required to avoid any high

electric field that might generate heat and damage cells. In a microfluidic channel the drag force increases with the square of velocity, therefore separation and centering cells in micro-channels are usually performed at low flow speed to obtain high separation accuracy.

The recent progress in micro device fabrication made possible the integration of different complex function within the device such as Lab-on-a-chip micro devices [34] [18, 28, 35-46]. With the advances in cell separation methods, the need of single cell detection, characterization and identification become the new interest in the bio medical area.

As of today, several techniques with very sophisticated and costly equipment were used to detect, trap, count, analyze, manipulate, sort, characterize and identify specific cells. Flow cytometer, Coulter counter and other biological technique such as Polymerase Chain Reaction (PCR) assays [47-49] are some of these techniques and assays commercially used. Flow cytometry which is based on optical-fluorescence detection is used to detect and count cells. It can also sort the cells at very high throughput at rates from 25 000 to 60 000 cells/second, and this within cell populations of relatively large size or big quantity of blood samples from 10 to 100 ml obtained from patients [50]. Several well established flow cytometer techniques are documented by several authors within the scientific community [51-60]. Good reviews as general reference about flow cytometry are found in [61-63].

Electrical measurement permits also rapid screening and counting (Coulter counting) providing an ideal format for rapid screening of a cell population with single cell resolution [36, 64-71].

In the last decade, several researchers and companies started looking at miniaturized technologies (Bio MEMS) for biological cell manipulation, analysis and cancer detection and characterization [4, 23, 24, 72-76]. Most of them use micro flow cytometers with optical detection methods, Coulter counters with microfluidic technology, impedance or capacitance measurement technique, magnetic and beads detection measurements and electromagnetic and spectrometry measurements.

For micro flow cytometer, tests were performed to observe the effects of Raman scattering on cells flowing into micro channels [77]. A silicon based V-groove microchannel with laser source and laser detection outside the microfluidic base material was patented [3, 78, 79]. The unit collects the small angle scattered light by a small angle photo detector. Large angle scattered and fluorescent lights are collected by a larger photo detector [80]. Veal and al presented a review on the developments in instrumentation and biological reagents for microbiological applications using cell fluorescent staining and flow cytometry for monitoring microbial cells [53]. Several other authors [4, 6, 12, 67, 78, 81-83] presented novel way of flow cytometry designs and operations of Fluorescence Activated Cell Sorters (FACS).

Coulter counters with microfluidic technology were investigated by several authors to count and detect cells [5, 65, 84, 85]. Electric based analysis of cells on a microfluidic platform was quantified and monitored in static and moving solutions [86]. The size and properties of cells are evaluated in real time by measuring the resistance change in a confined region.

Impedance or capacitance measurement techniques were used for immunodetection [87], and microbiological particles and cells detection and counting

[8, 37, 38, 68, 86, 88-90]. The principle is based on measuring the impedance through an AC signal to obtain the dielectric properties of the single cell.

Magnetic and beads detection measurements are used with magnetophoresis and electromagnetophoresis principles for micro separation of particles [91-93]. Magnetic field is used to induce the controlled migration of cells.

Electromagnetic and spectrometry measurements were suggested as a general microwave flow cytometry [94, 95].

From the problem description and the objective of the present research and after introducing the suspended particle in the injection zone of microfluidic device, the device needs to focus or center the cells at a detection/characterization location, detect/count the cells, characterize and identify the cells one by one for further validation steps. Therefore as first consideration, all these subjects are investigated through a literature review.

## **2.2 Cell centering at the interrogation point**

After the cells in media fed in the microfluidic device, the centering of cells enables the isolation and sequencing of each individual cell at the interrogation point for detection purposes and forces all cells to travel at the same velocity ensuring good detection. The passage of the cells requires the same transit pathway [96]. Without narrowing the microfluidic channel centering of cells avoids cells clogging in the narrow channels reducing the incidence of noisy and faulty results. The quality of centering is important in the good cell detection.

In what it follows, three major techniques for cell centering used by other researchers are summarized and elaborated description for each technique is given:

- Hydrodynamic centering
- Dielectrophoresis centering
- Electrokinetic centering

Different techniques and solutions are proposed in the literature for cell centering in microfluidic devices.

Hydrodynamic centering uses the laminar flow in micro channels. Thus, a sample flow containing the cell suspension is surrounded by a sheath. The sheath stream forces the cells specimen flow to get streamed in the middle of the channel and ensuring a flow of cells passing one by one through the center. The effect of the device geometry on the hydrodynamic centering of the cells flow is analyzed and the channel dimensions are assessed to achieve accurate hydrodynamic centering [97]. Several authors investigated different techniques using sample stream confined with sheath solutions at different flow rates to ensure an efficient hydrodynamic centering [13, 98-101]. Figure 2.1 shows the two input sheath flow and the vertical centering of the sample stream [73].

Dielectrophoretic manipulation and centering of particles under negative dielectrophoresis (nDEP) uses the principle of differential charge distribution on an electrical neutral charge by applying an AC harmonic signal on the two electrodes of different geometries (trapezoidal, arc form, etc.) surrounding a two-phase solution with the proper frequency and amplitude [35, 102-111]. Figure 2.2 shows the particles stream vertical/horizontal centered and confined particles between dielectrophoresis electrodes [73]. The AC signal with appropriate shape of electrodes creates a non-uniform electric field and the uncharged particles are moved under polarization effect.

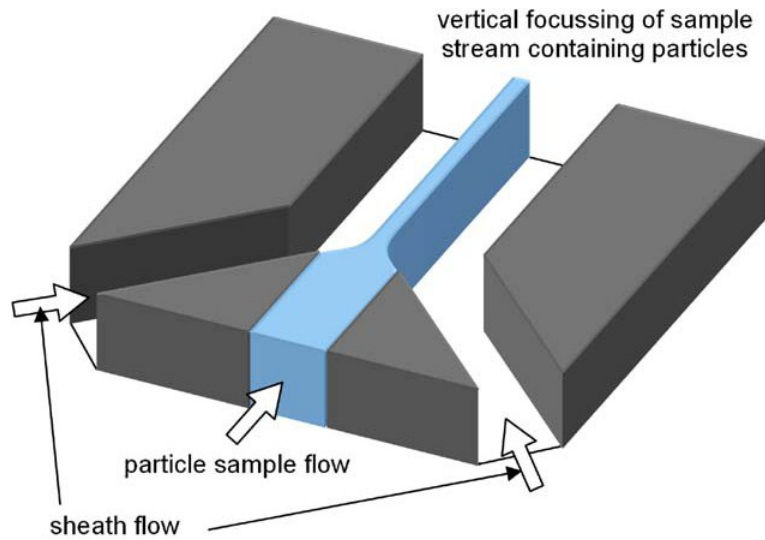


**Figure 2.1: Hydro fluidic centering of sample stream. The two input sheath flows push the particle sample flow and keep the particle vertically focused at the vertical center plane. Reprinted with permission from Holmes, Morgan et al. 2006 [73]**

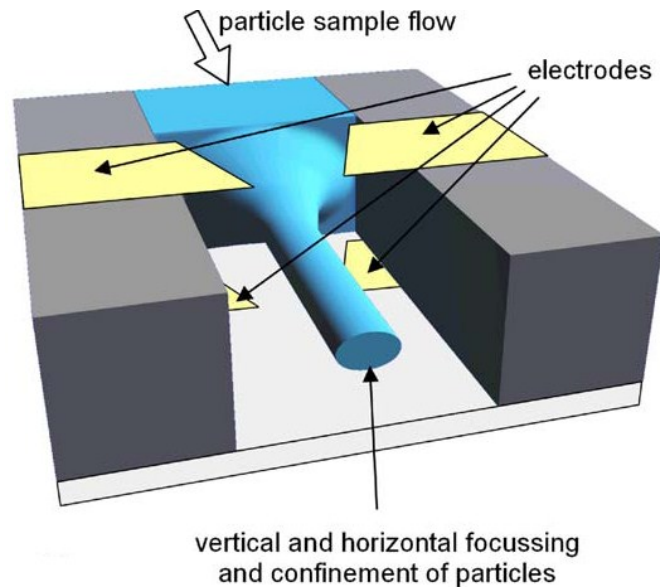


**Figure 2.2: Dielectrophoresis centering of sample stream. The electrodes are activated with low frequency voltage to create a negative dielectrophoresis force to repulse the particle flow and confined them at the center line of the microchannel. Reprinted with permission from Holmes, Morgan et al. 2006 [73]**

Electrokinetic centering uses high voltage or electrical fields to position the sample stream. This high voltage platform has the disadvantage to possibly affect the physiological property of the cells and also create noise in the measurements.

Electrokinetic focusing uses the electrokinetic transport to confine spatially both fluids and ions [20, 112].

Acoustic centering of flow cells is achieved with a piezo ceramic material modulated at the external surface of a glass capillary tube. Under this approach, the sheathless centering makes the assay cost significantly lower and simplifies the overall setup [110].

A detailed review about micro flow cytometry and specifically about the particle centering can be found in [13].

### **2.3 Cell detection and counting**

Some of electrical type research measurement techniques for cell detection and counting are summarized in what follows:

- Impedance change measurement
- Conductivity change measurement
- Resistance change measurement
- Capacitance change measurement

Sensing/detecting information can be identical to counting the cells as long as the information quality is significant, reliable with a good signal to noise ratio. The detected cells can be counted carefully since the sensing mechanism records the passage of the single cell within the channel. Nowadays, different techniques are investigated to detect cells.

Measurement of electrical impedance of single biological units is investigated using the Schwarz–Christoffel Mapping (SCM) method [8, 113, 114]. For example, electrometric analyzers monitoring impedance, conductance and capacitance change are commonly used to detect and count cells [88].

Microfluidic device to be used to capture physically single human cervical epitheloid carcinoma cells was suggested by [68] using impedance spectroscopy. The impedance spectroscopy is a technique used to characterize tissues or cells based on the knowledge of their electrical properties in the frequency domain [115].

Low cost micro Coulter counter [116] based on real time measurements of the impedance between electrodes is used to count particles. Several authors took the advantage of micro Coulter counter to detect and count cells within a microfluidic device [70, 84, 85, 117, 118].

Electronic gate detector (impedance change) is suggested by [119] where cells are in suspension in a carrier media and pass through a small channel or gate.

Resistance measurement with four electrodes and a current source are used to convert resistance to voltage taking advantage of the lower conductivity of cells compared to the carrier media [90, 119].

Capacitance change measurement using 3 electrodes to overcome the drop of the parasitic resistance is presented by [87]. At frequencies in KHz, the electrolyte resistance acts as a parasitic resistance in series with the sensing structure and this affects the measurement of the sensor capacitance.

Several capacitance sensors have been designed and tested by several authors with different configurations and approaches [89, 120].

## **2.4 Cell characterization and identification**

Major research techniques for cell characterization/sorting can be classified in two groups:

- Batch characterization
- Single cell characterization

These techniques are summarized in what follows and elaborated further:

- Polymerase Chain Reaction (PCR)
- Optical flow cytometry
- Microwave flow cytometry
- Impedance spectroscopy
- Dielectric spectroscopy
- Capacitance change measurement
- Anti-Resonant Reflecting Optical Waveguides (ARROW) refractometer
- Fourier Transform Infra-Red-Micro Spectroscopy (FTIR-MSP)

Cells can be characterized and analyzed by biological methods or assays. One of most popular commercial method is the RT-PCR [121] or specific PCR [49]. PCR amplification is carried out on a Deoxyribonucleic acid (DNA) template and the reaction is performed by temperature cycling. Basically, DNA polymerase is used to amplify a piece of DNA (Deoxyribo Nucleic Acid) by in vitro enzymatic replication. This

amplification generates millions of copies of the DNAs enabling the extraction of genes and getting more information about the genes. Real Time-PCR enables the detection and the quantification of a targeted DNA [122].

For at least the last decade commercial flow cytometers with optical detection at high speed are used to characterize and sort cells. Characterization is carried out by marking specific proteins that are expected to be overexpressed by cells with fluorescent fluids that will yield specific optical wavelength recognition by the optical system.. Finally all the information is processed and analyzed through a processor and a computer program [32].

As mentioned earlier, several other major techniques and tools for microfluidic channel are demonstrated by different authors. Microwave flow cytometry with a detection of the cells through microwave signal emission and reception [95] and capacitance or impedance or dielectric measurement tools were used in the study of the passive properties of biological cells and tissues [37, 114, 123-125]. Many other less important techniques such as ARROW refractometer and FTIR-MSP are also used [126, 127].

Figure 2.3, Figure 2.4 and Figure 2.5 show some examples of impedance measurement and operation of flow cytometer [8, 38, 68].

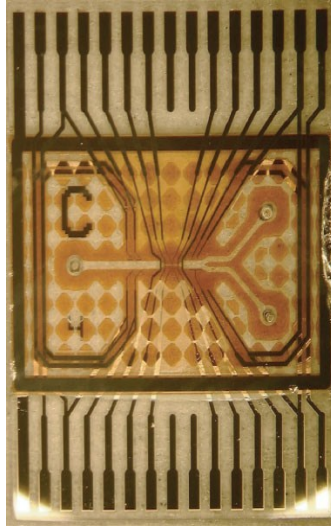


**Figure 2.3: Picture of the glass chip impedance spectroscopy flow cytometer. Reprinted with permission from Cheung, Gawad et al. 2005 [8]**

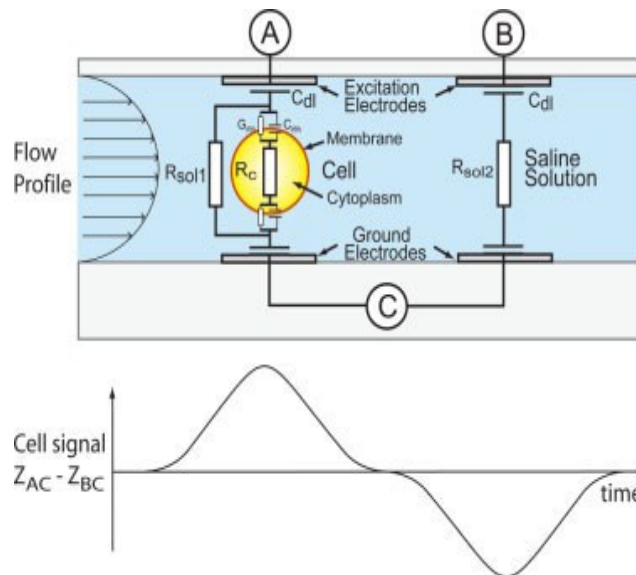


**Figure 2.4: Cross section of the microfluidic channel with the particle passing between electrodes and its electrical simplified model at the cell detection region. The graph shows the differential impedance versus the time. Reprinted with permission from Cheung, Gawad et al. 2005 [8]**

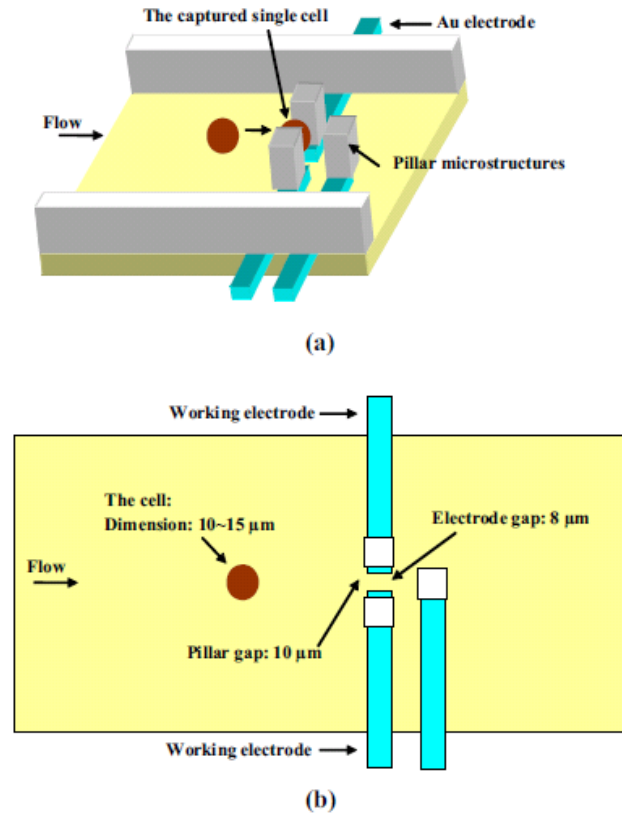


**Figure 2.5: 3D (a) and 2D (b) pictures where HeLa cell captured at micro pillar is measured for impedance with impedance spectroscopy system at low frequency. Reprinted with permission from Jang and Wang 2007 [68]**

The circuit of Figure 2.3 measures the impedance of cell population and can provide the cell size, the membrane capacitance and the cytoplasm conductivity as a function of frequency. Figure 2.4 presents the schematic of the side view of this microfluidic channel with the particle passing between the electrodes and its electrical simplified model at the cell detection area. Figure 2.5 is another example of impedance measurement system. When the HeLa (cervical cancer) cell is captured by the micro pillar then the impedance is measured by impedance spectroscopy at low frequency between 1 to 100 KHz.

As stated in the introduction, all these particles or living cells in the form of bulk or as single cell are characterized either with technologies and techniques using low frequencies or optical frequencies. The results obtained with these techniques could not address the expected outputs for prognostic evaluation and further cell investigation. For example the introduction of other agents to the cell, such as marker or fluorescent tags, could alter the properties of the cells for further assessment. No significant research investigation was performed for cell measurements in the vicinity of RF/Microwave within a microfluidic device. This is why a further investigation is needed for high frequency measurement in a microfluidic device without using any external agents.

## **2.5 Chapter Summary**

This chapter presents researchers works and investigations in developing devices and measurement techniques for cell manipulation and cell detection/characterization. Centering and confining cells at the center of the microchannel reduce the measurement errors for cell detection. Most of the existing investigated techniques use optical and low frequency detection. The technologies used do address bulk cells characterization and very little investigation is found for single living cell detection. Moreover some of these technologies require the use of tags or markers. Therefore there is a need to investigate a new technique and measurement method without using tags and characterizing cells one by one in a microfluidic channel.

## **Chapter 3: Theoretical Analysis for Single Cell Manipulation, Centering, Detection and Characterization**

### **3.1 Introduction**

There is evidence that single cell expression may reveal specific medical condition of the patient. The characterization of single cell is really challenging from the perspective of separation of the cells of interest, such as CTC, from the patient blood and individually characterization of these cells. Therefore the investigation of RF/Microwave technique for cell characterization implies the study of proper transmission lines for micro channels and the need to control the motion of cells by accurately position them in the length and height of the channel.

Most of the living cells have diameters between 5  $\mu\text{m}$  and 25  $\mu\text{m}$ . This dictates the height of the microchannel to be close to twice the maximum diameter to reduce the chances of clotting due to cell clustering and other effects. The width of the channel is also chosen to be about five times the height of the channel for better manipulation and control of cells. Trapezoid electrodes are used creating negative DEP forces on cells within the channel to center them into the interrogation region. At this point (mid center of the channel) cell diameter size overlapped facing electrodes are present for RF/Microwave measurement. Input and output holes are also created on one of the wafer for cell and media injection and recuperation.

The completion of this thesis requires the study of several theoretical subjects related to the specifications, design and fabrication of microfluidic devices. The role of single cell characterization and identification microdevice is to center first the cells in the

middle of the channel, at the interrogation point, then to detect and characterize them at high frequencies. For high frequency on line characterization and measurement validation, off line characterization or cell's dielectric properties determination is needed for capacitance modeling of cells. Therefore this chapter starts with the study of dielectrophoresis theoretical analysis for cell focusing, followed by high frequency transmission line analysis for RF electrodes in the microchannel. The single cell model within two facing electrodes at high frequency is presented considering the fringing capacitance effect. Then the theory of measurement of cell's complex permittivity at high frequencies is detailed. This measurement enables the characterization of dielectric properties of the living cell. Finally the analysis of fluid flow in microchannel with all present forces is overviewed.

## **3.2 Dielectrophoresis**

### **3.2.1 Principle of Dielectrophoresis (DEP)**

Theoretical and analytical studies of DEP are required for proper design of cell focusing at the center of a microchannel. Dielectrophoresis can direct the motion of a particle in suspended media under forces resulting from electric field gradient. Figure 3.1 shows the effect of a particle in a uniform and non- uniform electric field. With the presence of uniform electric field, each half of the induced dipole creates forces on the opposite direction giving a zero net force. By the presence of non-uniform electric field, the two forces are not equal producing an overall non-zero net force [128].

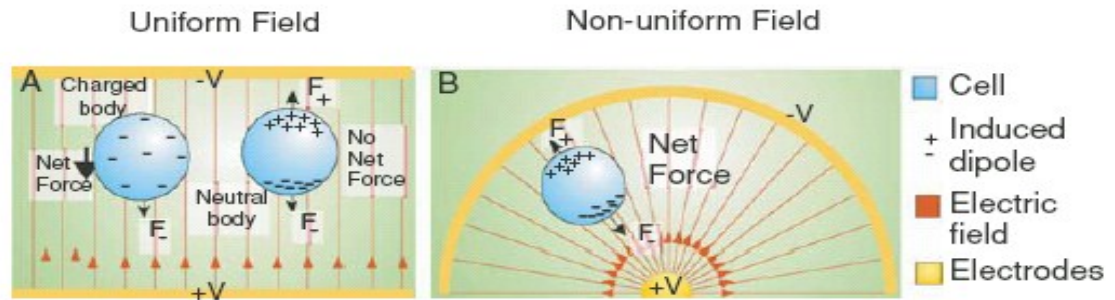


**Figure 3.1:** The effect of uniform and non-uniform electric fields on a cell or particle. Reprinted with permission from Voldman 2007 [129]

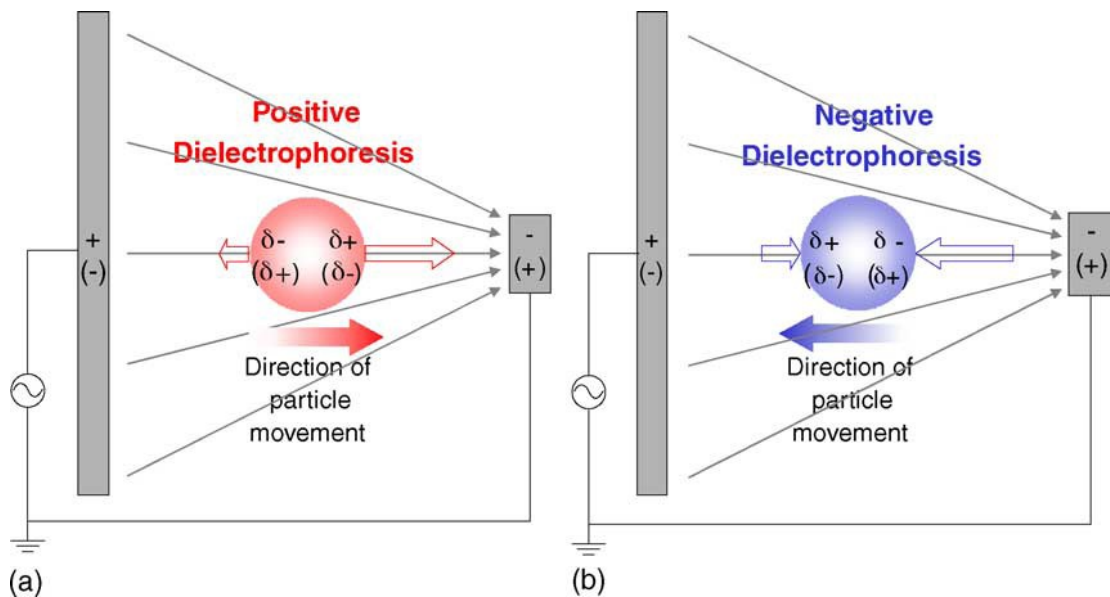


**Figure 3.2:** The effect of uniform and non-uniform electric fields on a cell or particle. a) When a particle is more polarized than the media, the particle moves towards the region with high electric-field strength and this is positive DEP. b) When a particle is less polarized than the media, the particle moves towards the region with low electric-field strength and this is negative DEP. Reprinted with permission from Doh et al 2005 [109]

Figure 3.2 shows the negative (nDEP) and positive (pDEP) dielectrophoresis effect. In fact depending on the dielectric properties of the particle and the media, the particle will move towards the region with high or low electric field strength.

Nevertheless, when a particle suspended in a solution is subjected to an electric field, the particle and the solution are polarized creating a net unpaired surface charges at the interface of the particle and the solution. These surface charges create another electric field disturbing the original one as shown in Figure 3.3 [130]. The interfacial surface charges depend on the field strength, the permittivity and conductivity of the particle and the solution. With this non uniform electric field distribution it results a net force different than zero as shown in Figure 3.3. This represents the physics of the dielectrophoresis mechanism. With DEP, particles acquire a dipole moment and interact with each another. Therefore, polarized particles have a tendency to align along the field direction.

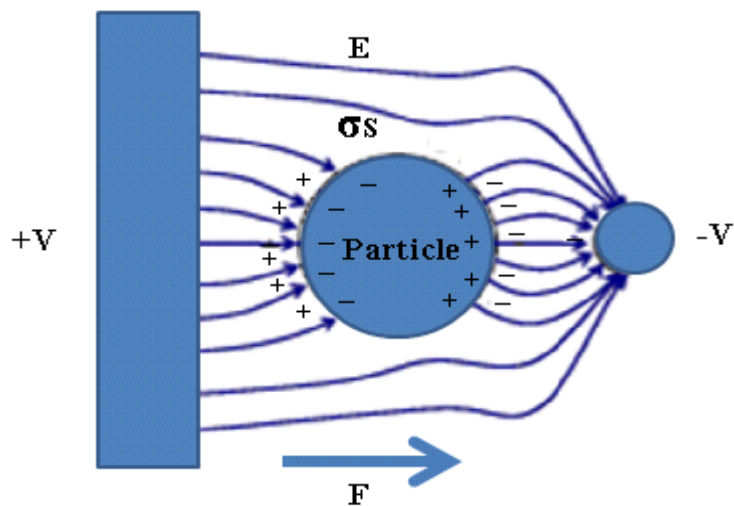


**Figure 3.3: Electric field distortions due to interfacial polarization. Adapted from Kua et al 2005 [130]**

### 3.2.2 Dielectrophoresis theory

In general the total force exerted by an electrical field on a particle consists of two terms (electrophoretic and polarization forces) [131]:

$$\mathbf{F} = Q_c \mathbf{E} + (\mathbf{P} \cdot \nabla) \mathbf{E} \quad (1)$$

where  $Q_c$  is the particle charge,  $\mathbf{P}$  is the particle dipole moment vector and  $\mathbf{E}$  is the electrical field vector. For a particle without a charge, the force is simply given by the polarization force:

$$\mathbf{F} = (\mathbf{P} \cdot \nabla) \mathbf{E} \quad (2)$$

Moreover, the polarization  $\mathbf{P}$  of a not perfectly insulating particle depends on the time variation of the applied electric field over some characteristic time interval in the recent past and is given by:

$$\mathbf{P} = 3V_p \varepsilon_0 \varepsilon_m \int_{-\infty}^t \bar{\beta}(t-t') \mathbf{E}(t') dt' \quad (3)$$

where  $V_p$  is the volume of the particle,  $\varepsilon_0$  is the air permittivity,  $\varepsilon_m$  is the dielectric constant of the media and  $\bar{\beta}(t)$  is the dielectric relaxation with:

$$\text{Re}(\beta^*) + j \text{Im}(\beta^*) = \int_0^{\infty} \bar{\beta}(t) e^{-j\omega t} dt \quad (4)$$

where  $j = \sqrt{-1}$  is the complex number,  $\text{Re}(\beta^*)$  and  $\text{Im}(\beta^*)$  are the real and the imaginary part of the Fourier transform of  $\bar{\beta}(t)$  respectively, and  $\omega$  is the AC signal oscillation frequency.

When an electric field is applied to suspended particles in a media, the orientation of the cell will depend on the frequency of the applied signal. Figure 3.4 gives the contribution of different polarization mechanisms [132, 133] described as  $\alpha$ ,  $\beta$  and  $\delta$  dispersion on a wide frequency range.  $\alpha$  dispersion region is the diffusion process of the ionic species.  $\beta$  dispersion region is the monitoring of dielectric properties of the biomass, where cell membrane and their interactions with the intra and extra cellular solutions are taken into

account (capacitive behavior). In the  $\delta$  dispersion region the electrical field can penetrate the cell membrane and dielectric properties are defined by the aqueous content of the biological molecules [134].

For a biological cell in a physiological solution, the interfacial polarization in the low frequency range of few KHz to about 10 MHz is of interest for particle transportation. The  $\beta$  relaxation or dispersion effect (interfacial polarization) is a Maxwell-Wagner induced dipole effect, with capacitive cell membrane charged through the cell interior and exterior fluids [135]. The  $\beta$  dispersion region can be looked as an important region with frequency variations in Clausius-Mossotti factor (CM) [129, 130].

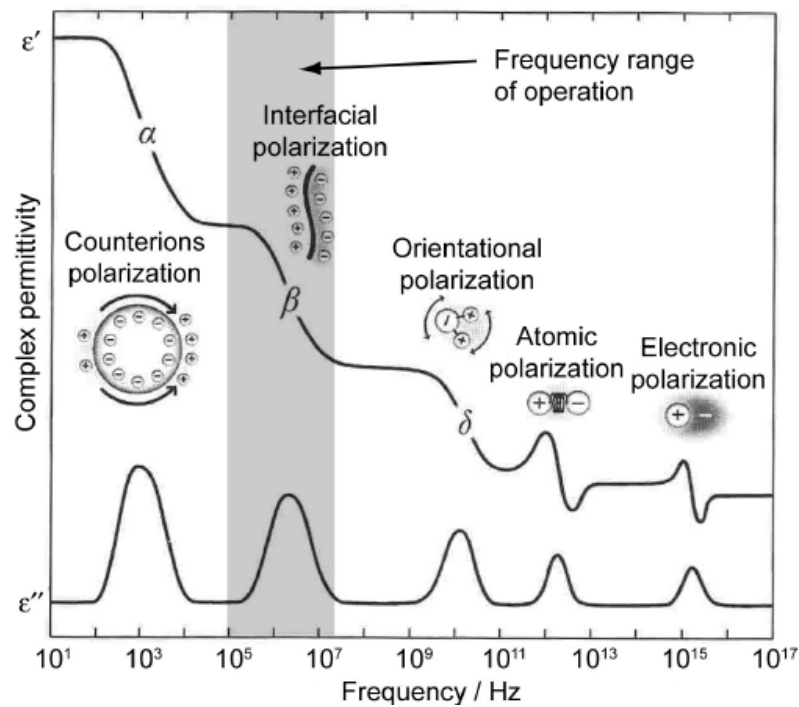


**Figure 3.4: Different polarization mechanisms of a dielectric particle in a solution. The curve shows the frequency dependence of the complex permittivity. The complex permittivity is composed by the dielectric constant  $\epsilon'$  and the dielectric loss  $\epsilon''$ . Reprinted with permission from Demierre 2008 [132]**

### 3.2.3 Clausius-Mossotti factor and DEP force

For a single low frequency AC applied signal, the polarization force  $\mathbf{F}$  or the time averaged DEP force on the particle is related to the instantaneous component of polarization [136] and is given by:

$$\mathbf{F}_{\text{DEP}} = \frac{3}{2} V_p \varepsilon_o \varepsilon_m \text{Re}[f_{CM}] \nabla |\mathbf{E}_{\text{RMS}}|^2 \quad (5)$$

where  $\text{Re}[f_{CM}] = \text{Re}(\beta^*)$  represents the real part of the Clausius-Mossotti factor identical to  $\text{Re}(\beta^*)$  and  $\mathbf{E}_{\text{RMS}}$  the root mean square value of the electrical field. Therefore the dielectrophoresis force depends on the particle volume, the dielectric constant of the media or the Clausius-Mossotti factor (dependent also of the AC signal frequency) and the amplitude of the AC signal (dependent also on the electrodes geometry).

When a particle is more polarized than the media (for positive real part of  $[f_{CM}]$ ), the particle moves towards the region with high electric-field strength and this is positive DEP. When a particle is less polarized than the media (for negative real part of  $[f_{CM}]$ ), the particle moves towards the region with low electric-field strength and this is negative DEP.

In general, the complex permittivity (CP) is given by:

$$\varepsilon^* = \varepsilon \varepsilon_0 - \frac{j\sigma}{\omega} \quad (6)$$

where  $\varepsilon$  is relative permittivity or dielectric constant,  $\sigma$  is conductivity and  $\omega$  is angular frequency.

For DEP,  $[f_{CM}]$  and  $\text{Re}[f_{CM}]$  can be related to the complex permittivity of the media and the particle by Maxwell-Wagner theory [137] and [138]:

$$[f_{CM}] = \frac{\varepsilon_p^* - \varepsilon_m^*}{\varepsilon_p^* + 2\varepsilon_m^*} \quad (7)$$

where  $\varepsilon_p^*$  and  $\varepsilon_m^*$  are the complex permittivity of the particle and the media respectively.

$$\text{Re}[f_{CM}] = \frac{(\varepsilon_p - \varepsilon_m)(\varepsilon_p + 2\varepsilon_m) + \left(\frac{\sigma_p - \sigma_m}{\omega}\right)\left(\frac{\sigma_p + 2\sigma_m}{\omega}\right)}{(\varepsilon_p + 2\varepsilon_m)^2 + \left(\frac{\sigma_p + 2\sigma_m}{\omega}\right)^2} \quad (8)$$

The dielectric constants in this formula are all relative values.

The transition from a positive DEP to negative DEP or vice versa happens at a frequency called cross frequency where the real value of CM factor becomes zero. When equation (8) equals to 0 the cross frequency is given by:

$$f_{CROSS} = \frac{1}{2\pi\varepsilon_0} \sqrt{\frac{\sigma_p^2 + \sigma_p\sigma_m - 2\sigma_m^2}{\varepsilon_p^2 + \varepsilon_p\varepsilon_m - 2\varepsilon_m^2}} \quad (9)$$

The DEP force is in general difficult to measure [139], therefore the real part of CM is calculated based on the relation between the applied frequency ( $f$ ), the cross over frequency ( $f_{CROSS}$ ) and  $C_{mem}$  the membrane capacitance [140]:

$$\text{Re}[f_{CM}] = \frac{f^2 - f_{CROSS}^2}{f^2 + 2f_{CROSS}^2} \quad (10)$$

$$f_{CROSS} = \frac{\sigma_m}{\sqrt{2\pi RC_{mem}}} \quad (11)$$

The cross frequency depends on the conductivity of the media, the size or the radius  $R$  of the particle and the membrane capacitance. These quantities are known for several type of cells [140] enabling the calculation of  $f_{CROSS}$ .

The cross frequency is also measured by varying the frequency and observing the transition from one type of DEP to another (nDEP to pDEP or pDEP to nDEP). With a more complex model of cells, two cross frequencies can be measured, one at low frequency and another one at higher frequency.

For transport and centering the cells toward the interrogation region low frequency electric potentials are used. The curves of Figure 3.5 and Figure 3.6 show the real value of CM factor versus the frequency of the AC signal for different living cell and different cell models [31, 132].

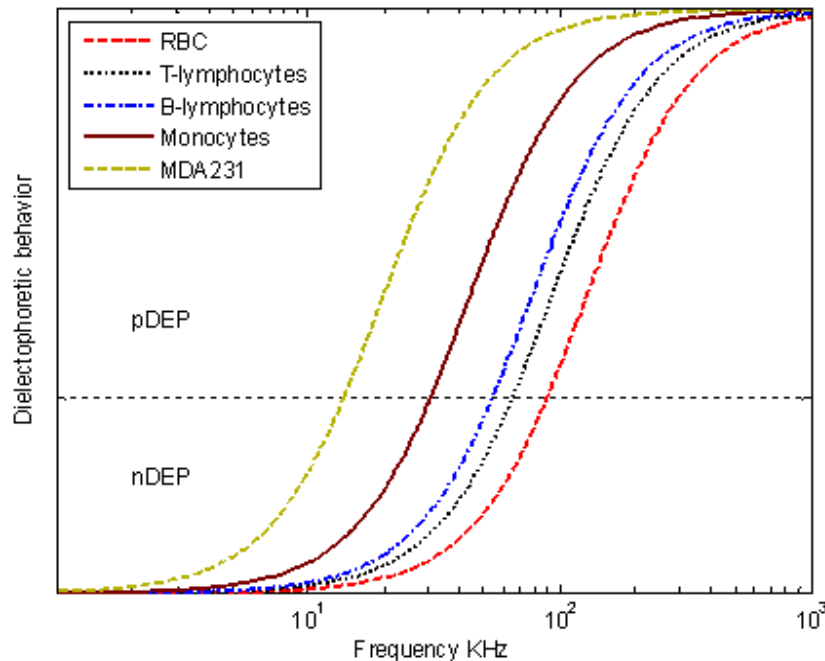


**Figure 3.5: Real part of CM versus AC frequency of the applied signal for different living cells in a media with conductivity of 10 mS/m. Reprinted with permission from Alazzam 2011 [31]**

Figure 3.5 shows the CM factor of different living cells. It is observed that all these cells present a negative DEP at low frequency and the MDA231 breast cancer cell line has the lowest cross frequency among these cells. The highest cross frequency is found for the RBC.

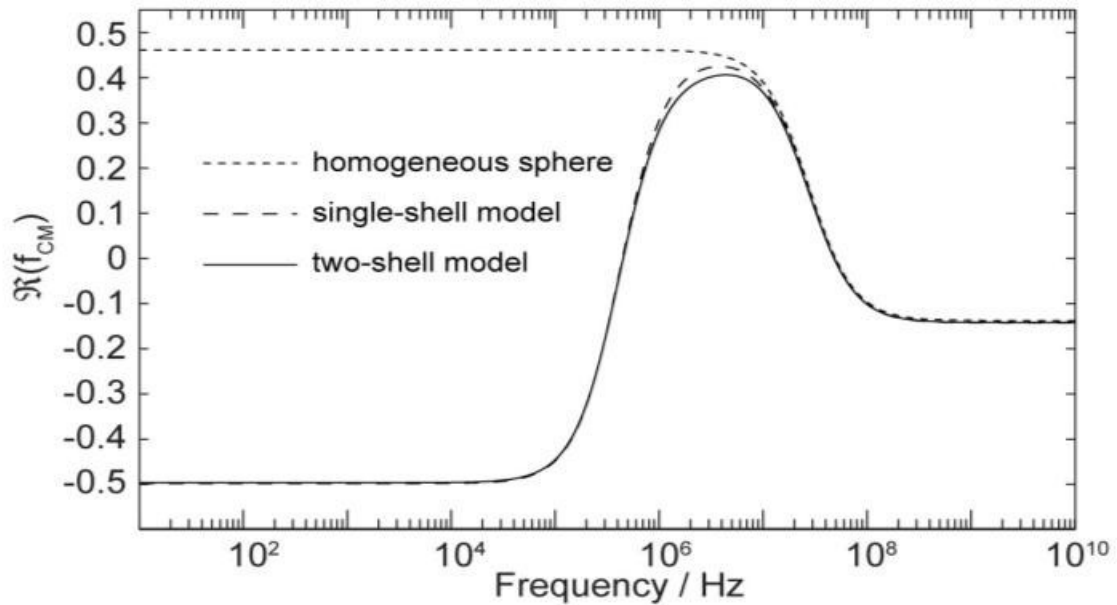


**Figure 3.6: Real part of CM versus AC frequency of the applied signal for different models of cells. Reprinted with permission from Demierre 2008 [132]**

### 3.3 RF/Microwave transmission lines

The characterization of the single cell at high frequencies is achieved using transmission lines between the high frequency emitter or source, measurement electrodes and receptor/ load. For microfluidic devices most used transmission lines are microstrip lines and CoPlanar Waveguides (CPW).

The microstrip line is made of a thin film line of conductor on one side of a dielectric substrate with a similar thin film ground plane conductor on the other side. The

electric and the magnetic fields travel in the dielectric substrate and the air. Therefore a Quasi-Transverse Electro Magnetic (Q-TEM) mode exists in this type of transmission line. The effective dielectric constant presented to the electromagnetic signal is calculated knowing the characteristics and dimensions of the dielectric and the conductors. The dielectric constant is related to the speed the wave travels in the transmission line and determines its characteristic impedance. The CPW line is made of a thin film center strip of conductor surrounded by two other films as ground conductors. Similarly its speed of propagation and the line characteristic impedance depend on the characteristics and the dimensions of the dielectric and the conductors. The advantage of CPW over the microstrip lines for microfluidic circuit is its planar configuration avoiding electrode deposition on both sides of the substrate such as glass or silicon. Therefore in what follows a theoretical analysis for CPW lines with different configurations is presented.

### 3.3.1 Coplanar waveguide transmission line theory

The general configuration of a CPW present in most of micro devices consists of three planar electrodes with three substrates, surrounded with two metal covers as shown in Figure 3.7. The presence of the two metal covers minimizes the noise at high frequencies. The study of this general case of CPW enables the calculation of all other CPW configuration variations.

The objective of analyzing the CPW line is to determine the overall effective permittivity ( $\epsilon_{eff}$ ) and characteristic impedance ( $Z_0$ ). The CPW lines consist of a signal electrode with a certain width  $2a$ , and adjacent finite ground electrodes deposited on a

substrate. The total separation of the ground electrodes is  $2b$  and the total distance between the two ground edges is  $2c$ .

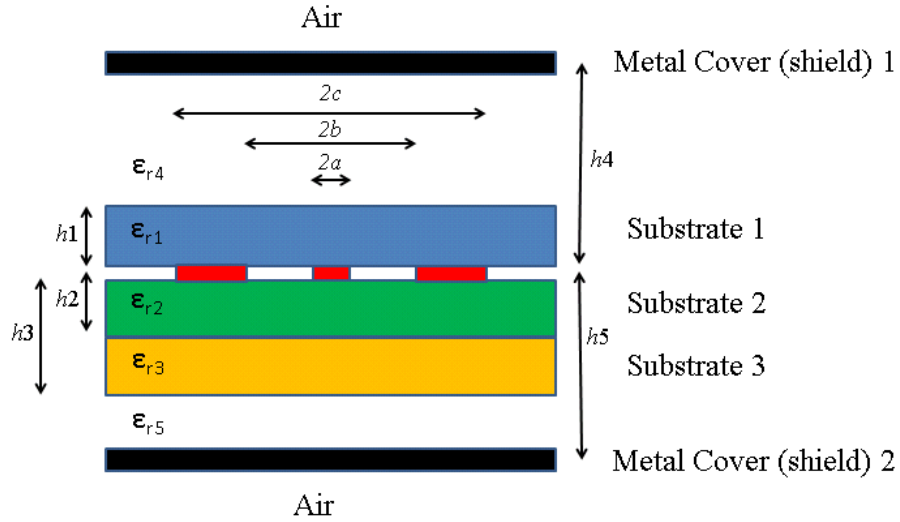


**Figure 3.7: Cross section of general CPW configuration**

The high frequency characteristics of the CPW, such as the effective dielectric constant of the line and the characteristic impedance, can be easily calculated if the dielectric constants of the substrates, of the gasket and the environment, and the geometric dimensions of electrodes as well as their spacing are known.

When the thickness of transmission lines is negligible and the dielectrics are infinitely wide, then the CPW line capacitance is calculated by:

$$C_{\text{CPW}} = C_{\text{air}} + C_1 + C_2 + C_3 + C_4 + C_5 \quad (12)$$

where the associated capacitances of Figure 3.7 configuration are well defined and described in the book of Simons [141] and in the article of Chen & Chou [142] and are given by:

$$C_{\text{air}} = 4\varepsilon_0 \frac{K(k')}{K(k)} \quad (13)$$

$$C_1 = 2\varepsilon_0 (\varepsilon_{r1} - \varepsilon_{r4}) \frac{K(k'_1)}{K(k_1)} \quad (14)$$

$$C_2 = 2\varepsilon_0 (\varepsilon_{r2} - \varepsilon_{r3}) \frac{K(k'_2)}{K(k_2)} \quad (15)$$

$$C_3 = 2\varepsilon_0 (\varepsilon_{r3} - \varepsilon_{r5}) \frac{K(k'_3)}{K(k_3)} \quad (16)$$

$$C_4 = 2\varepsilon_0 (\varepsilon_{r4} - 1) \frac{K(k'_4)}{K(k_4)} \quad (17)$$

$$C_5 = 2\varepsilon_0 (\varepsilon_{r5} - 1) \frac{K(k'_5)}{K(k_5)} \quad (18)$$

with

$$k = \frac{c}{b} \sqrt{\frac{b^2 - a^2}{c^2 - a^2}} \quad (19)$$

$$k' = \sqrt{1 - k^2}$$

$$k_i = \frac{\sinh\left(\frac{\pi c}{2h_i}\right) \sqrt{\sinh^2\left(\frac{\pi b}{2h_i}\right) - \sinh^2\left(\frac{\pi a}{2h_i}\right)}}{\sinh\left(\frac{\pi b}{2h_i}\right) \sqrt{\sinh^2\left(\frac{\pi c}{2h_i}\right) - \sinh^2\left(\frac{\pi a}{2h_i}\right)}} \quad (20)$$

$$k'_i = \sqrt{1 - k_i^2} \quad i = 1, 2, 3, 4, 5$$

$K$  represents the complete elliptical integral of the first kind and its arguments  $k$  and  $k_i$  are dependent on the physical dimensions of the line and the substrates or the environment.

The complete elliptical integral of the first kind is given by:

$$K(k) = \int_0^{\pi/2} \frac{d\theta}{\sqrt{1 - k^2 \sin^2 \theta}} = \int_0^1 \frac{dt}{\sqrt{(1 - t^2)(1 - k^2 t^2)}} \quad (21)$$

Therefore the effective dielectric constant and the characteristic impedance of CPW line in Figure 3.7 with  $c_o$  as the velocity of the light can be written as:

$$\varepsilon_{eff} = \frac{C_{CPW}}{C_{air}} = 1 + \frac{(\varepsilon_{r1} - \varepsilon_{r4})}{2} \frac{K(k)}{K(k')} \frac{K(k'_1)}{K(k_1)} + \frac{(\varepsilon_{r2} - \varepsilon_{r3})}{2} \frac{K(k)}{K(k')} \frac{K(k'_2)}{K(k_2)} + \frac{(\varepsilon_{r3} - \varepsilon_{r5})}{2} \frac{K(k)}{K(k')} \frac{K(k'_3)}{K(k_3)} + \frac{(\varepsilon_{r4} - 1)}{2} \frac{K(k)}{K(k')} \frac{K(k'_4)}{K(k_4)} + \frac{(\varepsilon_{r5} - 1)}{2} \frac{K(k)}{K(k')} \frac{K(k'_5)}{K(k_5)} \quad (22)$$

$$Z_0 = \left( \frac{1}{c_o C_{air} \sqrt{\varepsilon_{eff}}} \right) \quad (23)$$

$$Z_0 = \frac{30\pi}{\sqrt{\varepsilon_{eff}}} \cdot \frac{K(k)}{K(k')}$$

For different CPW configurations,  $Z_0$  formula is unchanged and  $\varepsilon_{eff}$  will change with dielectric permittivities of the environment surrounding the electrodes.

### 3.3.2 Different CPW line configurations within microfluidic devices

In a microfluidic device, three different configuration possibilities are found:

- Electrodes or lines on one substrate (standard CPW) as shown on Figure 3.8
- Electrodes or lines sandwiched between two substrates as per Figure 3.9
- Electrodes or lines sandwiched between two substrates with an addition gasket layer in between as per Figure 3.10

For simplicity, top and bottom ground layers of the entire following configuration are omitted.

#### 3.3.2.1 Standard CPW lines electrodes on one substrate

For a standard CPW line, with the equation **Error! Reference source not found.**)

and  $\varepsilon_{r2} = \varepsilon_{r3} = \varepsilon_{r4} = \varepsilon_{r5} = 1$ , then the effective dielectric constant becomes:

$$\varepsilon_{eff} = 1 + \frac{(\varepsilon_{r1} - 1)}{2} \frac{K(k)}{K(k')} \frac{K(k'_1)}{K(k_1)} \quad (24)$$

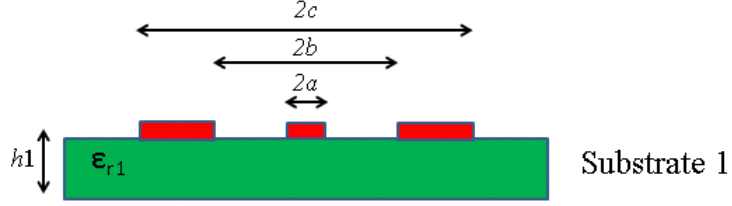


**Figure 3.8: Cross section of standard CPW line**

### 3.3.2.2 CPW lines electrodes sandwiched between two substrates

Similarly, for the configuration of Figure 3.9 the effective dielectric permittivity becomes:

$$\epsilon_{eff} = 1 + \frac{(\epsilon_{r1} - 1)}{2} \frac{K(k)}{K(k')} \frac{K(k_1)}{K(k_1')} + \frac{(\epsilon_{r2} - 1)}{2} \frac{K(k)}{K(k')} \frac{K(k_2)}{K(k_2')} \quad (25)$$

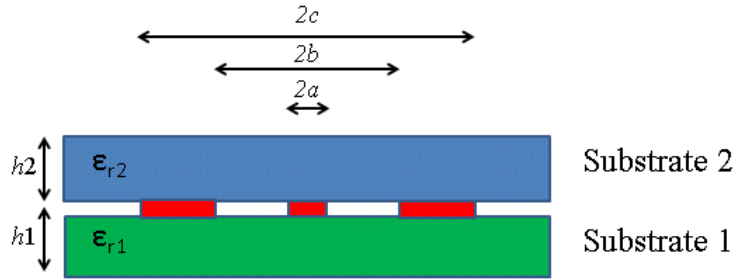


**Figure 3.9: Cross section of a CPW line sandwiched between two substrates**

For two identical substrates with dielectric constant  $\epsilon_{rs}$  and height  $h_l$ , the expression of the effective dielectric constant is simplified by:

$$\epsilon_{eff} = 1 + (\epsilon_{rs} - 1) \frac{K(k)}{K(k')} \frac{K(k_1)}{K(k_1')} \quad (26)$$

### 3.3.2.3 CPW lines electrodes sandwiched between two substrates with a gasket layer in between

For the configuration of Figure 3.10, the expressions of the effective dielectric constant can be written as:

$$\epsilon_{eff} = 1 + \frac{(\epsilon_{r1} - 1)}{2} \frac{K(k)}{K(k')} \frac{K(k'_1)}{K(k_1)} + \frac{(\epsilon_{r2} - \epsilon_{r3})}{2} \frac{K(k)}{K(k')} \frac{K(k'_2)}{K(k_2)} + \frac{(\epsilon_{r3} - 1)}{2} \frac{K(k)}{K(k')} \frac{K(k'_3)}{K(k_3)} \quad (27)$$

For two identical substrates with dielectric constant  $\epsilon_{rs}$  and height  $h_s$  (with  $h_{sg} = h_s + h_g$ ) and a gasket dielectric constant of  $\epsilon_{rg}$  with a height  $h_g$ , the expression of the effective dielectric constant is simplified by:

$$\epsilon_{eff} = 1 + \frac{(\epsilon_{rs} - 1)}{2} \frac{K(k)}{K(k')} \left[ \frac{K(k'_s)}{K(k_s)} + \frac{K(k'_{sg})}{K(k_{sg})} \right] + \frac{(\epsilon_{rg} - \epsilon_{rs})}{2} \frac{K(k)}{K(k')} \frac{K(k'_g)}{K(k_g)} \quad (28)$$

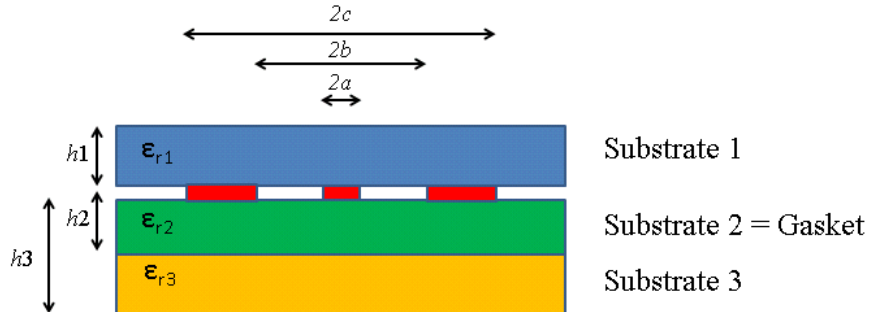


**Figure 3.10: Cross section of a CPW line sandwiched between two substrates with a gasket layer in between**

### 3.3.3 Transmission line matrix for CPW lines

A transmission lines are usually represented by different type of two port matrices. Some examples are  $Z$ ,  $Y$ ,  $ABCD$  and  $S$  matrices. When they are cascaded with each other, then the best transmission line representation in matrix form is the  $ABCD$

matrix since the overall matrix is the multiplication of all  $ABCD$  matrices together. The transformation from one type to another type representation is easily converted with standard transformation table that can be found in many books such as Pozar [143]. For a two port device, the  $ABCD$  matrix for Figure 3.11 is defined as:

$$\begin{pmatrix} A & B \\ C & D \end{pmatrix} \begin{pmatrix} v_1 \\ i_2 \end{pmatrix} = v \begin{pmatrix} v_2 \\ i_1 \end{pmatrix} \quad (29)$$

For a lossless transmission line of length  $l$ , the  $ABCD$  matrix is defined as:

$$\begin{pmatrix} A & B \\ C & D \end{pmatrix} = \begin{pmatrix} \cos(\beta_{lg}l) & iZ_o \sin(\beta_{lg}l) \\ \frac{i \sin(\beta_{lg}l)}{Z_o} & \cos(\beta_{lg}l) \end{pmatrix} \quad (30)$$

where  $\beta_{lg} = \frac{2\pi \text{ frequency} \sqrt{\epsilon_{eff}}}{c_o}$  is the phase constant .

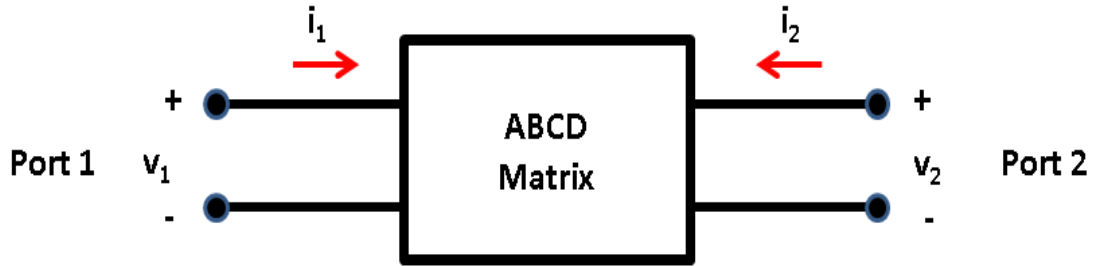


Figure 3.11:  $ABCD$  Matrix presentation with the input and output ports of the 2 ports device

### 3.3.3.1 Cascaded two ports or transmission lines

Cascaded transmission lines with known individual  $ABCD$  matrices can be represented by an overall  $ABCD$  matrix. As stated earlier, this is obtained by multiplying all the matrices together. Then the total  $ABCD$  matrix can be written as:

$$\begin{pmatrix} A_T & B_T \\ C_T & D_T \end{pmatrix} = \begin{pmatrix} A_1 & B_1 \\ C_1 & D_1 \end{pmatrix} \cdot \begin{pmatrix} A_2 & B_2 \\ C_2 & D_2 \end{pmatrix} \cdot \begin{pmatrix} A_3 & B_3 \\ C_3 & D_3 \end{pmatrix} \cdots \begin{pmatrix} A_n & B_n \\ C_n & D_n \end{pmatrix} \quad (31)$$

### 3.3.3.2 S parameters and extraction from ABCD matrix

S or scattering parameters are based on the reflection and transmission of waves, quantities that are complex numbers carrying amplitude and phase information. At RF and microwave frequencies, voltages and currents depend on time and also on space. Therefore at a certain point  $x_1$ , a voltage on a transmission line would be different than at another point  $x_2$  at a distance less than a wavelength. This is one of the reasons why power or incident/reflected waves are measured instead of voltages and currents. Hence, S parameters are defined as the reflection and the transmission of waves. For the two ports network of Figure 3.12 with incident waves defined as ‘a’ and reflected waves defined as ‘b’, the matrix form of S or scattering parameters is given [144]:

$$\begin{pmatrix} S_{11} & S_{12} \\ S_{21} & S_{22} \end{pmatrix} \begin{pmatrix} a_1 \\ a_2 \end{pmatrix} = \begin{pmatrix} b_1 \\ b_2 \end{pmatrix} \quad (32)$$

where  $S_{11}$ ,  $S_{22}$ ,  $S_{21}$  and  $S_{12}$  are complex scattering parameters expressed by amplitude and phase.

$S_{11}$  is defined as the reflection coefficient at port 1  $S_{11} = \frac{b_1}{a_1} \Big|_{a_2=0}$  .

$a_2=0$  means port 2 is terminated in  $50 \Omega$ .

$S_{22}$  is defined as the reflection coefficient at port 2  $S_{22} = \frac{b_2}{a_2} \Big|_{a_1=0}$  .

$a_1=0$  means port 1 is terminated in  $50 \Omega$ .

$S_{21}$  is defined as the transmission coefficient from port 1 to 2  $S_{21} = \frac{b_2}{a_1} \Big|_{a_2=0}$  .

$a_2=0$  means port 2 is terminated in  $50 \Omega$ .

$S_{12}$  is defined as the transmission coefficient from port 2 to 1  $S_{12} = \frac{b_1}{a_2} \Big|_{a_1=0}$ .

$a_1=0$  means port 1 is terminated in  $50 \Omega$ .

RF and Microwave signal has an internal impedance of  $50 \Omega$  and is usually terminated in  $50 \Omega$ . For different termination or load impedance a reflection is observed.

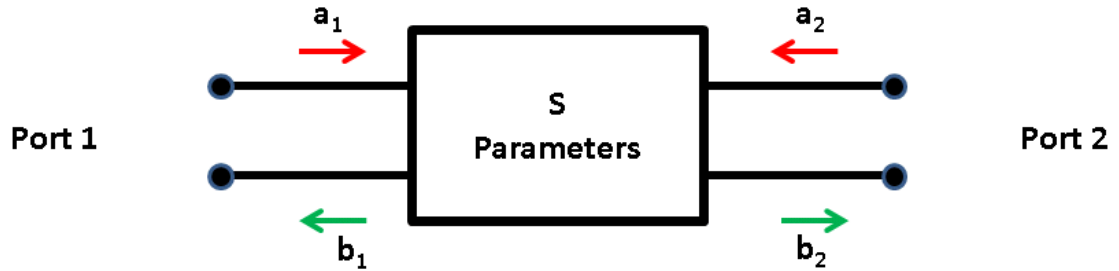


Figure 3.12:  $S$  parameter presentation with the input and output ports of the 2 ports device

When the overall  $ABCD$  matrix is known, the transformation from  $ABCD$  to  $S$  parameters is obtained [145] by the following expression:

$$S = \begin{pmatrix} S_{11} & S_{12} \\ S_{21} & S_{22} \end{pmatrix} = \frac{1}{A + \frac{B}{Z_o} + CZ_o + D} \begin{pmatrix} (A + \frac{B}{Z_o} - CZ_o - D) & 2(AD - BC) \\ 2 & -A + \frac{B}{Z_o} - CZ_o + D \end{pmatrix} \quad (33)$$

With the knowledge of the physical properties and dimensions of the transmission lines in the microfluidic device, cascaded CPW lines theory and extraction of overall  $S$  parameters can be numerically obtained by Matlab<sup>TM</sup>. With a Matlab code for the overall insertion loss, the actual single cell characterization structure can be estimated analytically.

## 3.4 Single cell model between two electrodes

### 3.4.1 Introduction

A particle or a cell is present between two parallel facing electrodes can be modeled as a lumped element at RF/Microwave frequencies as long as the electrodes dimensions are much less than the wavelength of the RF/Microwave signal. For microfluidic channel, the study of the impedance between two electrodes without suspended particle in media and with suspended particle in the media give an estimation of the impedance variation for these two situations. Moreover, for more complete model, electrodes fringing capacitances are added during the total capacitance estimation. If the channel geometrical dimensions, the media and the single cell high frequency dielectric properties are known (dielectric constant and dielectric loss), then an estimation of the impedance variation with and without the particle is found. The simple model of the single cell is a capacitance in parallel with a resistance extracted from its high frequency complex permittivity measurement. The length, width and height of the parallel facing plates are  $L$ ,  $W$  and  $h$  respectively. The two plates represent the overlapping electrodes where the single cell passes for RF/Microwave measurement. The overlapped electrodes surface area and height need to be optimized for reduced and optimal capacitance of the two plates with a particle. This optimization will ensure the high sensibility of the micro device. For simplicity, the particle between two facing electrodes is considered having a rectangular geometric shape with the length, width and height equal to  $L_p$ ,  $W_p$  and  $h_p$  respectively as shown in Figure 3.13.

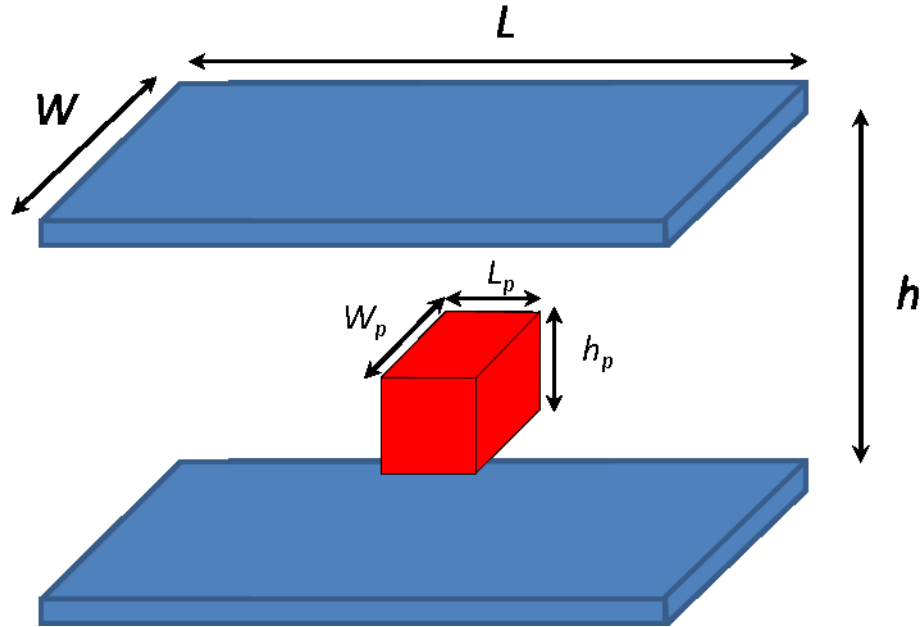


**Figure 3.13: Physical model of a particle between two parallel facing electrodes. The overlapped two plates are considered as the tips of electrodes where the centered particle will be present and be measured at RF/microwave frequencies.**

The overall model of the cell between two electrodes with parametric design considerations is assessed using a Matlab code to compare the results with experimental findings.

### 3.4.2 Model of two electrodes without cell or particle

Two facing parallel electrodes with a media in between are modeled as a simple capacitance in parallel with a resistance. When their geometrical dimensions are small, additional fringing capacitances are added to improve the model as shown in Figure 3.14. The main capacitance and the resistance are related to the physical dimensions of the electrodes, the gap in between and the dielectric constant and dielectric loss of the media respectively. For high frequency models, high frequency dielectric properties of the media are used. The main capacitance and the resistance are expressed as:

$$C_{media} = \varepsilon_0 \varepsilon'_m \frac{WL}{h} \quad (34)$$

$$R_{media} = \frac{h}{\sigma_m WL} \quad (35)$$

where  $\sigma_m = 2\pi f \varepsilon_0 \varepsilon''_m$

Moreover, the fringing capacitance is expressed as [146]:

$$C_{fringing} = \varepsilon_0 \varepsilon'_m \frac{WL}{h} \left[ \left( \frac{h}{\pi W} \right) + \left( \frac{h}{\pi W} \right) \ln \left( \frac{2\pi W}{h} \right) + \left( \frac{h}{\pi L} \right) + \left( \frac{h}{\pi L} \right) \ln \left( \frac{2\pi L}{h} \right) + \right. \\ \left. \left( \frac{h}{\pi W} \right) \left( \frac{h}{\pi L} \right) + \left( \frac{h}{\pi W} \right) \left( \frac{h}{\pi L} \right) \ln \left( \frac{2\pi L}{h} \right) + \left( \frac{h}{\pi W} \right) \left( \frac{h}{\pi L} \right) \ln \left( \frac{2\pi W}{h} \right) + \right. \\ \left. \left( \frac{h}{\pi W} \right) \ln \left( \frac{2\pi W}{h} \right) \left( \frac{h}{\pi L} \right) \ln \left( \frac{2\pi L}{h} \right) \right] \quad (36)$$

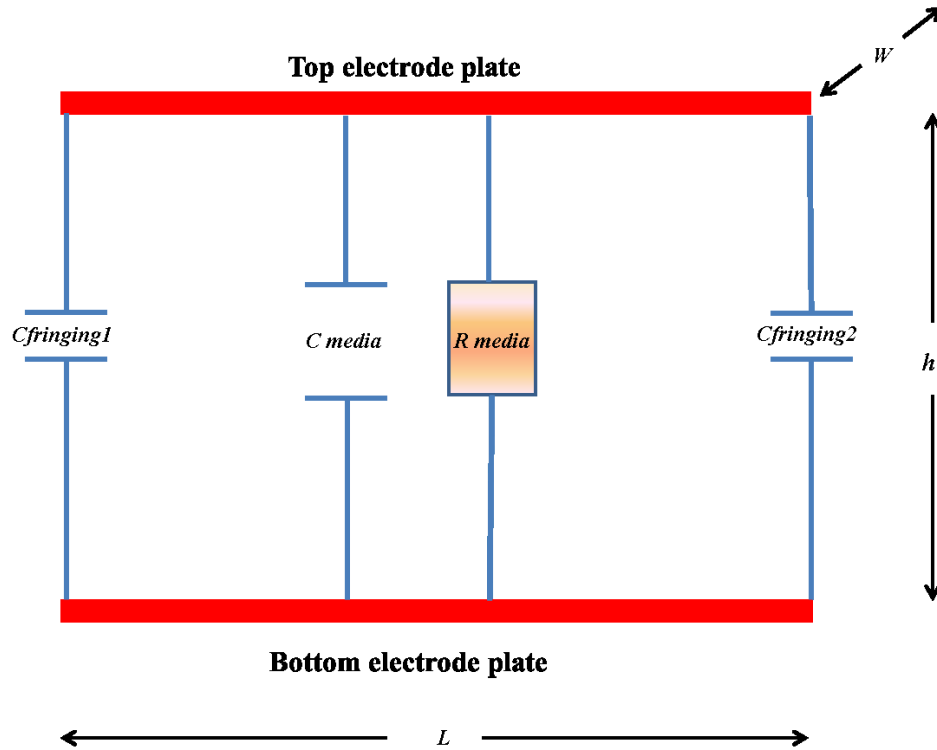


Figure 3.14: Model of the two facing electrodes separated by a media (with fringing effect). The picture shows a cross section of the electrodes with width equals to  $W$

Therefore, the total capacitance of the two facing parallel electrodes separated by a media is:  
is:

$$C_{mediawithfringing} = C_{media} + C_{fringing} \quad (37)$$

The total impedance of this configuration is equal to  $R_{media} = \frac{h}{\sigma_m WL}$  in parallel with the impedance of  $C_{mediawithfringing}$ .

### 3.4.3 Model of two electrodes with cell or particle

The model of a particle within parallel facing electrodes with the media in between is a more complex model resulting by several impedances in series and in parallel as shown in Figure 3.15.

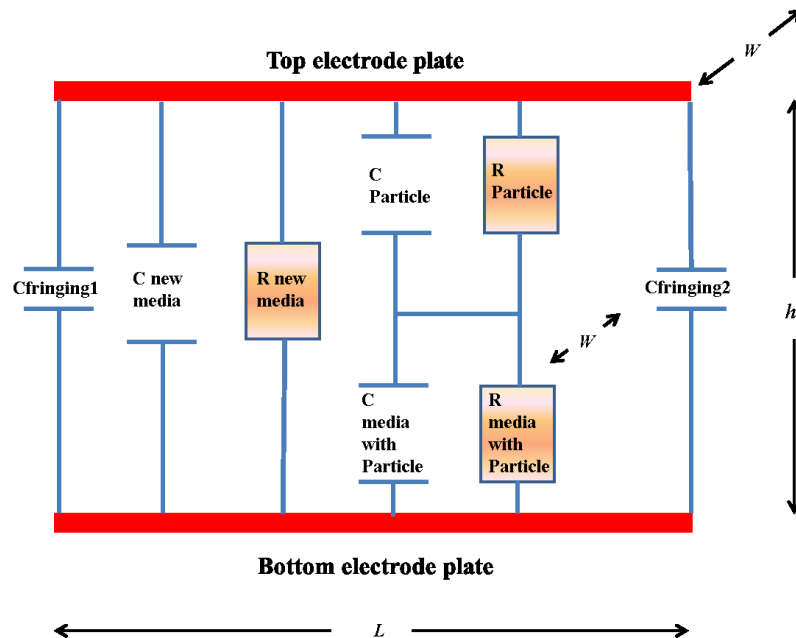


Figure 3.15: Model of the two facing electrodes separated by a media (with fringing effect) with the presence of the particle. The picture shows a cross section of the electrodes with width equals to  $W$

The capacitance and resistance of the particle are expressed as:

$$C_{particle} = \varepsilon_0 \varepsilon'_p \frac{W_p L_p}{h_p} \quad (38)$$

$$R_{particle} = \frac{h_p}{\sigma_p W_p L_p} \quad (39)$$

where  $\sigma_p = 2\pi f \varepsilon_0 \varepsilon''_p$

The capacitance and resistance of the media on the top and bottom of the particle under the electrodes are expressed as:

$$C_{media\ with\ particle} = \varepsilon_0 \varepsilon'_m \frac{W_p L_p}{h - h_p} \quad (40)$$

$$R_{media\ with\ particle} = \frac{(h - h_p)}{\sigma_m W_p L_p} \quad (41)$$

The capacitance and resistance of the remaining media under the electrodes excluding the particle are expressed as:

$$C_{new\ media} = \varepsilon_0 \varepsilon'_m \frac{(WL - W_p L_p)}{h} \quad (42)$$

$$R_{new\ media} = \frac{h}{\sigma_m (WL - W_p L_p)} \quad (43)$$

The total impedance is a combination of several elements in parallel and in series. The final electrical model with and without the particle is given at Figure 3.16.

A Matlab code gives the possibility to vary the geometric dimensions (for example the height of the microchannel and the dimension of the particle) and the dielectric properties

of the particle and the media to see their effect on the impedance or the insertion loss versus frequency with and without the particle. With known geometric dimensions of the microfluidic structure and the electrodes, this Matlab simulation is carried out in paragraph 7.4.2

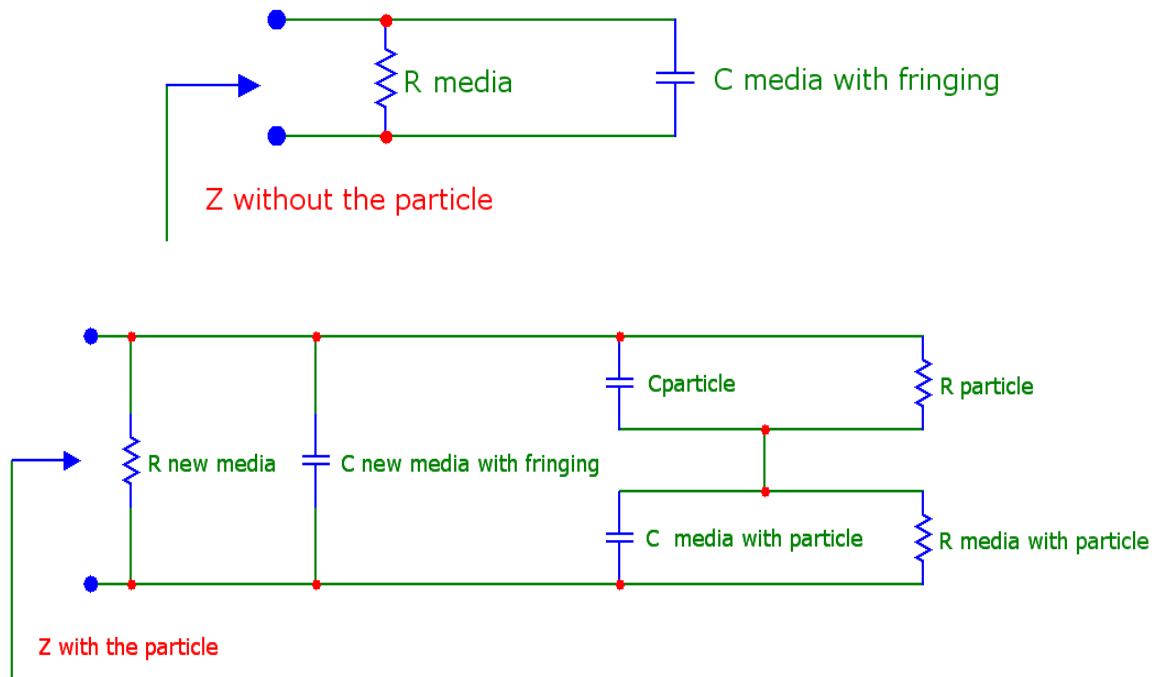


**Figure 3.16: The final electrical model of the two facing overlapped electrodes with and without the particle.**

### **3.5 Complex permittivity measurement theory (cavity perturbation method)**

#### **3.5.1 Introduction of complex permittivity**

Material dielectric properties can be characterized by the unique signature of the complex permittivity. Therefore dielectric property of a material determines how it will interact with an applied electromagnetic field. When biological samples are characterized

for complex permittivity, very small sample volumes are required. One of the effective and accurate measurement techniques is the cavity perturbation method.

In the resonant cavity perturbation method, the specimen of the material is introduced in the rectangular or circular cavity at the middle of the cavity in general. The measurement of resonant frequency and the quality factor of the cavity with and without the specimen enables the calculation of the complex permittivity of the specimen as in [147] and [148].

The complex permittivity has a relative real part defined as dielectric constant and a relative imaginary part representing the dielectric loss and the conductivity. These two parameters are relative to the dielectric constant of the air  $\epsilon_0 = 8.85 \times 10^{-12}$  F/m.

The complex permittivity can be written as [149]:

$$\epsilon^* = \epsilon_0(\epsilon' - j\epsilon'') = \epsilon_0\epsilon_r' - j\epsilon_0\epsilon_r''_{dielectric} - j\frac{\sigma}{\omega} \quad (44)$$

and the relative or normalized complex permittivity is given as [150]:

$$\epsilon_r^* = \epsilon_r' - j\epsilon_r'' = \epsilon_r' - j\epsilon_r''_{dielectric} - j\frac{\sigma}{\omega\epsilon_0} \quad (45)$$

where  $\epsilon_r'$  is the dielectric constant and  $\epsilon_r''$  is the DC conductivity  $\sigma$  and the dielectric loss ( $\epsilon_r''_{dielectric}$ ) and  $\omega$  is the angular frequency of the applied electric signal. All these quantities are frequency dependent.

### 3.5.2 Modes in rectangular resonant cavities

The principle of rectangular cavity perturbation method is obtained from the resonance of the cavity. Different modes can exist in the cavity depending on the

dimension or length of the rectangular cavity. The rectangular cavity can resonate at one frequency or several discrete frequencies (modes) depending on the dimension of the cavity. Several modes can be present in the cavity. A rectangular cavity with height, width and length equal to  $b$ ,  $a$  and  $d$ , where  $b$  is smaller than  $a$ ,  $a$  is smaller than  $d$  (Figure 3.17), then the dominant mode is  $TE_{101}$  (Transverse Electric). In the  $TE$  mode, the electric field is perpendicular to the direction of the propagation. The resonant frequencies of these different modes in the air filled cavity is given by the following expression [143]:

$$f_{101} = \frac{c_0}{2\pi\sqrt{\mu_0\epsilon_0}} \sqrt{\left(\frac{\pi}{a}\right)^2 + \left(\frac{\pi}{d}\right)^2} \quad (46)$$

where  $c_0$  is the speed of light in the air and  $\mu_0$  is the permeability of the air.  $TE_{101}$  is the waveguide dominant mode of the rectangular cavity having a length  $d$  equal to half of the wavelength  $\lambda$  divided by 2. This resonant cavity is a waveguide equivalent of short-circuited  $\lambda/2$  transmission line [143].

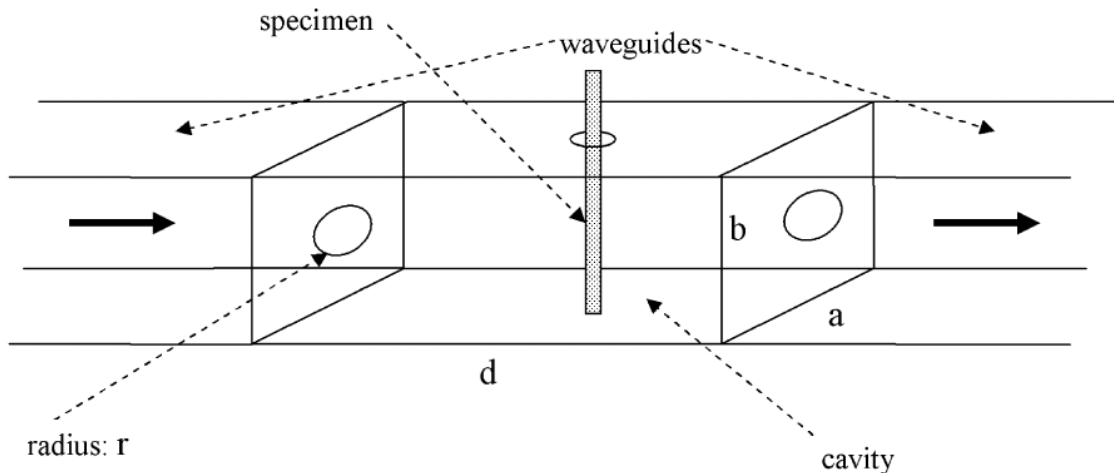


**Figure 3.17: A sketch of a rectangular cavity with the specimen capillary tube introduced at the position of the maximum electric field (at the center of the cavity). Reprinted with permission from Sheen 2009 [151]**

### 3.5.3 Rectangular cavity perturbation method

The theory and basic formulas for the calculation of the CP through the rectangular cavity perturbation method are given by several authors [148, 152-164].

Maxwell equations are formulated for two resonators, an empty cavity resonator and another cavity resonator that can be considered as the introduced non conducting specimen or perturber. The introduced specimen will create a perturbation by small deformation on the boundary surfaces of the cavity.

$$\begin{aligned}\nabla \times \mathbf{E}_o &= -j\omega_o \mathbf{B}_o \\ \nabla \times \mathbf{H} &= -j\omega \mathbf{D}\end{aligned}\tag{47}$$

In these two equations,  $\mathbf{E}_o$  and  $\mathbf{B}_o$  represent the electric field and magnetic flux density in the unperturbed or empty cavity and  $\mathbf{H}$  and  $\mathbf{D}$  are magnetic field strength and electric displacement field and respectively in the interior of sample. Waldron presented the specimen field's contribution as the perturbation fields added to the empty cavity fields [148]. The candidate adapted formulas of several authors and after elaboration and manipulation presented all the steps to come up with the final results. Using the scalar products of  $\mathbf{H}$  and  $\mathbf{E}_o^*$  fields over the preceding equations, where \* is the conjugate, the following formulation is obtained:

$$\mathbf{H} \cdot (\nabla \times \mathbf{E}_o^*) - \mathbf{E}_o^* \cdot (\nabla \times \mathbf{H}) = -j\omega_o \mathbf{H} \cdot \mathbf{B}_o^* - j\omega \mathbf{E}_o^* \cdot \mathbf{D}\tag{48}$$

with the equality

$$\nabla \cdot (\mathbf{E}_o^* \times \mathbf{H}) = (\mathbf{H} \cdot (\nabla \times \mathbf{E}_o^*) - \mathbf{E}_o^* \cdot (\nabla \times \mathbf{H}))\tag{49}$$

then

$$\nabla \cdot (\mathbf{E}_o^* \times \mathbf{H}) = -j\omega_o \mathbf{H} \cdot \mathbf{B}_o^* - j\omega \mathbf{E}_o^* \cdot \mathbf{D} \quad (50)$$

Since with the Gauss Theorem the integration over a volume can be transformed to integration over a surface, then:

$$\iint_S (\mathbf{E}_o^* \times \mathbf{H}) \cdot d\mathbf{S} = \iiint_V (-j\omega_o \mathbf{H} \cdot \mathbf{B}_o^* - j\omega \mathbf{E}_o^* \cdot \mathbf{D}) dV \quad (51)$$

In this formula  $V$  and  $S$  represent the empty cavity volume and surface respectively.

Similarly by duality the following formula is written:

$$\iint_S (\mathbf{E} \times \mathbf{H}_o^*) \cdot d\mathbf{S} = \iiint_V (-j\omega \mathbf{H}_o^* \cdot \mathbf{B} - j\omega_o \mathbf{E} \cdot \mathbf{D}_o^*) dV \quad (52)$$

With cavity perfectly conducting walls, the electric field is normal to the walls and the magnetic field is tangential. Therefore, this statement implies that the terms in double integrals vanish and hence:

$$\iiint_V (-j\omega_o \mathbf{H} \cdot \mathbf{B}_o^* - j\omega \mathbf{E}_o^* \cdot \mathbf{D}) dV = \iiint_V (-j\omega \mathbf{H}_o^* \cdot \mathbf{B} - j\omega_o \mathbf{E} \cdot \mathbf{D}_o^*) dV \quad (53)$$

$$\omega_o \iiint_V (\mathbf{E} \cdot \mathbf{D}_o^* - \mathbf{H} \cdot \mathbf{B}_o^*) dV = \omega \iiint_V (\mathbf{E}_o^* \cdot \mathbf{D} - \mathbf{H}_o^* \cdot \mathbf{B}) dV \quad (54)$$

With the specimen inserted in the cavity, the variation of the angular frequency represents the difference between empty and loaded cavity angular frequencies. The loaded cavity frequency is lower than the frequency of empty cavity then:

$$\omega = (\omega_o + \Delta\omega) \quad (55)$$

By rewriting and arranging all these formulas:

$$\iiint_V (-j\omega_o \mathbf{H} \cdot \mathbf{B}_o^* - j\omega \mathbf{E}_o^* \cdot \mathbf{D}) dV = \iiint_V (-j\omega \mathbf{H}_o^* \cdot \mathbf{B} - j\omega_o \mathbf{E} \cdot \mathbf{D}_o^*) dV \quad (56)$$

$$\omega_o \iiint_V (\mathbf{E} \cdot \mathbf{D}_o^* - \mathbf{H} \cdot \mathbf{B}_o^*) dV = (\omega_o + \Delta\omega) \iiint_V (\mathbf{E}_o^* \cdot \mathbf{D} - \mathbf{H}_o^* \cdot \mathbf{B}) dV \quad (57)$$

$$\begin{aligned} \omega_o \iiint_V (\mathbf{E} \cdot \mathbf{D}_o^* - \mathbf{H} \cdot \mathbf{B}_o^*) dV - \omega_o \iiint_V (\mathbf{E}_o^* \cdot \mathbf{D} - \mathbf{H}_o^* \cdot \mathbf{B}) dV = \\ \Delta\omega \iiint_V (\mathbf{E}_o^* \cdot \mathbf{D} - \mathbf{H}_o^* \cdot \mathbf{B}) dV \end{aligned} \quad (58)$$

then

$$\frac{\Delta\omega}{\omega_o} = \left( \frac{\omega - \omega_o}{\omega_o} \right) = \frac{\iiint_V [(\mathbf{E} \cdot \mathbf{D}_o^* - \mathbf{E}_o^* \cdot \mathbf{D}) - (\mathbf{H} \cdot \mathbf{B}_o^* - \mathbf{H}_o^* \cdot \mathbf{B})] dV}{\iiint_V (\mathbf{E}_o^* \cdot \mathbf{D} - \mathbf{H}_o^* \cdot \mathbf{B}) dV} \quad (59)$$

Since the integrand in the numerator is zero outside the volume of the perturbing specimen, then we can replace in the integration of the numerator the cavity volume by the specimen volume  $V_S$  and with  $V_o$  the empty cavity volume the new expression becomes:

$$\frac{\Delta\omega}{\omega_o} = \frac{\iiint_{V_S} [(\mathbf{E} \cdot \mathbf{D}_o^* - \mathbf{E}_o^* \cdot \mathbf{D}) - (\mathbf{H} \cdot \mathbf{B}_o^* - \mathbf{H}_o^* \cdot \mathbf{B})] dV}{\iiint_{V_o} (\mathbf{E}_o^* \cdot \mathbf{D} - \mathbf{H}_o^* \cdot \mathbf{B}) dV} \quad (60)$$

The only assumption made to obtain this expression is that the cavity walls are perfectly conductive. Moreover, when the specimen material is considered homogeneous and isotropic, and the cavity having air in it then

$$\mathbf{D}_o = \varepsilon_o \mathbf{E}_o \quad \text{and} \quad \mathbf{D} = \varepsilon_o \varepsilon_r^* \mathbf{E}, \quad \mathbf{B}_o = \mu_o \mathbf{H}_o \quad \text{and} \quad \mathbf{B} = \mu_o \mu_r^* \mathbf{H} \quad \text{and}$$

$$-\frac{\Delta\omega}{\omega_o} = \frac{\iiint_{V_S} [\varepsilon_o (\varepsilon_r^* - 1) \mathbf{E}_o^* \cdot \mathbf{E}] - [\mu_o (\mu_r^* - 1) \mathbf{H}_o^* \cdot \mathbf{H}] dV}{\iiint_{V_o} (\mathbf{E}_o^* \cdot \mathbf{D} - \mathbf{H}_o^* \cdot \mathbf{B}) dV} \quad (61)$$

Since permittivity and permeability are complex numbers then this expression shows that resonant frequency variation over resonant frequency of the unperturbed cavity is a complex quantity. If the following expressions are selected:

$$\begin{aligned}
\mathbf{E} &= \mathbf{E}_o + \mathbf{e} \\
\mathbf{H} &= \mathbf{H}_o + \mathbf{h} \\
\mathbf{D} &= \mathbf{D}_o + \mathbf{d} \\
\mathbf{B} &= \mathbf{B}_o + \mathbf{b}
\end{aligned} \tag{62}$$

then equation (60) becomes:

$$\frac{\Delta\omega}{\omega_o} = \frac{\iiint_{V_s} [(\mathbf{E}_o + \mathbf{e}) \cdot \mathbf{D}_o^* - \mathbf{E}_o^* \cdot (\mathbf{D}_o + \mathbf{d}) - (\mathbf{H}_o + \mathbf{h}) \cdot \mathbf{B}_o^* - \mathbf{H}_o^* \cdot (\mathbf{B}_o + \mathbf{b})] dV}{\iiint_{V_o} [(\mathbf{E}_o^* \cdot \mathbf{D}_o + \mathbf{d}) - \mathbf{H}_o^* \cdot (\mathbf{B}_o + \mathbf{b})] dV} \tag{63}$$

$$\frac{\Delta\omega}{\omega_o} = \frac{\iiint_{V_s} [(\mathbf{e} \cdot \mathbf{D}_o^* - \mathbf{E}_o^* \cdot \mathbf{d}) - (\mathbf{h} \cdot \mathbf{B}_o^* - \mathbf{H}_o^* \cdot \mathbf{b})] dV}{\iiint_{V_o} [(\mathbf{E}_o^* \cdot \mathbf{D}_o - \mathbf{H}_o^* \cdot \mathbf{B}_o) + (\mathbf{E}^* \cdot \mathbf{d} - \mathbf{H}_o^* \cdot \mathbf{b})] dV} \tag{64}$$

With the assumption that the perturbation is small, then the second term of the denominator is negligible and the latter equation can be written as:

$$\frac{\Delta\omega}{\omega_o} = \frac{\iiint_{V_s} [(\mathbf{e} \cdot \mathbf{D}_o^* - \mathbf{E}_o^* \cdot \mathbf{d}) - (\mathbf{h} \cdot \mathbf{B}_o^* - \mathbf{H}_o^* \cdot \mathbf{b})] dV}{\iiint_{V_o} (\mathbf{E}_o^* \cdot \mathbf{D}_o - \mathbf{H}_o^* \cdot \mathbf{B}_o) dV} \tag{65}$$

and therefore equation becomes:

$$-\frac{\Delta\omega}{\omega_o} = \frac{\iiint_{V_s} [\varepsilon_0(\varepsilon_r^* - 1)\mathbf{E}_o^* \cdot \mathbf{E}] - [\mu_0(\mu_r^* - 1)\mathbf{H}_o^* \cdot \mathbf{H}] dV}{\iiint_{V_o} (\mathbf{E}_o^* \cdot \mathbf{D}_o - \mathbf{H}_o^* \cdot \mathbf{B}_o) dV} \tag{66}$$

The negative sign of the complex frequency shift indicates that the resonant frequency of the empty cavity is lowered when the specimen is introduced in it.

Waldron mentioned that  $\mathbf{E}_o$  and  $\mathbf{D}_o$  have a  $j$  phasor factor in TE mode and  $\mathbf{H}_o$  and  $\mathbf{B}_o$  have a  $j$  phasor factor in TM mode [148]. Therefore a positive sign is observed in the denominator of the last equation and it becomes:

$$-\frac{\Delta\omega}{\omega_0} = \frac{\iiint_{V_s} [\varepsilon_0(\varepsilon_r^* - 1)\mathbf{E}_o^* \cdot \mathbf{E}] - [\mu_0(\mu_r^* - 1)\mathbf{H}_o^* \cdot \mathbf{H}] dV}{\iiint_{V_o} (\mathbf{E}_o^* \cdot \mathbf{D}_o + \mathbf{H}_o^* \cdot \mathbf{B}_o) dV} \quad (67)$$

In this expression, the numerator and the denominator represent the total energy stored in the specimen and in the cavity respectively. Therefore the total energy in the cavity ( $W_T$ ) is the sum of the electric energy ( $W_E$ ) and magnetic energy ( $W_M$ ) and hence one can write:

$$W_T = W_E + W_M = 2W_E = 2W_M = 2\iiint_{V_o} (\mathbf{E}_o^* \cdot \mathbf{D}_o) dV \quad (68)$$

The perturbation of the material or the specimen is introduced at the position of maximum electric field and the perturbation contribution of the magnetic field is minimum and equation (67) is expressed then as:

$$-\frac{\Delta\omega}{\omega_0} = \frac{\iiint_{V_s} [\varepsilon_0(\varepsilon_r^* - 1)\mathbf{E}_o^* \cdot \mathbf{E}] dV}{\iiint_{V_o} (\mathbf{E}_o^* \cdot \mathbf{D}_o + \mathbf{H}_o^* \cdot \mathbf{B}_o) dV} = \frac{\iiint_{V_s} [\varepsilon_0(\varepsilon_r^* - 1)\mathbf{E}_o^* \cdot \mathbf{E}] dV}{2\iiint_{V_o} (\mathbf{E}_o^* \cdot \mathbf{D}_o) dV} \quad (69)$$

When the specimen is introduced at the maximum electric field location in the cavity, the tangential electric field is continuous at the surface of the rod and therefore  $\mathbf{E} = \mathbf{E}_o$ . Since the perturbation is small, the electric field at that location is constant and hence the numerator of the last equation is the integrand multiplied by the specimen volume  $V_s$ . Taking the TE mode in the cavity, the denominator can be written as:

$$\begin{aligned}
& 2 \iiint_{V_o} (\mathbf{E}_o^* \cdot \mathbf{D}_o) dV = \\
& 2 \varepsilon_0 \iiint_{V_o} [E_{yMAX} \cos(\frac{\pi x}{a}) \cos(\frac{p\pi z}{d}) \cdot E_{yMAX}^* \cdot \cos(\frac{\pi x}{a}) \cos(\frac{p\pi z}{d})] dx dy dz = \\
& 2 \varepsilon_0 E_{yMAX} E_{yMAX}^* \iiint_{V_o} [(\cos^2(\frac{\pi x}{a})) \cos^2(\frac{p\pi z}{d})] dx dy dz = \\
& 2 \varepsilon_0 E_{yMAX} E_{yMAX}^* \int_0^b 1 dy \int_0^a (\cos^2(\frac{\pi x}{a})) dx \int_0^d (\cos^2(\frac{p\pi z}{d})) dz = \\
& 2 \varepsilon_0 E_{yMAX} E_{yMAX}^* \int_0^b 1 dy \int_0^a \frac{1}{2} [1 + \cos(\frac{2\pi x}{a})] dx \int_0^d \frac{1}{2} [1 + \cos(\frac{2p\pi z}{d})] dz = \\
& 2 \varepsilon_0 E_{yMAX} E_{yMAX}^* (b) (\frac{a}{2}) (\frac{d}{2}) = \varepsilon_0 E_{yMAX} E_{yMAX}^* \cdot (\frac{Volume\ of\ cavity}{2})
\end{aligned} \tag{70}$$

Then by replacing the tangential field at the maximum field location in the numerator, equation (69) becomes

$$\begin{aligned}
-\frac{\Delta \omega}{\omega_o} &= \frac{\varepsilon_0 (\varepsilon_r^* - 1) E_{yMAX} E_{yMAX}^* (Volume\ of\ sample)}{\varepsilon_0 E_{yMAX} E_{yMAX}^* (\frac{Volume\ of\ cavity}{2})} = \\
-\frac{\Delta \omega}{\omega_o} &= \frac{2(\varepsilon_r^* - 1)(Volume\ of\ sample)}{Volume\ of\ cavity} = \frac{2(\varepsilon_r^* - 1)V_s}{V_o}
\end{aligned} \tag{71}$$

Given the small perturbation ( $\Delta \omega \ll \omega_o$ ), then:

$$-\frac{\Delta \omega}{\omega} \approx \frac{2(\varepsilon_r^* - 1)V_s}{V_o} \tag{72}$$

This simple expression represents the complex resonant frequency shift which is dependent on the complex permittivity of the specimen and the volumes of the cavity and the specimen.

### 3.5.4 Measurable resonant frequency and quality factor

Complex resonant frequency is related to the measurable resonant frequency and quality factor (without and with specimen in the cavity) and the relation is given by [153, 156, 158-160, 165-170]:

$$-\frac{\Delta\omega}{\omega} = -\left[\left(\frac{f-f_o}{f}\right) + \frac{j}{2}\left(\frac{1}{Q} - \frac{1}{Q_o}\right)\right] \quad (73)$$

then the relation between the measurable quantities and the complex permittivity is given by:

$$\begin{aligned} -\left[\left(\frac{f-f_o}{f}\right) + \frac{j}{2}\left(\frac{1}{Q} - \frac{1}{Q_o}\right)\right] &= \frac{2(\varepsilon_r^* - 1)V_s}{V_o} = \frac{2(\varepsilon_r' - 1)V_s}{V_o} - 2j\frac{\varepsilon_r''V_s}{V_o} \\ \left(\frac{f_o-f}{f}\right) - \frac{j}{2}\left(\frac{1}{Q} - \frac{1}{Q_o}\right) &= \frac{2(\varepsilon_r^* - 1)V_s}{V_o} = \frac{2(\varepsilon_r' - 1)V_s}{V_o} - 2j\frac{\varepsilon_r''V_s}{V_o} \end{aligned} \quad (74)$$

$$\begin{aligned} \varepsilon_r' &= \left(\frac{f_o-f}{2f}\right)\frac{V_o}{V_s} + 1 \\ \varepsilon_r'' &= \frac{V_o}{4V_s}\left(\frac{1}{Q} - \frac{1}{Q_o}\right) \end{aligned} \quad (75)$$

where  $f_o$ ,  $Q_o$ ,  $f$  and  $Q$  are respectively empty cavity measurable resonant frequency and quality factor, followed by the same measures quantities when the specimen is inserted.

## 3.6 Fluid analysis in microfluidic channel

### 3.6.1 Navier-Stokes equations for a steady flow and incompressible fluids

The analysis of microfluidic channel with the presence of electromagnetic waves or signals requires the coupling of fluid dynamics and electromagnetic field equations.

The conservation of mass or continuity governing equation is given by [171]:

$$\frac{\partial \rho}{\partial t} + \nabla \cdot \rho \mathbf{v} = 0 \quad (76)$$

where  $\mathbf{v}$  is the velocity vector and  $\rho$  is the fluid density. In tri-axial coordinates this equation can be written in the form:

$$\frac{\partial \rho}{\partial t} + \frac{\partial(\rho v_x)}{\partial x} + \frac{\partial(\rho v_y)}{\partial y} + \frac{\partial(\rho v_z)}{\partial z} = 0 \quad (77)$$

For a steady flow and incompressible fluids, this expression is simplified and is given by:

$$\frac{\partial v_x}{\partial x} + \frac{\partial v_y}{\partial y} + \frac{\partial v_z}{\partial z} = 0 \quad (78)$$

From the continuity equation and the differential Euler's equations of motion, the Navier-Stokes equations in x, y and z directions are written as:

$$\begin{aligned} \rho \left( \frac{\partial v_x}{\partial t} + v_x \frac{\partial v_x}{\partial x} + v_y \frac{\partial v_x}{\partial y} + v_z \frac{\partial v_x}{\partial z} \right) &= -\frac{\partial p}{\partial x} + \rho g_x + \mu_d \left( \frac{\partial^2 v_x}{\partial x^2} + \frac{\partial^2 v_x}{\partial y^2} + \frac{\partial^2 v_x}{\partial z^2} \right) \\ \rho \left( \frac{\partial v_y}{\partial t} + v_x \frac{\partial v_y}{\partial x} + v_y \frac{\partial v_y}{\partial y} + v_z \frac{\partial v_y}{\partial z} \right) &= -\frac{\partial p}{\partial y} + \rho g_y + \mu_d \left( \frac{\partial^2 v_y}{\partial x^2} + \frac{\partial^2 v_y}{\partial y^2} + \frac{\partial^2 v_y}{\partial z^2} \right) \\ \rho \left( \frac{\partial v_z}{\partial t} + v_x \frac{\partial v_z}{\partial x} + v_y \frac{\partial v_z}{\partial y} + v_z \frac{\partial v_z}{\partial z} \right) &= -\frac{\partial p}{\partial z} + \rho g_z + \mu_d \left( \frac{\partial^2 v_z}{\partial x^2} + \frac{\partial^2 v_z}{\partial y^2} + \frac{\partial^2 v_z}{\partial z^2} \right) \end{aligned} \quad (79)$$

where  $g_x, g_y, g_z, \mu_d$  are the components of acceleration of gravity vector and the dynamic viscosity of the fluid and  $p$  the pressure. Neglecting the components of the acceleration of gravity vector, the general expression of Navier-Stokes equations is:

$$\frac{\partial \mathbf{v}}{\partial t} + \mathbf{v} \cdot \nabla \mathbf{v} = -\frac{1}{\rho} \nabla p + \nu \nabla^2 \mathbf{v} \quad (80)$$

with  $\nu$  being the kinematic viscosity and  $\nu = \frac{\mu_d}{\rho}$ . This equation provides the velocity

distribution of the fluid in the microchannel.

## 3.6.2 Forces present on an immersed spherical particle in a fluid

### 3.6.2.1 Introduction

A particle moving in a fluid is subjected to different forces acting on it. The equation of motion reveals different internal forces such as drag, gravity and buoyancy forces. Some forces are extrinsic and caused by external mechanisms/effects such as dielectrophoresis, electromagnetic or other forces. These effects are studied in the following sections.

### 3.6.2.2 DEP electrodes effect

In a microchannel with immersed spherical particle in the fluid, when the fluid is moving in the x direction and the gravity force acts in the y direction and with negligible buoyancy force, the equation of motion with the presence of dielectrophoresis force yields the following relations [172]:

$$\begin{aligned}\pi\varepsilon_m R^3 \operatorname{Re}[f_{CM}] \frac{\partial}{\partial x} |E^2| + 6\pi\eta R K_x (v_x - \frac{dx}{dt}) &= m \frac{d^2x}{dt^2} \\ \pi\varepsilon_m R^3 \operatorname{Re}[f_{CM}] \frac{\partial}{\partial y} |E^2| - 6\pi\eta R K_y \frac{dy}{dt} + (\frac{4}{3} \pi R^3) g(\rho_m - \rho_p) &= m \frac{d^2y}{dt^2} \\ \pi\varepsilon_m R^3 \operatorname{Re}[f_{CM}] \frac{\partial}{\partial z} |E^2| - 6\pi\eta R K_z \frac{dz}{dt} &= m \frac{d^2z}{dt^2}\end{aligned}\tag{81}$$

where  $v_x$  is x unidirectional fluid velocity acting on the particle,  $\frac{\partial}{\partial x}$ ,  $\frac{\partial}{\partial y}$ ,  $\frac{\partial}{\partial z}$  are gradient

operators in the x, y and z directions,  $K_x$ ,  $K_y$ ,  $K_z$ ,  $\frac{dx}{dt}$ ,  $\frac{dy}{dt}$ ,  $\frac{dz}{dt}$  and  $\frac{d^2x}{dt^2}$ ,  $\frac{d^2y}{dt^2}$ ,  $\frac{d^2z}{dt^2}$  are wall

correction factors, particle instantaneous velocity and acceleration in coordinates directions respectively. These relations link DEP, drag and gravity forces with the

acceleration force in x, y and z directions. The drag force is related to the velocities of the particle and the fluid in movement.

### 3.6.2.3 Electro- magnetic effect

When the particle within the fluid is passing close to an electric or magnetic field, then the electromagnetic signal will create the Lorentz force [173] is given by:

$$\mathbf{F}_{LORENTZ} = [\sigma(\mathbf{E} + \mathbf{v} \times \mathbf{B})] \times \mathbf{B} \quad (82)$$

In equation (82), the contribution of  $\mathbf{v} \times \mathbf{B}$  will be negligible and therefore the force will mainly depend on the passing current and the magnitude of magnetic field strength. In the absence of a magnetic field, the contribution of this force will mainly be due to the DEP force created by the RF/Microwave signal. Hence the equation of motion with the presence of a particle in a media and the presence of an RF/Microwave signal on electrodes yields the following relation:

$$\mathbf{F}_{DEP\ RF/Microwave} + \mathbf{F}_{DRAG} + \mathbf{F}_{GRAVITY} = \mathbf{F}_{ACCELERATION} \quad (83)$$

where  $\mathbf{F}_{DEP\ RF/Microwave}$  is the DEP force identified by the equation (5) when an RF/Microwave signal is applied to the electrodes with an amplitude  $A_{RF}$  and a frequency  $f_{RF}$ .

## 3.7 Chapter summary

This chapter gives the theoretical background for resources and the tools needed to complete this investigation. The theory of the particle polarization and the dielectrophoresis principle are explained. The DEP force and the associated Clausius-Mosotti factor are elaborated.

The single cell model and the RF/Microwave transmission path model for single cell detection in a microfluidic channel are generated. The single cell model is studied with overlapping parallel facing electrodes containing media and a suspended particle in a media. Due to the nature of the microfluidic device, non-standard CPW transmission lines are used to characterize the cells with RF/Microwave measurements. Therefore, a detailed theoretical analysis is performed to model properly these CPW transmissions lines.

Finally the theory about the complex permittivity of particles at high frequency and how to measure it is given for the needs of next chapters.

# **Chapter 4: Theoretical Analysis of Dielectrophoretic Force Generated by Parallel Facing Electrodes for Centering the Living Cells within the Microfluidic Channel**

## **4.1 Introduction**

In a micro biological device, micro particle or cell manipulation and characterization require the use of electric field of specific 3D configuration that would be ensured by different electrodes in several configurations and shapes. To efficiently design micro electrodes within a microfluidic channel for dielectrophoresis focusing, manipulation and characterization of cells, the designer will seek the exact distribution of the electric potential, electric field and hence dielectrophoresis force exerted on the cell within the microdevice. Therefore, the theoretical analysis of the dielectrophoretic force expression within a microchannel is essential information to perform the design parametric study. Non-uniform electric field can be generated using same size parallel facing electrodes, for example in trapezoid shape, present on the two faces of channel substrates. The application of the difference of potential on the pair electrodes generates the desired DEP force to attract or repulse the cells moving along the channel. The attraction or repulsion of cells depends on their internal characteristics and of the surrounding media, on the external applied voltage amplitude and frequency of the low frequency harmonic signal. In this analytical solution for dielectrophoretic phenomena, simple Fourier series mathematical expressions are derived for electric potential, electric field and dielectric force between two distant finite size electrodes. Analytical results, calculated using Matlab<sup>TM</sup>, are compared with numerical solutions obtained by COMSOL and excellent agreement is found between them. Bio-micro devices are also designed and

fabricated to compare and illustrate the theoretical solution with the experimental data. The experiments used RBCs within the suspending media. Low frequency signal is applied to the parallel facing electrodes creating DEP force on the cells in the channel affecting the motion of the RBCs. The dielectrophoretic force contour plots of the analytical data matched to the experimental results.

This chapter presents the thesis adapted version of the article published in the Journal of Electrophoresis with the title: Analytical Solutions and Validation of Electric Field and Dielectrophoretic Force in a Bio-microfluidic Channel, 2012, Volume 33, Issue 3, p. 426-435.

## **4.2 Cell centering micro device**

In a microfluidic channel equipped with several electrodes for different purposes, the understanding of DEP mechanism is very important. Since the DEP force is directly related to the gradient and the strength of electric field, and then the formulation of the electric field determines the exact DEP force strength on cells or particles. The distribution of the electric field can be found analytically or through simulation.

The specific case regarding a microfluidic structure with the presence of parallel facing electrodes for cell centering, detection and characterization represents the main subject of this theoretical and experimental study. The electric field and the dielectrophoretic force depend on the electrodes geometry of the specific micro device. These two quantities can be analytically determined using charge density method [113, 174], Green's theorem [139, 175], Green's function [105, 176], half-plane Green's function [106, 177] and Fourier series [35, 107, 178] and other methods. They can also be

solved numerically with Finite Element Methods (FEM) [106, 108, 179]. This analytical study presents a simple mathematical solution to evaluate the electric potential, electric field and dielectrophoretic force using Fourier series in a micro device with identical size parallel facing electrodes in the microchannel when opposite voltage is applied. There are several advantages of this analytical solution over previous works and numerical simulations.

The present method is based on Fourier series that uses trigonometric and exponential functions while Schwarz-Christoffel mapping method requires the calculation of several functions that need, to some extent, the calculation of several elliptical integrals and numerical computations [114, 180]. Moreover, the solutions of mathematical expressions produce precise and quick computer simulations in Matlab<sup>TM</sup> and it can be easily used to perform design parametric studies.

The micro device is designed and fabricated with two glass substrates having parallel facing electrodes for characterization of living cells in a controlled conductivity media. For measurement of the electric response of a single cell at observation point, the injected cells into the channel have to be carefully focused into the middle of the channel and then different electrodes can be used to characterize each cell response at low and high frequencies. The exact knowledge of the electric field distribution under the electrodes could permit easy parametric analysis and characterize cell movement through the channel as shown in Figure 4.1 parts a and b. The strength of the force in the device can be easily found by numerical simulation but for parametric analysis during the design of the microfluidic device, a mathematical analysis is indeed essential and very beneficial. Moreover the knowledge of the dielectrophoretic force and other present

forces, such as gravity, drag and buoyancy forces, would determine the trajectory of the cells within the microchannel.

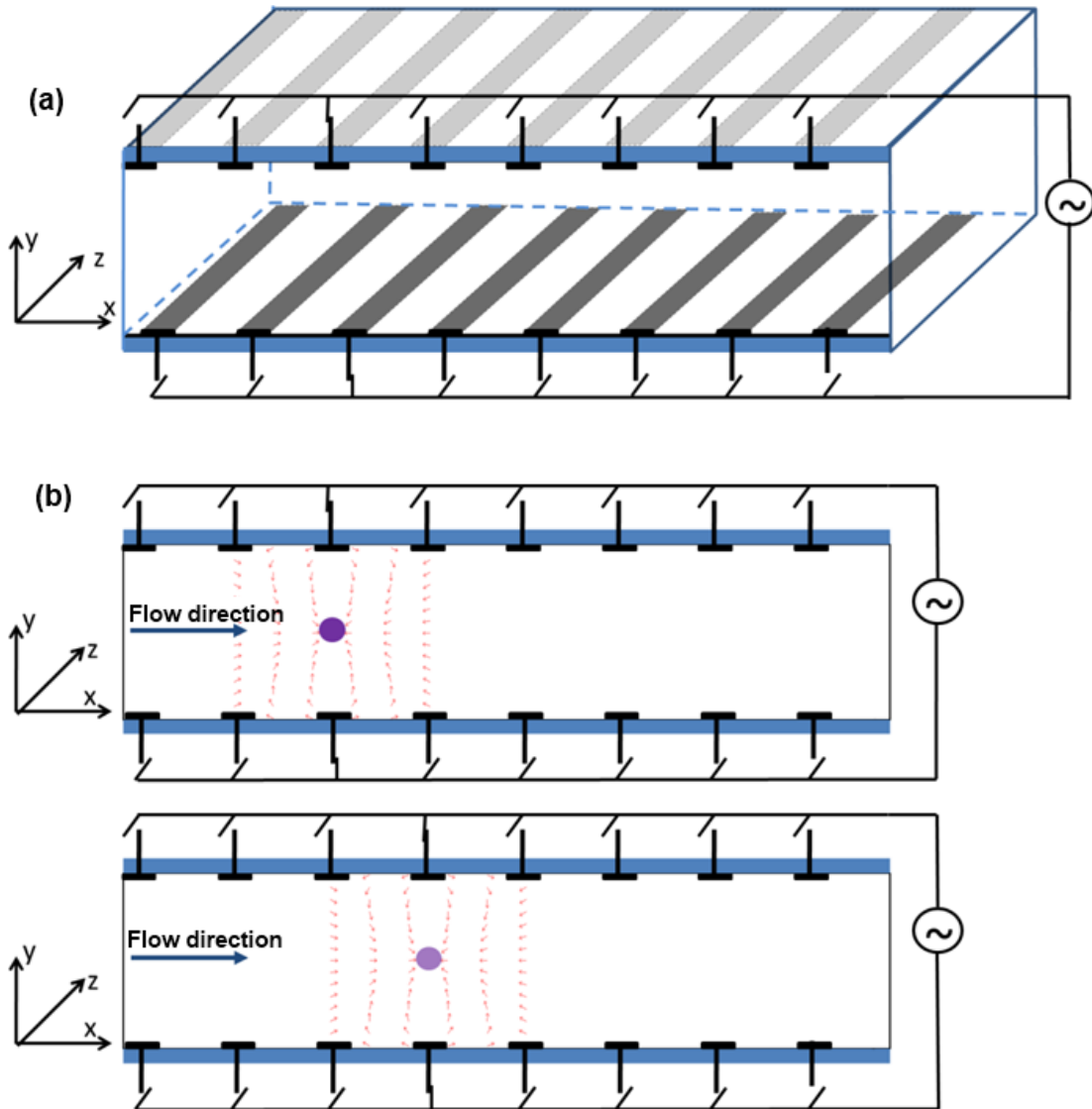


**Figure 4.1: (a) Schematic diagram showing the experimental arrangement of the electrodes used for manipulation of cells. Series of electrodes are patterned on the upper and bottom parts of the channel. Energizing one pair of electrodes “third from the left” influences the movement of cells toward the electrodes (positive DEP) or far from the electrodes (negative DEP). (b) 2D schematic diagram showing the cells displacement under the influence of moving dielectrophoresis. The circles represent cells. In the first part of figure b, only the third pair of electrodes is actuated while in the second part only the fourth pair electrodes. Sequential energizing of the electrodes causes the cells to move in the microchannel due to the dielectrophoretic phenomenon**

In earlier work, analytical solutions were found using Fourier series for another type of structure with different electrodes configuration in the application of moving particles by DEP [181]. For these parallel facing electrodes within the microchannel for cell's frequency characterization application, this chapter provides the analytical solution using Fourier series method. The contribution of this chapter consists in providing simple and parametric solutions of this type of structure configuration. This configuration is currently used in cells manipulation and characterization. The present analytical solution will help the designer to perform a meaningful parametric analysis, which will yield to an optimized set of dimensions. Numerical solutions could equally be used for such problems but the investigation becomes time consuming and inefficient. The following section presents the theory of the electric potential, electric field and dielectrophoretic force with the associated physical structure and boundary conditions.

### 4.3 Problem description for DEP parallel facing electrodes

The general expression of the dielectric force acting on a spherical polarisable cell placed in a non-uniform electrical field and in a suspending media is given by the following equations [181] and [182] and this equation was already written in one of the preceding chapters :

$$\mathbf{F}_{DEP} = \pi\epsilon_0\epsilon_m R^3 \operatorname{Re}[f_{CM}] \nabla(\mathbf{E} \cdot \mathbf{E}) \text{ or } \mathbf{F}_{DEP} = 2\pi\epsilon_0\epsilon_m R^3 \operatorname{Re}[f_{CM}] \nabla(\mathbf{E}_{RMS} \cdot \mathbf{E}_{RMS}) \quad (84)$$

where  $\operatorname{Re}[f_{CM}]$  is the real part of Clausius-Mossotti factor and  $\mathbf{E}$  ,  $\mathbf{E}_{RMS}$  represent the maximum and the 'Root Mean Square' amplitude of the applied electric field respectively. The real part of Clausius-Mossotti factor  $(\frac{\epsilon_p^* - \epsilon_m^*}{\epsilon_p^* + 2\epsilon_m^*})$  can vary between - 0.5

and +1 since it depends basically on the complex permittivities of the particles  $\varepsilon_p^*$  and the media  $\varepsilon_m^*$  [183].

Knowledge of the dielectrophoresis force in the microchannel enables modeling the movement of the cell. Therefore a mathematical formulation of the distribution of the electric field between the DEP electrodes has to be determined. Buoyancy, gravitational, vertical components of DEP and drag forces influence the vertical motion of cells in the microchannel. The cell movement on horizontal plane is controlled by the horizontal components of the DEP and drag forces. DEP velocity of cells is derived at the equilibrium of forces. In a horizontal plane, the velocity component of cells moving in laminar media with low Reynolds number is derived at the equilibrium of DEP force and drag forces [184].

In order to generate the dielectrophoretic force relation adapted to the proposed electrode configuration, we consider the expression of the electric field given by Gauss's law as it follows:

$$\nabla \cdot \mathbf{E} = \frac{\rho_c}{\varepsilon_0} \quad (85)$$

where  $\rho_c$  is the total electric charge density. In the present case the charge density including both the free and the bounded charge is zero. Equation (85) becomes:

$$\nabla \cdot \mathbf{E} = 0 \quad (86)$$

The quasi-electrostatic form of Maxwell's equation relates the electric field with the electric potential in the following formulation:

$$\mathbf{E} = -\nabla V \quad (87)$$

where  $V$  represents the electric potential. Substitution of equation (87) into (86) yields:

$$V_{xx} + V_{yy} + V_{zz} = 0 \quad (88)$$

Where  $V_{xx}$ ,  $V_{yy}$  and  $V_{zz}$  are the second partial derivatives of  $V$  with respect to  $x$ ,  $y$  and  $z$  respectively. Under the assumption that the width of the microchannel is sufficiently large, the system is simplified to the schematic illustrated in Figure 4.2 where Laplace equation (88) becomes:

$$V_{xx} + V_{yy} = 0 \quad (89)$$

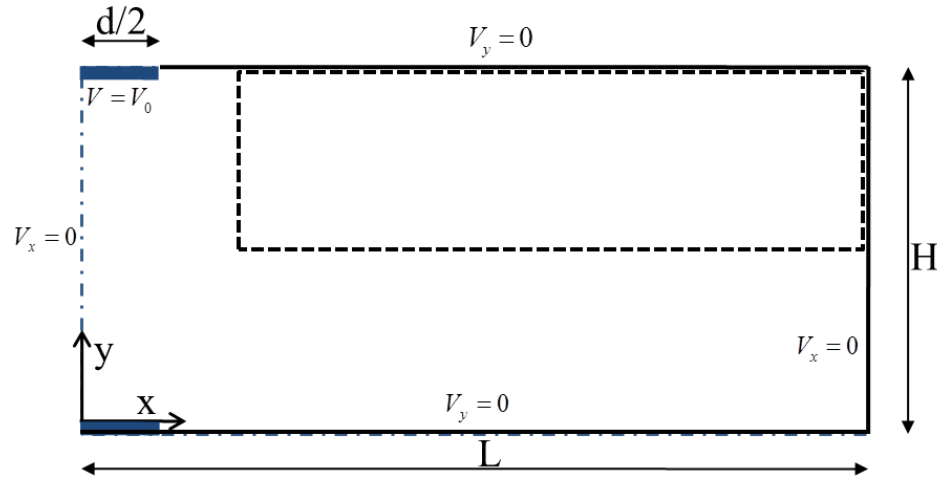


**Figure 4.2: Illustration of the geometry of the unit segment and the boundary conditions used in the analytical solution. The unit segment consists of finite size pair of electrodes of length  $d/2$  with a potential of  $V_0$  and  $-V_0$ . The Gaussian surface used in the solution is shown as dashed line at the upper right part of the channel. The electrodes are shown with some thickness for better visualization but they are considered thin compared with the height of the channel**

The following boundary conditions are assumed in the formulation:

- The upper electrode is energized at a potential  $V_0$ .
- The upper part of the channel is insulated; change of potential across the upper part of the considered segment is set to zero.

- c. The bottom electrode is energized at a potential  $-V_0$ .
- d. The change in potential at the right side, which is theoretically at infinity, is assumed to be zero. The right side of the unit segment is assumed to be at a finite distance  $L$  from the left extremity of the considered unit segment.
- e. The unit segment is symmetrical about y-axis (left side).

The boundary conditions applied for the Laplace equation (89) are shown in Figure 4.2 and are given by:

$$V(x, H) = V_0 \quad 0 \leq x \leq \frac{d}{2} \quad (90)$$

$$V_y(x, H) = 0 \quad \frac{d}{2} \leq x \leq L \quad (91)$$

$$V(x, 0) = -V_0 \quad 0 \leq x \leq \frac{d}{2} \quad (92)$$

$$V_y(x, 0) = 0 \quad \frac{d}{2} \leq x \leq L \quad (93)$$

$$V_x(L, y) = 0 \quad (94)$$

$$V_x(0, y) = 0 \quad (95)$$

where  $V_x$  and  $V_y$  are the first partial derivatives of  $V$  with respect to  $x$  and respectively.

To normalize the equation with respect to the specific coordinates, the following normalized -dimensionless parameters are assumed:

$$\bar{x} = \frac{x}{L}, \bar{y} = \frac{y}{H} \quad (96)$$

Substituting equations (96) into (89) yields:

$$\frac{1}{L^2} V_{\bar{x}\bar{x}} + \frac{1}{H^2} V_{\bar{y}\bar{y}} = 0 \quad (97)$$

Using the normalized non-dimensional parameters of equation (96), the boundary conditions become:

$$V(\bar{x}, 1) = V_0 \quad 0 \leq \bar{x} \leq \frac{d}{2L} \quad (98)$$

$$V_{\bar{y}}(\bar{x}, 1) = 0 \quad \frac{d}{2L} < \bar{x} \leq 1 \quad (99)$$

$$V(\bar{x}, 0) = -V_0 \quad 0 \leq \bar{x} \leq \frac{d}{2L} \quad (100)$$

$$V_{\bar{y}}(\bar{x}, 0) = 0 \quad \frac{d}{2L} < \bar{x} \leq 1 \quad (101)$$

$$V_{\bar{x}}(1, \bar{y}) = 0 \quad (102)$$

$$V_{\bar{x}}(0, \bar{y}) = 0 \quad (103)$$

Where  $V_{\bar{x}}$  and  $V_{\bar{y}}$  are the first partial derivatives of  $V$  with respect to  $\bar{x}$  and  $\bar{y}$  respectively.

Equations (99) and (101) can be represented in the form:

$$V(\bar{x}, 1) = \phi(\bar{x}) \quad \frac{d}{2L} < \bar{x} \leq 1 \quad (104)$$

$$V(\bar{x}, 0) = -\phi(\bar{x}) \quad \frac{d}{2L} < \bar{x} \leq 1 \quad (105)$$

where  $\phi(\bar{x})$  represent the electric potential distribution function from the edge of the electrode to the right side of the considered segment. With the equations modeling the dielectrophoretic phenomena and with the proper boundary conditions, analytical solution

based on Fourier series in the attempt to evaluate as accurate as possible the value of the electric potential and electric field within the environment is carried out.

#### 4.4 Solution of the governing equations by Fourier series

Based on the nature of the boundary conditions and using the separation of variables technique, the present formulation assumes the solution to be the sum of two solutions that satisfy Laplace equation; linear part and a harmonic form as it follows:

$$V(\bar{x}, \bar{y}) = A + B\bar{x} + C\bar{y} + D\bar{x}\bar{y} + F(\bar{x})G(\bar{y}) \quad (106)$$

where  $A$ ,  $B$ ,  $C$  and  $D$  are constants.

Following the separation of variables technique the subsequent formulation is obtained:

$$V(\bar{x}, \bar{y}) = A + B\bar{x} + C\bar{y} + D\bar{x}\bar{y} + \sum_{m=1}^{\infty} \left[ (a_{0m} \cos(K_s \bar{x}) + a_{1m} \sin(K_s \bar{x})) \left( b_{0m} \sinh\left(\frac{K_s H}{L} \bar{y}\right) + b_{1m} \cosh\left(\frac{K_s H}{L} \bar{y}\right) \right) \right] \quad (107)$$

Substituting the boundary condition (103) in (106), the constants  $B$ ,  $D$  and  $a_1$  are found to be zero.

$$V(\bar{x}, \bar{y}) = A + C\bar{y} + \sum_{m=1}^{\infty} \left[ (a_{0m} \cos(K_s \bar{x})) \left( b_{0m} \sinh\left(\frac{K_s H}{L} \bar{y}\right) + b_{1m} \cosh\left(\frac{K_s H}{L} \bar{y}\right) \right) \right] \quad (108)$$

Substituting the boundary conditions (102) in (108) yields:

$$V(\bar{x}, \bar{y}) = A + C\bar{y} + \sum_{m=1}^{\infty} \cos(K_s \bar{x}) \left( b_{2m} \sinh\left(\frac{K_s H}{L} \bar{y}\right) + b_{3m} \cosh\left(\frac{K_s H}{L} \bar{y}\right) \right) \quad (109)$$

where  $b_{2m}$  and  $b_{3m}$  are constants as function of  $m$  and  $K_s = m\pi$ .

The nature of the potential at the upper and bottom parts of the microchannel requires solving Laplace's equation between the edge of the finite electrode and the right side of the unit segment represented in Figure 4.3.

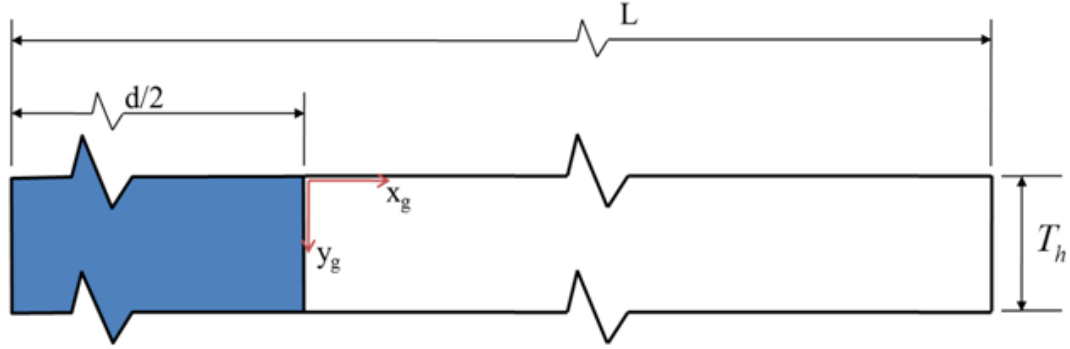


**Figure 4.3: Schematic diagram includes the upper part of the microchannel showing the energized electrode and the coordinate system used in the solution to indicate the potential distribution at the upper part of microchannel**

To overcome the analytical solution of equation (109) a new potential function is introduced with new coordinates and set of boundary conditions. This proposed technique enables the solution of Laplace equation with the following potential function:

$$\phi_{x_g x_g} + \phi_{y_g y_g} = 0 \quad (110)$$

$$\phi(0, y_g) = V_0 \quad y_g \leq T_h \quad (111)$$

$$\phi(\infty, y_g) = 0 \quad (112)$$

where  $\phi_{x_g x_g}$  is  $\frac{\partial^2 \phi}{\partial x_g^2}$ ,  $\phi_{y_g y_g}$  is  $\frac{\partial^2 \phi}{\partial y_g^2}$ ,  $T_h$  is the thickness of the electrodes layer and  $x_g$  and  $y_g$

are the coordinates inside the considered domain (Figure 4.3). Since the electrodes are deposited on an insulated layer the following boundary condition is implied:

$$\phi_{y_g}(x_g, 0) = 0 \quad (113)$$

In order to use dimensionless coordinates in equation (110), the following dimensionless parameters are proposed:

$$\bar{x}_g = \frac{x_g}{H}, \bar{y}_g = \frac{y_g}{T_h} \quad (114)$$

The dimensionless form of equation (110) and its boundary conditions are:

$$\frac{1}{H^2} \phi_{\bar{x}_g \bar{x}_g} + \frac{1}{T_h^2} \phi_{\bar{y}_g \bar{y}_g} = 0 \quad (115)$$

$$\phi(0, \bar{y}_g) = V_0 \quad \bar{y}_g \leq 1 \quad (116)$$

$$\phi_{\bar{x}_g}(\infty, \bar{y}_g) = 0 \quad (117)$$

$$\phi_{\bar{y}_g}(\bar{x}_g, 0) = 0 \quad (118)$$

Using the separation of variables principle, the solution of equation (115) is assumed to take the form of:

$$\phi(\bar{x}_g, \bar{y}_g) = F_g(\bar{x}_g) G_g(\bar{y}_g) \quad (119)$$

Following the standard procedure of separation of variables the solution becomes:

$$\phi(\bar{x}_g, \bar{y}_g) = \sum_{m=1}^{\infty} \left( C_{1g} e^{(K_g \bar{x}_g)} + C_{2g} e^{(-K_g \bar{x}_g)} \right) \left( C_{3g} \cos\left(\frac{T_h K_g}{H} \bar{y}_g\right) + C_{4g} \sin\left(\frac{T_h K_g}{H} \bar{y}_g\right) \right) \quad (120)$$

where  $C_{1g}$ ,  $C_{2g}$ ,  $C_{3g}$  and  $C_{4g}$  are constants and  $K_g$  is the separation constant with all these constants as being function of  $m$ . Substituting the boundary condition (117) and (118) into (120) yields:

$$\phi(\bar{x}_g, \bar{y}_g) = \sum_{m=1}^{\infty} C_{5g} e^{(-K_g \bar{x}_g)} \cos\left(\frac{T_h K_g}{H} \bar{y}_g\right) \quad (121)$$

where  $C_{5g}$  is a constant to be determined. A new substitution for the boundary conditions

(116) in ((121) gives:

$$V_0 = \sum_{m=1}^{\infty} C_{5g} \cos\left(\frac{T_h K_g}{H} \bar{y}_g\right) \quad (122)$$

The dimensionless variable  $\bar{y}_g$  ranges from 0 to 1. The maximum value for the term

$\cos\left(\frac{T_h K_g}{H} \bar{y}_g\right)$  is 1 while the minimum value is  $\cos\left(\frac{T_h K_g}{H}\right)$ . The cosine term in equation

(122) can be neglected if the value of the cosine term approaches 1. The thickness of the electrodes layer ranges between tens of nanometers to less than one micrometer. This work assumes zero thickness for the deposited electrodes.

With the relation  $\sum_{m=1}^{\infty} \left(\frac{1}{2^m}\right) = 1$ , one can write that:

$$V_0 = \sum_{m=1}^{\infty} \left(\frac{1}{2^m}\right) V_0 \quad (123)$$

Therefore solving equation (122) for  $C_{5g}$  gives:

$$C_{5g} = \frac{V_0}{2^m} \quad (124)$$

As a result, the potential distribution at the upper part of the microchannel is written as:

$$V(\bar{x},1) = V_0 \quad 0 \leq \bar{x} \leq \frac{d}{2L} \quad (125)$$

$$V(\bar{x}_g,1) = \sum_{m=1}^{\infty} \frac{V_0}{2^m} e^{-m\beta\bar{x}_g} \quad 0 \leq \bar{x}_g < \infty \quad (126)$$

where  $m\beta = K_g$  and  $\beta$  is a constant to be determined. The two boundary conditions (125) and (126) can be joined as one boundary condition using the Fourier cosine series as follows:

$$V(\bar{x},1) = A_0 + \sum_{n=1}^{\infty} A_n \cos(n\pi\bar{x}) \quad (127)$$

where  $A_0$  and  $A_n$  can be found as:

$$A_0 = V_0 \left( R + \sum_{m=1}^{\infty} \frac{H}{2^m m L \beta} \right) \quad (128)$$

$$A_n = 2V_0 \left[ \frac{\sin(n\pi R)}{n\pi} + H \sum_{m=1}^{\infty} \frac{m\beta L \cos(n\pi R) - n\pi H \sin(n\pi R)}{2^m (\beta^2 m^2 L^2 + n^2 \pi^2 H^2)} \right] \quad (129)$$

where  $R$  is the ratio  $\frac{d}{2L}$ .

Following the same procedure, the potential at the bottom part of the unit segment can be written as:

$$V(\bar{x},0) = - \left( A_0 + \sum_{n=1}^{\infty} A_n \cos(n\pi\bar{x}) \right) \quad 0 \leq \bar{x} \leq 1 \quad (130)$$

Substituting of the boundary condition (130) in equation (109) yields:

$$A = -A_0 \quad (131)$$

$$b_{3m} = -A_n \quad (132)$$

A new substitution for the boundary conditions (127) gives:

$$C = 2A_0 \quad (133)$$

$$b_{2m} = A_n \left( \frac{1 + \cosh\left(\frac{n\pi H}{L}\right)}{\sinh\left(\frac{n\pi H}{L}\right)} \right) \quad (134)$$

The profile of the electric potential inside the unit segment used for the formulation is given by the equation:

$$V(\bar{x}, \bar{y}) = A_0 (2\bar{y} - 1) + \sum_{n=1}^{\infty} A_n \cos(n\pi\bar{x}) \left( \frac{1 + \cosh\left(\frac{n\pi H}{L}\right)}{\sinh\left(\frac{n\pi H}{L}\right)} \sinh\left(\frac{n\pi H}{L}\bar{y}\right) - \cosh\left(\frac{n\pi H}{L}\bar{y}\right) \right) \quad (135)$$

#### 4.4.1 The electric field

The electric field distribution is calculated using the composition of the unidirectional electric field expressed in (87) as it follows:

$$\mathbf{E}(\bar{x}, \bar{y}) = E_1 \mathbf{i} + E_2 \mathbf{j} \quad (136)$$

where  $i$  and  $j$  are unit vectors along the  $\bar{x}$  and  $\bar{y}$  directions, respectively.  $E_1$  and  $E_2$  are the components of the electric field vector deduced from the electric potential:

$$E_1(\bar{x}, \bar{y}) = \sum_{n=1}^{\infty} \frac{A_n n \pi}{L} \sin(n\pi \bar{x}) \left[ \frac{1 + \cosh\left(\frac{n\pi H}{L}\right)}{\sinh\left(\frac{n\pi H}{L}\right)} \sinh\left(\frac{n\pi H}{L} \bar{y}\right) - \cosh\left(\frac{n\pi H}{L} \bar{y}\right) \right] \quad (137)$$

$$E_2(\bar{x}, \bar{y}) = -\frac{2A_0}{H} - \sum_{n=1}^{\infty} \frac{A_n n \pi}{L} \cos(n\pi \bar{x}) \left[ \frac{1 + \cosh\left(\frac{n\pi H}{L}\right)}{\sinh\left(\frac{n\pi H}{L}\right)} \cosh\left(\frac{n\pi H}{L} \bar{y}\right) - \sinh\left(\frac{n\pi H}{L} \bar{y}\right) \right] \quad (138)$$

Using the Gaussian surface integration shown in dashed line in Figure 4.2 the following equality is found:

$$H \int_{0.5}^1 \sum_{n=1}^{\infty} \frac{A_n n \pi}{L} \sin(2n\pi R) \left[ \frac{1 + \cosh\left(\frac{n\pi H}{L}\right)}{\sinh\left(\frac{n\pi H}{L}\right)} \sinh\left(\frac{n\pi H}{L} \bar{y}\right) - \cosh\left(\frac{n\pi H}{L} \bar{y}\right) \right] d\bar{y} = \quad (139)$$

$$L \int_{2R}^1 -\frac{2A_0}{H} - \sum_{n=1}^{\infty} \frac{A_n n \pi}{L} \cos(n\pi \bar{x}) \left[ \frac{1 + \cosh\left(\frac{n\pi H}{L}\right)}{\sinh\left(\frac{n\pi H}{L}\right)} \cosh\left(\frac{n\pi H}{L} \bar{y}\right) - \sinh\left(\frac{n\pi H}{L} \bar{y}\right) \right] d\bar{x}$$

The integration and arrangement of equation (139) gives:

$$\left( \sum_{n=1}^{\infty} A_n \sin(2n\pi R) \left[ \frac{1 + \cosh\left(\frac{n\pi H}{L}\right)}{\sinh\left(\frac{n\pi H}{L}\right)} \left( \cosh\left(\frac{n\pi H}{L}\right) - \cosh\left(\frac{n\pi H}{2L}\right) \right) - \sinh\left(\frac{n\pi H}{L}\right) + \sinh\left(\frac{n\pi H}{2L}\right) \right] \right) = \quad (140)$$

$$\left( -\frac{2LA_0}{H} (1 - 2R) - \sum_{n=1}^{\infty} A_n \sin(2n\pi R) \left[ \frac{1 + \cosh\left(\frac{n\pi H}{L}\right)}{\sinh\left(\frac{n\pi H}{L}\right)} \cosh\left(\frac{n\pi H}{2L}\right) - \sinh\left(\frac{n\pi H}{2L}\right) \right] \right)$$

Equation (140) was solved using Matlab<sup>TM</sup> to determine the value of the constant  $\beta$  at different microchannel height. Figure 4.4 shows the variation of the constant  $\beta$  as the microchannel height changes. It is found that the constant  $\beta$  does not relate to the distance  $d$  for length  $L$  value greater than  $5H$ . However, the computation of  $\beta$  for increasing height of the channel from 20 to 60  $\mu\text{m}$  shows fluctuations of + 3.6% which is due to the numerical manipulations.

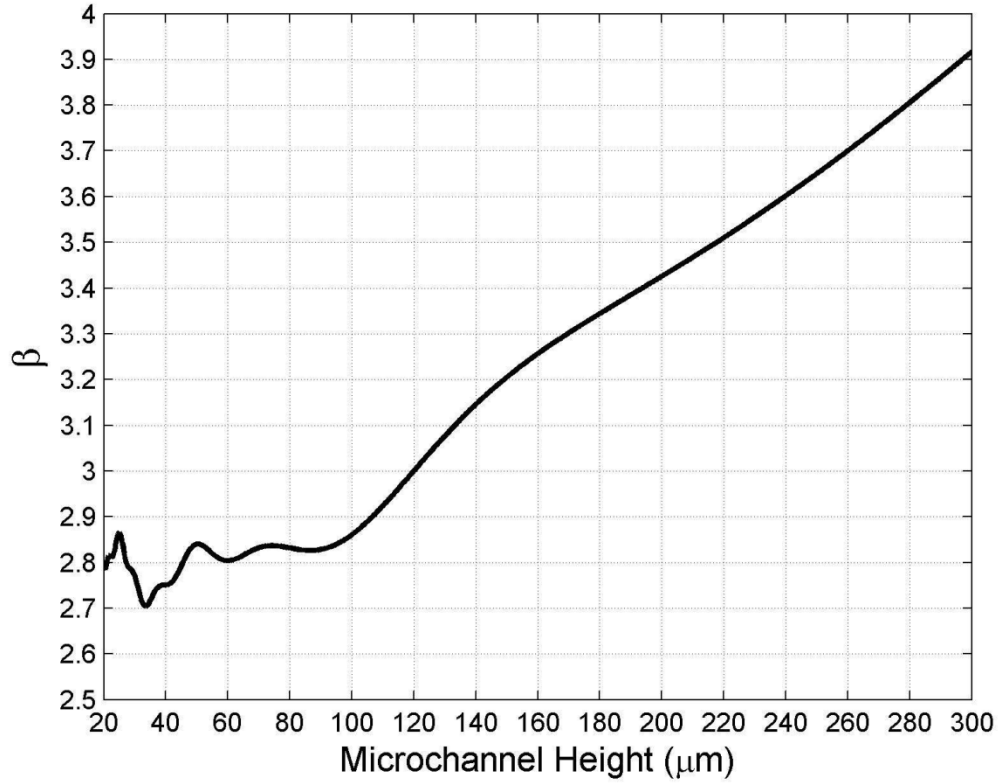


**Figure 4.4:** The variation of the constant  $\beta$  as the microchannel height  $H$  changes. The constant  $\beta$  is used to describe the potential function at the upper and the bottom parts of the microchannel between the edge of the electrode and the right end of the unit segment. The value of  $\beta$  was calculated up to three significant digits using Matlab<sup>TM</sup> based on equation (53) with ( $m=n=100$  terms)

#### 4.4.2 Dielectrophoretic force

Equation (84) implies that the dielectrophoretic force acting on particle or cell in the channel is linearly proportional to the gradient of squared electric field intensity. Therefore, the gradient of the electric field intensity can be expressed as a combination of vector components:

$$F_{DEP} = \pi \epsilon_0 \epsilon_m r^3 \operatorname{Re}[f_{CM}] \left[ \left( 2E_1 \frac{\partial E_1}{\partial x} + 2E_2 \frac{\partial E_2}{\partial x} \right) i + \left( 2E_1 \frac{\partial E_1}{\partial y} + 2E_2 \frac{\partial E_2}{\partial y} \right) j \right] \quad (141)$$

where the derivatives  $\frac{\partial E_1}{\partial x}$ ,  $\frac{\partial E_2}{\partial x}$ ,  $\frac{\partial E_1}{\partial y}$  and  $\frac{\partial E_2}{\partial y}$  are the sub terms of  $\nabla(\mathbf{E} \cdot \mathbf{E})$  vector and are

given as follow:

$$\frac{\partial E_1}{\partial \bar{x}} = -\frac{\partial E_2}{\partial \bar{y}} = \sum_{n=1}^{\infty} \frac{A_n n^2 \pi^2}{L^2} \cos(n\pi \bar{x}) \left[ \frac{1 + \cosh\left(\frac{n\pi H}{L}\right)}{\sinh\left(\frac{n\pi H}{L}\right)} \sinh\left(\frac{n\pi H}{L} \bar{y}\right) - \cosh\left(\frac{n\pi H}{L} \bar{y}\right) \right] \quad (142)$$

$$\frac{\partial E_2}{\partial \bar{x}} = \frac{\partial E_1}{\partial \bar{y}} = \sum_{n=1}^{\infty} \frac{A_n n^2 \pi^2}{L^2} \sin(n\pi \bar{x}) \left[ \frac{1 + \cosh\left(\frac{n\pi H}{L}\right)}{\sinh\left(\frac{n\pi H}{L}\right)} \cosh\left(\frac{n\pi H}{L} \bar{y}\right) - \sinh\left(\frac{n\pi H}{L} \bar{y}\right) \right] \quad (143)$$

In order to compare the results of the analytical solutions with the numerical solutions, the electrical potential, electric field and the gradient of the term  $|E|^2$  (proportional to dielectrophoretic force) are plotted using a Matlab<sup>TM</sup> code. The numerical solution is obtained using the COMSOL Multiphysics<sup>TM</sup> software. The size of the triangular mesh used in the numerical solution was set to be 0.5  $\mu\text{m}$ . Figure 4.6 shows the contour plot for the electric potential, the magnitude of the electric field and the gradient of the term  $|E|^2$  respectively in the unit segment for analytical and numerical solutions. The analytical formulation of DEP force presented in this paper can be used in developing models for particles and cells movement in microchannel having two identical electrodes with opposite sign voltages.

## 4.5 Experimental results

### 4.5.1 Micro device design and fabrication

The results of the analytical solution are also validated through experimental work. The validation is performed using living cells. When an electric potential is applied to the parallel facing electrodes, the cells will align according to the configuration of the electric

field. A micro device is fabricated with a channel height of  $80\ \mu\text{m}$ , width of  $300\ \mu\text{m}$  and a length of  $5\ \text{mm}$ . Several metal electrodes mainly  $50\ \mu\text{m}$  long with separations of  $50\ \mu\text{m}$  and more are deposited by sputtering. The metallic electrodes are made of a layer of  $20\ \text{nm}$  Ti (as adhesion coating) followed by a layer of  $1\ \mu\text{m}$  Au. After deposition steps, photoresist process was used to etch Ti and Au with Iodine solution and Hydrogen Peroxide 35 % respectively to obtain the desired design pattern. The channel is fabricated with two fused silica glasses separated by an insulator acting as the channel height. The insulator material used is biocompatible. Input and output holes are created on one of the glasses to enable the cells, within the media, to travel from the inlet to the outlet. The transparency of the glass on two sides permitted the visual observation through a microscope. The device is shown in Figure 4.5. The pattern of electrodes was created using AutoCAD and the printing was insured through a standard photolithography process.

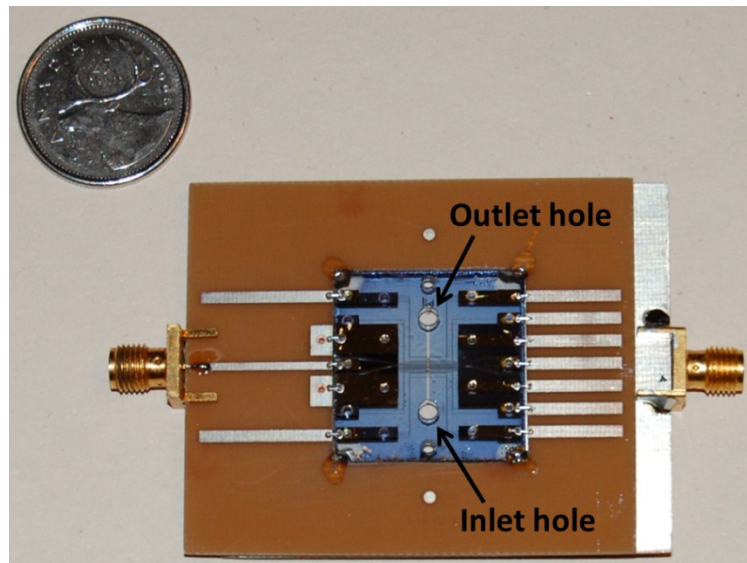


**Figure 4.5:** Picture taken of the experimental device lies beside a Canadian twenty five cent coin. The Bio Microchannel is made by blue tape and several electrodes are shown in the picture (DEP, Low frequency and high frequency electrodes). The inlet and outlet holes can be seen on the top glass

### 4.5.2 Cell preparation

Human blood was obtained the same way as described in earlier article by the authors [181, 185]. The separation of erythrocytes cells from blood is carried out using Ficoll-Paque Plus product containing 5.7% w/v Ficoll™ PM400 and 9% w/v diatrizoate sodium was mixed with blood anterior diluted two times with phosphate buffered saline plus (PBS+) and 2% fetal bovine serum (2% FBS). The complex solution was mixed at room temperature (25°C) for 30 minutes at 400 x g with brake off. The upper plasma layer was isolated without disturbing the interface between Ficoll™ and plasma. Subsequently the red blood cell layer was removed and suspended in a solution of 8.5% (w/v) sucrose plus 0.3 % (w/v) dextrose buffer that provides a low conductivity media for the dielectrophoretic phenomenon [186]. Media conductivity has been adjusted to 5 mS/m by adding a small amount of Trypsin in 0.53 mM EthyleneDiamineTetraacetic Acid (EDTA).

### 4.5.3 Experimental set up and procedure

The response of the living cells was observed under the effect of DEP. Erythrocytes cells suspended in the sucrose/dextrose low conductivity media were injected into the micro device. The cells concentration has been chosen to be  $10^5$  - $10^6$  per ml and suspended in 5 mS/m media. The flow of cells and media in the device has been controlled by a syringe pump (Harvard Apparatus). The experiments have been performed at different flow rates up to 0.5 ml/hr. Experiments employed other equipment including an inverted microscope (Omano OM900) equipped with a digital camera (Moticam 1000) and a computer. AC signals (Tektronix CFG280) of 100 KHz and higher

with voltages from 2 to 10 Volts peak were applied to the two electrodes. From 100 KHz to 1 MHz, red blood cells experienced a positive DEP phenomenon and gathered all around the finite size electrode with the higher density of cells at its edge. This phenomenon was observed on both electrodes. The high end of the applied voltage (about 10 Volts peak) induced an elongation of the red blood cells with elastic and plastic behaviors.

## 4.6 Results and discussion

The analytical results obtained with the Fourier series method are compared with a Finite Element Analysis code COMSOL Multiphysics<sup>TM</sup> software. The value of the constant  $\beta$  characterizing the Fourier series  $A_0$  and  $A_n$  was calculated for different channel height. The constant  $\beta$  (Figure 4.4) is used to calculate the electric potential at the upper and the bottom parts of the microchannel between the edge of the electrodes and the right end of the unit segment. For channel heights between 20 and 100  $\mu\text{m}$ , the constant  $\beta$  value is close to 2.85. The value goes to around 3.9 for channel heights of 300  $\mu\text{m}$ . The analytical results for the electric potential, the electrical field and the gradient of  $(E.E)$  terms were calculated using Matlab<sup>TM</sup> and the number of terms included in the solution was chosen to be 300 with  $L$  value set to  $5H$ . Increasing the number of terms more than 300 in the solution caused no noticeable change in the results. The mesh size used in the numerical solution was set to be 0.5  $\mu\text{m}$ . The slight difference between the numerical results and the analytical ones in Figure 4.6 is due to Matlab<sup>TM</sup> round off error when calculating *Sinh* and *Cosh* functions with large parameters.

Figure 4.6 shows the analytical and simulated results for the electric potential, the electrical field and the gradient of  $(E.E)$ . Analytical results show very good agreement with simulated results. Figure 4.6 shows that the electric field reaches its maximum value at the edges of the pair electrode and it decreases at positions far from the electrodes.

This analysis assumed that the right side of the unit segment is at a finite distance  $L$  from the left extremities. This assumption was validated by observing the error percentage of electric potential as  $L$  value changes at different selected points in the domain. Figure 4.7 shows the error percentage of the electric potential

$$100 \times \sqrt{\frac{\sum_{n=1}^N (V_{i+1} - V_i)^2}{\sum_{n=1}^N V_{i+1}^2}}$$

of the entire domain. The step size in x and y direction were

taken to be  $\frac{1}{2} \mu\text{m}$ . The parameter shows that with the assumption of  $L$  value to be more than  $3H$ , analytical solution calculation does not influence the results. These results confirm the hypothesis of a finite distance used in this work. Moreover, the presented analytical solution shows that the channel height is inversely proportional with the magnitude of the DEP force.

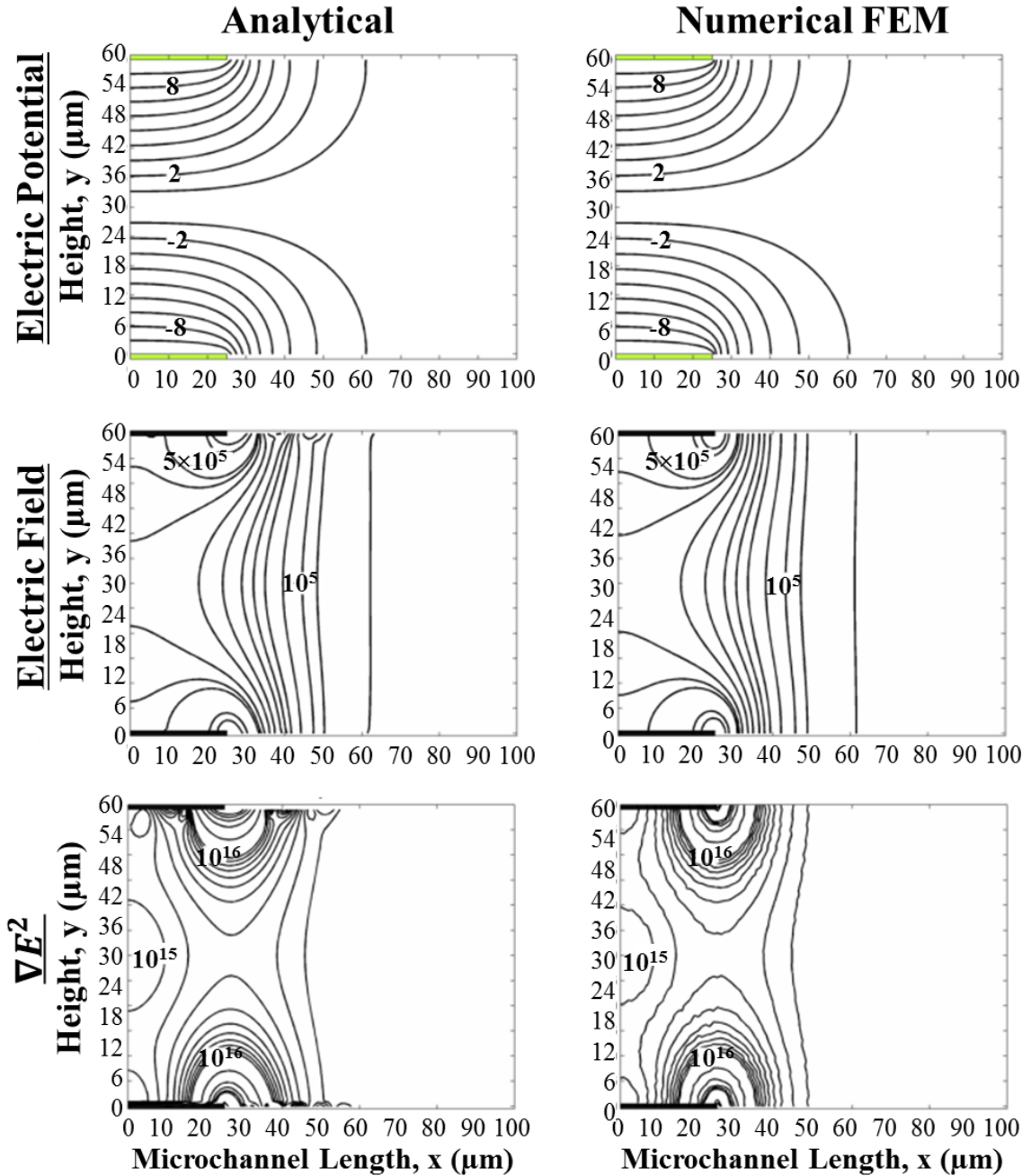
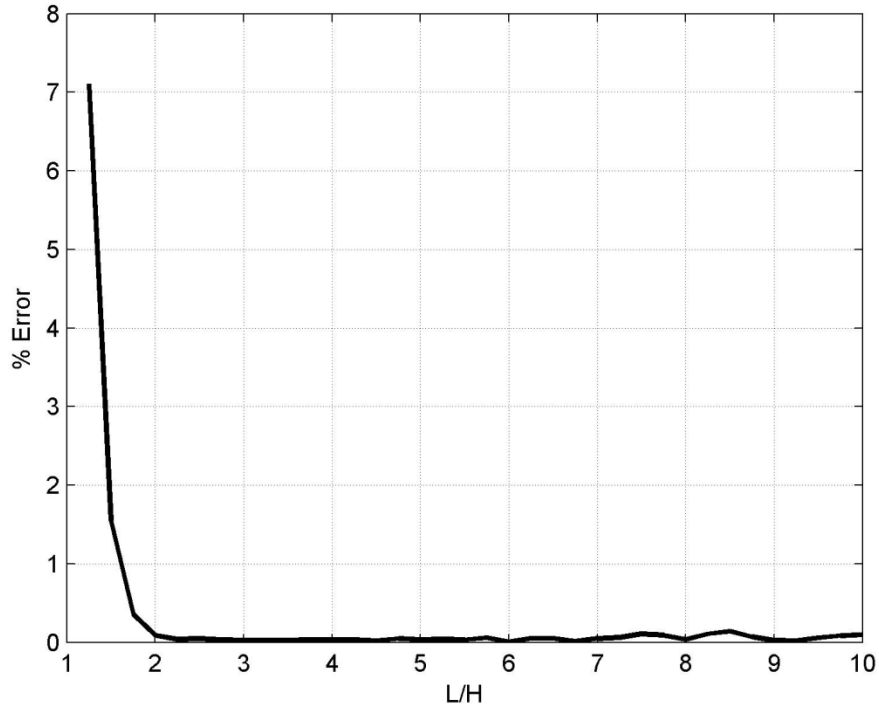


Figure 4.6: Comparison of analytical results and numerical simulations for the electric potential (V), magnitude of electric field (V/m) and the gradient of  $\nabla(E.E)$  ( $V^2/m^3$ ). Numerical simulations were obtained by finite element methods using COMSOL Multiphysics<sup>TM</sup>. The contour plots of the same level in the microchannel are shown for analytical and numerical results respectively. The thick lines at the top and bottom of the figures represent the electrodes and calculation were carried out using (upper electrode voltage of 10 Volts, lower electrode voltage of -10V,  $d=50\mu m$ , and  $H=60\mu m$ )



**Figure 4.7:** The error percentage of the electric potential in the microchannel as the parameter  $\frac{L}{H}$  changes. The step size in the x and y direction is selected to be  $\frac{1}{2} \mu\text{m}$  and the values of d and H were assumed  $20\mu\text{m}$  and  $60 \mu\text{m}$  respectively

Vector plots of dielectrophoretic force obtained analytically are shown in Figure 4.8a. The vector plot shows the direction and the magnitude of the DEP force in the micro device. Based on these results most of the cells should move and accumulate at the corner of the electrodes. Microscope taken picture of the experimental results of the behavior of red blood cell to positive DEP force under a sinusoidal voltage of 2 Volts peak and a frequency of 1 MHz is illustrated in Figure 4.8b. The analytical data and the experimental results are in a very good agreement. As expected, the dielectrophoretic force is at its maximum at the edges of the electrodes. Cells have been attracted by positive DEP and accumulated at the edges as shown in Figure 4.8a, Figure 4.8b and Figure 4.8c. In Figure 4.8, one can clearly see that the larger electrodes

(100  $\mu\text{m}$ ), with better edge resolution during photolithographic process, show larger positive DEP force at the edges compared to the smaller electrodes (50  $\mu\text{m}$ ) having large curvature radius at the edges. When the applied voltage is increased to 10 Volts peak, the high electric field obtained between the two pair electrodes affects the shape of red blood cells changing them from biconcave to elongated ellipsoid shape in only few seconds (Figure 4.8d). No lysing was observed. Most of the red blood cells have recovered their original shape when the voltage was reduced.

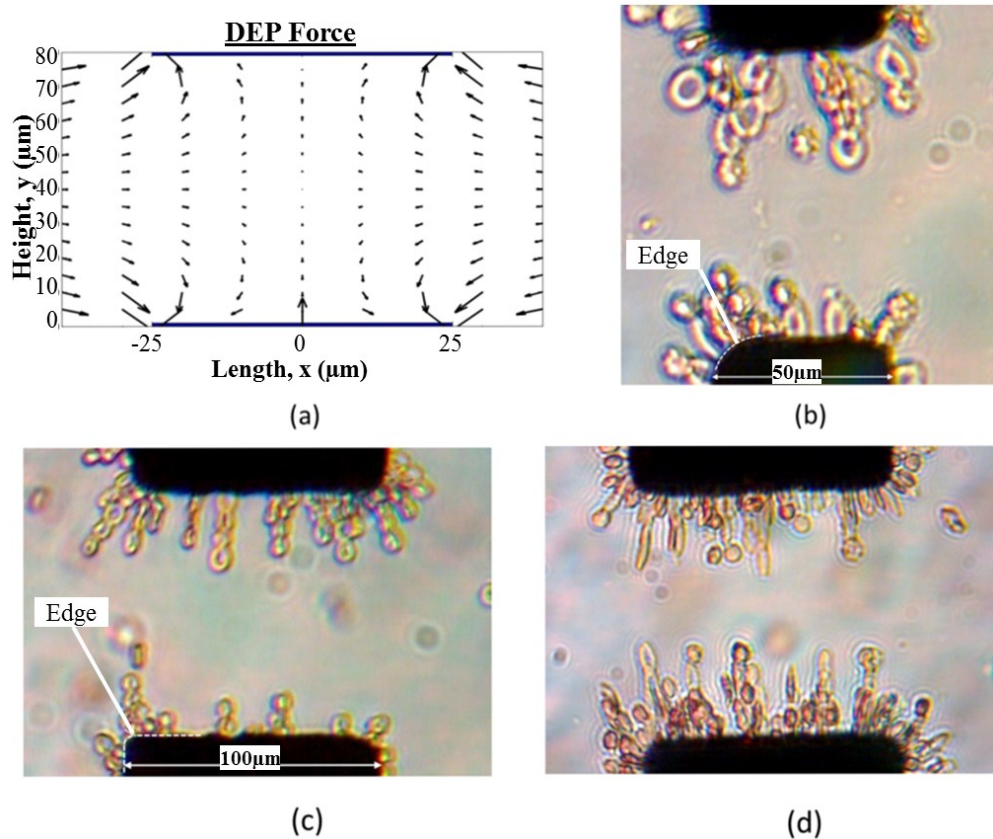


**Figure 4.8:** Analytical and experimental results (a) Vector plot of the magnitude of  $\nabla(E \cdot E)$  using the analytical solution (the electrodes are shown as thick lines); (b-d) Microscopic images showing the accumulation of red blood cells under positive DEP force with different applied voltages (b) 2 Volts peak and 1 MHz with round edges electrodes (c) 2 Volts peak, 1 MHz with sharp edges electrodes (d) 10 Volts peak, 1 MHz. Clustering of the cells correspond to the configuration of the electric field

## 4.7 Conclusions

In this analytical study, the microchannel DEP force strength and distribution is determined using an analytical solution through Fourier series for Laplace equation. The analytical solution gives information about the electric potential, electric field and DEP force acting on particles within a microfluidic channel. A judicious Gaussian surface analysis permitted the determination of all Fourier series parameters. The analytical solution was compared with the numerical simulation results and with the experimental data and the results showed a very good agreement among them. Since the electric field reaches the maximum value at electrode edges, electrodes with sharp edges create higher DEP force compared to electrodes with less sharp edges (more curvature shape). An increased of electric voltage on the electrodes changed the shape of the red blood cells and moreover, some did not return to their initial shape after the removal of the electric voltage.

The advantage of having the analytical solution is that it can provide some insight to the designer in the understanding of specific influence of geometric parameters of the physical design for appropriate cell manipulation within a microchannel. The analytical solution also provides a way to estimate cell transport trajectory within the microchannel with variation of channel characteristics such as the height, the electrodes dimensions and others physical parameters. Thus the analytical solution provides a very useful tool for the microfluidic system used for cell manipulation. The analytical solution could also provide the user with the capability to design the geometry of the electrodes for a desired configuration of the electric field within the microfluidic channel for DEP manipulation.

The experiments results confirmed the DEP phenomena aligning with the modeling results. Red blood cells aggregated according to the force distribution found analytically.

## **4.8 Chapter summary**

This chapter presents the theoretical analysis of the DEP force within a microchannel with parallel facing electrodes and opposite applied voltages. Simple mathematical solution is used to evaluate the electric potential, electric field and dielectrophoretic force using Fourier series with simple trigonometric and exponential functions. The exact distribution of the DEP force in the microdevice with the studied electrodes is important information for design parametric study.

All mathematical details and boundary conditions are given to reach the final results for DEP force distribution

With a designed and fabricated Bio-micro devices the analytical solution is compared with the experimental data. The measurements with the device use RBCs within the suspending media and experimental DEP force are assessed.

# **Chapter 5: Designs, Simulation and Fabrication of Micro Device for Cell Centering, Single Cell Detection and Characterization**

## **5.1 Introduction**

In the last two decades, with the advance of Bio MEMS (Bio Micro Electro Mechanical Systems) components and Lab on a chip concept, several methods were developed to characterize different cells or particles present in a biological media suspension. Most of these methods used single cell detection and characterization with different measurement techniques. These measurements provide information on cellular characteristics such as size, complexity and cell dielectric properties at low frequencies. This chapter provides the details of the design and fabrication process of a technique that produces hybrid microfluidic system with parallel facing electrodes using glass as base material. The fabricated micro device is used to center, detect and characterize the dielectric properties of a single biological cell at low and high frequencies. Two fused silica glass substrates with deposited gold electrodes and separated by a patterned silicone gasket layer are clamped together between two aluminum blocks ensuring a hermetic microchannel of 300  $\mu\text{m}$  width by 50  $\mu\text{m}$  height for measurement of a single living cell in a biological media without the use of pressurized or high temperature equipment. The technique is based on screen printing of silicone rubber on fused silica substrate with high reproducibility, fast fabrication and low cost. The manufactured packaged device is tested for dielectrophoresis particle focusing within the center of the channel. The success of this unique fabrication process enables the development of complex prototypes for biological applications such as single living cell detection, optical detection by

introducing optical fibers, microwave detection of biological fluids and particles, and other assays.

Microfluidic devices have multiple applications in different fields such as chemical synthesis and sensing, and biomedical solution testing and analysis [187, 188]. Diversity of microfluidic chips have been used by researchers for different applications with different designs and fabrication processes using structures made by plastics such as polymethylmethacrylate (PMMA), glass and silicon. The channels were constructed with SU-8 epoxy based negative photo-resist and polyimide [34, 189-191]. Other channels were embedded in polydimethyl siloxane (PDMS) presenting unique features and allowing 2D electrode systems for protein and cell manipulations [190, 192-195]. With a substrate material of PMMA, silicon and glass substrate, dry etching, wet etching, injection molding, laser ablation and high temperature stamping/embossing or imprinting process were used to create channels, and hermetic sealing were achieved using wafer level bonding and adhesive film bonding [34, 187, 191, 193, 194, 196].

This chapter presents two devices for cell assessment and characterization:

- Device 1: To study the effect of the exposure of RF energy on living cells, permitting the determination of RF operation frequency and power level for single cell characterization
- Device 2: For single cell centering, cell detecting/counting and cell characterization.

Fabrication procedures and details are given for the two devices. The device for RF exposure uses copper tape stripes over the 96 well plates and the RF signal is injected through SMA connectors. In the following section, adapted version of the poster

presented at the ARVO and simulation results at COMSOL conference are provided. In the subsequent section, all the details of the microfluidic device are adapted from the paper to be submitted to a scientific journal. Single cell characterization microfluidic chip is obtained by screen printing or serigraphy of patterned silicone rubber layer on fused silica having gold patterned electrodes. Two aluminum plates retain the two fused silica wafers and ensure a hermetic sealing for the microfluidic chip. The main benefit of this microfluidic chip resides in the design and fabrication process of a simple, fast, low cost and 3D hermetic ‘easy sealed’ channel with integrated parallel facing electrodes that can yield to separate living cells. The aim of this micro device is to develop a system suitable for cell or particle analysis and characterization. This objective is achieved by focusing the cells to flow one by one at the center of the microfluidic chip. This micro device is fabricated and its operation effectiveness was confirmed by negative and positive dielectrophoresis (nDEP and pDEP) force application on polystyrene particles and *Saccharomyces cerevisiae* or budding yeast cells.

## **5.2 Effect of Non Thermal Radio Frequency Radiation on Uveal**

### **Melanoma Cells**

#### **5.2.1 RF signal exposure on living cells**

The investigation of RF effect on cells is important to insure the viability of cells under electromagnetic exposure. Such test enables to determine the power levels with its associated operation frequency for future RF measurement and testing. In fact during the exposure of RF signal on living cells, the cells shall not be altered. This investigation requires an experimental set-up to apply the RF energy on cells and an evaluation process

and mechanism for cell viability. Waves in the frequency ranges of RF/Microwave affect the particles or cells by  $\delta$  relaxation (orientation polarization of particles) in Rayleigh region. The Rayleigh scattering happens when the particles are very small compared with the wavelength of the RF/Microwave signal. The radiation penetrates the cell membrane and dielectric properties affecting the content of the biological molecules. The Rayleigh scattering is based on absorption, reflection or scattering of the electromagnetic energy at the contact with the particles.

### **5.2.2 Specification of the RF signal frequency and the power level on normal and cancer living cells**

Predetermined specifications are required to design and fabricate the measurement apparatus and determine the overall set-up and evaluation process. The RF/Microwave spectrum being too large, it was decided to limit the exposure frequencies from 1 GHz to 3 GHz for measurement practicality purposes, keeping in mind that the Industrial, Scientific and Medical (ISM) [23] radio band covers the frequency range from 902 MHz to 5.875 GHz.. The microwave oven frequency is identified as 2.45 GHz. The power level was limited to 20 dBm or 100 mWatts out of the RF generator in 50  $\Omega$  load. The choice of this power level is appropriate since most of the RF/Microwave equipment power levels are less than this power level.

The goal of this study is to examine and investigate the effect of low power Radio Frequency (RF) effect on the human uveal melanoma cell lines 92.1. The effect is measured and assessed by proliferation assays on cell lines exposed to RF radiation. In addition, the aim is to determine a method and set-up to perform viable experiments for

proliferation and further apoptosis assays and evaluations. In the literature, assessment of low level RF frequency is performed to see the negative impact of that radiation on human's cells [197-202].

### **5.2.3 Determination of frequency and power level of RF signal**

Nowadays, very little studies are conducted to investigate and evaluate the effect of low power electromagnetic radiation on melanoma cells and assess proliferation, apoptosis and quality of the invasive assays. The proliferation assay on cancer and normal cells under the application of low power RF signals could help the evaluation of radiation effect on melanoma cells and the RF characterization/detection in micro cytometry. Therefore the experiment aims to establish the effect of the exposure of non-thermal electromagnetic field radiation on melanoma and fibroblasts cells by proliferation assay.

### **5.2.4 RF apparatus and measurement set-up**

Several RF pieces of equipment and systems are used for measurements namely:

- RF/Microwave generator (Agilent 83732B)
- RF/Microwave spectrum analyzer (Agilent 8593E)
- RF electrodes made of 3 copper adhesive stripes (taper shaped on one end) connected to 3 RF SMA connectors. The RF ground plane is insured through a single block of copper metal. The RF electrodes and the RF ground plane are separated by the 96 well plate and held by a Plexiglas corner blocks

RF/Microwave frequency band with a power level of 100 mWatts is divided into three ranges namely:

- Range 1 (1 GHz to 1.6 GHz)
- Range 2 (1.7 GHz to 2.3 GHz)
- Range 3 (2.4 GHz to 3 GHz)

These ranges were chosen to accommodate the designed measurement apparatus and the overall measurements time was less than 2 hours for the viability of cells.

Figure 5.1 shows the picture of the apparatus and Figure 5.2 presents the complete measurement set-up

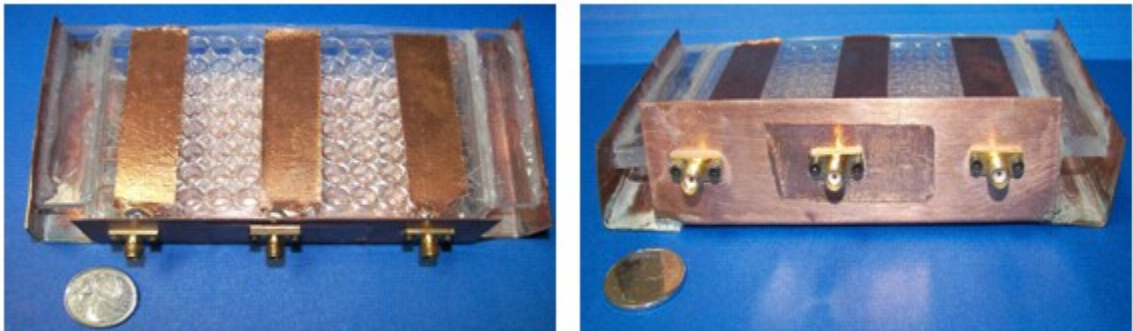


**Figure 5.1: The RF electrodes with copper stripes and 3 SMA connectors. The generator is connected to one of the inputs of the RF apparatus for RF radiation exposure. Uveal melanoma cell lines 92.1 and Fibroblast in a media are filled in 96 well plates**



**Figure 5.2:** The generator is connected to one of the inputs of the RF apparatus for RF radiation exposure. Uveal melanoma cell lines 92.1 and Fibroblast in a media are filled in 96 well plates

#### 5.2.4.1 Methods

The 92.1 cell line was derived from a choroidal melanoma and has been proved by previous studies from Witelson Ocular Pathology laboratory to be highly proliferative and invasive in nature. The fibroblast cell line was derived from human foreskin. The 92.1 and fibroblast cell lines were cultured until confluence. Media was changed biweekly and was monitored for signs of contamination.

Cells were passaged by treatment with 0.05% Trypsin in EDTA (Fisher) at 37°C followed by washing in 7 ml RPMI 1640 before centrifugation at 120 x g for 10 minutes to form a pellet. Cells were next seeded into a 96 well plate at a concentration of  $5.0 \times 10^3$  cells per well.

The first, sixth, and eleventh columns contained the 92.1 cell in six fold (six rows per column) while the second, seventh, and twelfth columns contained the fibroblast cell lines, also in six fold. A second 96 well plate following the same experimental setup

(containing 92.1 and fibroblast cells) was used as a control. While this plate was not exposed to RF radiation, it was removed from the incubator and placed in a sterile environment at 21 degrees Celsius while the first plate was exposed to RF radiation.

The RF energy is injected through the 3 SMA connectors and swept from 1 to 3 GHz with a generator power level of about 100 mWatts. The first and second columns are exposed to the frequency range 1 (1 to 1.6 GHz) for 35 minutes. The sixth and seventh columns are exposed to the frequency range 2 (1.7 to 2.3 GHz) for 35 minutes. The eleventh and twelfth columns are exposed to the frequency range 3 (2.4 to 3 GHz) for 35 minutes. Each range (1, 2 and 3) is composed by 7 discrete frequencies with steps of 100 MHz.

#### **5.2.4.2 Proliferation test**

Cells were allowed to adhere overnight before the start of the Sulforhodamine B based (TOX-6).

The experimental protocol can be summarized as follows: culture media was removed from all wells and 25  $\mu$ l of Trichloroacetic acid was overlaid atop each well to fix the cells. Plates were next incubated for one hour at four degrees Celsius and then washed to remove the excess acid. A solution of Sulforhodamine B was then added to each well for 30 minutes of staining. Next cells were washed several times with 1% acetic acid before the incorporated dye was finally released by a tris base solubilization solution. Dye absorbance was read with a microplate reader at a wavelength of 565 nm.

### 5.2.4.3 Experimental results and discussions

RF Energy was swept over band ranges of 21 discrete frequencies with 100 MHz separation. Continuous sweep from 1 to 3 GHz was applied to each of 3 RF connectors for a total period of 35 minutes per connector. This limitation was used to keep the cells outside the incubator for no more than 2 hours (within 2 hours the cells were considered viable for RF tests). It was desired to apply RF radiation for longer period. This could be done by inserting the well plate into the incubator and applying the RF energy in the incubator. Care must be taken to not affect the other cells in the incubator by the RF energy.

The reflection coefficient at the input of the each connector was not uniform with respect to the frequency ranges (1, 2 and 3). This has a power variation effect on the RF radiation within the 3 bands of frequencies.

Energy level on cells within the six fold column of wells was different due to the variation of power level on RF micro strip lines. Several well plates were subjected to RF radiation in order to increase the statistical validity of the results. Therefore, proliferation results were an average number per column and number of well plates

The proliferation results on cell lines 92.1 showed a reduction from 2 to 9 % over the frequency range from 1 to 3 GHz as shown on Figure 5.3. The proliferation results on fibroblast cell lines showed an increase from 7 to 53 % over the frequency range from 1 to 3 GHz as shown on Figure 5.4.

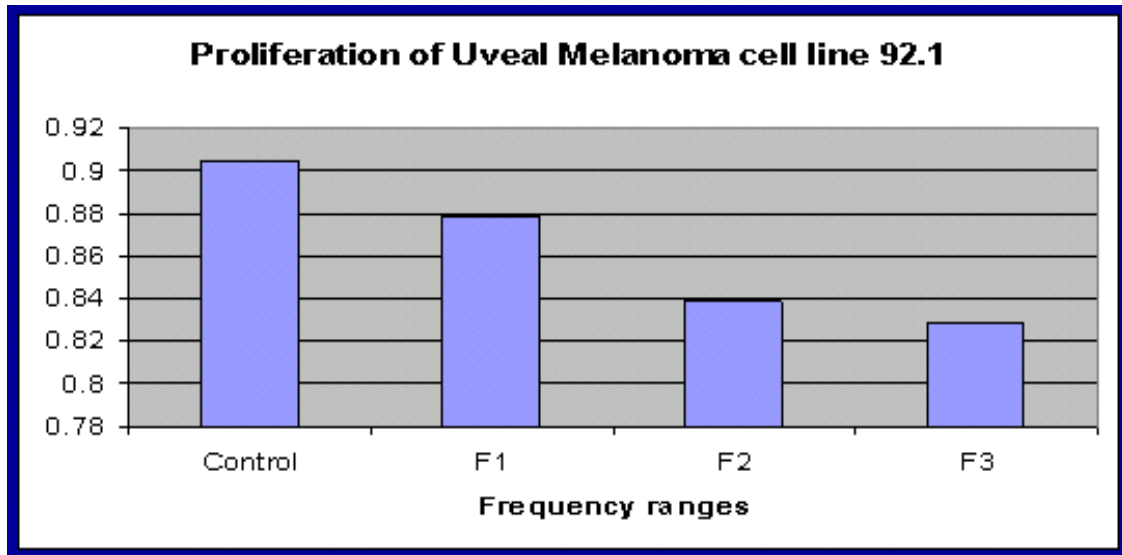


**Figure 5.3.** RF radiation proliferation results on 92.1 uveal melanoma cells in a media. F1, F2 and F3 present RF frequency ranges of (1 to 1.6 GHz), (1.7 to 2.3 GHz) and (2.4 to 3 GHz) respectively. The vertical axis presents the proliferation rate compared to the control 92.1 cells that were not subjected to RF radiation. The value of 0.9 for the control is an arbitrary value obtained from the proliferation test results

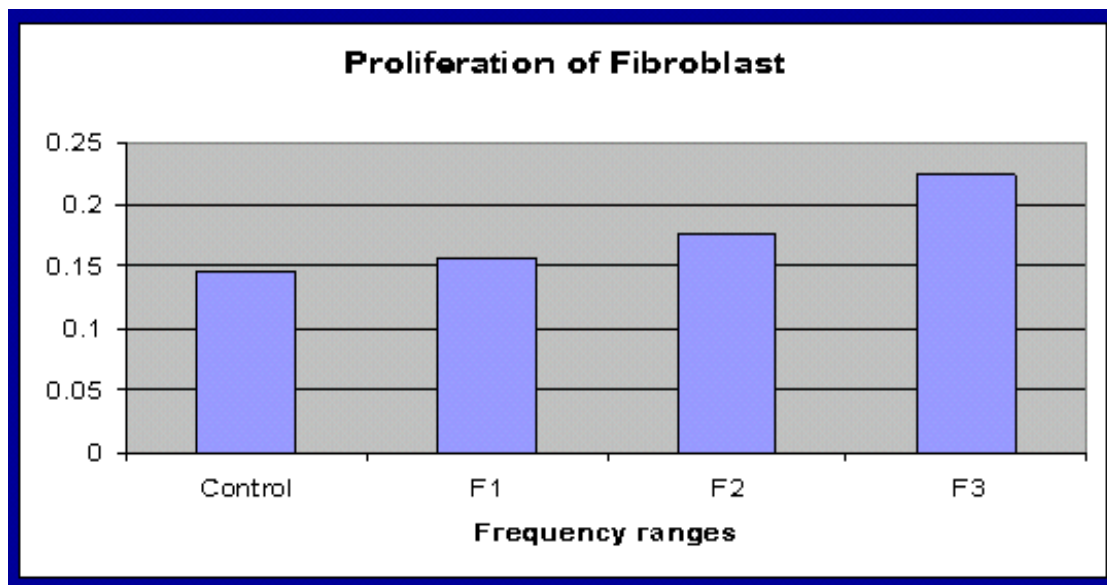


**Figure 5.4.** RF radiation proliferation results on Fibroblast in a media. F1, F2 and F3 present RF frequency ranges of (1 to 1.6 GHz), (1.7 to 2.3 GHz) and (2.4 to 3 GHz) respectively. The vertical axis presents the proliferation rate compared to the control Fibroblast cells that were not subjected to RF radiation. The value of 0.15 for the control is an arbitrary value obtained from the proliferation test results

Amplitude and phase modulated RF/Microwave radiation needs further investigation. For stronger electrical field on the cells, a special apparatus with 2 mm separation between RF electrodes are made to see the visual changes of cells under the RF radiation (Figure 5.5). Electrodes are formed by evaporation of Indium Tin Oxide on microscope glass slides. The electrodes are conductive for RF signal and transparent for cell observation. This set-up cannot enable a direct proliferation assay. At this stage, the evaluation of cells exposure with this apparatus was not performed.

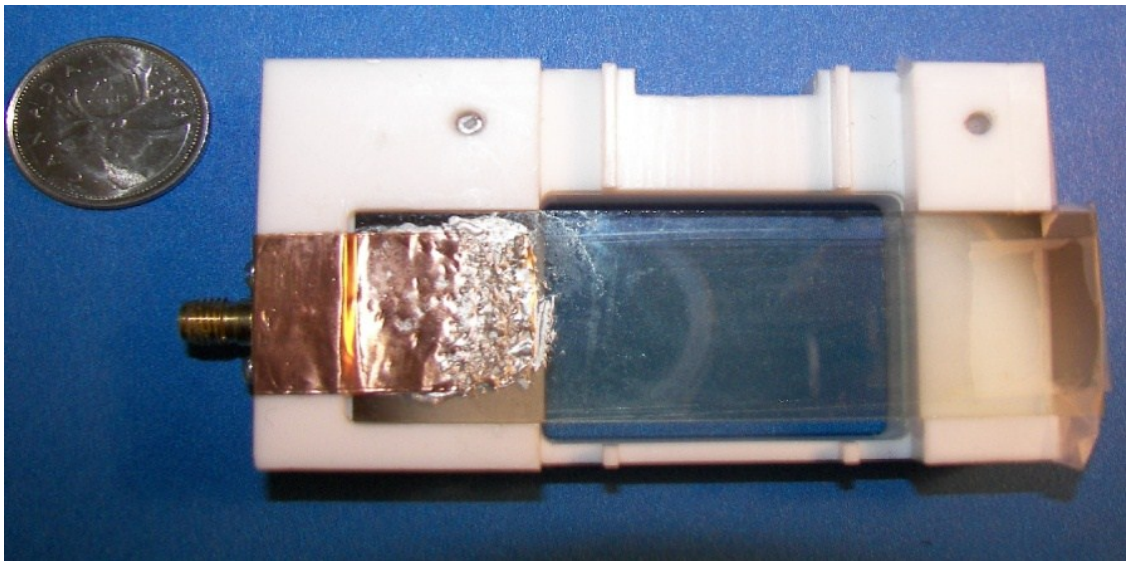


**Figure 5.5. New RF apparatus to inject RF radiation with stronger electrical field. The RF signal can be injected through the SMA connector. Indium Tin Oxide (ITO) films are evaporated on the two glasses acting as the conducting electrodes and permitting visual observation under the microscope**

RF/Microwave radiation at low energy affects human uveal melanoma cell lines 92.1. The effect is seen through the reduction of proliferation in the frequency range between 1 to 3 GHz. Based on the proliferation results on uveal melanoma cells, it is anticipated that with RF energy much smaller than 20 dBm (about 0 dBm and less) the effect will be almost negligible.

RF/Microwave radiation at low energy affects fibroblast cell lines. The effect is seen through the increase of proliferation in the frequency range between 1 to 3 GHz.

Future studies suggest repeating the findings on other uveal melanoma cell lines with additional apoptosis assays. Evaluation across a wider frequency ranges and longer radiation exposure time are desired and anticipated in the future with more uniform power level on RF lines. The simulation structure with COMSOL finite element analysis (FEA) [203] of the electrode stripes on the center well column of the RF apparatus is described in Figure 5.6. Figure 5.7 shows the return loss of the input port versus the frequency. The return loss close to 3 GHz is better than 12 dB. At other frequencies poor return loss indicates that a big amount of energy is returned back to the source instead of radiating.

A mismatch adaptation circuit would improve the return loss over the measurement frequency range.

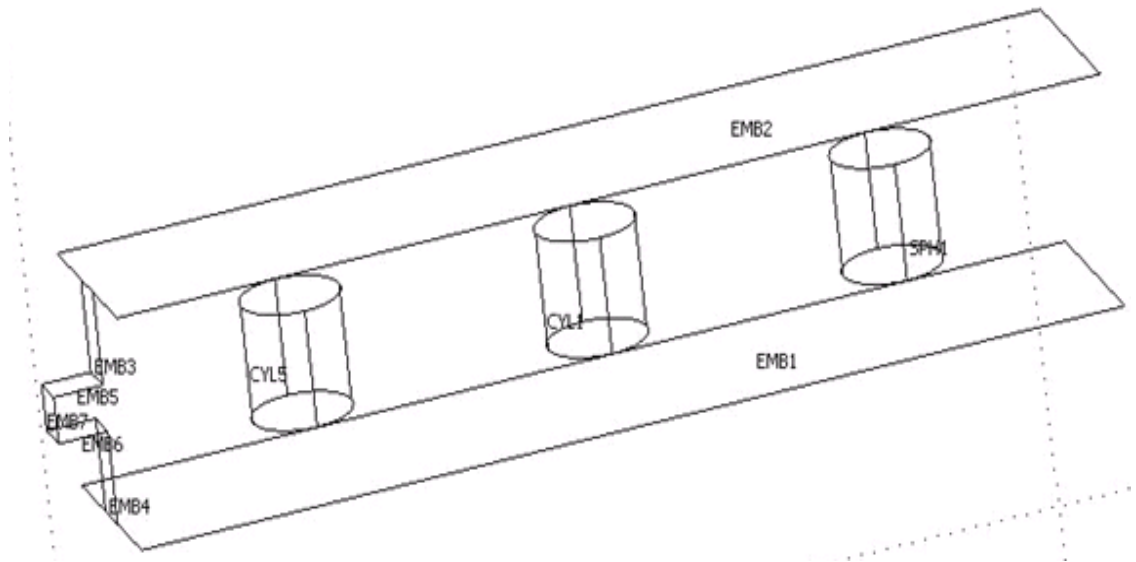


**Figure 5.6. The FEA simulation structure of electrode stripe on middle column of wells of the RF apparatus**

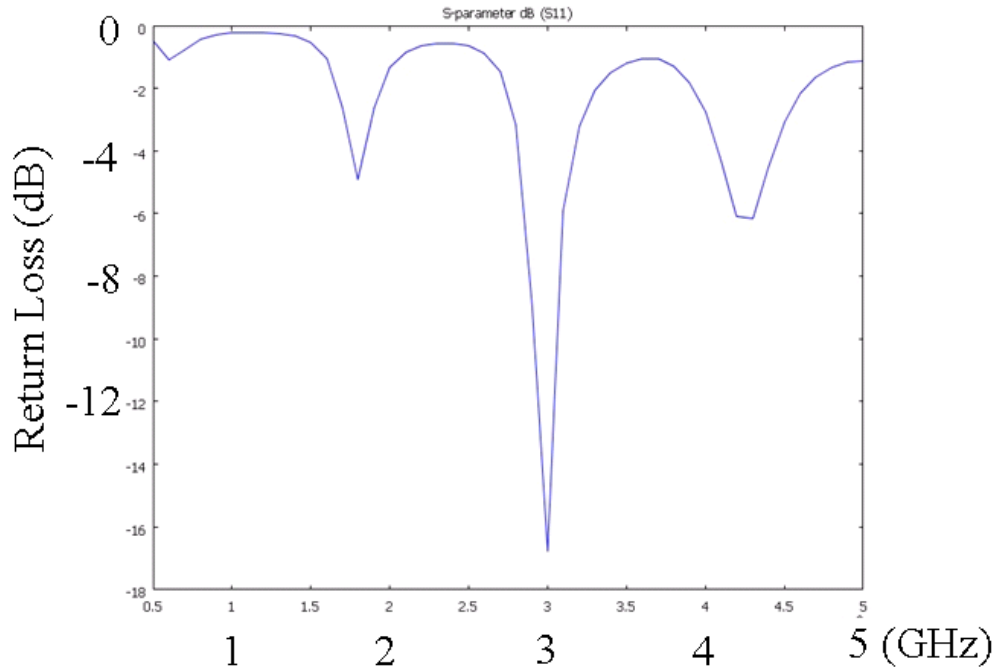


**Figure 5.7. Return Loss of the input port of the RF apparatus versus the frequency**

### **5.3 Single Cell Characterization Device**

The role of the single cell characterization microchannel device is to permit the injection of cells by focusing them at the center of the microchannel. Then the cells are present one by one in a zone where the RF/Microwave signal is injected, and transmission/reflection of that signal is measured.

#### **5.3.1 Materials**

Before discussing the design and fabrication of microfluidic chip, several points need to be addressed for the choice and availability of the:

- Equipment and facilities

- Needed technologies
- Desired application
- Channel features, such as dimensions, biocompatibility and sterilization
- Substrate and electrode materials
- Restrictions of the application. With the targeted widths and gaps in the order of few tens of micrometers, one mask photo-exposer and grey room access would be sufficient during the micro device fabrication.

The features used for the design and fabrications of this microfluidic chip are summarized as follows:

- Biocompatible microfluidic chip materials
- Inlet and outlet holes for liquid fluid access for count and flow
- Cross section of the channel within tens of micrometers in size and tolerance of micrometer, in the specific case of 300  $\mu\text{m}$  width x 50  $\mu\text{m}$  height
- Possibility to reuse the structure for performance evaluation purpose
- Ensure no leak from the channel
- Overlapped electrodes with at least 50  $\mu\text{m}$  width and gaps, within the channel for dielectrophoresis application (moving and sorting) and for low and high frequencies detection and characterization.

As it is observed, most of these characteristics are standard for all microfluidic chips. The major difference, beside its specific dimension for this design, resides in the overlapping parallel facing microelectrodes. In fact, the tight dimensions and overlapping electrodes feature require an innovative design and fabrication process.

### 5.3.1.1 Channel substrate material

The fabrication of the microfluidic chip is intended to enable the observation, the manipulation, the detection/counting and the characterization at low and high frequencies of biological cells within a media injected in the microchannel. In order to observe the cells or particles moving in the channel under a microscope, two practical solutions were available for the substrate material: transparent plastic or glass. PMMA material showed some difficulties of warping while depositing electrode materials by sputtering technique. This is due to the high temperature during the deposition process. The use of cyclic olefin copolymer supporting high temperatures would be a solution but it has some disadvantages in the precision of the photolithographic process and achieving low electrical resistivity electrodes with simple deposition process [204]. Glass material also showed some drawbacks. After several iterations of microfluidic circuit fabrication, glass substrate started to crack under even low pressure. In fact, media inlet and outlet holes made by laser ablation or by alumina powder abrasion showed some micro cracks in the glass creating serious issues related to leaks in the micro device, and thus jeopardizing the hermetic sealing of the microfluidic circuit. As a solution, fused silica glass was chosen as the substrate material due to its excellent mechanical, thermal and electric properties compared to PMMA and glass. The flow rate in rectangular cross-sectional microchannel is higher than the flow rate in other shape of microchannel cross section [31]. In the single cell characterization device, the flow rate is not a dominant desired requirement, nevertheless since the rectangular shape channel fabrication is more practical, then the fabricated channel for this application will have the rectangular shape cross section.

### 5.3.1.2 Electrodes Material (Thin Film)

In general different electrode materials are used to pattern electrodes in a microfluidic chip: such as copper, gold and other such metals. The biocompatibility of the electrodes material, the reduced frequency electrolysis corrosion effect of the electrodes [205] and the possibility to clean the channel with ethanol and other solvent had directed to the solution of using gold as electrode material. Titanium was used before patterning gold electrodes for good adhesion of gold on the fused silica substrate. Thin film Indium Tin Oxide (ITO) could have been a possible solution also used for its optical transparency, but for this application under-electrode transparency was not required for the stated objective. Moreover, ITO resistivity is significantly higher than gold (under some conditions of deposition, ITO layer has a resistivity 60 times higher than layers with ITO/gold) [206].

### 5.3.2 Channel fabrication

The presence of parallel facing electrode configuration in the channel did not permit the use of PDMS. Most of the time PDMS is used for patterned planar electrodes on a hard material like glass or PMMA and embedded PDMS ensures only the realization of hermetic 3D channel. Since the height of the channel is set to 50  $\mu\text{m}$ , several solutions were considered to create the microfluidic chip. The use of double-sided adhesive tape with a certain thickness (ARclear<sup>TM</sup> 8154, Adhesives Research, USA) and patterned with the desired shape of the channel could be used to create the 3D channel. This solution could ensure a hermetic microfluidic chip but the microscopic alignment of the parallel facing electrodes for a specific design would become a difficult task due to the

tight dimension specifications at electrode overlapping stage and the complex alignment manipulation of double sided adhesive, requiring specialized sophisticated alignment equipment. Photo-imageable film was used to form the channel by photolithography. This material is commonly used in photolithography of Printed Circuit Board (PCB), but the issue of hermetic channel sealing is difficult to overcome at the edges of the substrate when glue was used. It is noted that any liquid glue can infiltrate by surface tension, diffusion or dispersion and can clot the channel. Moreover, the use of alcohol and other solvent for subsequent sterilization stages limits the use of this film given the solubility with alcohol or other solvent.

Therefore, the interesting solution was in creating the channel with screen printing liquid silicone rubber (GE112A, General Electric) on the first fused silica wafer with a metal mask made at the desired shape and height of the channel. This material is biocompatible, resistant to solvents and cleaning solutions used in clinical applications. Its most important characteristic is that it remains soft after curing permitting a perfect sealing of the channel.

### **5.3.3 Hermetic channel and flexibility of channel re-utilization**

Silicone rubber rings were also screen printed on the second fused silica substrate in which previously the appropriate holes were made. The complete structure was sealed by squeezing and retaining the two fused silica substrates between two aluminum blocks while aligning the parallel facing electrodes overlapping under the microscope. The thickness of aluminum blocks were designed for good flatness. The tightening of the two aluminum blocks with four two screws during the alignment ensured the hermetic sealing

of the microfluidic chip. The pressure applied on each screw is less than 0.1 MPa to ensure a value less than the polymer yield strength. This microfluidic chip could be flushed and cleaned with alcohol or ethanol without affecting the silicone rubber layer and keeping the channel hermetic.

#### 5.3.4 Fabrication procedure

Figure 5.8 shows a picture of the assembled structure of the microfluidic device. The inlet and outlet ports are made of aluminum insert studs within the aluminum block, giving more mechanical resistance to the applied pressure from the inlet/outlet tubing. These ports are connected to the glass structure via the holes in the studs. Sealing between fused silica holes and the aluminum block studs are ensured with the silicone rubber rings.

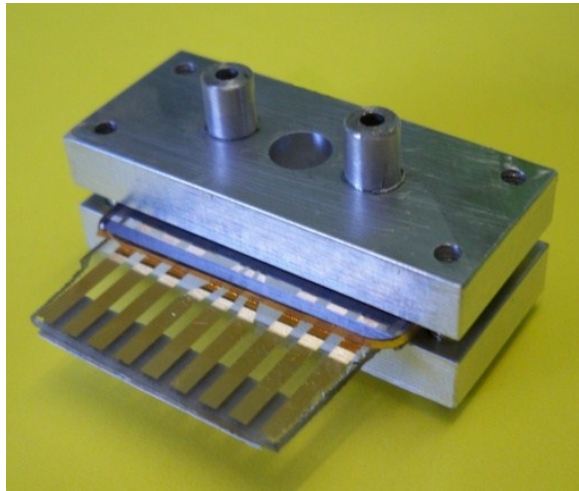


**Figure 5.8: Assembled structure of the microfluidic device**

Figure 5.9 shows a cross section and side cut views of the actual device. As indicated earlier, fused silica glass is the final choice for the substrate given its mechanical and optical properties. On these substrates a thin film process for the

fabrication of the electrode is used. Gold is retained as electrode material for its biocompatibility and low resistivity. The fabrication steps are the following: cutting the substrates, patterning the electrodes, drilling the holes, creating the channel and assembling for hermetic sealing.

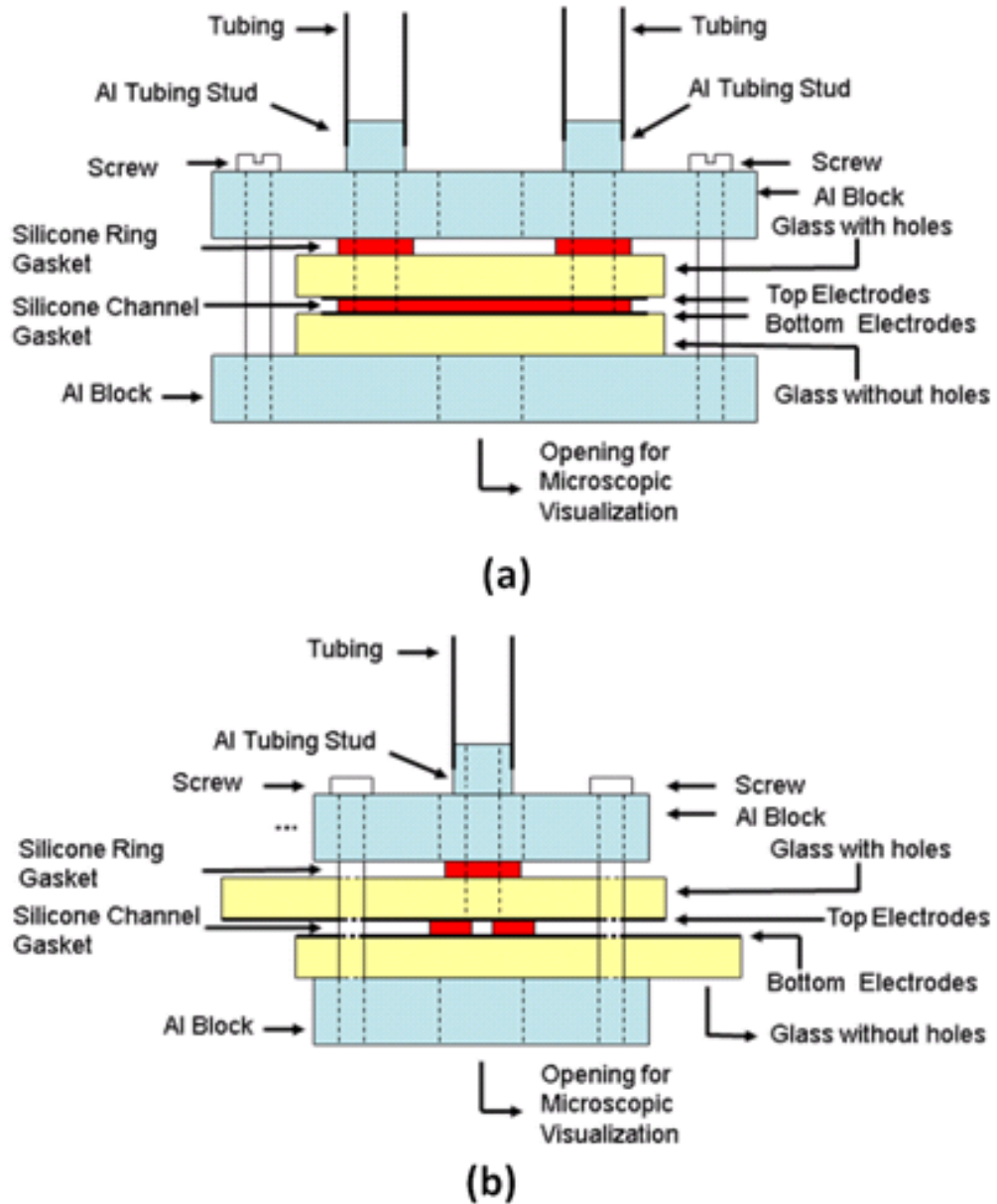


Figure 5.9: Cross section view (a) and side cut view (b) of the entire structure

After cutting the substrates and the patterning the electrodes on the substrate, two holes one each end of localization of channel were drilled to enable the fluid reach the channel. Then a thin layer of silicone rubber is applied using screen printing technique aligned with respect to the holes are the electrodes. The pattern of silicone rubber, to create the microchannel, is printed on one layer of the substrate. Ring of silicone rubber patterns are made surrounding the holes on the second substrate. After curing the silicone the substrates are aligned together in micron range with respect to the interrogation electrodes to obtain the 3D structure. In final step, the two substrates are mounted between two aluminum blocks, and the entire unit is tightened at the optimal pressure by screws on each corner to ensure that no leaks on the channel and the port connections are present.

#### **5.3.4.1 Substrate preparation**

The following steps describe the preparation of the channel substrate:

- Fused silica wafer of seven inches square with 1 mm thickness was cut to obtain two pieces of  $1 \times 1^{3/8}$  inch fused silica substrates using diamond saw
- The two substrates were cleaned by ultrasonic bath using strong degreasing solution and final cleaning with acetone.

#### **5.3.4.2 Electrodes Deposition (Thin Film Process)**

The thin film process is based on wet etching process using standard lithography. Prior to make the lithography a set of masks was required to pattern the desired structure. Due to the symmetry of the structure design, only one mask with alignment marks was

required for patterning the electrodes on both fused silica substrates. The steps for printing the electrodes on the first substrate are the following:

- The metal was deposited by sputtering (Plasma Science Inc. Model 150). A layer of 20 nm Ti (as adhesion coating) was followed by a layer of 1  $\mu\text{m}$  of Au
- The photo resist was spun having a final thickness of 3  $\mu\text{m}$
- The mask 1 was aligned to the substrate 1 and exposed with standard UV mercury lamp integrated to the mask aligner (OAI, Model 200)
- This photo resist (AZ1518) was developed to get the desired electrode pattern
- The Au was etched using Iodine solution at room temperature for 2 minutes
- The Ti was etched using Hydrogen Peroxide 35% at 70  $^{\circ}\text{C}$  for 10 minutes
- The resist was stripped off and the substrate was cleaned with acetone.

The thin film process block diagram is given in Figure 5.10. Those steps were repeated for the second substrate using the same mask 1. The first substrate is at the bottom of the structure according to figure 2 and the second substrate is at the top of the structure. On the second substrate two holes are required to allow the fluid pass through the microfluidic channel.

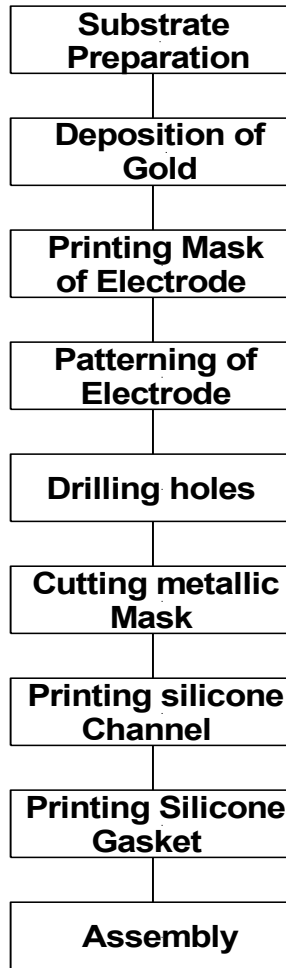


**Figure 5.10: Block diagram of thin film process and channel fabrication**

### **5.3.4.3 Holes drilling**

Drilling holes on fused silica substrate is a difficult task for many reasons. The laser technique does not work well as glass is transparent. After several trials, it was realized that small cracks induced by the huge thermal load were created making the substrate fragile and not appropriate for the next steps. The abrasion technique gave much better results.

The abrasion technique is simple and less expensive than laser, but its drilling produces less accurate holes than laser. For this application the accuracy of holes positioning was not a critical issue. A micro jet of alumina powder was sprayed on the second substrate at high pressure 100 PSI. The minimum size of nozzle available on the market is 250  $\mu\text{m}$  and the alumina powder grain size is 50  $\mu\text{m}$ . This nozzle was mounted on a small X-Y table to make possible the alignment to the substrate. After 1 minute of blasting, a hole of roughly 250  $\mu\text{m}$  in diameter was drilled on the 1000  $\mu\text{m}$  thick substrate. To increase the size of this hole, second and third holes were drilled adjacent to the first one to obtain a total hole of roughly 500  $\mu\text{m}$  in diameter.

#### **5.3.4.4 Channel fabrication process**

To generate the channel, several iterations were tried using many materials. The most appropriate material found was the silicone rubber. Silicone includes all the qualities sought for the application. The steps to create the channel are the following:

- For the printing of silicone, a screen was patterned on a sheet of brass with 60  $\mu\text{m}$  thickness by laser ablation using mask 2
- For alignment, the substrate 2 was attached on a Plexiglas base
- Using a microscope, the brass screen was aligned over the substrate 2 and fixed
- A small quantity of silicone rubber was applied over the screen using a small squeegee
- After the screen was removed, touch up was used to close the edges of the two round sections silicone rubber. The silicone was left for 12 hours curing at room temperature

- The same technique of screen printing was used to create the two silicone rubber rings with mask 3.

The patterned brass screens for the microchannel and the sealing rings are shown in Figure 5.11. Figure 5.12 shows a picture of the channel formation on the substrates. In this figure, the electrodes for focusing the particles and measurement at low and high frequencies can be observed. The white colored material on the top of the fused silica substrate and the gold electrodes represents the silicone rubber that will form the microchannel.

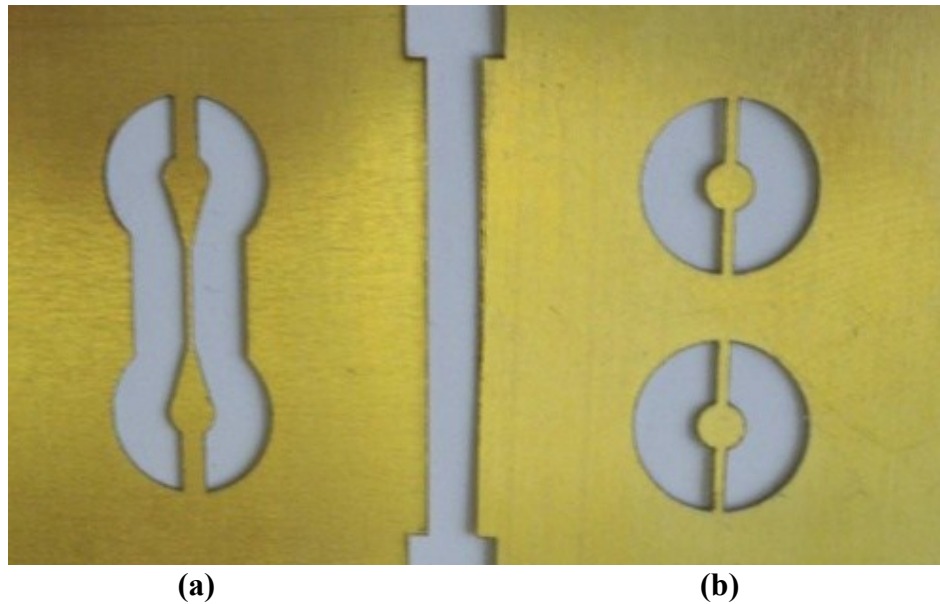


**Figure 5.11: Patterned screen used for screen printing the silicone rubber creating the microchannel - mask 2 (a) and the sealing rings - mask 3 (b)**

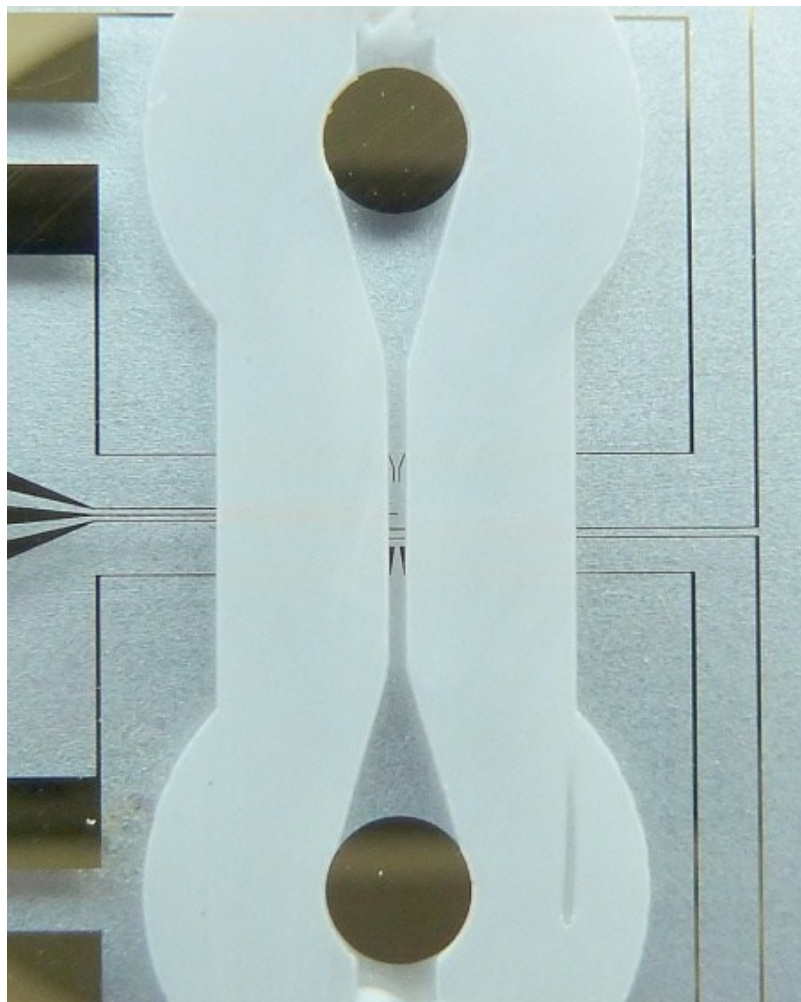


**Figure 5.12: Sandwiched fused silica substrates showing the channel and the parallel facing electrodes**

#### **5.3.4.5 Channel sealing and structure assembly**

To ensure a good hermetic channel sealing, the silicone ring layer as described earlier was selectively deposited around the inlet/outlet holes at the location where the aluminum block's holes were pressing the substrates. With the help of the two aluminum blocks and the four screws, the two substrates were aligned under the microscope and the screws were tightened with controlled pressure ensuring good sealing of the channel and the final structure. Circular openings were created in the middle of both aluminum blocks

to permit the observation or visualization of the electrodes and biological cells within the microchannel. With the softness of the silicone rubber the squeezed channel thickness was approximately 50  $\mu\text{m}$  and the channel width close to 300  $\mu\text{m}$ .

### 5.3.5 Microfluidic chip integration

Figure 5.13 shows a picture of the microfluidic chip associated with all the electronic circuits for the focusing of cells to the interrogation point, for the detection, the counting and the characterization of cells at low and high frequencies.

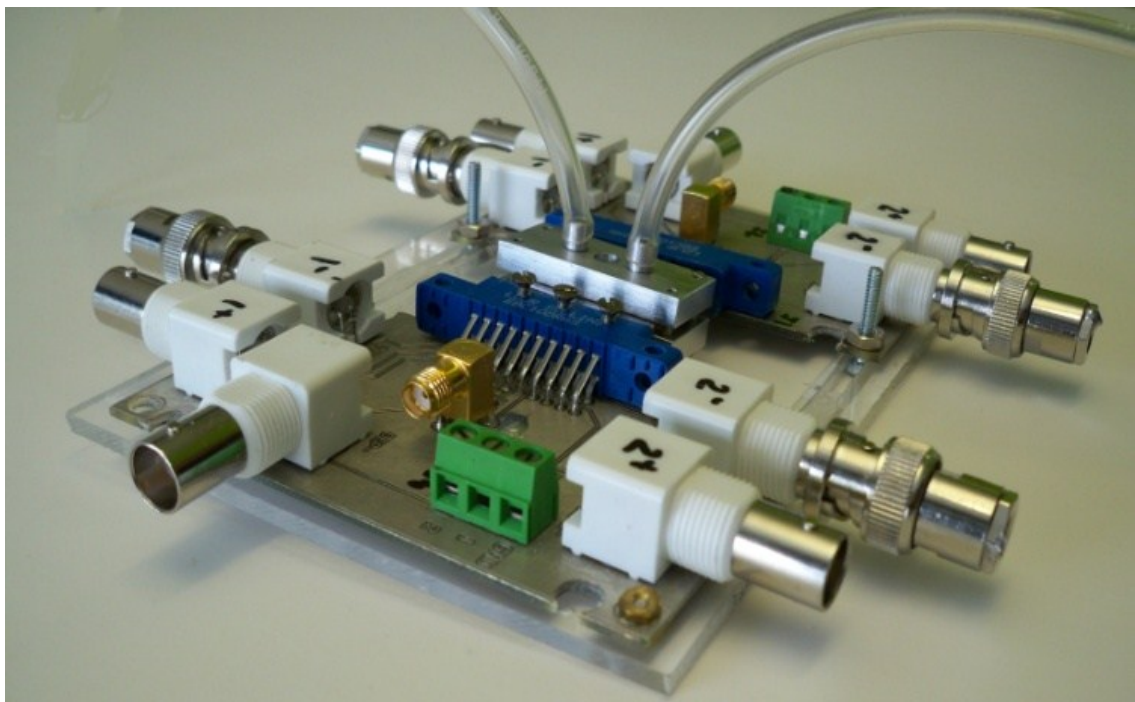


**Figure 5.13: Integrated microfluidic channel with electronic circuits for system control and measurements**

### 5.3.6 Simulation

To validate the microfluidic chip design and demonstrate the multiple operation of the device on living cells at the interrogation point, dielectrophoresis (DEP)

experimentation was performed using non uniform electric field by the focusing patterned electrodes.

Dielectrophoresis was first time described as the motion of neutral, polarisable particles subjected to non-uniform electrical fields [207]. Non uniform electrical field can be created using an array of metallic electrodes with a certain arrangement or configuration [113, 191, 208, 209]. The expression of dielectrophoretic force acting on a spherical polarisable cell placed in a non-uniform electrical field within a media was already seen in previous chapter as:

$$\mathbf{F}_{DEP} = \pi\epsilon_0\epsilon_m R^3 \text{Re}[f_{CM}] \nabla(\mathbf{E} \cdot \mathbf{E}) \quad (144)$$

The fabricated microfluidic chip configuration enables centering of particles in a single stream with a negative DEP (nDEP). As the suspended particles in the media are introduced into the channel, the particles can either be focused towards the center of the channel due to nDEP or attracted by the electrodes due to positive DEP (pDEP), both phenomena created by the applied AC electric voltage on the electrodes with specific frequency. The amplitude of the resultant DEP force depends on the polarizability difference of the particles and its suspended media, the non-uniformity degree of the applied electric field and its frequency. Design parameters and material properties are such that the vector force resulting from DEP and drag force on the particle will direct the particle toward the center of the channel at the measurement interrogation points (with nDEP) or to the edges of the focusing electrodes (with pDEP).

Figure 5.14 shows the schematic representation of the focusing principle. The trapezoid electrodes with non-uniform electric field induce positive gradient of the

electric field and are designed to focus single cell at the center of the microchannel followed by other patterned electrodes for cell or particle characterization. The control parameters for nDEP effect are the proper media conductivity preparation and the frequency of the applied signal on the focusing electrodes.

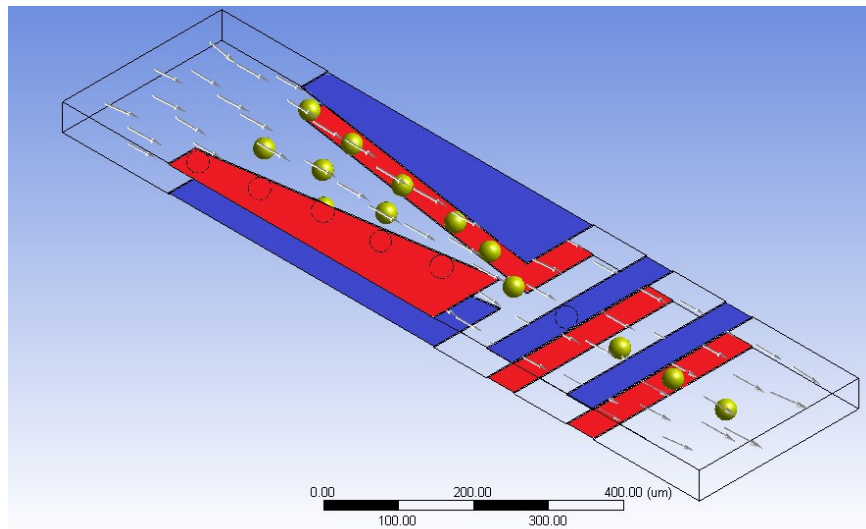


**Figure 5.14: Focusing principle based on negative dielectrophoresis. Particles injected at the input of the channel follow the direction of the arrows and they are focused at the center of the channel. The two different colors on the electrodes represent the applied two electric potentials**

Different electrode configurations are used for particles manipulation and measurements. Figure 5.15 shows the configuration of the electrodes for particle focusing and the particle measurement at low and high frequencies. Two stripes of electrodes for low frequency measurements are located after the focusing trapezoidal electrodes followed by other high frequency measurement and focusing electrodes. The gaps and electrode widths between the focusing and high frequency measurement electrodes are designed to be the minimum process applicable dimensions ( $50 \mu\text{m}$ ) to ensure the centering of cells at the RF/Microwave interrogation point. All these electrodes are

necessary for the versatility of the operation of the micro device mainly for focusing, detecting, counting, characterizing and sorting of single living cell.

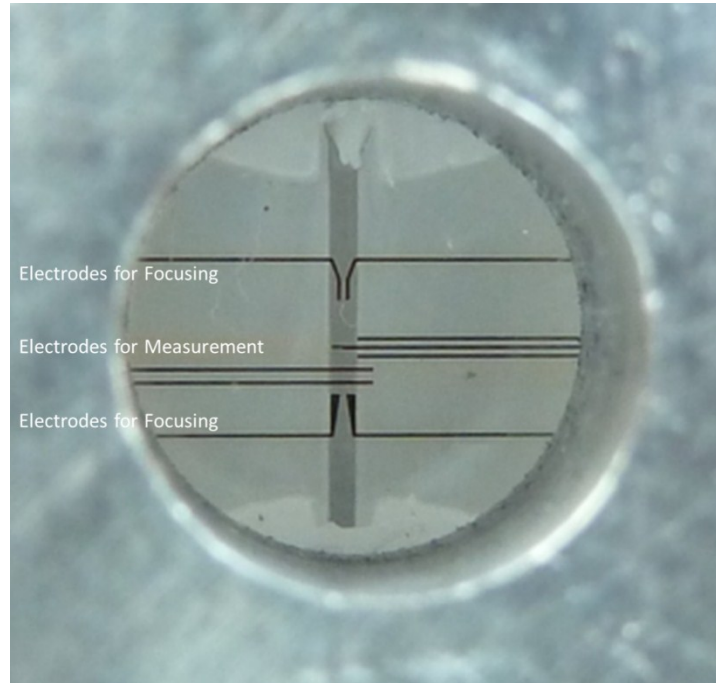


**Figure 5.15: Close up picture, through the aluminum blocks' opening, of the microchannel with the focusing and measurement electrodes**

In pressure driven steady state flow, the velocity of the particle can be determined from the vector force equilibrium between the DEP, hydrodynamic drag, gravity and buoyancy forces [183]:

$$\mathbf{F}_{\text{DEP}} + \mathbf{F}_{\text{DRAG}} + \mathbf{F}_{\text{GRAVITY}} + \mathbf{F}_{\text{BUOYANCY}} = 0 \quad (145)$$

With gravity and buoyancy forces assumed as negligible, equation (145) becomes:

$$\mathbf{F}_{\text{DEP}} + \mathbf{F}_{\text{DRAG}} = 0 \quad (146)$$

From Equations (145) and (146) it is obvious that the main force contributions are the DEP and drag forces. Therefore, with a DEP force dominating the drag force at low flow

speed in the microchannel, the control of the movement of cells in the microchannel is ensured by properly choosing the conductivity of the media, the applied signal frequency and its amplitude.

### 5.3.6.1 Simulation Results

Particle trajectories in the microchannel (Figure 5.14) were predicted using commercial Finite Element Method (FEM) Software (ANSYS, COMSOL Multiphysics<sup>TM</sup>) and Matlab<sup>TM</sup>. The electric field and the gradient of its square were numerically studied to understand the distribution of the 3D structure DEP force in the micro-device. The FEM results for the electric potential and electric field are shown in Figure 5.16. The simulation results of the particles trajectory are similar to focusing principle of Figure 5.14. The displacement of the particles was simulated with 10 and 0 Volts applied electric potential on the trapezoidal electrodes and 1 and 0 Volt for the stripes.

The gradient of square of the electric field with perfect alignment and misalignment of the two substrates are shown in Figure 5.17.

The effect of the misalignment of the two substrates on the DEP force distribution in the microchannel was studied numerically with 10  $\mu\text{m}$  shift in the x-direction. The simulation result for the gradient of squared electric field with 10  $\mu\text{m}$  shift in the x-direction shows that the force reaches maximum values at the edges of the electrodes and the force will be repulsive or attractive for the particles or cells depending on the sign of the Clausius-Mossotti factor and the frequency of the applied electric field on the focusing electrodes. The effect of this shift of alignment does not have a big influence on the overall DEP force.

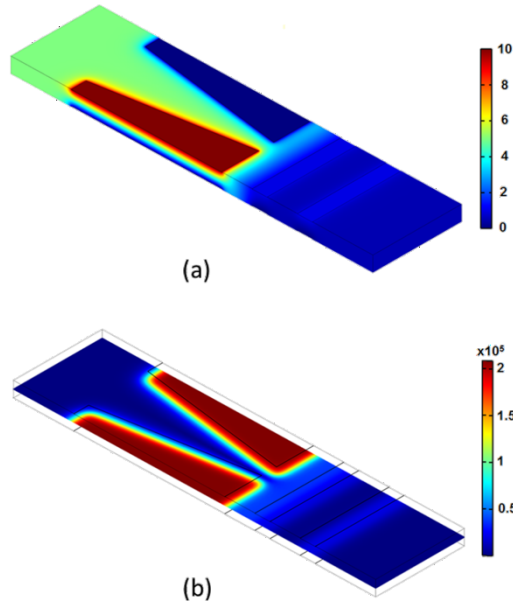


**Figure 5.16: 3D structure electric potential distribution in the channel (a) and electric field distribution at the mid plane of the channel (b). Applied voltage is 10 and 0 Volts on the opposite electrodes of the trapezoid electrodes. Applied voltage is 1 and 0 Volt on the stripe electrodes. Scaled values are in Volts for electric potential and in Volts/meter for electric field**

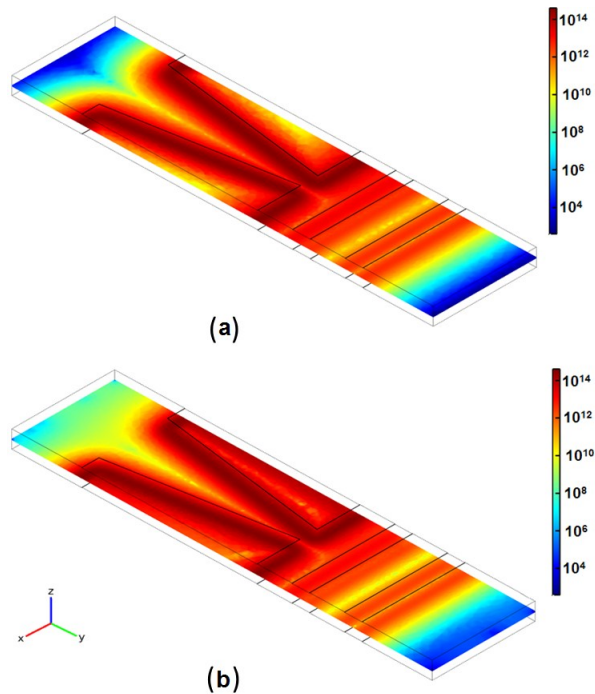


**Figure 5.17: The mid plane distribution of gradient of squared electric field distribution at the focused interrogation point for perfect alignment of electrodes (a) and with 10  $\mu$ m x-direction shifted electrodes due to the misalignment of the substrates (b). Applied voltage is 10 and 0 Volts on the opposite electrodes of the trapezoid electrodes. Applied voltage is 1 and 0 Volt on the stripe electrodes. Scaled values are in Volts<sup>2</sup>/meter<sup>3</sup>**

### 5.3.7 Experimental Results

Channel operation was verified by investigating the negative and positive Dielectrophoresis effect on different particles or cells such as polystyrene microspheres and *Saccharomyces cerevisiae*. These particles and cells were diluted in media with different conductivities.

#### 5.3.7.1 Media preparation for polystyrene microspheres

Monodisperse polystyrene microspheres of 15  $\mu\text{m}$  diameter (Megabead NIST Traceable Particle Size Standard) with 1% solids suspensions in de-ionized water with surfactant (from Polysciences, Inc.) were used to test single particle focusing in the microchannel. A media was prepared with 10 ml of water and 0.1 ml of Trypsin (0.05%) to obtain a conductivity of 20 mS/m. Low media conductivity is needed to ensure proper DEP mechanism since the DEP force depends on the real part of Clausius-Mossotti factor and the media conductivity. The dominant factor is the Clausius-Mossotti factor which is increased with the reduced media conductivity value. The conductivity was measured with Oyster PH-Conductivity-TDS meters, model 341350 from Extech. Five drops of 50  $\mu\text{l}$ /drop of polystyrene bead solution was mixed with the prepared media. The diluted beads within the media were injected through the inlet port of the microfluidic chip through a syringe pump. The used syringe pump was from Harvard Apparatus, Inc. (Pump 11 plus) with characteristics of volume flow rates of 0.0014  $\mu\text{l/hr}$  to 7.91 ml/mn.

#### 5.3.7.2 Media preparation for *Saccharomyces cerevisiae*

*Saccharomyces cerevisiae* or budding yeast samples were prepared in a distilled water solution by letting them grow at a temperature of 25°C for about 30 minutes.

Different yeast concentration samples were prepared. The first sample with high yeast concentration had a conductivity of 330 mS/m and the second sample having lower yeast concentration with 25 mS/m conductivity. The same pump was used to push the media through the microchannel.

### **5.3.7.3 Media preparation for different cancer cells**

Sucrose/dextrose low conductivity media was prepared. The cells concentration has been chosen to be  $10^3$  - $10^4$  per ml and suspended in 5 mS/m media. The flow of cells and media in the device has been controlled by a syringe pump (Harvard Apparatus). The experiments have been performed at different flow rates up to 0.5 ml/hr. Experiments employed other equipment including an inverted microscope (Omano OM900) equipped with a digital camera (Moticam 1000) and a computer. AC signals (Tektronix CFG280) of 100 KHz and higher with voltages from 2 to 10 Volts peak were applied to the two electrodes. From 100 KHz to 1 MHz, red blood cells experienced a positive DEP phenomenon and gathered all around the finite size electrode with the higher density of cells at its edge. This phenomenon was observed on both electrodes. The high end of the applied voltage (about 10 Volts peak) induced an elongation of the red blood cells with elastic and plastic behaviors.

### **5.3.7.4 Experiments with polystyrene microspheres and**

#### ***Saccharomyces cerevisiae***

In a confined flow, with a steady and constant density fluid flowing through a fixed volume (different inlet and outlet cross section), continuity equation shows that the

volume flow rate is constant at the two cross sections [171] and can be written using the following equation:

$$Q_1 = Q_2 = v_1 A_{CS1} = v_2 A_{CS2} \quad (147)$$

$Q_n$ ,  $v_n$  and  $A_{CSn}$  represent the volume flow rate at different cross sections, the velocity and the area cross section at port n (n= 1 and 2) respectively. In order to characterize single particle at a time and be able to observe the movement of the particle within the microchannel under the microscope some judicious choices were made for the velocity flow rate calculation. A 1cc syringe was used in order to get low volume rates for the syringe pump and the velocity of media/particle was desired to be equal to 100  $\mu\text{m}/\text{sec}$ . With the approximate cross section of  $15 \times 10^{-9} \text{ m}^2$  of the microchannel and the equation (147), the flow rate of the syringe pump was calculated and adjusted to about 0.1  $\mu\text{l}/\text{min}$ . Moreover, before starting the experiments, the channel hermeticity was verified by injecting distilled water with different high flow rates in the microchannel. The microfluidic chip preserved its integrity and no liquid leak was observed within the channel.

Figure 5.18 shows the movement of the polystyrene beads within the channel with the particles focused at the center of the trapezoid electrodes of the channel. The applied voltages on trapezoid electrodes were 10 and 0 Volts on opposite trapezoid electrodes and the frequency was set to 500 KHz. In Figure 5.18 several snap pictures (1, 2, 3 and 4) are showing the movement of the 15  $\mu\text{m}$  diameter beads through the focusing electrodes. As seen in these pictures, when the particle gets close to the center of the channel with a smaller electrodes gap, the velocity of the particle is higher and the clarity of the picture

of the particle is reduced due to this higher speed effect. From 100 KHz to 5 MHz nDEP effect was observed on the polystyrene beads.

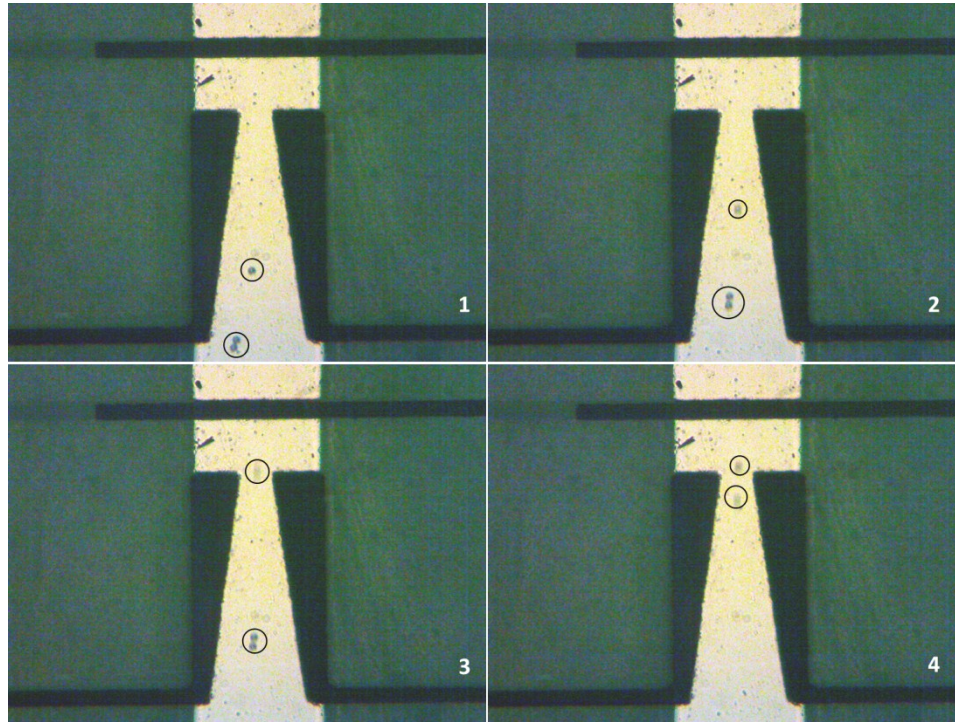


**Figure 5.18: Polystyrene beads movement within the center of the microchannel. The polystyrene beads diameter is  $15 \mu\text{m}$  and the flow rate is  $0.1 \mu\text{l}/\text{mn}$**

Figure 5.19 a and b show the movement of the bulk yeast cells stream within the channel for the two focusing electrodes. The design solution for the inlet was at the trapezoid focusing electrodes and the outlet was at the Y shape focusing electrodes. For this experiment, the media conductivity was  $330 \text{ mS}/\text{m}$ ; the signal frequency was  $500 \text{ KHz}$  with amplitude of  $10 \text{ Volts}$ . Under these conditions, nDEP effect was observed on the yeast cells. Clearly the cells were repulsed from the edges of the trapezoid and Y electrodes and are focused to the center of the channel. Figure 5.19 c and d show the effect of pDEP on the yeast cells under the same conditions except with a frequency of  $2 \text{ MHz}$ . In this case, the cells are attracted and gathered at the edges of the trapezoid and Y

electrodes. The movement of yeast cells with a lower conductivity of 25 mS/m showed pDEP for frequencies above 100 KHz and nDEP below 100 KHz.

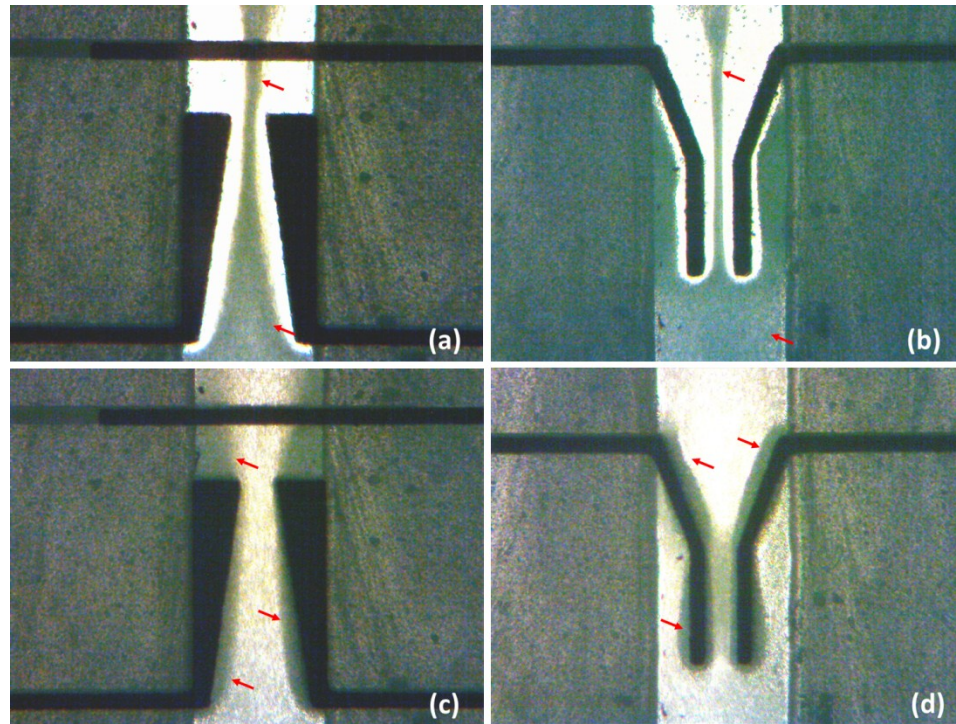


**Figure 5.19: Bulk stream of yeast cells movement under nDEP within the center of the microchannel between trapezoid and Y electrodes (a and b) and their movement under pDEP (c and d)**

Finally, Figure 5.20 shows nDEP effect on formation of bubbles on the focusing electrodes with the presence of high conductivity media of 330 mS/m and reduced frequency signal of about 1 KHz and below. Electrolysis of water is the cause of the bubbles of hydrogen and oxygen gases that are created at the edges of the electrodes and the media in suspension which is known to occur at the application of DC in high conductivity water (mixed with salt) [210-212]. This effect was eliminated by increasing the frequency of the applied signal on the focusing electrodes. After the bubbling effect, the microchannel was flushed by increasing the flow rate of the pump and the bubbles were removed from the observation and interrogation area.

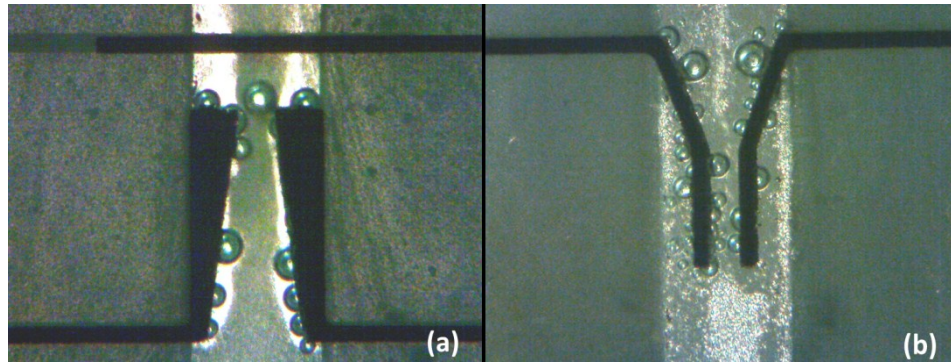


**Figure 5.20: Bulk yeast cells with bubbles formed due electrolysis with high conductivity of the media and low frequency of the applied voltage on trapezoidal electrodes (a) under nDEP and (b) Y electrodes under pDEP**

## 5.4 Discussions

The major advantage in designing transparent microfluidic device consists of capability to observe, in real time, the manipulation and movement of cells or single cell in the microchannel at the interrogation point. Without the need of this observation facility, silicon could have been used as substrate material with its easier to achieve shallow geometries manufacturing characteristics. The microfluidic chip was fabricated using specific materials for the substrate (glass and fused silica) and for the channel (photo-imageable film and silicone). Fused silica and silicone were the final choices for the substrate and the channel. The alignment of the two substrates for parallel facing electrodes was completed within few minutes under a microscope with the help of the alignment marks. For a larger number of prototypes a special jig could be made for alignment simplicity. A finite element analysis for a misalignment of 10  $\mu\text{m}$  offset electrodes did not show a major disturbance of the DEP force. The major challenge following the channel fabrication was the hermeticity of the channel without the use of high pressure and temperature equipment. The two fused silica substrates were

sandwiched between two thick blocks of aluminum plates. Blocks of correct thickness were necessary to ensure the proper pressure at the middle of the blocks and avoid any block curvature associated with channel leak. Four screws at the edges of the blocks tighten at the proper torque and order ensured the sealing of the channel. All these fabrication steps were repeated in several iterations with associated difficulties to overcome all the fabrication difficulties. The conductivity of the media was critical in the determination of the nature of the force (attractive or repulsive) since the sign of the Clausius-Mossotti factor is directly dependent on this value.

During the experiments carried out with high conductive media of 330 mS/m, special care was given to reduce the effect of bubble creation due to electrode heating at low frequencies. Nevertheless at frequencies below 1 KHz bubbles started to get formed at the edges of the electrodes where the electric field was high. The n-DEP effect (for focusing) was observed with AC signal source of 10 Volts at a frequency of 500 KHz.

Very low speed of the media (0.1 $\mu$ l/mn) was set in order to observe, under the microscope, the nDEP movement of the polystyrene particles. At high flow rates, the nDEP force being smaller than the other present forces in the channel, particles were passing through the channel without being focused at the center.

## **5.5 Conclusion**

A simple, low cost and fast microfluidic device with 300  $\mu$ m width by 50  $\mu$ m height microchannel cross section area was fabricated using two fused silica substrates and screen printing silicone rubber. The challenge of the design of this micro device consists in the screen printing technique with the hermeticity obtained by using two

aluminum blocks with four screws at the edges. With gold electrodes within the two fused silica substrates, a hermetic microfluidic chip was fabricated with parallel facing electrodes for single cell/particle manipulation and characterization. The microchannel dimension and the biocompatible materials used to fabricate this micro device would accommodate the single living cancer cell measurement. Detecting and measuring different cancer cells, such as uveal melanoma, prostate, HeLa, breast and many other cancer cells within this micro device would permit the characterization of each cancer cell at low and high frequencies with unique cancer type signature.

## **5.6 Chapter summary**

This chapter presents a measurement apparatus that investigates the effect of non-thermal RF radiation on uveal melanoma cells. Simultaneously it provides the information about the power and frequency to be applied during single cell measurement. The device uses 96 wells with some RF electrodes adaptation for RF signal injection. The evaluation is made through 92.1 cell line proliferation test. The proliferation results show a reduction from 2 to 9 % over the frequency range from 1 to 3 GHz.

Another microfluidic device is designed and fabricated using two fused silica substrates with pattern gold electrodes separated by a silicone patterned layer acting as the microchannel. The serigraphy technique to apply the silicone layer is simple and less costly than other methods. The device is sealed by squeezing and retaining the two fused silica substrates between two aluminum blocks while aligning the parallel facing electrodes overlapping under the microscope.

The good performance of this device is verified by applying AC low frequency signal on the centering electrodes within the channel. Polystyrene microspheres and *Saccharomyces cerevisiae* particles are used for these tests and nDEP/pDEP are observed under the microscope by changing the frequency of the AC signal. No leak is observed on the microdevice structure during these measurements.

## Chapter 6: Off Line Characterization of Biological Cells

### 6.1 Introduction

Knowledge of the microwave dielectric properties of biological material (tissues and cells) is important information in the applied research and development of new diagnosis and therapeutic medical devices [213, 214]. In general, a material can be characterized by its unique signature of permittivity and conductivity. These dielectric properties are mainly determined by that material's molecular structure. Once these are known, then a material's physical and chemical properties can be estimated. Hence, the dielectric properties of a material determine how it will interact with an applied electromagnetic field.

Extensive experimental research was performed to determine dielectric properties of different human tissues, body fluids and cells within a large frequency spectrum [135, 215-222]. Dielectric parameters were mostly measured at low frequencies from 1 KHz to 100 MHz [218], and at high (up to microwave) frequencies in the UHF to Ku bands with frequencies ranging from 100 MHz to 18 GHz [139, 149, 223]. Some research also focused on millimeter wave range measurements [224, 225].

For the last two decades, several low frequency measurement research studies were carried out using impedance-based techniques to measure a material's or particles' complex permittivity (CP) values in a specific media [8, 38, 88, 139], determining those dielectric properties mainly through dielectric spectroscopy measurements. Various impedance models with different respective hypotheses were used to determine the CP of particles in a media solution. The results obtained, either in frequency or time domains,

were presented in the form of CP frequency response [113, 226-229]. The same parameters were used to estimate the Clausius-Mosotti factor, the cross frequency and the relaxation time constants [108, 130, 230]. Some analytical models were also derived to validate the frequency and time domain results [231-233]. Moreover, numerous microwave CP measurements were also considered, based on different microwave measurement techniques in frequency and time domain, such as coaxial probing, transmission line, free space and resonant cavity measurements [170, 234].

At microwave frequencies, the physical properties of materials containing water could be determined by measuring CP given that the amount of absorbed energy at high frequency is a function of this parameter. The high frequency energy interaction with any material is predominantly governed by that material's polar nature and thus its water content, therefore no appreciable ionic conductivity effect or low frequency relaxation phenomena can be observed [235].

For biological specimen characterization, very small specimen volume is needed and cavity perturbation is an appropriate and accurate measurement technique. In the literature, rectangular cavity perturbation has been extensively used for measurements of the CP of biological tissues and cells and has showed very different results for healthy individuals versus cancerous patients [147].

The CP of materials exhibits dispersion characteristics induced by polarization, indicating the dependence of the CP of a dielectric material on the frequency of an applied external electric field. In general, each material has a polarization in a wide frequency spectrum identified by ionic, interfacial, dipolar, atomic and electronic polarizations [132, 236].

The motivation of this chapter is to investigate and estimate in vitro the dielectric properties of biological particles such as various cancer cells at microwave frequencies. In this study, biological cell microwave S-band CP measurements are performed. Knowledge of a cancer cell's dielectric properties should enable their detection and characterization at microwave frequency ranges. It also opens a future research topic to investigate how a bio chemical alteration (cells altered with some agent) affects the dielectric properties of a cancer cell line.

This chapter presents the dielectric properties and characteristics of different cancer cells in the frequency range between 2 GHz and 4.5 GHz using a WR284 resonant cavity. The dielectric constant and the dielectric loss of cells are measured using the resonant cavity perturbation technique. All design and fabrication steps of the microwave resonant cavities are detailed. Also presented, are specimen preparation and automatic measurement setups for determination of normalized complex permittivity given a wide frequency range. The outcome of the dielectric properties obtained for cancer cells from different cell lines will enable the detection, identification and characterization of those cells at microwave frequencies in the S band. HeLa, Prostate, Breast and uveal melanoma cancer cells' complex permittivity measurements gave bulk relative dielectric constant values between 42 and 68, and relative dielectric loss values between 12 and 22. Similar test is performed also on white blood cells (WBC). With the advantage of automatic test set-ups, cancer cells' time-series complex permittivity measurements gave important information about the apoptosis behavior of these cells. The time-dependent changes in the cells' dielectric property results in a decrease of their complex permittivity.

## **6.2 Theoretical background**

### **6.2.1 Polarization, permittivity, conductivity and dispersion of materials**

When a material is placed in an electric field, dipole moments are induced at microscopic levels and the material is considered to be polarized. The polarizability of the material is its ability to neutralize a part of that field and acts as a form of energy storage. Macroscopically, the response of a material to an electric field is fully described by its CP. The real part of the relative CP, also defined as dielectric constant, is proportional to the ratio of the charge to the applied electric field and is a measure of the storage effect, or polarization, of the localized charges in the material under this field.

The imaginary part of the relative CP, representing the dielectric loss or conductivity, is the ratio of the electric current density to the applied electric field and is a measure of the ability to delocalize charge carriers moving through the material under that field [237]. When the dielectric material is subjected to an electric field, the bound positive and negative charges in the material move locally relative to each other and create a field in the direction which is opposite to the applied field. The movements of charges need to overcome inertial and viscous forces. In this mechanism, the energy is dissipated via heat generation or dielectric loss.

The dielectric constant describes the interaction of the material with the electric field and the conductivity determines how easily the electrons travel through the material under the electric field. When an external electric field is applied to a material, its polarization response takes some time to relax after the field is removed, and a phase lag

between the polarization and the electric field is created. The relaxation time due to this lag depends on the frequency of the applied electric field and the stored and dissipated energies depend on the time variation of the electric field. Hence, the complex permittivity of a material, consisting of the dielectric constant and the conductivity, is frequency dependent and there is basically a dispersion of the complex permittivity. Different polarization mechanisms can be defined according to the frequency of the electric field applied to the material. They are ionic, interfacial, orientation, atomic and electronic polarizations. The dispersion associated to these polarizations happens within the material or at the interface of two materials. The first dispersion is called Debye relaxation and the second is the Maxwell-Wagner relaxation. The Debye relaxation is due to the inability of the dipole or the permanent dipole (like water molecules) to reorient in time with respect to the applied electric field. The Maxwell-Wagner relaxation is due to the interface polarization between the two unlike materials [214].

For each polarization, a relaxation frequency is identified and every next polarization occurs at frequencies below the subsequent relaxation [132]. A simple explanation of the polarization type of a material associated with the frequency dependent dispersions is defined as follows [135, 236, 238]:

- a.  $\alpha$  dispersion due to ion conductivity of membrane channels or the flow of ions across cell surface. This is identified as ionic polarization
- b.  $\beta$  dispersion associated with the polarization of cellular membranes and polarization of protein and other organic macromolecules. It is the consequence of charge build-up at cell membranes and the media due to the Maxwell–Wagner effect. The effect is the conduction of ions within and outside the cell and is

related to the properties of the cell membrane, the cytoplasm, and the extracellular media. Therefore  $\beta$  dispersion provides information about cell membrane and cytoplasm. This is called the interfacial polarization

- c.  $\delta$  dispersion associated with the rotation of macromolecular side-chains and with the polarization of water molecules. Since the rotation creates an orientation, this is said to be orientation polarization
- d.  $\gamma$  dispersion associated with the distortion of the electron distribution about the nuclei and the stretching of chemical bonds between unlike atoms. This mechanism is the atomic and electronic polarizations.

All biological molecules are polar material and the applied electric field on the material induces a dielectric polarization. When a particle suspended in a solution is subjected to an electric field, the particle and the solution are polarized creating net unpaired surface charges at the interface of the particle and the solution. These surface charges create another electric field disturbing the original one. The interfacial surface charges depend on the field strength, the frequency dependent complex permittivity of the particle and the solution [130]. Moreover, the polar substance dispersion can be attributed to the relaxation of water molecules in the bulk phase [238] and polar liquids, such as water, are considered as high loss liquids [170]. Since the biological material is polar in nature, its molecules can follow the low frequency applied electric field resulting in maximum values of  $\epsilon_r'$ . At these low frequencies, the positive and negative ions move in accordance to the electric field and the electric current corresponds to an energy loss dominated by the conduction loss. Therefore at low frequencies the ionic conduction is the prevalent mechanism. At media frequencies, when biological cells are within a media,

the  $\beta$  dispersion is mainly due to the Maxwell-Wagner effects of interface between the cell membrane and the media and the charging/relaxation. At microwave frequencies, the biological molecules can no longer follow the changing electric field resulting in less energy storage and higher rotational losses dominated by dielectric loss on a disappearing DC conductivity [239]. Then the frequency response of the dielectric constant decays with the increase in frequency. Therefore in general, the effect of the polarization results in an accumulation of charges at interfaces for low frequencies and rotation/reorientation of molecules at microscopic level for high frequencies [240].

In most cases, we can define the bio-molecular frequency dispersion in the following ranges [241]:

- a.  $\alpha$  dispersion from about 10 Hz to about 1KHz
- b.  $\beta$  dispersion from about 1KHz to about 100 MHz
- c.  $\delta$  dispersion from about 100 MHz to about 10 GHz
- d.  $\gamma$  dispersion from about 10 GHz to about 100 GHz.

Molecules with water content are dipolar and at low frequencies they tend to rotate and line up with the applied field. Energy is stored due to this directional alignment and this is reflected by a certain dielectric constant value dependent of the material. At high frequencies, the rotation of the molecules cannot follow the applied field frequency and a lag exists between the rotation of water molecules and the reversion of the applied field. This will reflect in a decrease of the dielectric constant and an increase in the dielectric loss [242]. Moreover, the polar characteristic of the molecules leads to temperature and pressure dependent complex permittivity. In fact, when the temperature of the material increases, the thermal motion reduces the alignment of the permanent

dipole subjected to the electric field and the orientation polarization decreases giving rise to a decrease in the dielectric constant and an increase of the conductivity. In summary the complex permittivity is mainly frequency, temperature and pressure dependent. At atmospheric pressure, polar molecule at Radio Frequency (RF) and microwave frequencies has the following theoretical dispersion characteristic:

$$\frac{d[\varepsilon_r'(f, T^o)]}{df} < 0 \quad (148)$$

The variation of the complex permittivity with frequency gives the information about natural rotational motion of dipolar molecules in a material when the electric field is absent. Similarly, the variation of the electrical conductivity with frequency gives the information about material natural translation motion of ions in a material when the electric field is absent [243]. It is well observed that cancer cells have different permittivity than healthy cells since they have different electrical and chemical properties than normal cells. The dielectric constant and conductivity of cancer tissue are higher than normal tissues [244].

### **6.2.2 Microwave frequency biological material permittivity and conductivity measurement theory**

In general, microwave energy penetrates within the volume of a material and not only on the surface [239], and the incident energy can be transmitted, reflected and diffracted [245]. Therefore microwave dielectric measurement is the response of all these energy transformation mechanisms.

As stated earlier, microwave complex permittivity measurement techniques for biological material can be carried out in frequency domain or time domain. The following work will concentrate on the frequency domain. The frequency domain permittivity measurement of a material can be divided into three major methods or techniques consisting basically of:

- a. Coaxial probe technique
- b. Transmission line technique
- c. Resonant cavity perturbation technique [170].

The coaxial probing is very convenient and can measure complex permittivity of materials in a very wide frequency band [166, 238, 246-248]. Nevertheless, this method exhibits reduced accuracy and is limited by the accessibility to small biological specimen. Open-ended coaxial line sensors are used for in-vivo measurements of the dielectric properties of biological specimens. This measurement technique is based on the measurement of the fringing-field capacitance of the specimen placed at the open end. The measurement of the reflection coefficient permits the calculation of the complex permittivity [249].

With the transmission line system, very large frequency band can be achieved but the method usually requires large specimens (in general solid samples) and it is limited by the resolution and the accuracy specifically at microwave frequencies [250]. From the measurements of transmission and reflection coefficients of the specimen in a waveguide, the complex permittivity can be computed. Nevertheless, the computation formulas are very complicated and several assumptions and approximations are used [225, 251-259].

Finally the resonant cavity perturbation method [170] is the most appropriate method for small volume specimen with high accuracy, linear perturbation [260] and nondestructive measurement. For the rectangular or circular cavity perturbation method, the specimen should be much smaller than the physical dimension of the cavity. This condition is required since the effect of introducing the specimen into a cavity on the resonant frequency and the quality factor of the cavity is treated by the first order perturbation theory. Therefore, the ratio of the stored electromagnetic energy in the specimen to the energy in the entire volume of the resonator will be small giving high values of quality factor [261]. The deviation of this condition tends to obtain non accurate results for complex permittivity. The complex permittivity is deduced by measuring the resonant center frequency and the quality factor with and without the specimen inserted in the cavity. The volumes of the specimen and the cavity are needed also for the computation. For the measurement of biological specimen, a small hole is opened (with a diameter smaller than the cutoff and the guide wavelengths) in the waveguide wall without interrupting the currents flow currents on the walls. With the small size, this opening will not couple the energy to the outside environment of the waveguide and hence the internal fields will remain unchanged. Therefore, the electric and magnetic fields distribution for each cavity resonant mode will approximately be the same with and without hole. A small piece of glass (low loss) capillary tube with and without the specimen is introduced at the center of the resonant cavity at the position of the maximum electric field [151].

For odd modes, the geometrical center of the cavity ( $d/2$ ) is always one of the maximum electric field positions [262]. In order to measure accurately the resonant

frequencies of the even modes, a slot is created along the height  $b$  of the waveguide. Before each even mode measurement the tube will be set at a certain position in the slot where the electric field is at its maximum. The specimen inserted at the position of the maximum electric field will perturb strongly the field [213].

The principle of rectangular cavity perturbation method is obtained from the resonance of the cavity. Different modes can exist in the cavity depending on the dimensions of the rectangular cavity. Basic formulas for the calculation of the complex permittivity through the rectangular cavity perturbation method are given by:

$$\varepsilon'_r = \frac{V_o(f_o - f_s)}{2V_s f_s} \quad (149)$$

$$\varepsilon''_r = \frac{V_o}{4V_s} \left( \frac{1}{Q_s} - \frac{1}{Q_o} \right) \quad (150)$$

where  $V_o$  and  $V_s$  represent the volumes of the cavity and the specimen respectively,  $f_o, f_s$ ,  $Q_o$  and  $Q_s$  are the resonant frequencies and quality factors of the empty cavity and the cavity filled with the specimen. As it can be seen by the formulas, with  $f_o$  greater than  $f_s$  and  $Q_o$  greater than  $Q_s$  then complex permittivity value is positive. Therefore the real and imaginary part of the permittivity can be calculated from the shifts of the resonant frequency and the quality factor. The accuracy of  $\varepsilon'_r$  depends on the accuracy of the resonant frequency measurements and the accuracy of  $\varepsilon''_r$  depends on the accuracy of the quality factor measurements.

With known dimensions of  $a$  and  $b$ , and using the formula of the resonant frequency, the resonant frequencies of different modes in any cavity having a predefined length  $d$  can be calculated. When the specimen in a capillary tube is introduced in the geometrical center

of the cavity, all the odd resonant mode peaks permit to calculate accurate values of complex permittivity. For each even mode the tube needs to be placed at a position of maximum electric field by moving it through the slot or opening along the height of the cavity.

### 6.2.3 Complex permittivity of cells at microwave frequencies

When particles or biological cells are submerged in a media, the knowledge of the mixture effective complex permittivity enables the determination of cells complex permittivity when dielectric properties of the media are known. At microwave frequencies, the conductive loss is negligible compared to the dielectric loss of the material. Therefore the complex permittivity of a material at microwave frequencies depends on the dielectric constant and the dielectric loss of the material, both dependent on the applied electric field frequency and the temperature. Several authors developed different approximate formulations relating the mixture complex permittivity to the particle and media complex permittivity. When spherical particles much smaller than the wavelength of a uniform electric field are scattered in an homogenous media, the Maxwell and Garnett mixing formula can be written as [263]:

$$\varepsilon_{eff}^* = \varepsilon_m^* + 3f_f \varepsilon_m^* \frac{(\varepsilon_p^* - \varepsilon_m^*)}{(\varepsilon_p^* + 2\varepsilon_m^*) - f(\varepsilon_p^* - \varepsilon_m^*)} \quad (151)$$

where  $\varepsilon_{eff}^*$  is the complex permittivity of the mixture and  $f_f$  represents the volume fraction of the spheres. This equation is a good approximation for low volume fraction (less than 0.1). For densely packed particles in the media, Bruggeman introduced another

formula improved by Hanai [264] that can be used for large volume fraction and it is given by:

$$\frac{(\varepsilon_p^* - \varepsilon_{eff}^*)}{(\varepsilon_p^* - \varepsilon_m^*)} = (1 - f_f) \left( \frac{\varepsilon_{eff}^*}{\varepsilon_m^*} \right)^{1/3} \quad (152)$$

Therefore, measurements of mixture and media complex permittivity (with known volume fraction) can provide the exact estimation of the particle complex permittivity. Figure 6.1 and Figure 6.2 show the theoretical result of a particle complex permittivity with different volume fractions for fixed given effective mixture complex permittivity  $\varepsilon_{eff}^* = (50 - j15)$  and media complex permittivity  $\varepsilon_m^* = (70 - j20)$ . This effective mixture relative complex permittivity is chosen since experimentally it is shown that at high volume fraction this value is close to most living cancer cell's dielectric property. Similarly, the mixture dielectric properties are close to standard measured media at high frequencies. The theoretical results show that, for volume fraction values higher than 0.7, the particle dielectric constant and dielectric loss values are almost linear having small slopes.

Analyzing theoretically the packing of spheres, the density of an arrangement of non-overlapping equal spheres could not exceed 0.7797. Mathematicians and physicist demonstrated a value of 0.7404 for face centered cubic packaging and the best properly established value was given as 0.828 [265]. Randomly packed spheres gave a packing density value of 0.64.

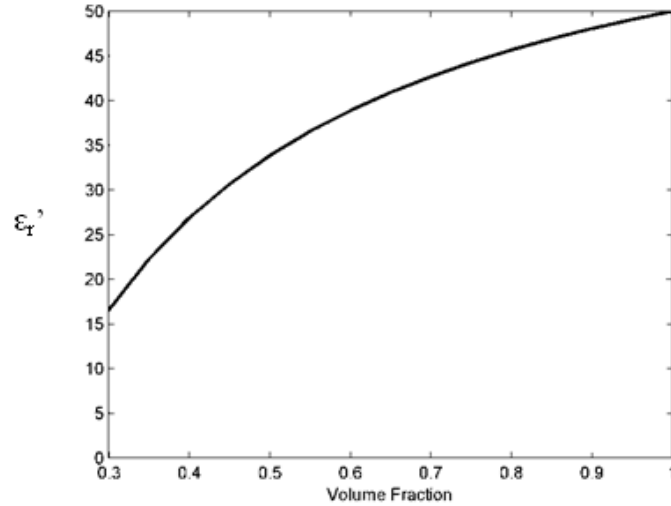


**Figure 6.1:** The Y axis presents the particle dielectric constant when the mixture effective complex permittivity is  $\epsilon_{eff}^* = 50 - j15$  and media complex permittivity is  $\epsilon_m^* = 70 - j20$  for different values of volume fraction

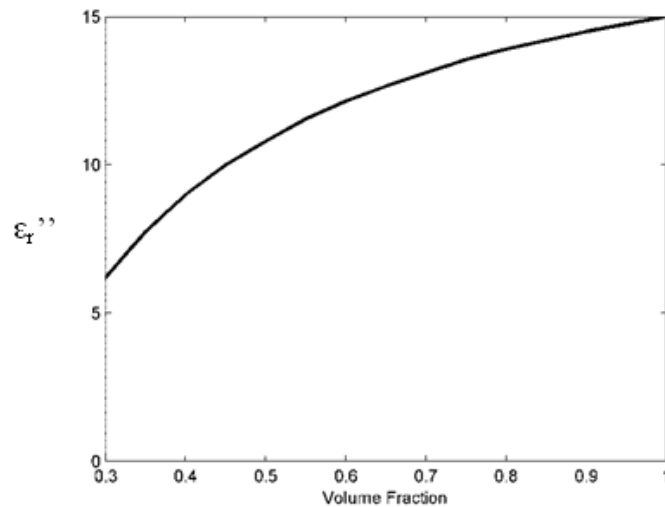


**Figure 6.2:** The Y axis presents the particle dielectric loss when the mixture effective complex permittivity is  $\epsilon_{eff}^* = 50 - j15$  and media complex permittivity is  $\epsilon_m^* = 70 - j20$  for different values of volume

In the detection and characterization of cells, cells can be subjected to low frequency and high frequency electric fields and the presence of a non-uniform distribution of this field can attract or repel the cells (Dielectrophoretic force). The repelling or attracting force depends on the real value of Clausius-Mosotti factor where

the Clausius-Mosotti factor is dependent of the complex permittivity of the particle and the media and is given by:

The real part of Clausius-Mosotti factor is the parameter used for the calculation of Dielectrophoretic force on the particle within the media. From equation of CM, it is clear that the real part of Clausius-Mosotti factor limits is -0.5 and +1. When this quantity is negative (particle less polarized than the media) the particle is repulsed and when it is positive (particle more polarized than the media) the particle is attracted. The knowledge of the real part of Clausius-Mosotti factor at low and microwave frequencies is very important during the manipulation and characterization of biological cells at those frequencies. Once the dielectric properties at high frequencies are measured, the cells can be properly modeled and characterized. For frequencies below 100 MHz, the dielectric properties of material with the surrounded environment can be presented by lumped circuit representation with capacitors and resistors. For frequencies in the microwave ranges, the lumped circuit representation is replaced by distributed circuit representation describing the propagation of the electromagnetic waves in the material and its surrounded environment. Complex equivalent electric circuit representation with lumped element fitting technique can be also extracted from measurements [243, 266].

## **6.3 Cavity design and fabrication**

### **6.3.1 Design of cavities at S-Band**

A cavity resonator is fabricated from sections of copper waveguide. This material ensures a good thermal stability [267]. The rectangular waveguide is shorted with copper walls by solder sealing on both ends (these walls will create standing waves in the

cavity). The tangential electric field and the normal magnetic field are zero at these wall interfaces. Both walls have small irises (holes) in order to excite the mode (at one end a swept signal is injected and at the other the resonant signal is measured). The iris diameter ranges between  $\lambda/20$  and  $\lambda/10$  (a fraction of the wavelength) in the frequency range of cavity operation. The resonator cavity is excited through a magnetic coupling mechanism through the irises and different possible modes are excited at different discrete frequencies depending on the length of the resonator.

In transmission measurements, noted as  $S_{21}$ , low magnetic or inductive coupling factor is used to obtain good signal-to-noise ratio [170]. Since the magnetic coupling coefficient is very dependent on the iris diameter size and the direction of the coupling loop, an optimized iris size and loop direction are needed during the coupling mechanism fabrication and adjustment processes. Since the cavity is made of a standard waveguide, it has a wall thickness of 2 mm.

The S-band cavity resonator is constructed from a WR284 waveguide. The width  $a$  and the height  $b$  of this guide are 7.22cm and 3.4 cm respectively. A length  $d$  of 35.6 cm is chosen to obtain several modes and several discrete resonant frequencies. Table 1 gives a summary of the design parameters of S band resonator cavity. Table 2 shows the calculated different modes resonant peak frequencies present in the S-Band resonant cavity structure having a length of 35.6 cm. The odd frequencies are obtained when the specimen is inserted at the geometrical central or the middle of the cavity where the electric field is at its maximum. For even modes the specimen needs to be set at a position where the electric field is at its maximum. This is ensured by

physically measurement and manual adjustment of the plunger in the manufactured slot for this purpose.

Table 1: The geometrical dimensions of the S band cavity

SUMMARY OF THE DESIGN PARAMETERS FOR S- BAND CAVITY RESONATOR

Dimensions of the cavity	S-Band Dimensions (cm)
-Width `a`	7.22
-Height `b`	3.40
-Length `d`	35.60
-Diameter of coupling hole	0.88
-Length of slot on broad wall	10.00
-Width of slot	0.3

Table 2: The TE<sub>10l</sub> mode frequencies in the S band cavity

CALCULATED RESONANT FREQUENCIES FOR DIFFERENT MODES IN THE S- BAND CAVITY

Resonant Cavity Mode	S-Band Frequency (GHz)
- $\ell = 1$ (At cavity center)	2.12
- $\ell = 2$ (SAFMEF)*	2.24
- $\ell = 3$ (At cavity center)	2.43
- $\ell = 4$ (SAFMEF)*	2.70
- $\ell = 5$ (At cavity center)	2.96
- $\ell = 6$ (SAFMEF)*	3.28
- $\ell = 7$ (At cavity center)	3.61
- $\ell = 8$ (SAFMEF)*	3.96
- $\ell = 9$ (At cavity center)	4.33

(SAFMEF)\* = Slot Adjustment For Maximum Electric Field

Figure 6.3 shows the physical S-band resonant cavity with the magnetic coupling mechanism at the input and the output of the cavity. The two identical coupling mechanisms are inserted in the hole within the input and output of the cavity and held by 2 screws after manual adjustment for minimum magnetic coupling. With the fabrication

process limitation, the inner walls of the cavity were not silver plated to reduce the waveguide wall losses.

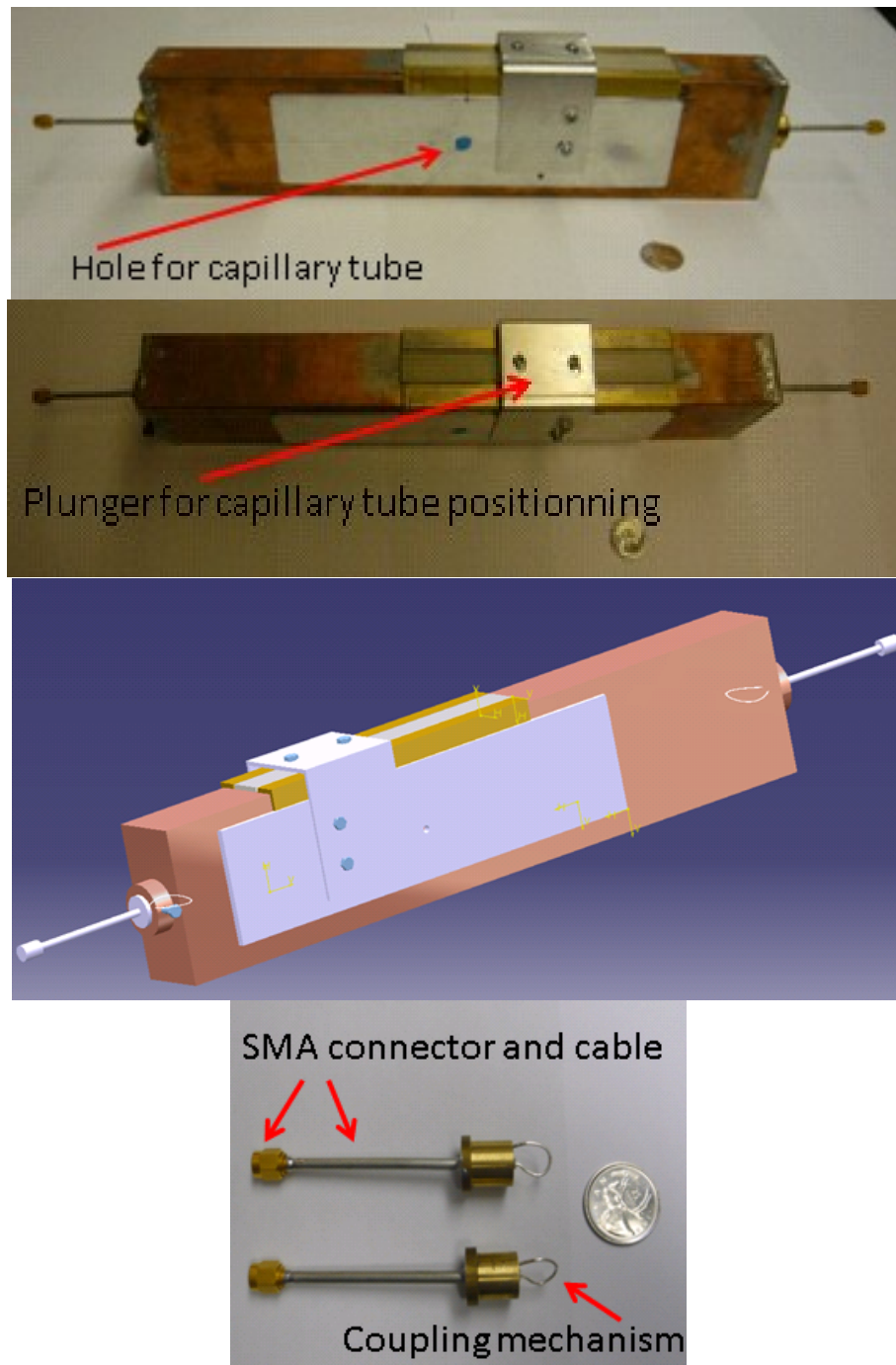


**Figure 6.3: S-band physical cavity with two real views and a Catia™ drawing. The last picture shows the magnetic coupling mechanism at the input and output ports of the cavity connected to an SMA high frequency connector through 0.141 inch cable**

When the empty cavity is excited by sweeping the frequency of the network analyzer, several discrete resonant peaks (modes) are observed on the screen of the microwave frequency network analyzer. The network analyzer used is Agilent 8722ES.

Figure 6.4 shows the measured 9 resonant frequency peaks of the cavity on the Agilent 8722ES network analyzer.

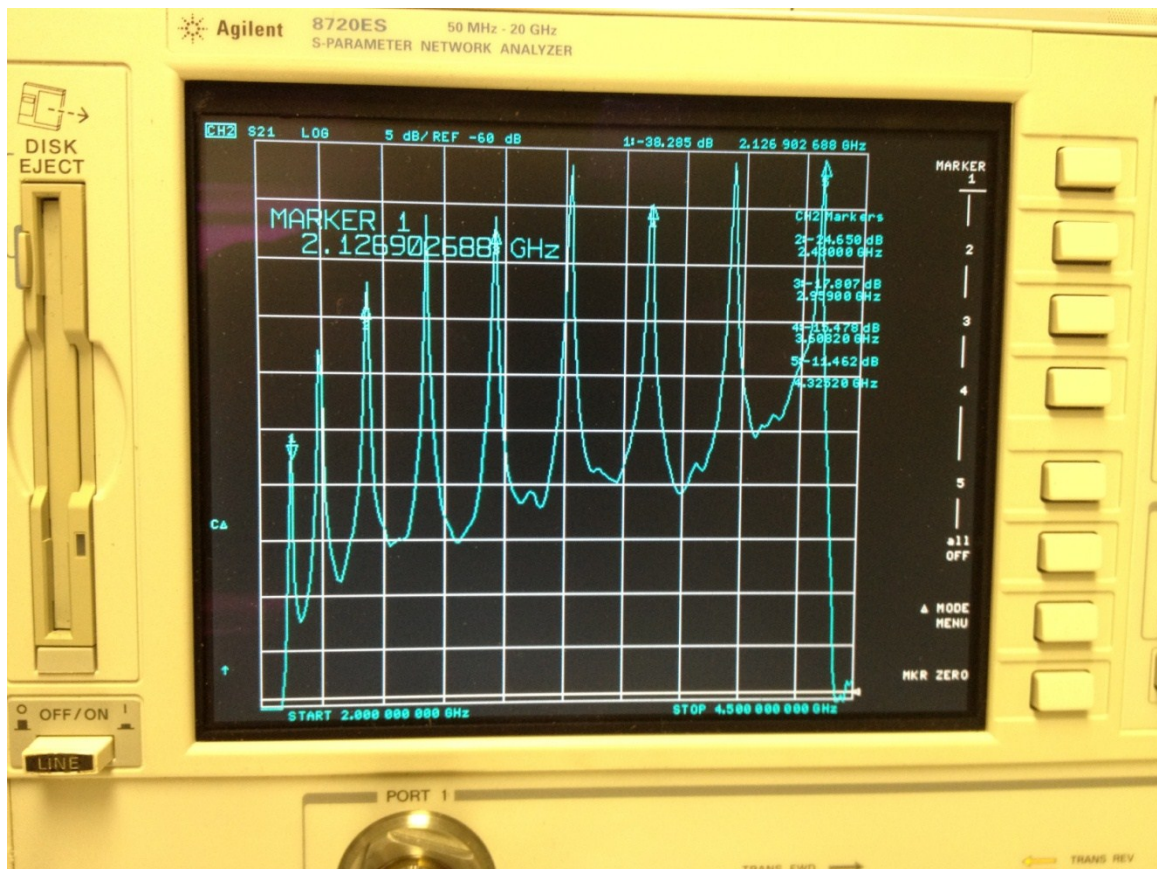


**Figure 6.4: S-band cavity resonant frequency peaks observed on the Agilent 8722ES network analyzer. 9 Peaks are observed for the S-band cavity with 35.6 cm of length**

## 6.4 Set up for permittivity and conductivity measurement

The microwave frequency network analyzer Agilent 8722ES is set on for 1 hour before measurement for heat up in order to ensure that the frequency measurement error

is minimized, and ports 1 and 2 are connected to the ports of the cavity. The network analyzer is set on transmission measurement (S21). The number of points for sweep frequency is set to 1600 with an averaging of 16 and the output power of the network analyzer is less than 0 dBm to avoid the heating effect of the cells. In order to get automatic and continuous complex permittivity measurements, a program is written in Labview™ to control the network analyzer and to obtain a real time continuous measurement of complex permittivity on the computer. Temperature was measured at different points of the cavity and the variation was within  $\pm 0.2$  °C of the nominal temperature value. The set-up of this temperature measurement is shown at Figure 6.5. An image of the complete measurement set-up of the complex permittivity is given at Figure 6.6.

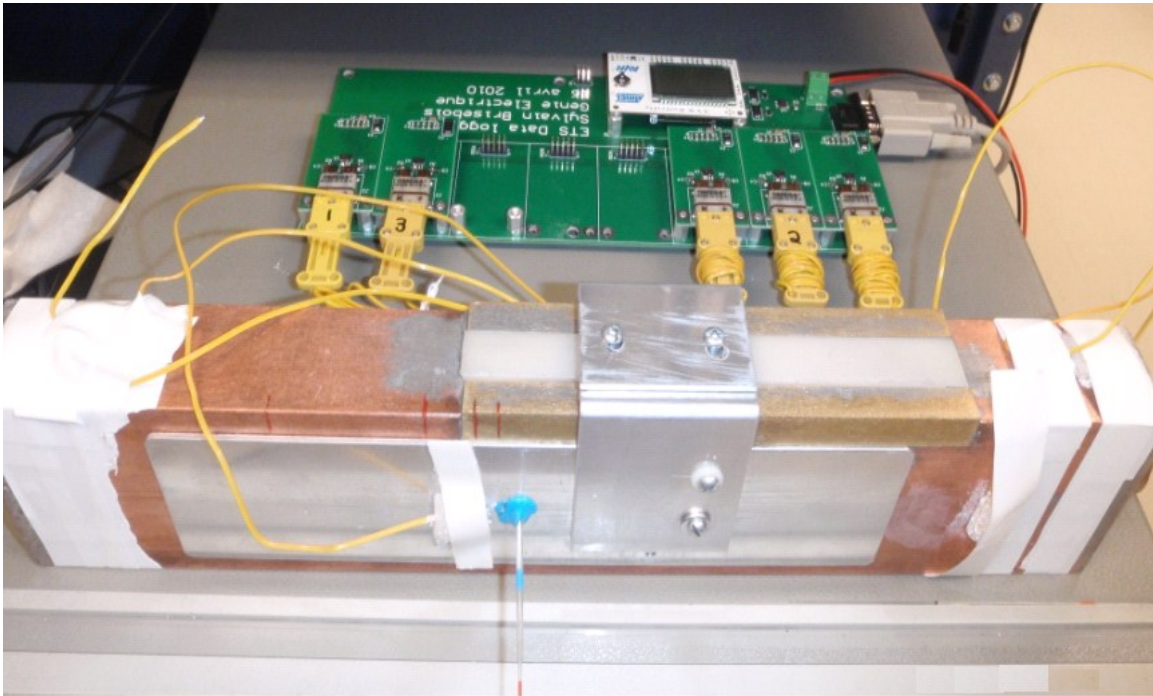
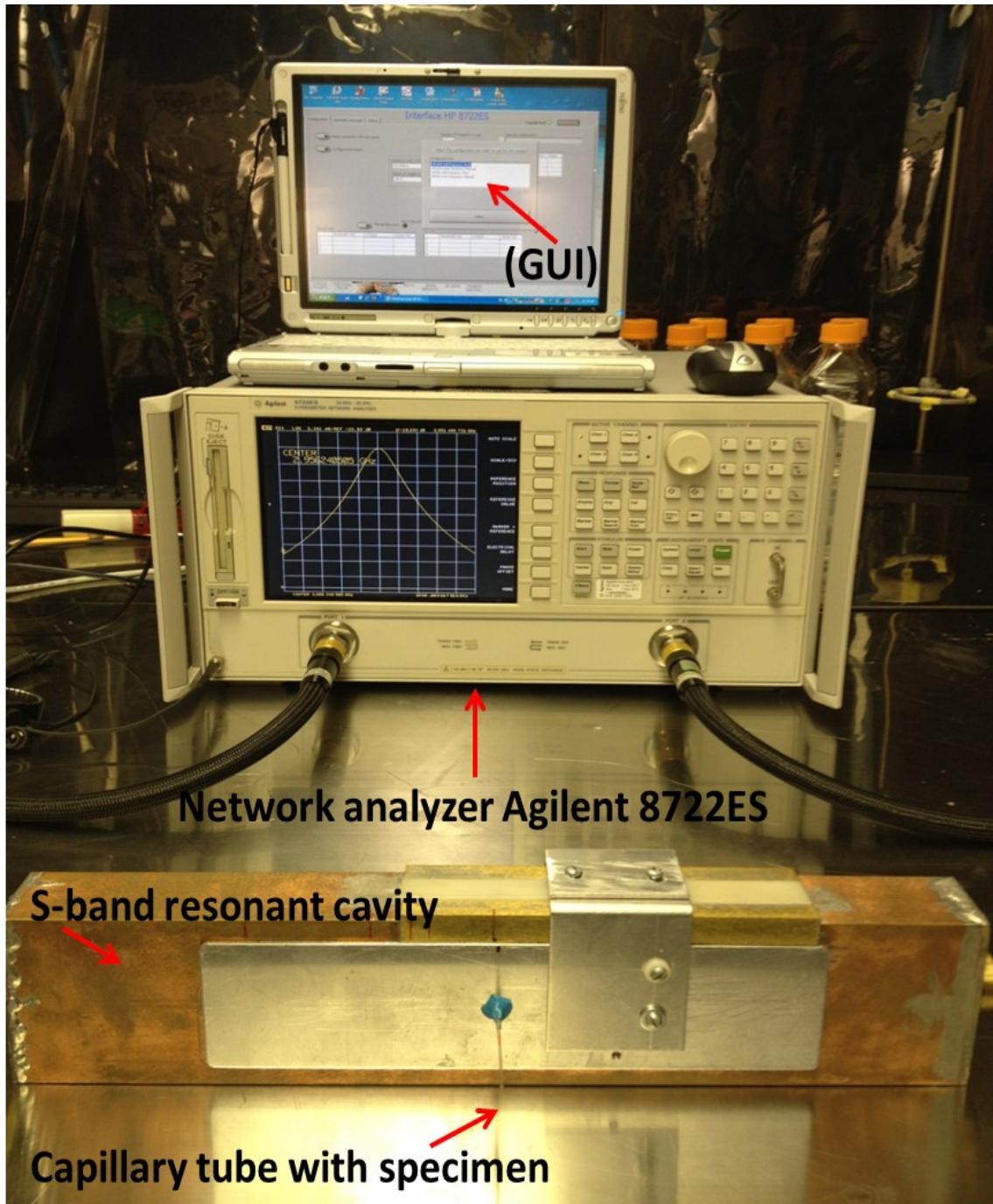


Figure 6.5: Temperature measurement setup on the S-band cavity



**Figure 6.6: Complete measurement setup showing the S-band cavity, the capillary tube in the center of the cavity, the 8722ES network analyzer for insertion loss measurement and the computer for automatic control of the network analyzer giving automatic output results of the complex permittivity of the biological material**

## **6.5 Software for automatic measurements**

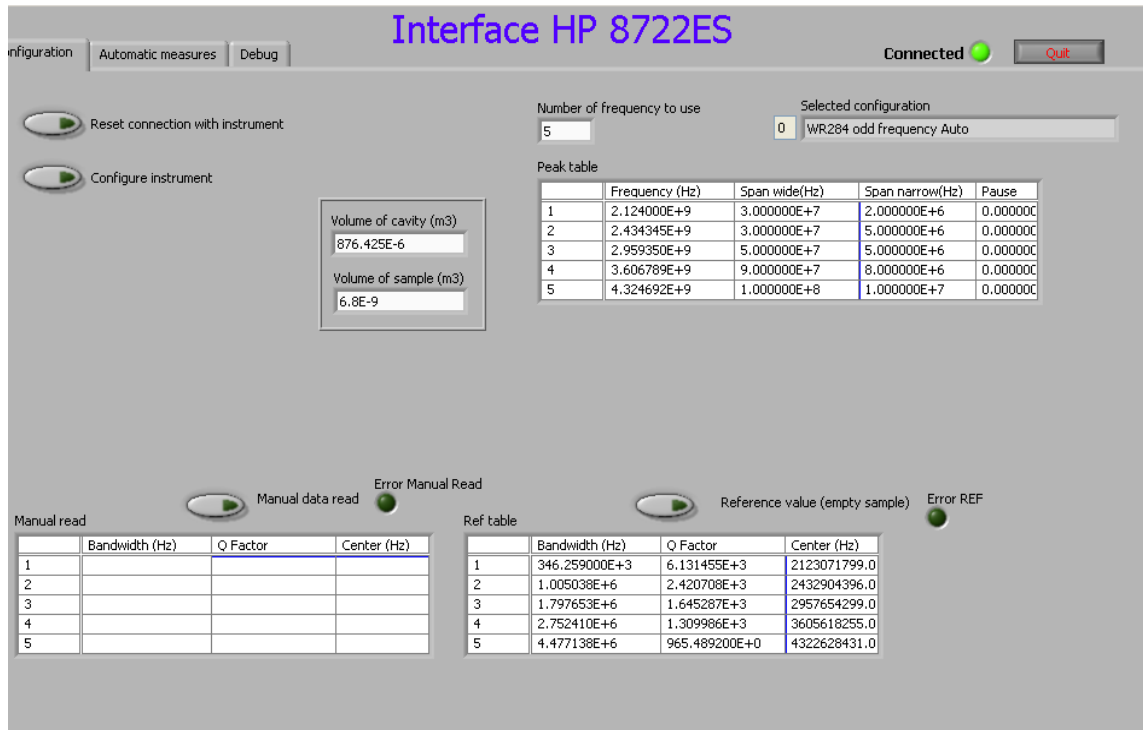
The network analyzer Agilent 8722ES is connected to the computer via a GPIB/USB adapter to ensure the communication between the network analyzer and the computer. The software program written in Labview™ has a practical Graphic User Interface (GUI) and an example of set up for calibration and measurement via GUI is shown at Figure 6.7. The automatic measurement is very powerful and time efficient for the acquisition of rapid measurement of complex permittivity of the biological material within the micropipette and for continuous monitoring of the complex permittivity with time. The complex permittivity change with time generates important information about the material property variation with time and enables the estimation of cell properties evolution with time. Within a minute about 5 different frequency measurements for complex permittivity can be performed with the automatic system.

## **6.6 Permittivity and conductivity measurement procedure**

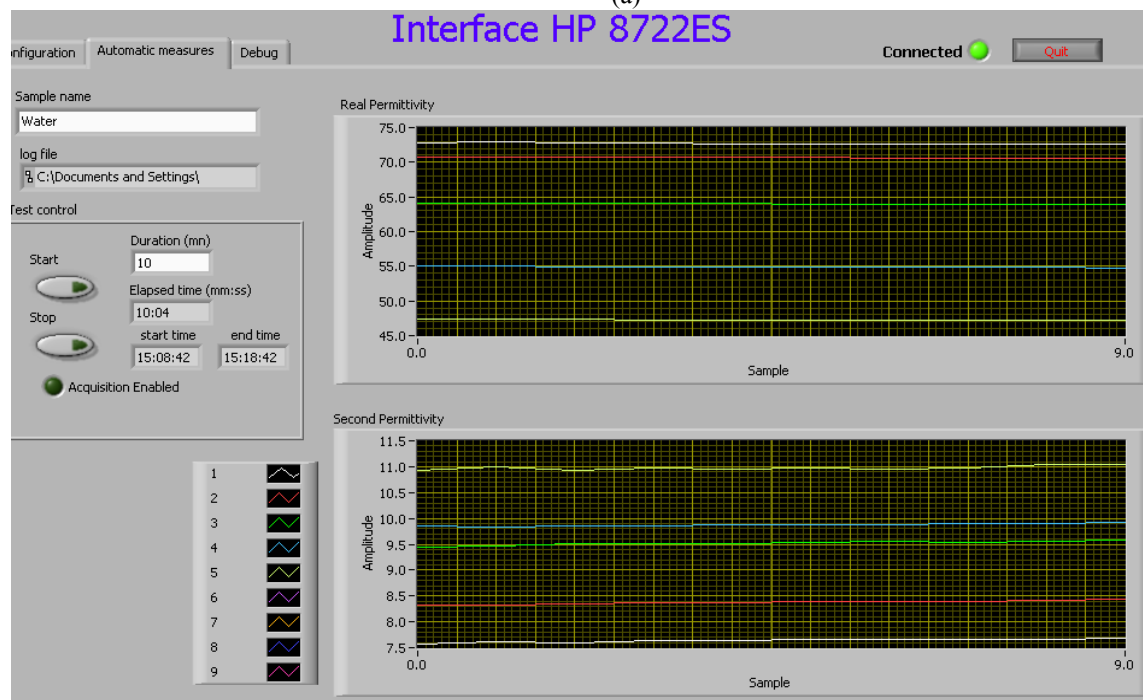
In order to get automatic and continuous complex permittivity measurements, the Labview program is run on the computer. The procedure for the complex permittivity measurement is as follows:

- a. An empty capillary tube is inserted at the geometrical center of the cavity and unloaded measurements of resonant frequency and quality factor are obtained for all odd modes (maximum electric field at the center)
- b. Liquid or biological specimen is filled in the capillary tube that is inserted at the same center for measurements

- c. Measurement time, in minutes, is set and measurements of the resonant frequency and the quality factor for the loaded capillary for all odd modes are performed. The internal diameter of the capillary tube being very small (0.5 mm), no evaporation of specimen is observed during measurement. The external diameter of the tube is 2 mm.
- d. From the measured values and known physical dimensions of the cavity and the specimen volume, the program performs calculation for every resonant frequency involved the complex permittivity and displays the results versus time
- e. With the increase of measurement time, a real time measurement of the relative permittivity and conductivity could be obtained
- f. For measurements of even mode resonant frequencies, the software program informs the user to manually position the plunger holding the capillary tube within the slot. After manual adjustment and at each even mode frequency, the program measured the complex permittivity. Since this manual manipulation is time consuming, during this research this option was not used to preserve the viability of cells
- g. During all measurements, a coupled thermometer is used to measure the cavity room temperature value with time. The tests were run at temperature of 23 degrees Centigrade.



(a)



(b)

Figure 6.7: An example of Labview calibration image (a) and generated measurement image (b) on the GUI

## **6.7 Material preparation and method**

Before starting the measurements with cells, different cancer cells are prepared for testing readiness. HeLa, prostate cancer, breast cancer cell line MDA 231, uveal melanoma cell lines 92.1 and OCM are removed from the flasks using the standard adherent cell detachment protocol. The detached cells are counted and verified under the microscope to evaluate the average size of the cells. A media solution is prepared with D-PBS and mixed with cancer cells in a tube. Bulk form cancer cells with minimum amount of media were sucked into 10  $\mu$ l micropipette from VWR Int. Care was taken to remove most of the media solution from the tube. Bulk cells were diluted after measurement in a known volume of RPMI and then recounted to estimate the volume fraction value. The measured and estimated volume fraction of the inclusion or the bulk cancer cells in the remaining media was close to 0.7. This value was chosen in order to facilitate the calculation and estimation of the exact complex permittivity of the cancer cells from the mixture formulas of equation (152). Similar preparation was used for non-adherent WBC - Jurkat, Clone E6-1.

## **6.8 Test results and measurements**

### **6.8.1 Calibration or reference measurement**

Cavity perturbation method measurement is validated by permittivity measurements of several referenced liquids such as distilled water, acetone, ethanol 99%, methanol, glycerol and glycerol-distilled water 1:1. D-PBS media dielectric properties are also measured for the dielectric properties of the media. These measurements are critical

and act as the base line measurements since the complex permittivity of most of these solutions is already measured at different frequencies by other authors [214, 250, 260, 268, 269]. Figure 6.8 and Figure 6.9 give the dielectric constant and the dielectric loss of these solutions at different frequencies. Several measurements were repeated to ensure the repeatability of the results. Measurement results (3 tests) for distilled water, ethanol, acetone and methanol compared with other authors results are close and present the same frequency response behavior.

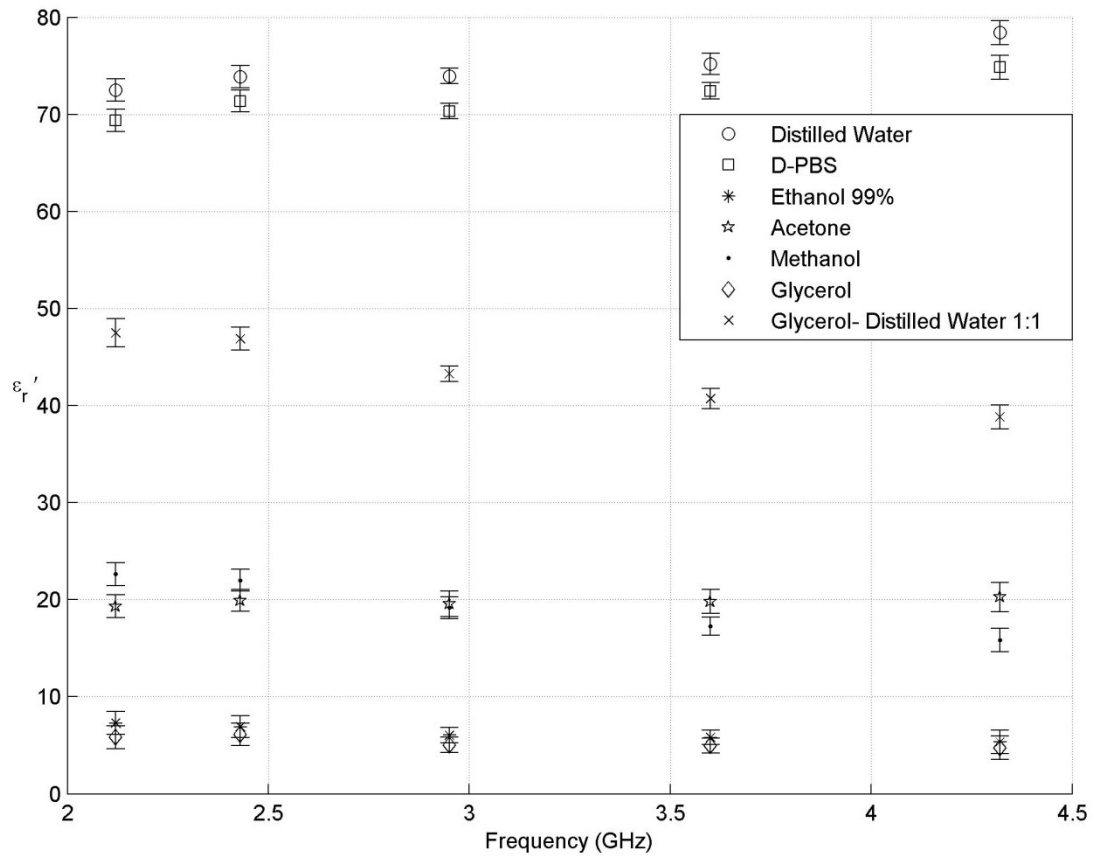


**Figure 6.8: Relative dielectric constant of distilled water, Acetone, Ethanol 99%, Methanol, Glycerol, Glycerol-distilled water 1:1 and D-PBS at different S-Band frequencies (at temperature of 23°C)**

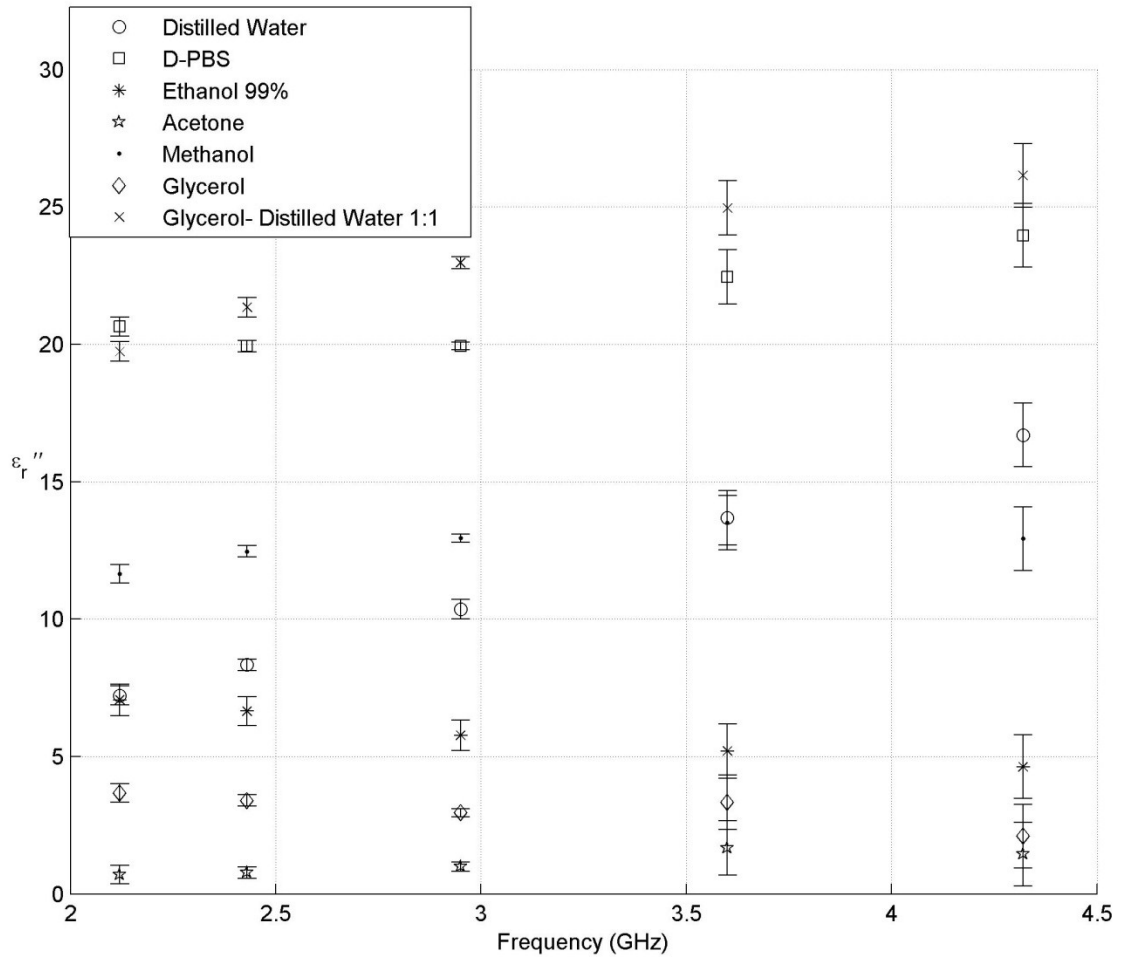


**Figure 6.9: Relative dielectric loss of distilled water, Acetone, Ethanol 99%, Methanol, Glycerol, Glycerol-distilled water 1:1 and D-PBS at different S-Band frequencies (at temperature of 23°C)**

The dielectric constant of distilled water shows an increase from 72 to 78 whereas for D-PBS the increase is from 69 to 75. Glycerol and ethanol (99%) do have the same decreasing behavior from about 8 to 5. Methanol and acetone show values close to 20. Therefore ethanol and Glycerol show the largest dielectric constant difference compared to the distilled water. The dielectric losses of some lossy liquids such as distilled water, D-PBS, Glycerol/distilled water (1:1) increase from about 7 to 27. Methanol dielectric loss is about 12, whereas ethanol, Glycerol and acetone show small constant values close to 3.

Glycerol dielectric constant is much different than distilled water and most cancer cells as is observed in the next paragraph. This characteristic could be very useful to create a good contrast between the Glycerol (as media) and the cells. Nevertheless to reduce the high viscosity of the Glycerol, it is mixed with water having ratios of 4:1 and 1:1. With the Glycerol/distilled water (4:1), the dielectric loss is close to 18 and the dielectric constant close to 15.

### **6.8.2 Different biological cells (reference, WBC, Hela, prostate, breast and uveal melanoma cancer) measurement**

Permittivity and conductivity measurement procedure is used and automatic measurements are performed at room temperature of 23°C on different cancer cells and cell lines with volume fraction close to 0.7. The effective complex permittivity measurement of bulk cancer cells (WBC - Jurkat, Clone E6-1, Hela, prostate PS3, breast MDA231, uveal melanoma 92.1 and OCM) in the D-PBS media, the complex permittivity measurement of D-PBS media and the estimated volume fraction of 0.7, the complex permittivity of different cancer cell is deduced from equation (152). Figure 6.10 and Figure 6.11 illustrate the dielectric constant and the dielectric loss for all cancer cells at different frequencies.

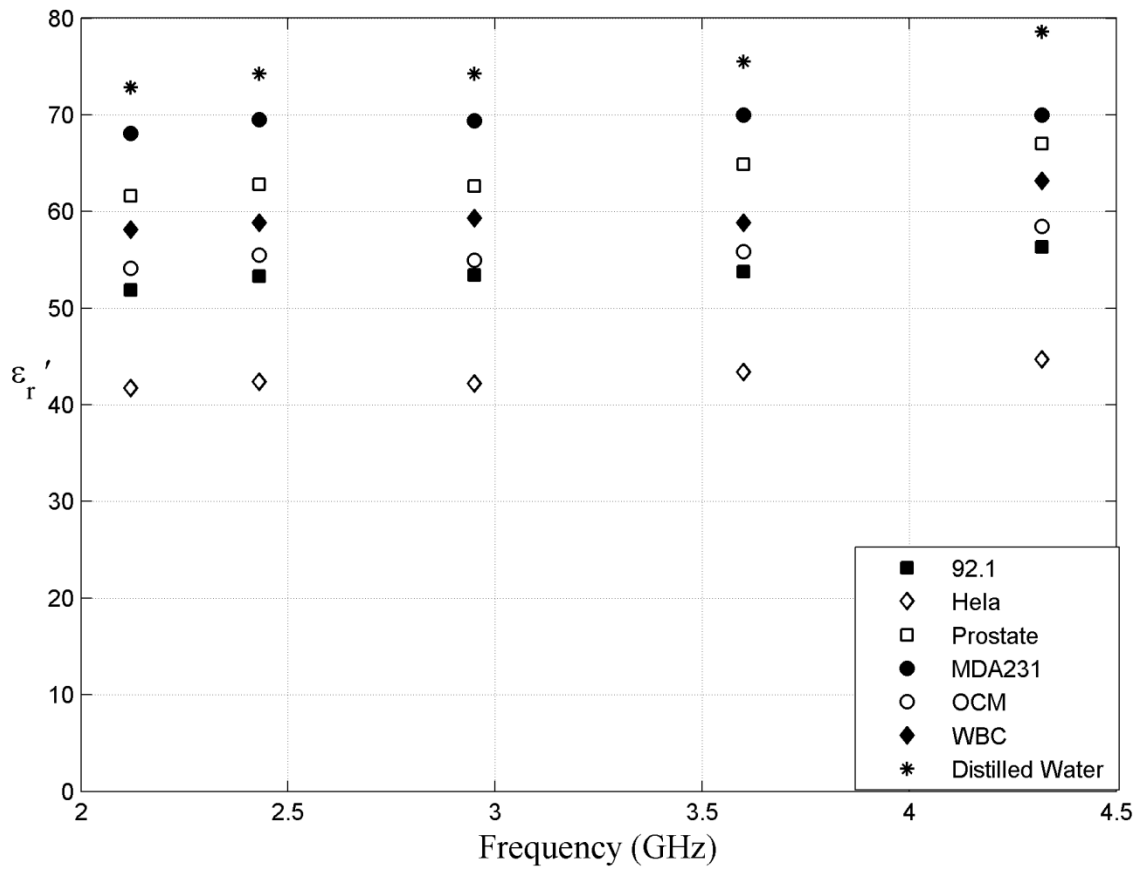


**Figure 6.10: Relative dielectric constant of WBC HeLa, prostate, breast, uveal melanoma cancer cells with volume fraction of inclusion equal to 0.7 at different S-Band frequencies (at temperature of 23°C)**

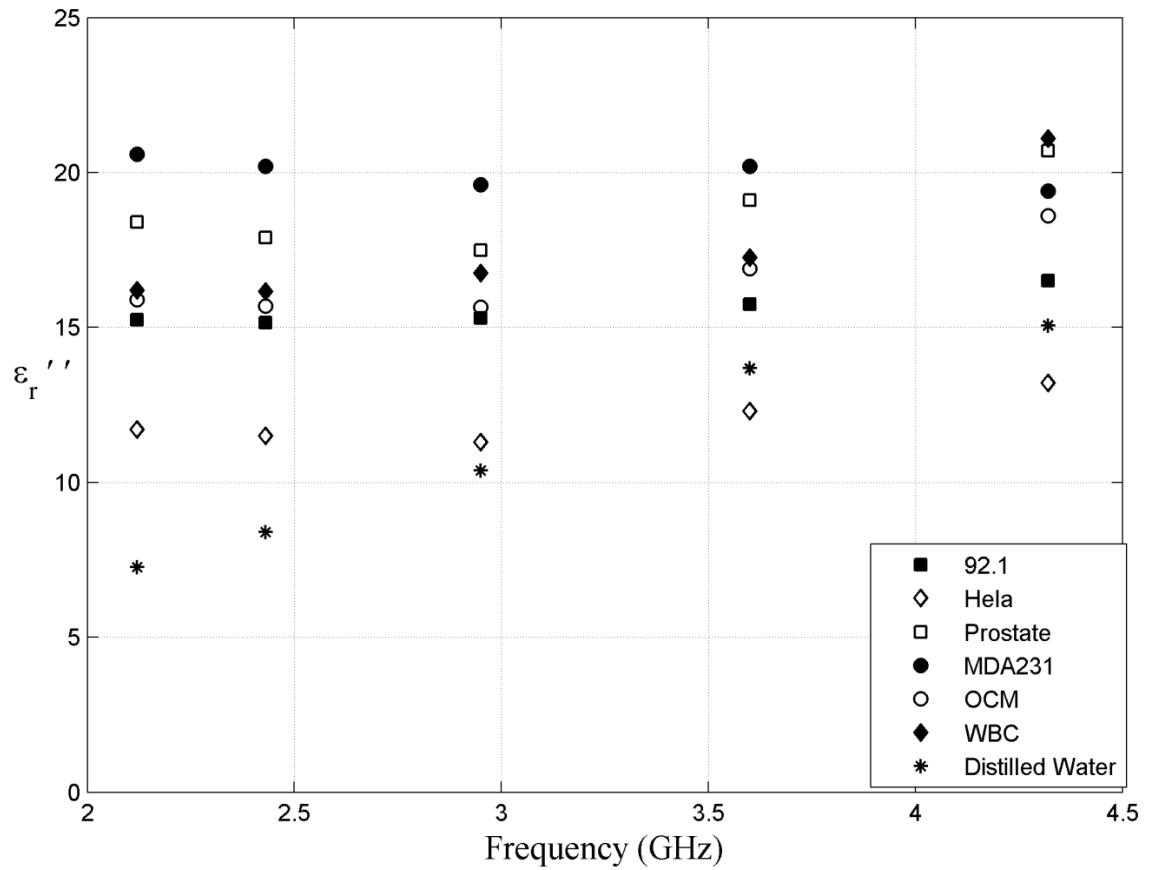


**Figure 6.11: Relative dielectric loss of WBC, Hela, prostate, breast, uveal melanoma cancer cells with volume fraction of inclusion equal to 0.7 at different S-Band frequencies (at temperature of 23°C)**

Uveal melanoma cell lines 92.1 and OCM were measured continuously with time using the automatic software program that controlled the network analyzer during cell dielectric property measurement. The variation with time of the dielectric constant and dielectric loss with frequency for OCM did not show a significant change. Nevertheless the line 92.1 showed a change in these two dielectric parameters Figure 6.12 and Figure 6.13 show uveal melanoma cancer cell line 92.1 variation of the dielectric properties after 1 hour versus the frequency.

**Uveal melanoma line 92.1  
Dielectric constant variation after 1 hour  
versus frequency**

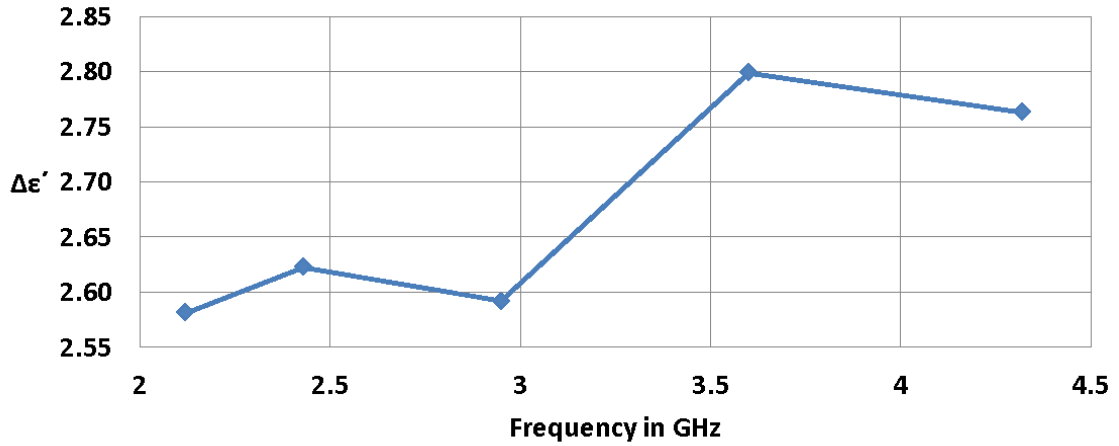


Figure 6.12: Uveal melanoma cancer cell line 92.1 dielectric constant reduction ( $\Delta\epsilon'$ ) after 60 minutes of test. Results are shown for each discrete mode frequency

**Uveal melanoma line 92.1  
Dielectric loss variation after 1 hour  
versus frequency**

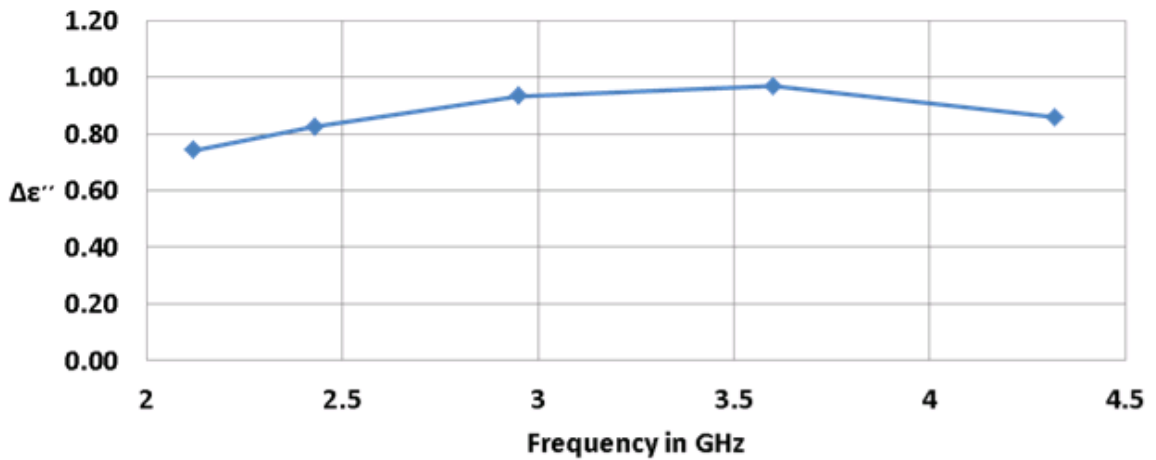


Figure 6.13: Uveal melanoma cancer cell line 92.1 dielectric loss reduction ( $\Delta\epsilon''$ ) after 60 minutes of test. Results are shown for each discrete mode frequency

## 6.9 Discussions

Characterizing the dielectric properties of cells can help the proper detection and possible identification of cells in microfluidic systems. Therefore the identification and understanding the dielectric properties of cells enables the modeling of the cells at different frequencies. Depending on the type of detection at low or high frequencies, the frequency band of the measurement is determined. In this investigation, the need of high frequency detection implies the measurement of complex permittivity of the cells at high frequencies. The use of small quantity of biological material with high measurement accuracy incited the use of cavity perturbation technique for complex permittivity measurements. An S-Band cavity was fabricated with a minimum magnetic coupling at the input and output ports. The coupling was manually adjusted by turning the magnetic loop in the cavity and monitoring the transmission with the best signal to noise level. A maximum electric field adjustment slot was also created within the wall of the cavity to get measurements at several discrete frequency measurements (9 frequencies for the length of 35.6 cm).

Nevertheless it was decided to keep the micropipette, holding the biological specimen, in the middle of the cavity to record only 5 discrete frequency values to ensure the good condition of cells during the timeframe of the measurements.

The most significant measurement challenge was the introduction of bulk cancer cells into the 10 $\mu$ l micropipette to provide the desired high volume fraction. The tube containing the cells and the media was centrifuged at 1000 turn/minute for 5 minutes. The media was removed from centrifuged tube. With very small traces of media in the tube, cells in bulk form were aspirated into the 10 $\mu$ l micropipette for measurement.

Automatic complex permittivity measurements using the microwave network analyzer enabled the monitoring of the dielectric properties evolution of cells with time. The Labview program recorded the measurement over long period of time and recorded the data in minutes and hours. Data were automatically uploaded in Excel sheet format. All calculations of central resonant frequency, bandwidth and quality factor with and without the biological specimen were performed automatically using equation (150) to obtain the values of the dielectric constant and of the dielectric loss.

Different reference other solutions such as distilled water, ethanol 99 %, acetone, methanol, glycerol and glycerol-distilled water (1:1) were measured and compared to the existing data provided by other references. Use of glycerol was driven by its dielectric properties exhibited by the low dielectric constant and good compatibility with biological material. Although glycerol-distilled water mixture 1:1 showed a dielectric constant jump from 5 to about 45 and a dielectric loss from 5 to about 25, the mixture will be easily filled in the measurement capillary tube.

Finally, the measurement of the dielectric properties of bulk cancer cells (Hela, prostate, breast and uveal melanoma) with the automatic system provided the effective complex permittivity of the cell. Using the experimental results of the effective complex permittivity, the Hanai formula and a Matlab<sup>TM</sup> code, the permittivity of each cancer cell line was estimated.

The relative dielectric constant of the cancer cells within 2 to 4.35 GHz varied from 42 to 68 depending on the type of cancer line. The relative dielectric loss of the same cancer cells varied from 12 to 22. For the same cancer line, it was observed that the dielectric constant was almost constant in the S-Band frequency range between 2 and

4.35 GHz. Only a small increase was observed with increased frequency. One can therefore deduce that the relaxation time for cells was not attained at the far edge frequency of these measurements, ensuring an appropriate frequency range for dielectric properties measurement needed to detect and characterize one cell type from the other. The dielectric constant and the dielectric loss values of the WBC are between the ones of prostate cancer cell line PC3 and uveal melanoma line OCM

Therefore, measurement at any frequency between the ranges of 2 to 4.35 GHz would be appropriate for single cell measurement at microwave frequencies.

## **6.10 Conclusions**

From the dielectric property results of different cancer cells and WBC, these living cells present higher dielectric loss than the water at RF/Microwave frequencies between 2 to 4.35 GHz. The explanation of this observation could be explained by molecular study but this is out of the scope of this research. Knowledge of the complex permittivity of each cancer cell type enables the modeling of these micro level particles at high frequencies which are present in microwave transmission lines and systems. Cancer cells in a flask kept inside an incubator at 37°C with 5 % CO<sub>2</sub> can proliferate and grow easily as long as the cell culture protocol is used. When the same cancer cells are kept outside the incubator at 23°C, then it is estimated that after one to two hours, the cells will switch to apoptosis mode. Time evolution measurement (cells kept outside the incubator and present in the micropipette at 23°C) showed a reduction of the dielectric constant and dielectric loss of all the cancer cells within 1 hour except for the OCM uveal melanoma cell line that showed almost no change after 1 hour. This is an observation that

can be related with the fact that OCM cancer is not as aggressive as the one of the 92.1 cell line and can almost be considered as benign cancer cells.

## **6.11 Chapter summary**

The dielectric properties of different cancer cells are found using high frequency resonant cavity. This chapter presents the WR284 resonant cavity design and fabrication details to obtain nine different resonant frequencies ranging from about 2.1GHz to 4.3 GHz. The dimension of the cavity is 3.4 cm x 7.22cm x 35.6 cm. A slot designated to receive the sample is arranged with a manually adjustable plunger for measurements of these nine resonant frequencies. Nevertheless, during the measurement the plunger is set at the geometrical central where the electric field is at its maximum. Therefore, only five resonant frequencies are measured. The magnetic coupling mechanism between the input and the output cavity is adjusted for minimum magnetic coupling.

A software program written in Labview with graphic user interface was produced to perform network analyzer automatic measurement of the complex permittivity of the specimen. The advantage of the program is that it can store the evolution of the complex permittivity with time. After measuring bulk samples of cancer cells, single cell complex permittivity is estimated. In the frequency range between 2.1 to 4.3 GHz, the dielectric constants vary between 42 and 68 and the dielectric losses between 12 and 22.

## **Chapter 7: On Line Characterization of Biological Cells and Bulk measurement of cells**

### **7.1 Introduction**

The first objective of this chapter is to identify the cross frequency of different type of cells that enables the centering of single cell in the microchannel. This finding enables the choice of the proper AC signal frequency for centering different types of cancer cells or clustering of frequencies for groups of cells.

The second aim is to perform RF/Microwave experimental measurements on single cell and investigate if this method can be used for characterization of single cell by signature identification. Simultaneously, cells passing at the interrogation point are also detected and counted with the RF/Microwave mechanism.

Several devices are used for the purpose of these investigations. For the cross frequency identification, a chip with several planar electrodes is used to create and measure the nDEP and the pDEP effect on the living cells. For the single cell characterization, two microfluidic chips with parallel facing electrodes are used to detect/count the cells and to perform single cell characterization and signal identification measurement also called ‘on line measurement of single cell’ by the author. In the first device, several electrodes are present to center cells by nDEP to the interrogation region and others for characterization of cells at low and high frequencies. In this device the overlapping electrodes dimension is 25  $\mu\text{m}$  by 50  $\mu\text{m}$ . In the second device only characterization electrodes are present and the overlapping electrodes dimension is 15  $\mu\text{m}$  by 120  $\mu\text{m}$ .

In the earlier chapters, theory showed that real part of the Clausius-Mossotti factor is negative (nDEP) in some frequency ranges, and positive (pDEP) at others. For single or two shell particle model, CM could become zero at two different frequencies called cross frequencies. One cross frequency ranges in KHz region, and another one at several hundreds of MHz to GHz region [132]. Measuring the first cross frequency of different cancer living cells provides the AC frequency needed for each cancer cell centering. Centering of cells is accomplished by nDEP and is mainly controlled by the low frequency AC signal's frequency and amplitude. Measurement of the second cross frequency (at high frequencies) would be quite challenging and requires special technique as described in of the research articles [270, 271], hence the pDEP or nDEP forces at the interrogation point close to RF/Microwave electrodes would be small due to the low amplitude of the RF/Microwave signal.

## **7.2 Cross frequency determination of living cells**

### **7.2.1 Introduction**

Single cell centering of different living cells requires the determination of the cross frequency of each cell in the appropriate media. The use of sucrose/dextrose as media is important to preserve the viability of living cells. Equation (7) of section 3.2.3 shows that the cross frequency is related to the low frequency media conductivity. Therefore the cross frequency is measured for different media conductivity. DEP effect is difficult to obtain with high conductivity media [31]. Therefore the measurements are limited to conductivities between 0 to 20 mS/m. The following section provides results of cross frequency for different types of cancer cells, RBCs and WBCs, all suspended in

media with different conductivities. In chapter 5, while tests were performed with polystyrene microspheres and *Saccharomyces cerevisiae*, sucrose/dextrose media was not used since these two types of particles were well performing in water media.

### 7.2.2 Material and media preparation

The following steps were performed to prepare the experiments. Melanoma cell lines 92.1 and OCM and breast cancer cell line MDA231 were removed from flasks using the standard adherent cell detachment protocol. RBCs were also prepared as described in chapter 4. The non-adherent WBCs - Jurkat, Clone E6-1 were also removed from flasks and were ready for mixing with the media for future measurement.

Media consisting of sucrose/dextrose/distilled water is prepared with the following quantities 85g/3g/912ml respectively. Five tubes of 50 ml are filled with 40 ml of this solution that presented a conductivity of 0 mS/m. Trypsin is added to change the conductivity of the media. An amount of 167  $\mu$ l of Trypsin in the 40 ml solution increased the conductivity of the media to 5 mS/m. Each additional quantity of 167  $\mu$ l of Trypsin increased the conductivity by 5 mS/m. Therefore the media with conductivity of 20 mS/m contained 0.83 ml of Trypsin.

The prepared living cells are mixed with 10 ml of 0 mS/m Sucrose/Dextrose media and centrifuged. This step is necessary to remove RPMI traces. Then 1 ml of media with the desired conductivity is added and the specimen is ready for testing.

### 7.2.3 Cross frequency measurement and results of RBCs, WBCs and different types of cancer cells

With different media conductivity, different types of cancer cells, RBCs and WBCs are placed over the cross frequency measurement chip. The chip and its different size electrodes are shown in Figure 7.1.

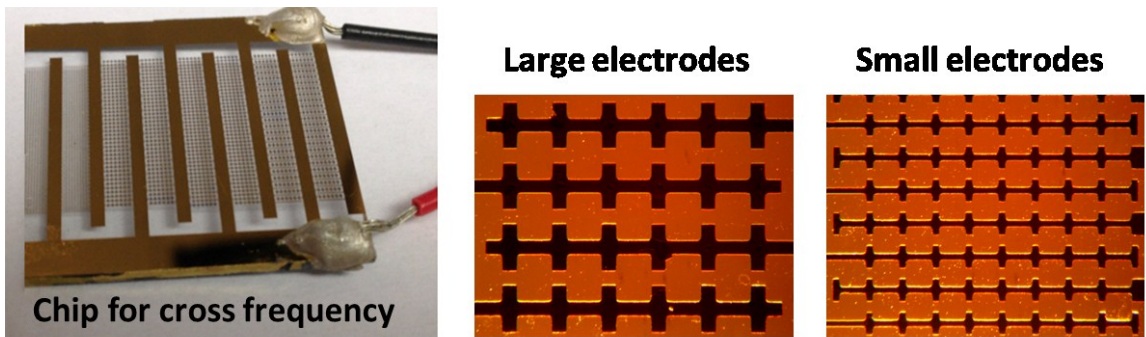


**Figure 7.1: Cross frequency measurement chip. The chip consists of several planar electrodes with different sizes permitting the application of low AC signal and creating dielectrophoresis forces**

The electrodes are designed to create non-uniform electric field enabling dielectrophoresis forces between electrodes. For the large electrode configuration of Figure 7.1, the width of electrodes and the smallest gap in between are  $150\ \mu\text{m}$ . For the small electrode configuration, these dimensions are  $50\ \mu\text{m}$ . All these electrodes are connected to the main two wide lines of the chip to receive the AC voltage through the two red and black electric wires.

By varying the AC applied signal frequency of the generator connected to the two electric wires, the attraction and repulsion of cells are observed at position where high electric and low electric fields exist.

The frequency with a variation of less than 5 % is noted when nDEP is changed to pDEP. This is the measured cross frequency of living cells suspended in media with different conductivities. Table 3 shows the cross frequency of different cancer cells, RBCs and WBCs suspended in five different media conductivities. The AC generator used in these measurements (RIGOL DG4062) was set to amplitude of 10 V peak to peak with a variable frequency from few KHz to 60 MHz. The increase of the voltage to 20 V peak to peak showed some blow up of cells. This is most probably due to the increased electric field deforming the physical properties and the shape of the cells. Molecule analysis to understand the microbiological effect of this high electric field is out of the scope of this research.

Table 3: The cross frequency of different living cells with different media conductivities. The measurement error for cross frequency is less than 5 % for all living cells and all conductivities used during measurement. The max AC signal frequency of the generator is 60 MHz

Cross frequency	$\sigma_m = 0 \text{ mS/m}$	$\sigma_m = 5 \text{ mS/m}$	$\sigma_m = 10 \text{ mS/m}$	$\sigma_m = 15 \text{ mS/m}$	$\sigma_m = 20 \text{ mS/m}$
RBC	From nDEP to pDEP $f = 5 \text{ KHz} \pm 5 \%$	From nDEP to pDEP $f = 20 \text{ KHz} \pm 5 \%$	From nDEP to pDEP $f = 30 \text{ KHz} \pm 5 \%$	From nDEP to pDEP $f = 100 \text{ KHz} \pm 5 \%$ From pDEP to nDEP $f = 12 \text{ MHz} \pm 5 \%$	No DEP effect
WBC	pDEP all frequencies	pDEP all frequencies	pDEP all frequencies	No DEP effect	No DEP effect
92.1 (UM)	pDEP all frequencies	From nDEP to pDEP $f = 28 \text{ KHz} \pm 5 \%$	From nDEP to pDEP $f = 48 \text{ KHz} \pm 5 \%$	From nDEP to pDEP $f = 90 \text{ KHz} \pm 5 \%$ From pDEP to nDEP $f = 42 \text{ MHz} \pm 5 \%$	No DEP effect
OCM (UM)	From nDEP to pDEP $f = 8 \text{ KHz} \pm 5 \%$	From nDEP to pDEP $f = 12 \text{ KHz} \pm 5 \%$	From nDEP to pDEP $f = 38 \text{ KHz} \pm 5 \%$	From nDEP to pDEP $f = 78 \text{ KHz} \pm 5 \%$	From nDEP to pDEP $f = 90 \text{ KHz} \pm 5 \%$
MDA 231	From nDEP to pDEP $f = 7 \text{ KHz} \pm 5 \%$	From nDEP to pDEP $f = 17 \text{ KHz} \pm 5 \%$	From nDEP to pDEP $f = 21 \text{ KHz} \pm 5 \%$	From nDEP to pDEP $f = 33 \text{ KHz} \pm 5 \%$	From nDEP to pDEP $f = 36 \text{ KHz} \pm 5 \%$

## **7.3 Cell detection and counting**

### **7.3.1 Introduction**

RF electrodes in microfluidic chips with microchannel are used to detect and count the cells that pass by the interrogation point between the facing electrode tips using a dedicated detection circuit. The 25  $\mu\text{m}$  overlap of the facing RF electrodes helps this detection. The counting is based on the change of the RF/Microwave signal occurring every time a cell passes through the interrogation point. The RF/Microwave source is injected at the input of the microfluidic device and the output is connected to a detector system including an RF detector with its matching network, followed by a filter and a low frequency amplifier with a high gain. The detector system is connected to the oscilloscope (Tektronix 2236) at very low detection level and when cells pass slowly through the tips of the electrodes, a spike can be observed. This information can be connected to a signal processor to count the number of passing cells. This processing analysis is not part of this project as it would not pose any challenge to design and build.

### **7.3.2 RF/Microwave detector**

The detector system is made of an input matching network of 24  $\Omega$  resistor followed by the detector diode HSMS 2850 and a parallel resistor and capacitor filter of 50 K $\Omega$  and 1 pF. The input of the low frequency amplifier includes an input 100 K $\Omega$  resistor with a non-inverting Op-Amp configuration with a gain of 100 as shown on Figure 7.2. The DC supply on the Op-Amp TLC271 is  $\pm 5$  Volts. Several capacitors are added to the supply inputs to remove noise and offset voltages. The resistor of 24  $\Omega$

matches the diodes at high frequency for a wide frequency band. When the RF signal arrives at the input of this circuit, the high frequency Schottky diode rectifies the signal and after the filtering and amplification a rectified/filtered signal is observed at the output of the detector circuit.

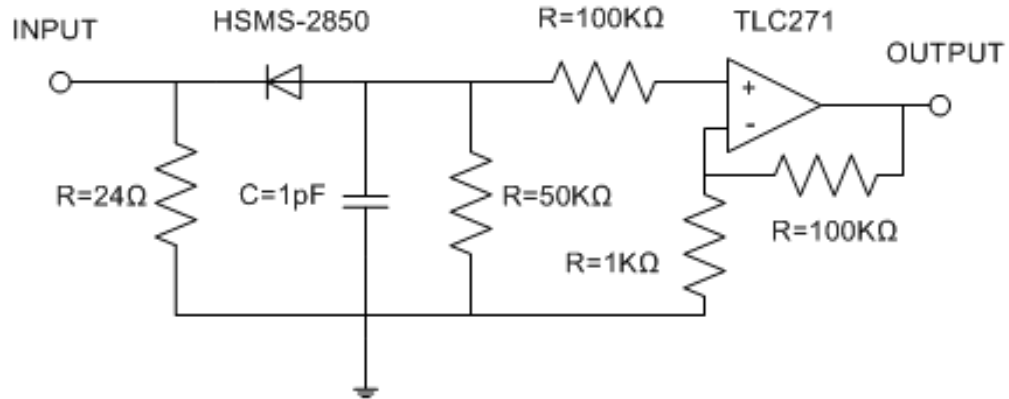


**Figure 7.2: High frequency signal detector circuit containing the RF/Microwave detector, the filtering and amplification components**

### 7.3.3 Cell detection and counting

Figure 7.3 shows the picture of the simple set-up of the counting measurement system. The input signal is the signal obtained from the high frequency sensing electrodes. In fact this signal is divided by a high frequency power divider with one path to the network analyzer for cell characterization and another path to the detection circuit. The oscilloscope Tektronix 2236 is set to the following detection set-up: 10 millivolt/division and 100 millisecond sweep. This sweep time is adapted to the slow cell flow in the micro channel required for cell characterization. When cells pass through the RF sensing electrodes, spikes of 5 to 25 mVolts are observed on the oscilloscope. The picture of the detector circuit is shown in Figure 7.4.

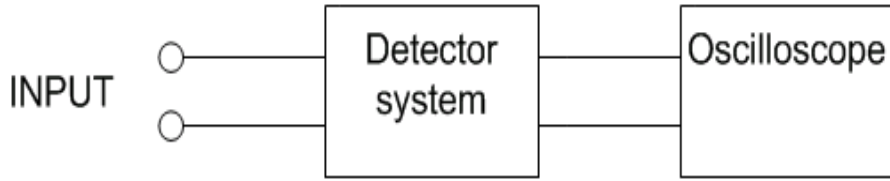


**Figure 7.3: Simple measurement set-up for high frequency detection of cells**

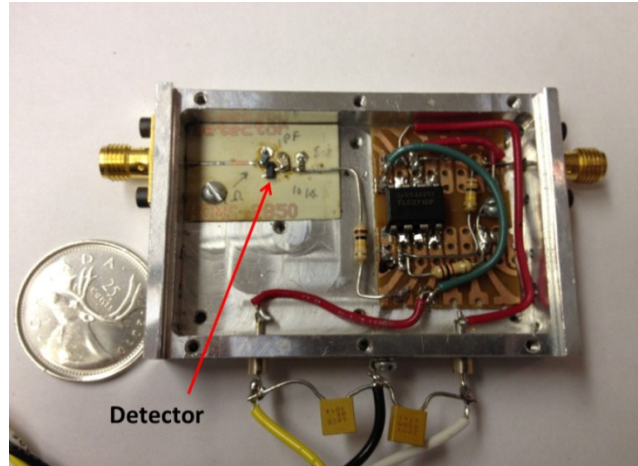


**Figure 7.4: A picture of the detector circuit with the Schottky diode detector at the left and the amplifier circuit at the right**

### 7.3.4 Discussions

Several authors used low frequency detection method to detect and count cells passing through a low frequency system. With this experiment, since high frequency electrodes are already present for characterization measurement, they are also used to detect and count cells. The set-up and components needed for this measurement is simple and only a detector with a surrounding electronic and processing system is needed. The main requirement is to divide the RF output signal of the microfluidic device through a divider. The loss due to the division of the signal is not critical since the characterization measurement is a relative measurement (insertion loss change) that can be amplified if needed.

## **7.4 On line characterization and identification**

### **7.4.1 Introduction**

Single cell measurements are performed with devices having microfluidic channel as presented in chapter 5. As described earlier, the first device contains electrodes for centering and cell characterization, and the second device has only RF/Microwave characterization electrodes. The presence of different electrodes in the first device enables centering, detection of cells and RF/Microwave measurements. Suspended cells in a prepared media are injected with Harvard Apparatus pump via syringe and plastic tubing into the microchannel. Very low rate of about 0.5 ml/hr is set on the pump for single cell characterization. When cells enter into the channel, appropriate low frequency AC signal is applied on centering electrodes to focus the cells into the RF/Microwave interrogation point in the channel. At the interrogation point, the RF electrode overlapped tips detect the passage of single cell. The fluidic movement is observed under the microscope (OMANO OM900). Insertion loss and return loss measurements are performed without and with the cell in the media. The change in the frequency response (insertion loss and return loss) with and without the cell presents the signature identifying the type of the cell.

In this section, the description of each device is provided, followed by the analytical results of the transmission line characteristics of the entire structure. The measurement results for dielectric properties of each cell and different media presented in chapter 6 is the main input information for modeling the single cell under the electrodes. In fact, the single cell present under the overlapping electrodes is studied numerically by

simulation on HF Works and analytically, considering the dielectric properties of the living cells and the media to be used during the measurements. The capacitances presented by the different types of living cells being very small, the height of the microchannel is critical for the sensitivity of the RF/Microwave measurement. With the RF/Microwave measurement and measured complex permittivities of the living cells and the media, the single cell under parallel facing electrodes is easily modeled enabling the comparison between the experimental single cell measurement and the simulated/analytical models of the cell and the RF/Microwave path. The complex permittivity of living cells used in the model is a simple lumped capacitance in parallel with a resistance.

#### **7.4.2 Single cell model in the in the RF/Microwave path**

The transmission line model of section 3.3, the single cell model of section 3.4, the cell and the media complex permittivity results of section 6.8.2 and the exact dimensions of the electrodes in the microchannel enable the exact modeling and simulation of the entire characterization structure with and without the particle. In the following paragraphs, a discussion on the geometric dimensions of microfluidic devices followed by modeling and simulation of the structure is presented.

##### **7.4.2.1 Geometrical dimensions of the electrodes and the microchannel of the two devices**

The two fabricated microfluidic devices for cell characterization have different geometrical dimensions and are presented in the next sub-sections.

### 7.4.2.1.1 The first device

The width and the height of microchannel are  $300\ \mu\text{m}$  and  $50\ \mu\text{m}$  respectively. A channel width of  $300\ \mu\text{m}$  is initially considered to avoid cell clotting if cells happen to be in cluster form. Considering the diameter of cells to be close to  $25\ \mu\text{m}$ , a channel height of  $50\ \mu\text{m}$  is chosen to avoid clotting of the cell while moving by the interrogation point. The overlapped electrode dimensions are  $50\ \mu\text{m}$  by  $25\ \mu\text{m}$  with a gap of  $50\ \mu\text{m}$  representing the height of the channel (Figure 7.5). The design of the  $25\ \mu\text{m}$  overlap is performed to improve the sensitivity of the system with and without the presence of the particle or the living cell. A better sensitivity is obtained when the cell takes all the volume under the overlapping electrodes and when the fringing capacitance is at its minimum effect. This microfluidic device is already described in chapter 5.

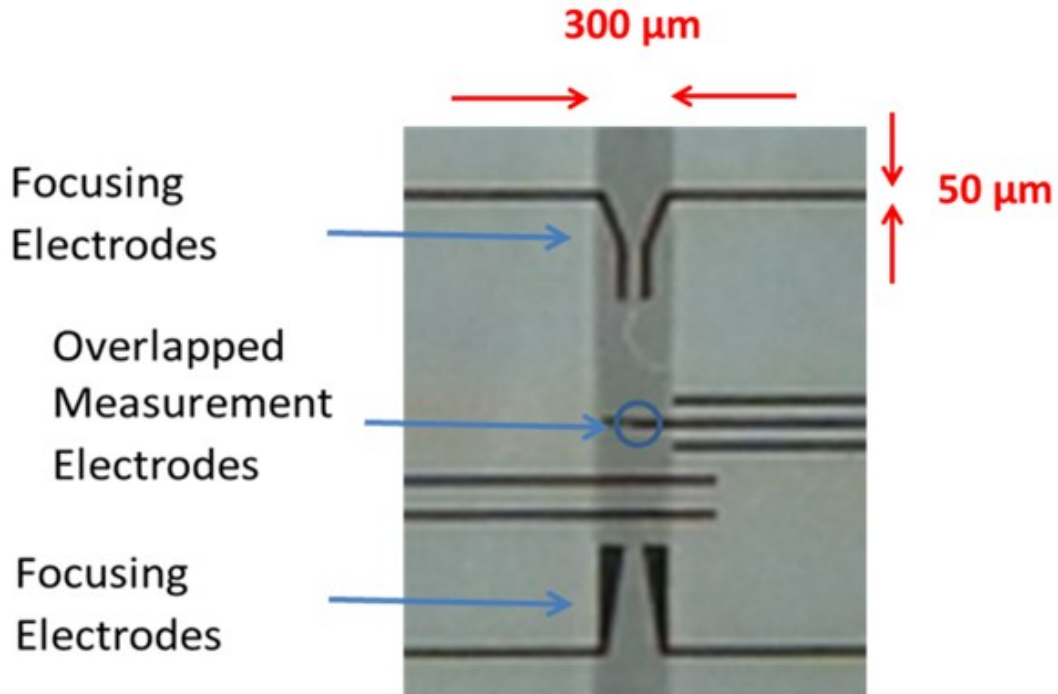


**Figure 7.5:** A top view picture of the microchannel and the electrodes of first device for single cell characterization. The height of the channel is  $50\ \mu\text{m}$  and all electrodes widths and gaps are  $50\ \mu\text{m}$

### 7.4.2.1.2 The second device

The second microfluidic channel is fabricated using two substrates with gold patterned electrodes (part number IAME 15 04 Au) from ABTECH Scientific, Inc. All the patterned electrodes at the tips have the same length, with width and gap equal to 15  $\mu\text{m}$ . At the interrogation tips of these substrates, the electrodes are covered by a silicon nitride layer.

The microchannel is made of silicone layer as described by the fabrication procedure of chapter 5. The width and the height of microchannel are 120  $\mu\text{m}$  and 40  $\mu\text{m}$ . Since the tips of all electrodes have the same length, then the overlapping is covered for the entire width of the channel and the overlapped electrode dimensions are 120  $\mu\text{m}$  by 15  $\mu\text{m}$  with a gap of 40  $\mu\text{m}$  (Figure 7.6). The major difference between this device and the first device is the height that is reduced from 50 to 40  $\mu\text{m}$ . The height of this device is smaller than the first device for better sensitivity. Nevertheless this device does not include centering electrodes and having smaller channel width compared to the first device will help the centering of cells.

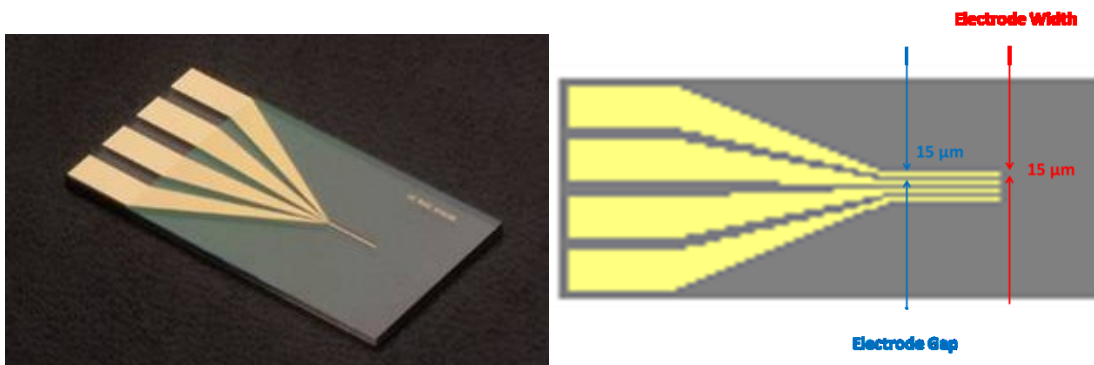


**Figure 7.6: The substrate of the second device (ABTECH Scientific, Inc.) fabricated for a height of 40  $\mu\text{m}$  and line widths and gaps of 15  $\mu\text{m}$**



**Figure 7.7: A picture of the second device with the 2 SMA high frequency connectors**

#### 7.4.2.2 Analytical model of the CPW of the entire microstructure

The first microdevice is made of four different CPW transmission line segments (Figure 7.8). The first segment is a standard CPW configuration and the others are modified configurations as described in chapter 3. The insertion loss and the return loss of the entire device including the repetition of 4 segments to the left and to the right of the overlap section, and the middle 5<sup>th</sup> segment representing a gap capacitance including a suspending particle in a media, are computed using a Matlab code. In the model of the entire CPW lines, the particle and the media are simplified by modeling them as capacitances without any parallel resistances.

The theoretical study made in chapter 3 for CPW transmission lines considered that the lines are lossless. If the transmission lines are considered to have loss, then for a transmission line with a length  $l$ , the ABCD matrix is defined as:

$$\begin{pmatrix} A & B \\ C & D \end{pmatrix} = \begin{pmatrix} \cosh(\gamma l) & Z_o \sinh(\gamma l) \\ \frac{\sinh(\gamma l)}{Z_o} & \cosh(\gamma l) \end{pmatrix} \quad (153)$$

where  $\gamma$  is the propagation constant,  $\alpha$  is the attenuation and  $\gamma = \alpha + j\beta_{lg}$ .

With  $\alpha = 0.01$  dB/mm, an acceptable value for transmission lines in the frequency range close to 2 GHz [272], the analytical results obtained with Matlab for the insertion loss and the return loss for the entire system (including the 9 segments) are shown in Figure 7.9 and Figure 7.10 respectively.

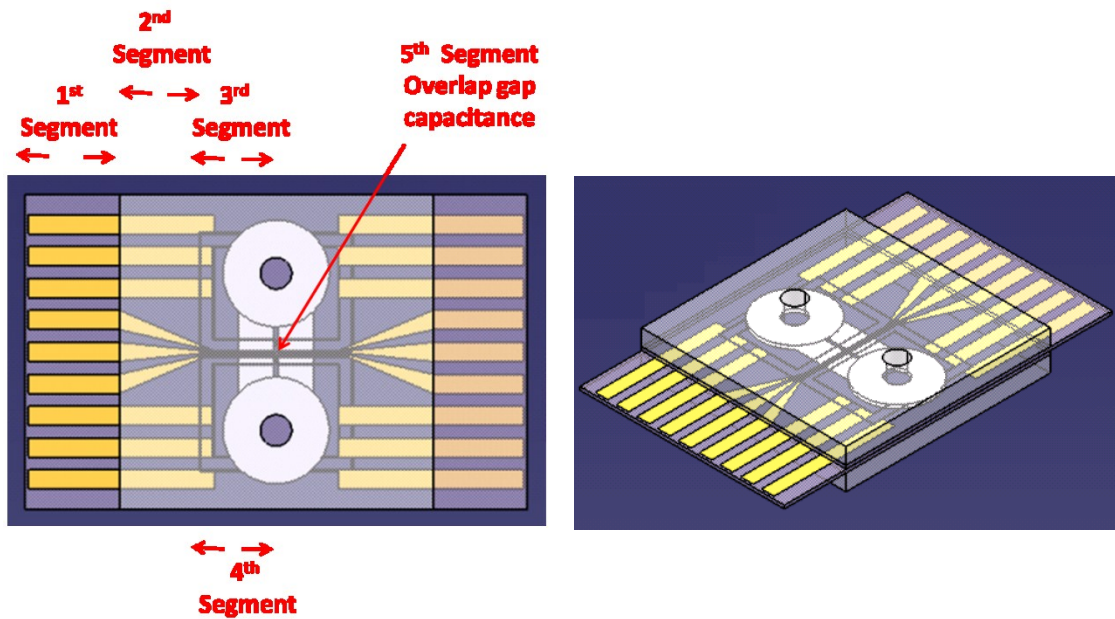


**Figure 7.8:** Different CPW line segments in the microdevice. The 4 segments on the left of the center overlap section are repeated on the right

The insertion and return losses of the RF/Microwave transmission lines with and without the particle are plotted for the following dielectric constant of the particle and the media:  $\epsilon_p = 50$ ,  $\epsilon_m = 75$  and  $\epsilon_m = 18$ . With and without the particle, the return losses in the 2 to 4.5 GHz range are close to -0.7 dB indicating that most of the injected signal is returned back to the source. This is expected due the presence of the gap enabling small capacitances or high impedances compared to  $50 \Omega$ . For  $\epsilon_m = 75$ , the insertion losses with and without the particle in the 2 to 4.5 GHz range are -35 and -45 dB, and for  $\epsilon_m = 18$  they are -45 and -47. The increase of the insertion losses by 4 to 7 dB from 2 to 4.5 GHz

is due to the decrease of the capacitance reactance of the overlapped region versus the

frequency ( $X_c = \frac{1}{2\pi fC}$ ).

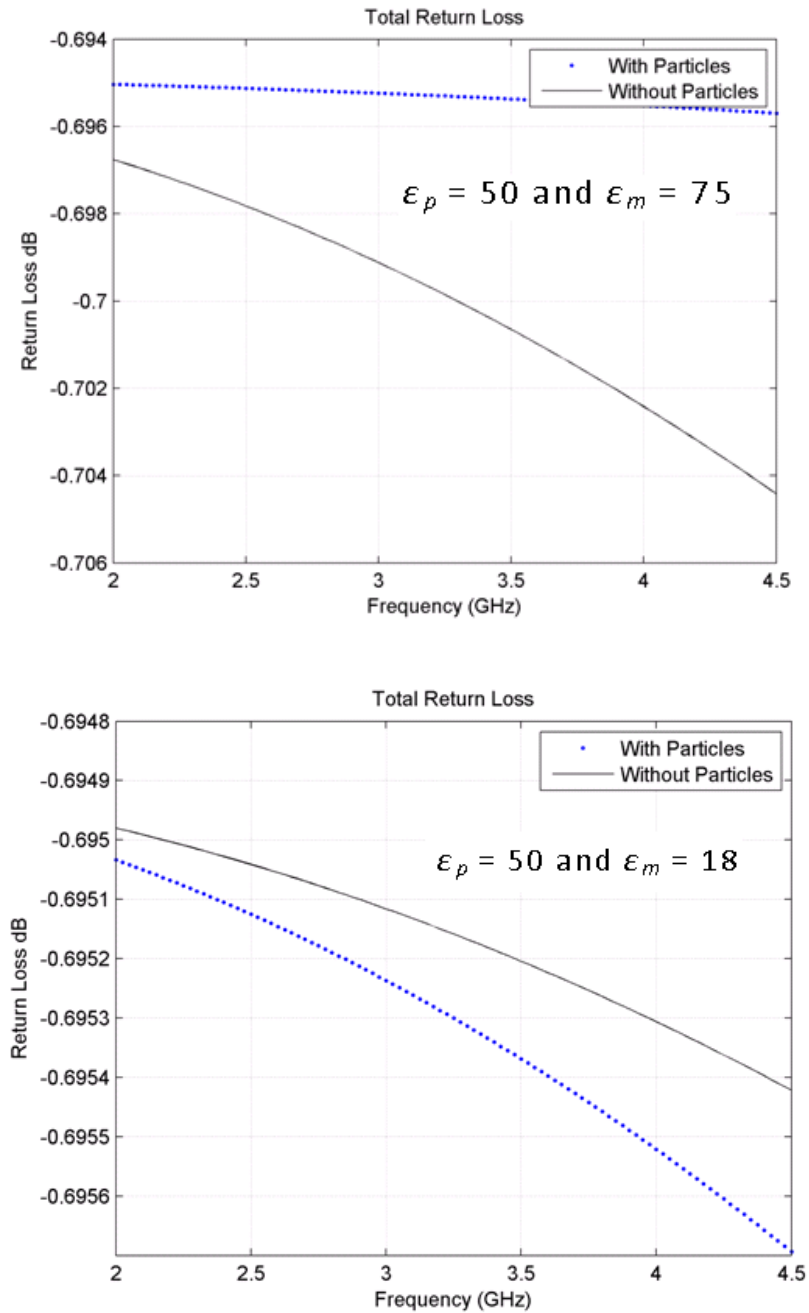


**Figure 7.9: Analytical results of the return loss of the RF/Microwave path consisting of CPW lines and with or without a particle between the parallel facing electrodes with different media dielectric constant of  $\epsilon_m = 75$  and  $\epsilon_m = 18$**

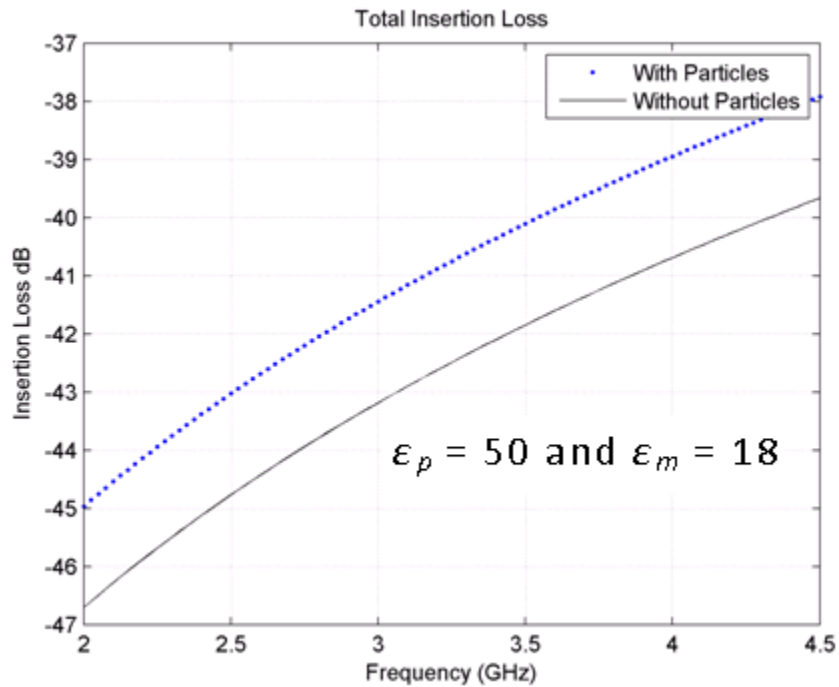
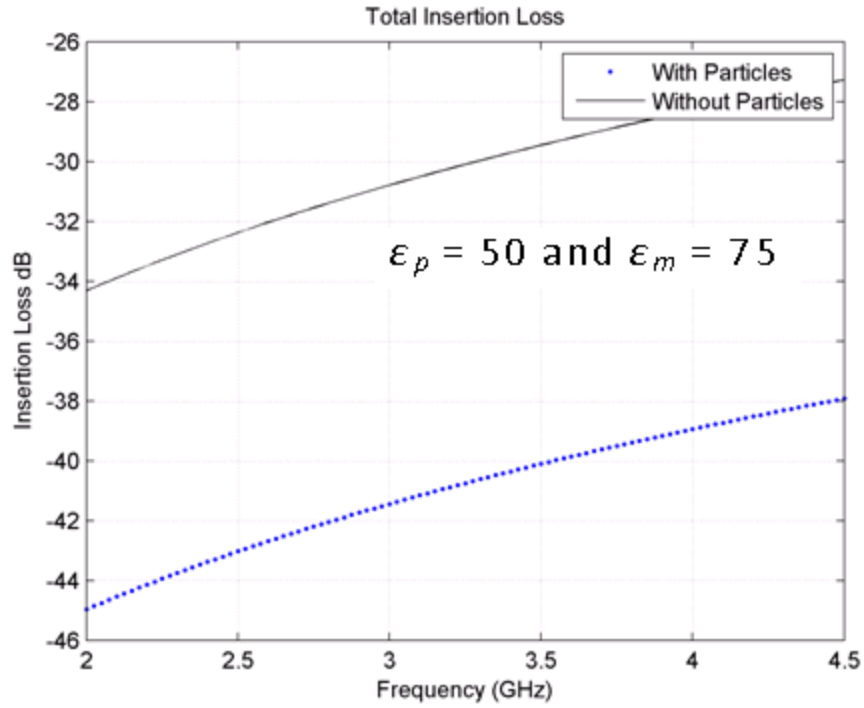


**Figure 7.10: Analytical results of the insertion loss of the RF/Microwave path consisting of CPW lines and with or without a particle between the parallel facing electrodes with different media dielectric constant of  $\epsilon_m = 75$  and  $\epsilon_m = 18$**

### 7.4.2.3 Simulation of the single living cell in between two parallel facing overlapping electrodes within the micro devices

Knowing the RF/Microwave frequency dielectric properties of the cells and the media, it is possible to model the cell under the overlapping parallel facing electrodes. This is accomplished numerically and analytically. In this section, the single cell between the overlapping electrodes is simulated using HFWorks high frequency simulator.

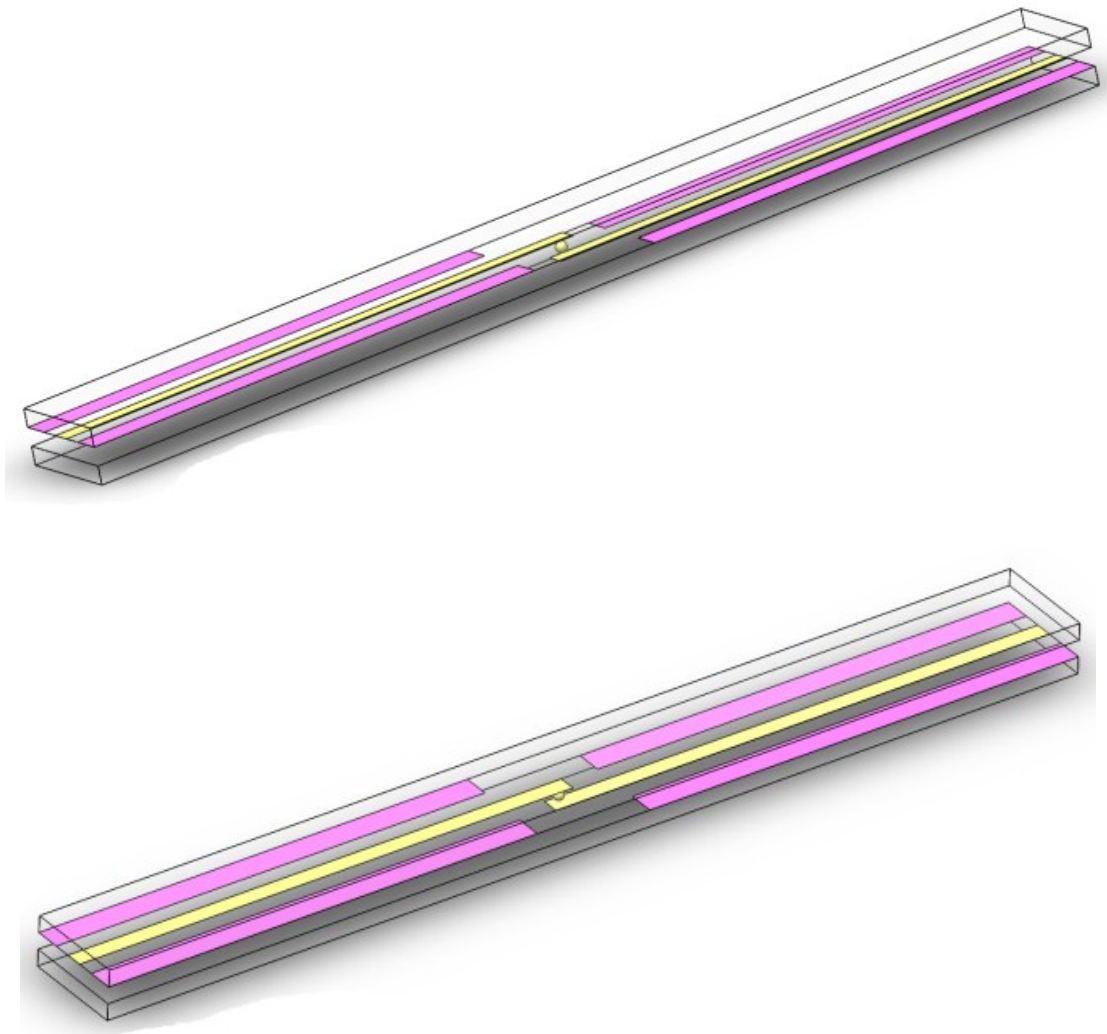


**Figure 7.11:** A picture with two different angles (in HFWorks) of a particle between two facing electrodes. The particle is assumed spherical. The overlapped electrodes are seen at the tips

The simulation is performed with  $\epsilon_p^* = 50 - j18$  and  $\epsilon_m^* = 75 - j18$ . The results in Figure 7.12 show that with the particle present between electrodes the insertion loss in the 2 to 4 GHz range varies from -32 dB to about -26 dB. High values for insertion loss at high frequencies are due to the gap and the particle impedances between the two electrodes. In the same frequency range, the return loss varies between -1.5 dB to -3 dB. Therefore this path shows bad reflection due to the high impedance of the particle compared to the  $50 \Omega$  transmission line characteristic and load impedance.

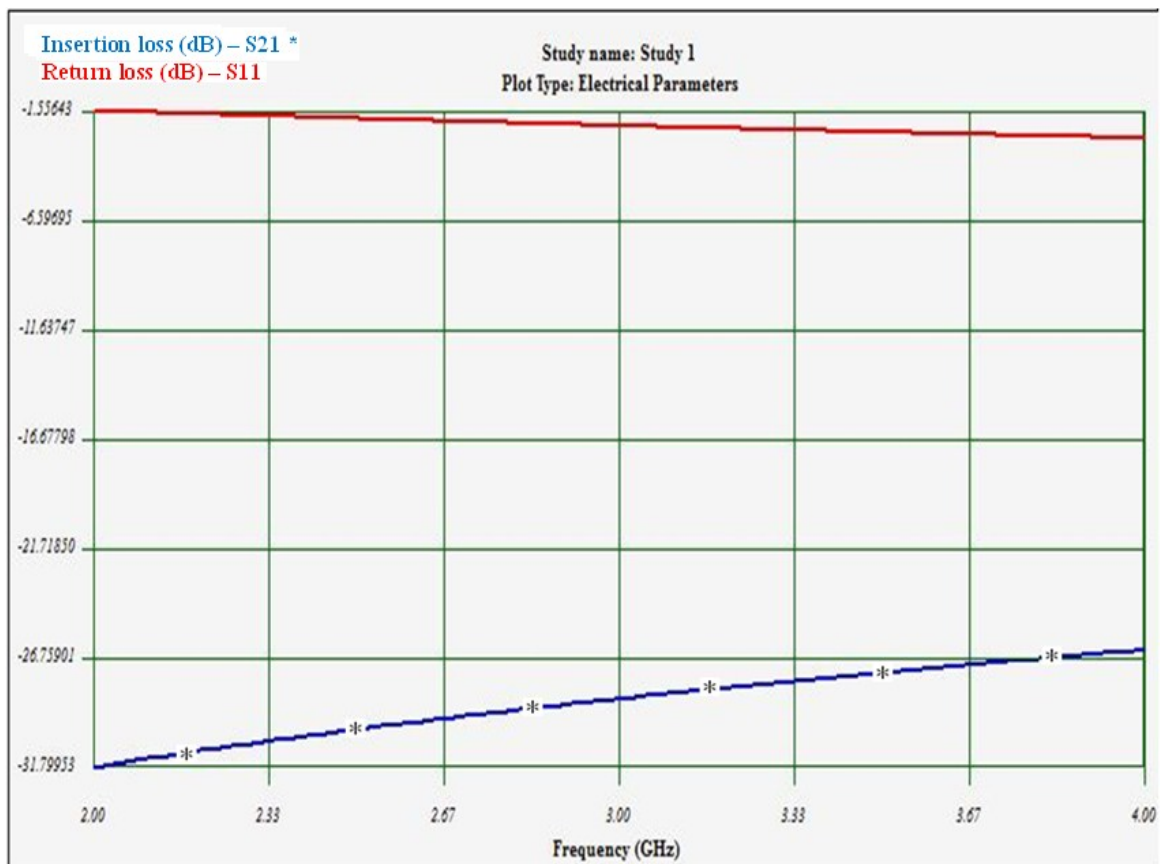


**Figure 7.12: Simulation results of the insertion loss and the return loss of the RF/Microwave path with the particle between the overlapped parallel facing electrodes**

Figure 7.13 shows the comparison of the insertion losses with and without the particle. The insertion loss variation is about 1.5 dB.

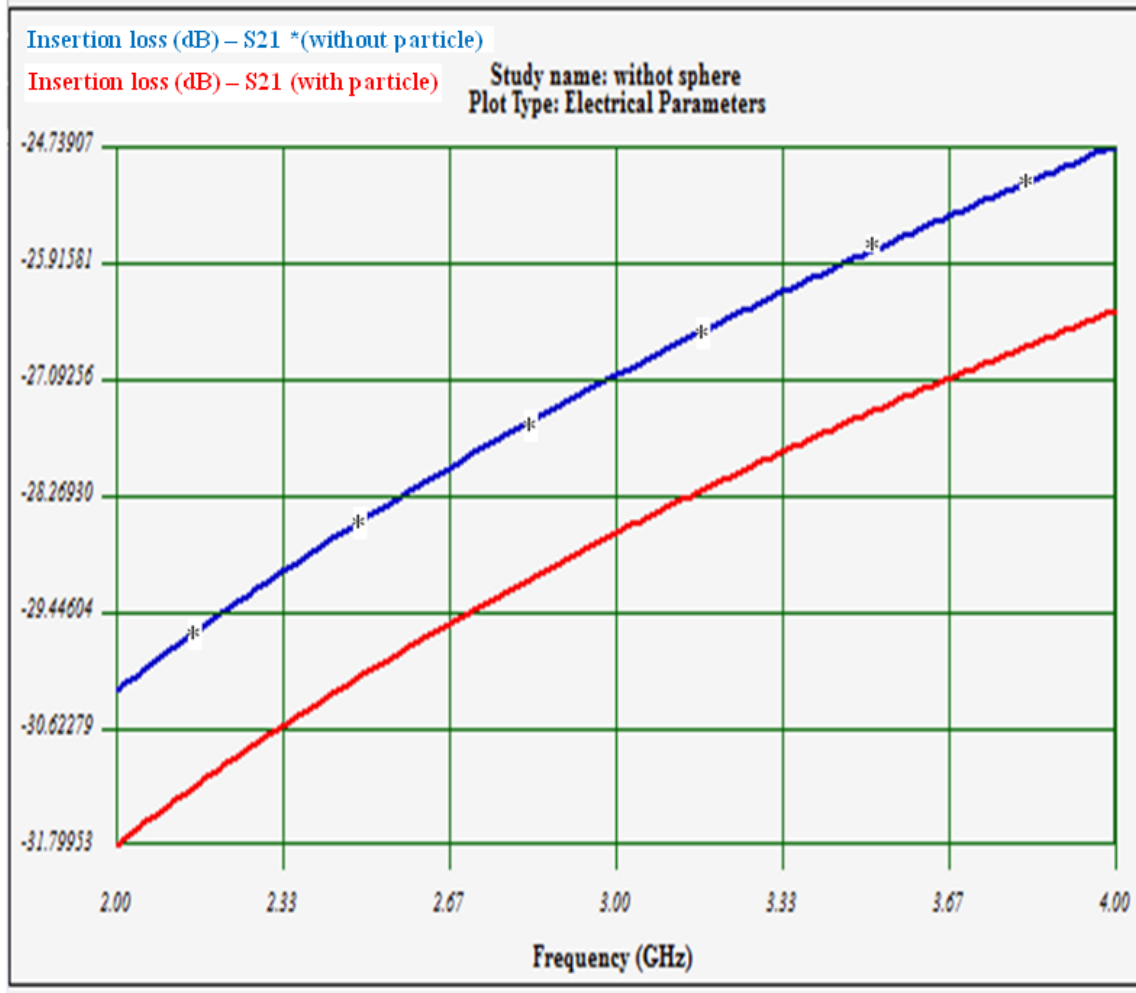


**Figure 7.13: Simulation results of the insertion losses of the RF/Microwave path with and without the particle between the overlapped parallel facing electrodes**

In this simulation, particle and media dielectric properties are chosen close to the values of uveal melanoma cell line 92.1 (for the particle) and of sucrose/dextrose (for the media). The geometric dimensions are chosen identical to the first device where overlapped electrodes are 50  $\mu\text{m}$  by 25  $\mu\text{m}$  with a channel height of 50  $\mu\text{m}$ . The insertion

loss of the overlapped electrodes without the particle is smaller than the insertion loss with the particle.

#### **7.4.2.4 Analytical model of the single living cell in between two parallel facing overlapping electrodes within the micro devices**

With the knowledge of geometric dimensions of the micro channels and electrodes and the single cell models of section 3.4, this section presents the analytical model of overlapped parallel facing electrodes with and without a single living cell. The impedance models and the insertion losses (with and without the cell) are evaluated for different heights of the microchannel. The cell models used in this analysis are for uveal melanoma cell line 92.1 and WBC - Jurkat, Clone E6-1. These cells are suspended in different media namely a mixture of water with sucrose/dextrose and a mixture of Glycerol with Trypsin. The purpose of using the sucrose/dextrose is to preserve the viability of cells by avoiding the osmotic blow-up of cells [31].

Glycerol with Trypsin is mainly used to obtain a dielectric constant value much different from those of the cells. This will increase the sensitivity of the system with and without the cell.

The dielectric properties of cells and media at high frequencies, and the cell dimensions used in this analysis are:

- For 92.1,  $\epsilon_p^* = 52 - j15$ , with cell modeled as a cube having 20  $\mu\text{m}$  side
- For WBC,  $\epsilon_p^* = 58 - j17$ , with cell modeled as a cube having 8  $\mu\text{m}$  side

The cube shape is assumed, as continuity of the cells and media are required in this type of analysis.

- For sucrose/dextrose,  $\varepsilon_m^* = 75 - j10$
- For Glycerol,  $\varepsilon_m^* = 18 - j18$

These complex permittivity values are used from the cell permittivity measurements of chapter 6. The impedance models and the insertion losses with and without particles are computed using a Matlab code.

#### 7.4.2.4.1 Analytical model results for cell line 92.1 in Glycerol

For the overlapped parallel facing electrodes, the total impedance model  $Z_1$  (without the cell) and the total impedance model  $Z_2$  (with the cell) are shown in Figure 7.14. The difference between  $Z_2$  and  $Z_1$  is shown in Figure 7.15.

The insertion loss for series capacitance is calculated using the following matrix:

$$\begin{pmatrix} A & B \\ C & D \end{pmatrix} = \begin{pmatrix} 1 & Z \\ 0 & 1 \end{pmatrix} \quad (154)$$

where  $Z = \frac{1}{j2\pi fC}$  and  $Z$  takes the value of  $Z_1$  or  $Z_2$ .

Similarly the associated insertion losses and the insertion loss difference are shown in Figure 7.16 and Figure 7.17. Figure 7.18 is drawn explicitly to clearly show the influence of the height of the channel on the difference of the insertion loss with and without the cell. The change in the insertion has an exponential behavior for heights smaller than 30  $\mu\text{m}$ .

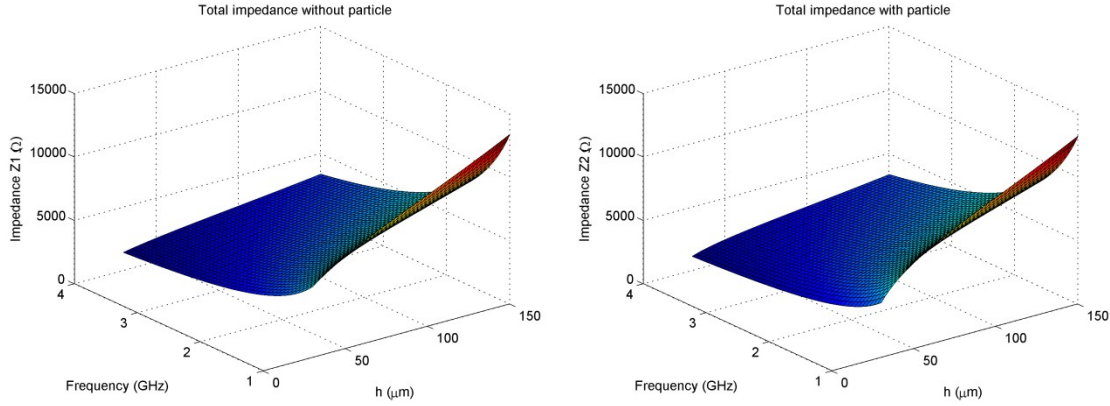


**Figure 7.14: The total impedance of overlapped parallel facing electrodes with ( $Z1$ ) and without ( $Z2$ ) the 92.1 cell. The cell is suspended in Glycerol**

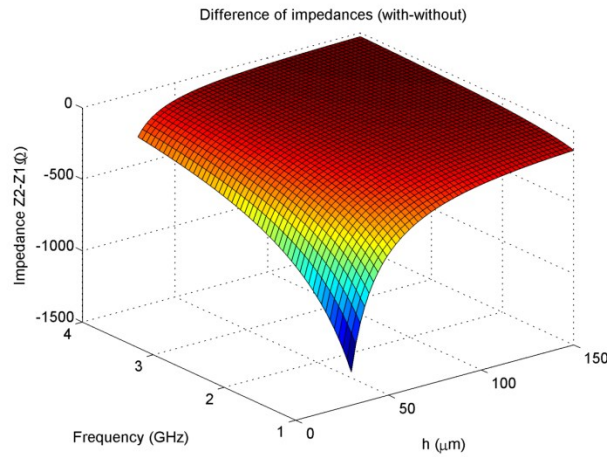


**Figure 7.15: The difference of the total impedance with and without the 92.1 cell (Glycerol)**

The impedances  $Z1$  varies between about  $1300 \Omega$  to  $3280 \Omega$  at  $4 \text{ GHz}$  with the increase of channel height from  $30$  to  $150 \mu\text{m}$ . At  $2 \text{ GHz}$   $Z1$  varies between  $2750 \Omega$  to  $6750 \Omega$ . The impedances  $Z2$  varies between about  $1000 \Omega$  to  $3250 \Omega$  at  $4 \text{ GHz}$  with the increase of channel height from  $30$  to  $150 \mu\text{m}$ . At  $2 \text{ GHz}$   $Z2$  varies between  $2150 \Omega$  to  $6700 \Omega$ . The difference between  $Z2$  and  $Z1$  is at its maximum  $1300 \Omega$  at  $30 \mu\text{m}$  and  $1 \text{ GHz}$ . Therefore when the channel height becomes smaller, the impedance change is greater between measurements with and without the cell.

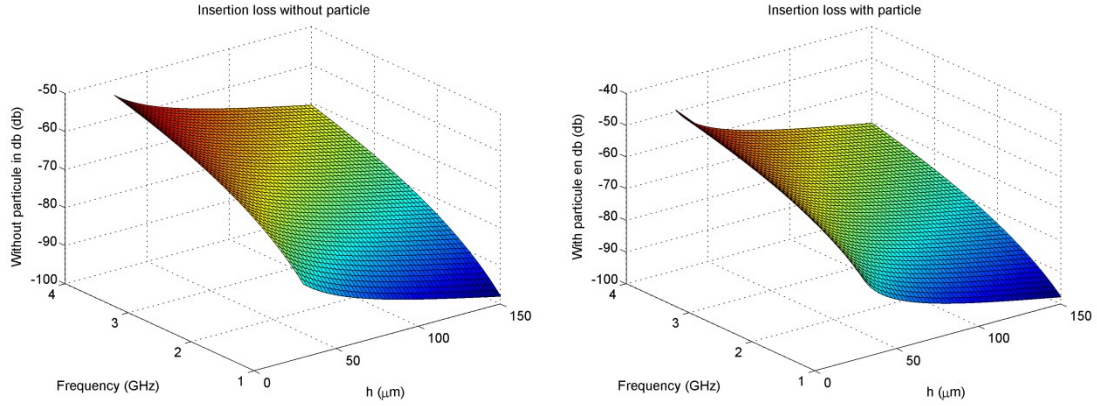


**Figure 7.16: The insertion loss of overlapped parallel facing electrodes with and without the 92.1 cell. The cell is suspended in Glycerol**

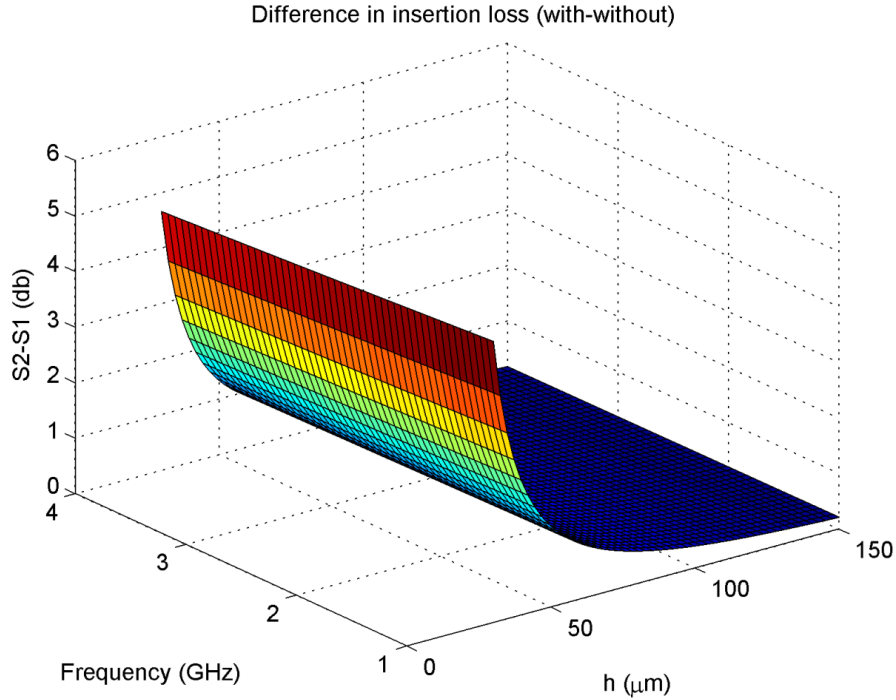


**Figure 7.17: The difference of the insertion loss with and without the 92.1 cell (Glycerol)**

The insertion loss difference is larger when the channel height is reduced. When the height is equal to 30  $\mu\text{m}$  the insertion loss difference between the measurements with and without the cell is close to about 5 dB for all frequencies in the range of 1 to 4 GHz.

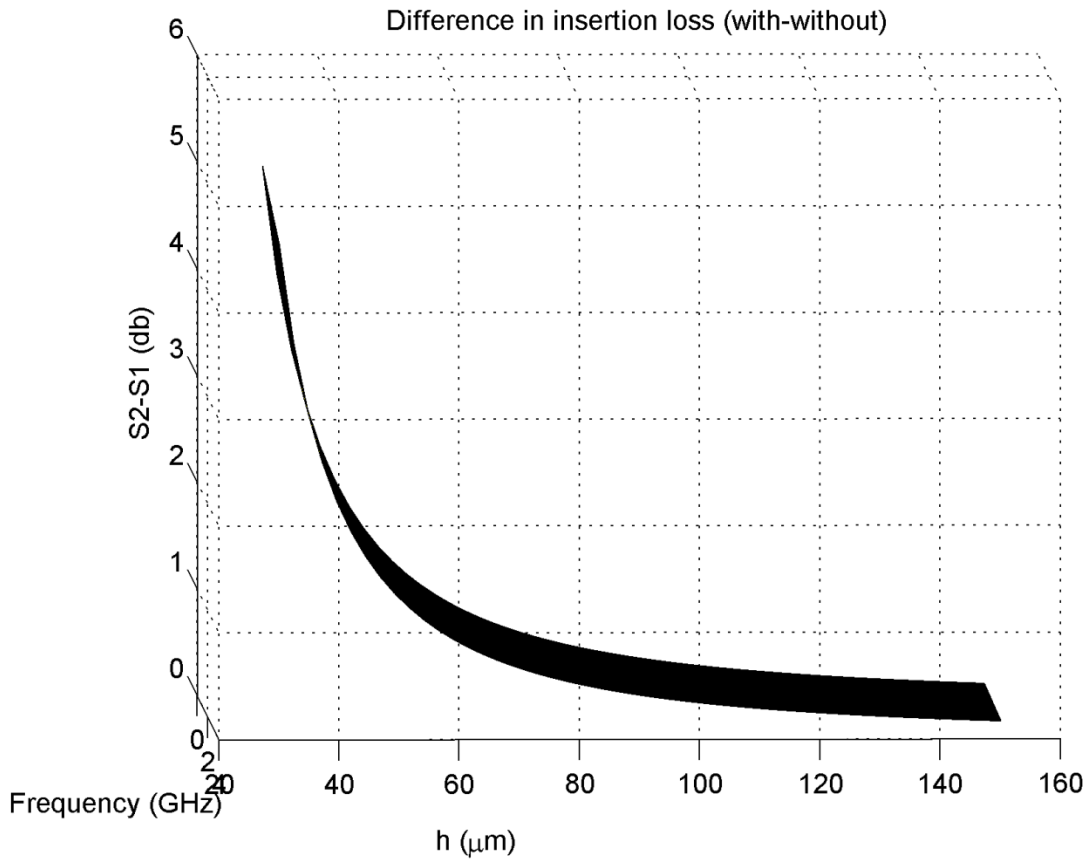


**Figure 7.18: Another view of the difference of the insertion loss with and without the 92.1 cell (Glycerol)**

#### **7.4.2.4.2 Analytical model results for cell line 92.1 in sucrose/dextrose**

The last section analysis is repeated with sucrose/dextrose media. As observed on Figure 7.22 and Figure 7.23, the variation in the insertion loss with and without the cell is less and this is attributed to the fact that in this model, the dielectric properties of the cell is closer to the sucrose/dextrose dielectric properties than to the Glycerol. The total impedance model  $Z_1$  (without the cell) and the total impedance model  $Z_2$  (with the cell) are shown in Figure 7.19. The difference between  $Z_2$  and  $Z_1$  is shown in Figure 7.20.

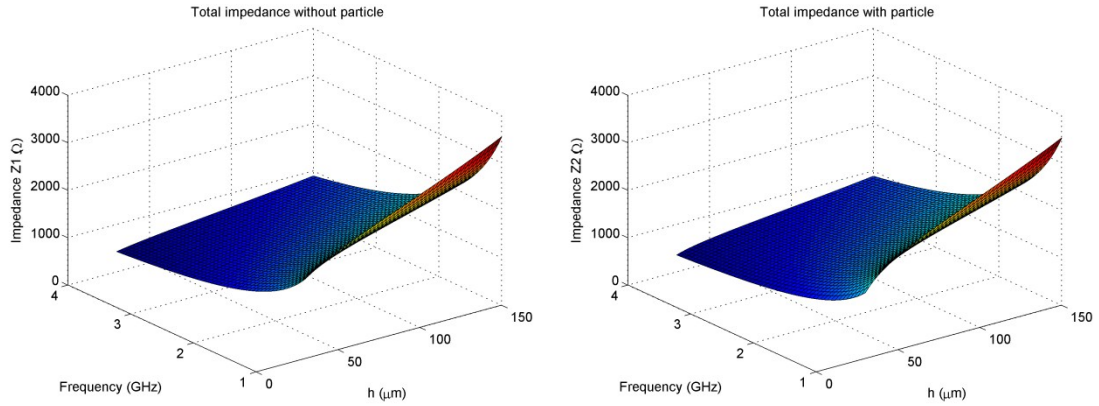


**Figure 7.19: The total impedance of overlapped parallel facing electrodes with ( $Z1$ ) and without ( $Z2$ ) the 92.1 cell. The cell is suspended in sucrose/dextrose**

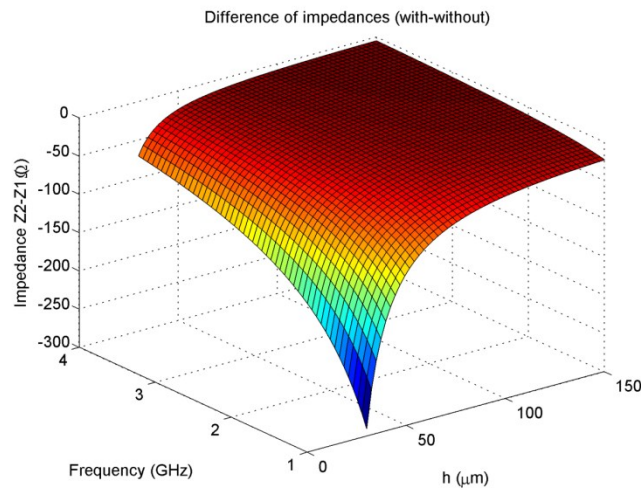


**Figure 7.20: The difference of the total impedance with and without the 92.1 cell (sucrose/dextrose)**

The impedances  $Z1$  varies between about 400  $\Omega$  to 900  $\Omega$  at 4 GHz with the increase of channel height from 30 to 150  $\mu\text{m}$ . At 2 GHz  $Z1$  varies between 850  $\Omega$  to 1750  $\Omega$ . The impedances  $Z2$  varies between about 350  $\Omega$  to 900  $\Omega$  at 4 GHz with the increase of channel height from 30 to 150  $\mu\text{m}$ . At 2 GHz  $Z2$  varies between 700  $\Omega$  to 1780  $\Omega$ . The difference between  $Z2$  and  $Z1$  is at its maximum 290  $\Omega$  at 30  $\mu\text{m}$  and 1 GHz. Therefore when the channel height becomes smaller, the impedance change is greater between measurements with and without the cell.

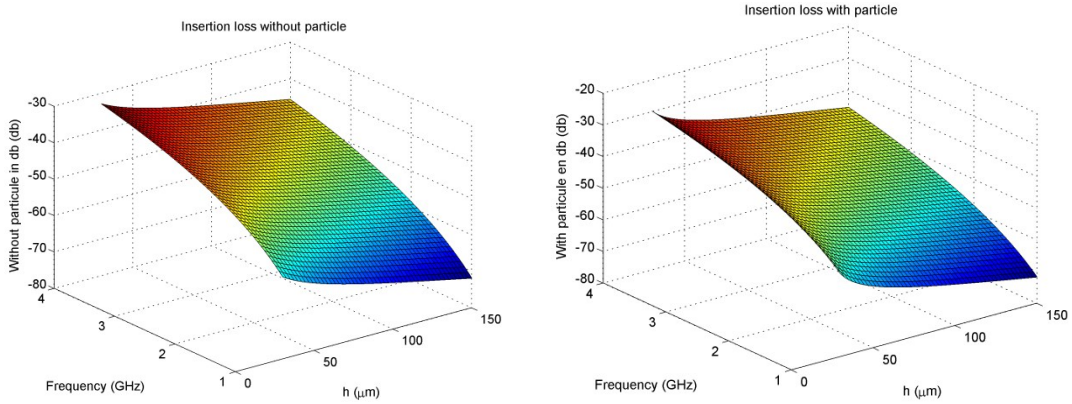


**Figure 7.21: The insertion loss of overlapped parallel facing electrodes with and without the 92.1 cell. The cell is suspended in sucrose/dextrose**

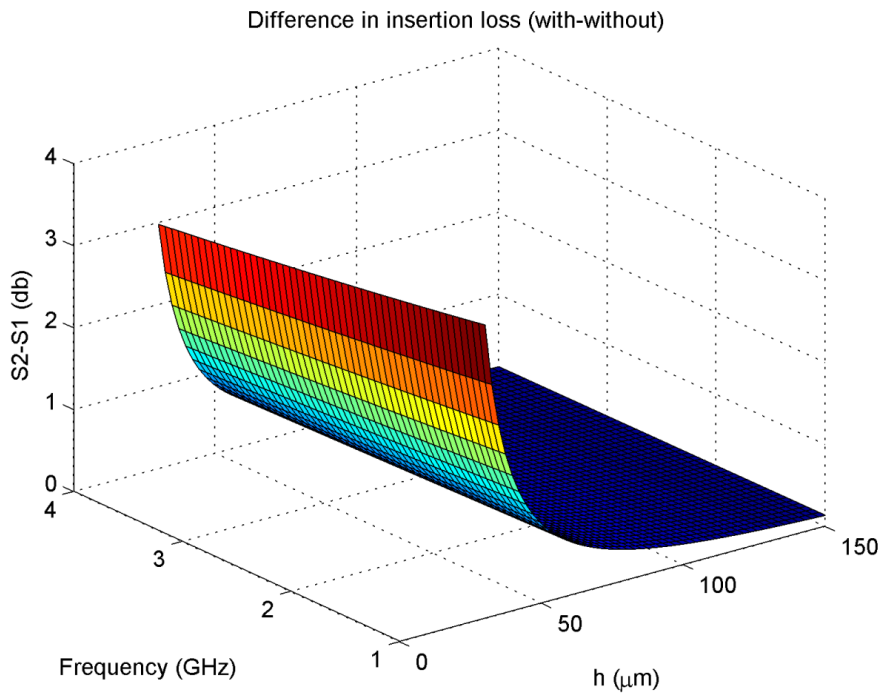


**Figure 7.22: The difference of the insertion loss with and without the 92.1 cell (sucrose/dextrose)**

The insertion loss difference is larger when the channel height is reduced. When the height is equal to 30  $\mu\text{m}$  the insertion loss difference between the measurements with and without the cell is close to about 3 dB for all frequencies in the range of 1 to 4 GHz.

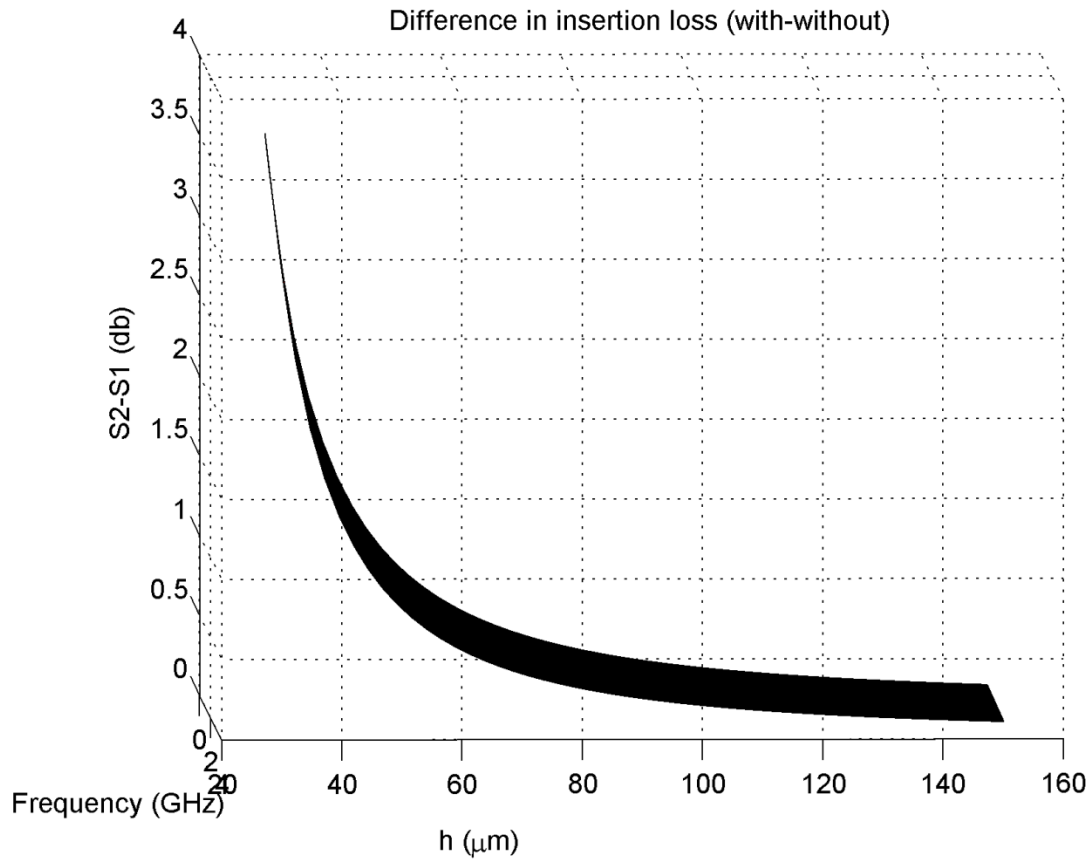


**Figure 7.23: Another view of the difference of the insertion loss with and without the 92.1 cell (sucrose/dextrose)**

#### **7.4.2.4.3 Analytical model results for WBC in Glycerol**

WBC - Jurkat, Clone E6-1 being small compared to the 92.1 cell, the volume of the media occupied under the electrodes is much bigger than the volume of WBC. As observed on Figure 7.25, Figure 7.27 and Figure 7.28, this situation has the effect to reduce the variation of the impedances and the insertion losses when cell is present or not. The total impedance model  $Z_1$  (without the cell) and the total impedance model  $Z_2$  (with the cell) are shown in Figure 7.24. The difference between  $Z_2$  and  $Z_1$  is shown in Figure 7.25.

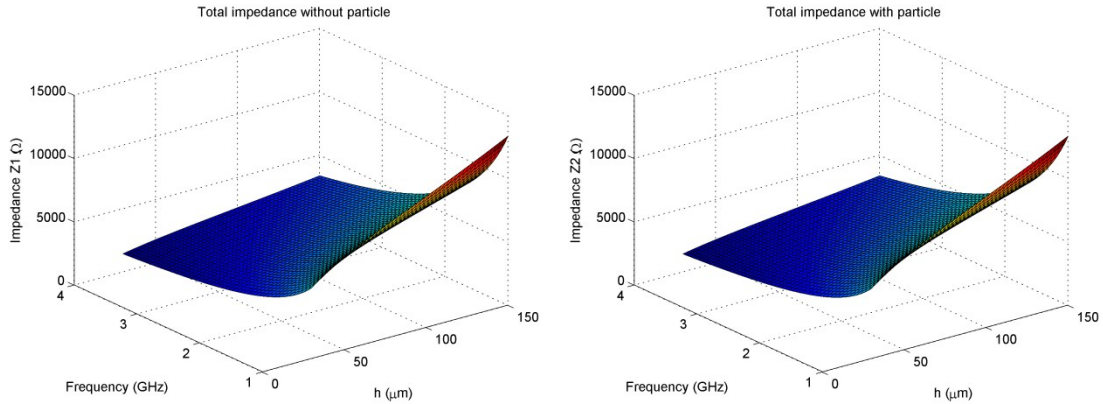


**Figure 7.24: The total impedance of overlapped parallel facing electrodes with ( $Z_1$ ) and without ( $Z_2$ ) the WBC. The cell is suspended in Glycerol**

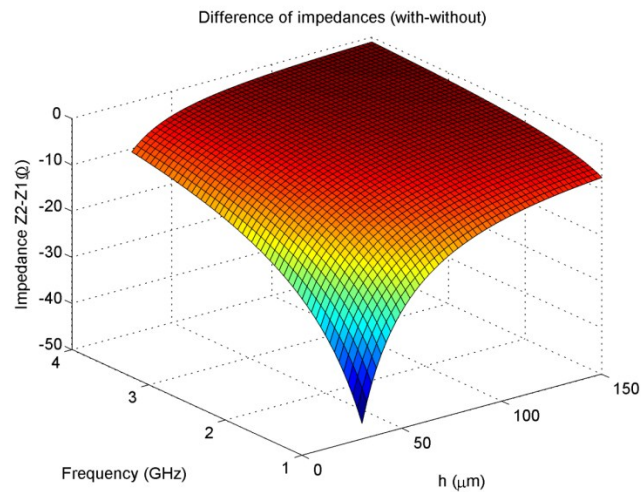


**Figure 7.25: The difference of the total impedance with and without the WBC (Glycerol)**

The impedances  $Z_1$  varies between about  $1410 \Omega$  to  $3400 \Omega$  at 4 GHz with the increase of channel height from 30 to 150  $\mu\text{m}$ . At 2 GHz  $Z_1$  varies between  $2775 \Omega$  to  $6755 \Omega$ . The impedances  $Z_2$  varies between about  $1400 \Omega$  to  $3400 \Omega$  at 4 GHz with the increase of channel height from 30 to 150  $\mu\text{m}$ . At 2 GHz  $Z_2$  varies between  $2750 \Omega$  to  $6750 \Omega$ . The difference between  $Z_2$  and  $Z_1$  is at its maximum  $48 \Omega$  at 30  $\mu\text{m}$  and 1 GHz. Therefore when the channel height becomes smaller, the impedance change is greater between measurements with and without the cell.

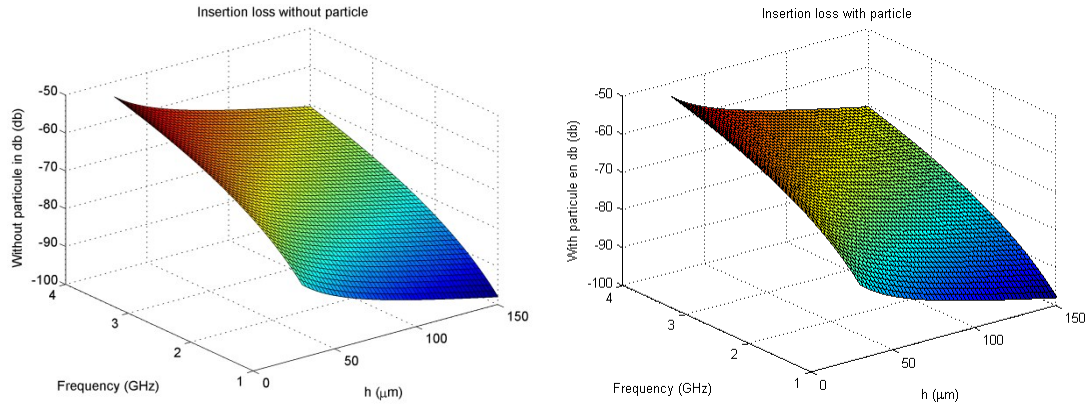


**Figure 7.26: The insertion loss of overlapped parallel facing electrodes with and without the WBC. The cell is suspended in Glycerol**

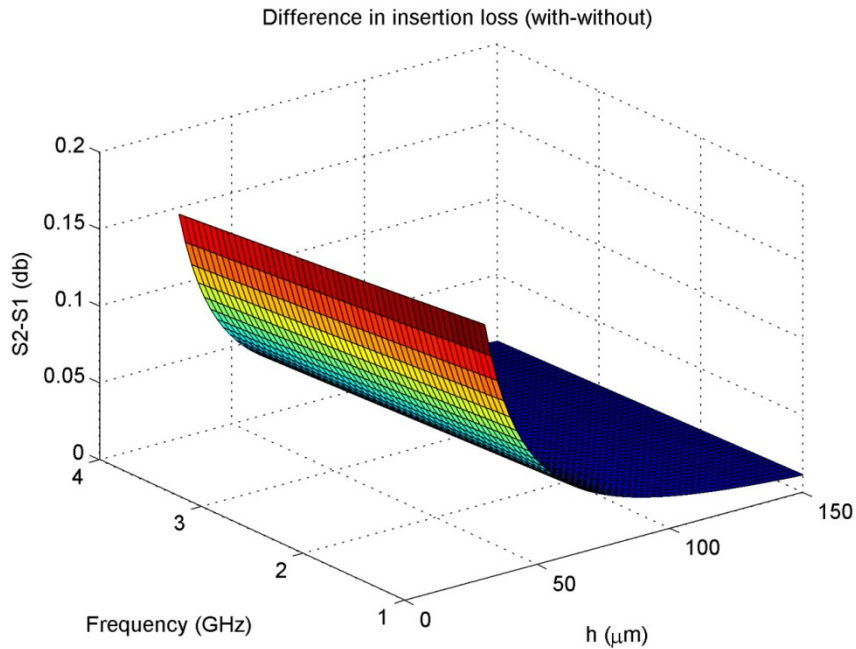


**Figure 7.27: The difference of the insertion loss with and without the OCM (Glycerol)**

The insertion loss difference is larger when the channel height is reduced. When the height is equal to  $30\ \mu\text{m}$  the insertion loss difference between the measurements with and without the cell is close to about 0.2 dB for all frequencies in the range of 1 to 4 GHz.

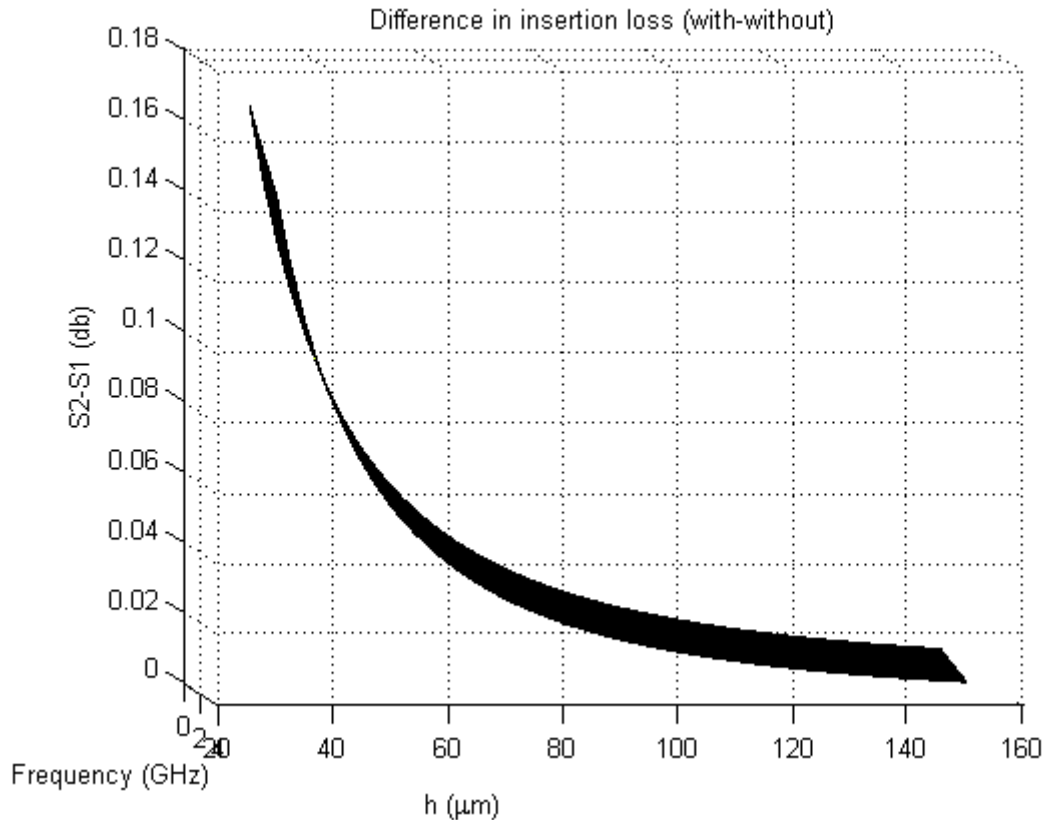


**Figure 7.28: Another view of the difference of the insertion loss with and without the WBC (Glycerol)**

#### **7.4.2.4.4 Analytical model results for WBC in sucrose/dextrose**

When Glycerol is replaced by sucrose/dextrose, the variation in the insertion loss is less than the one encountered for the case of with and without WBC. This reduction is observed on Figure 7.32 and Figure 7.33. It is attributed to the fact that in this model, the dielectric properties of the cell is closer to sucrose/dextrose properties compared to Glycerol. The total impedance model  $Z_1$  (without the cell) and the total impedance model  $Z_2$  (with the cell) are shown in Figure 7.29. The difference between  $Z_2$  and  $Z_1$  is shown in Figure 7.30.

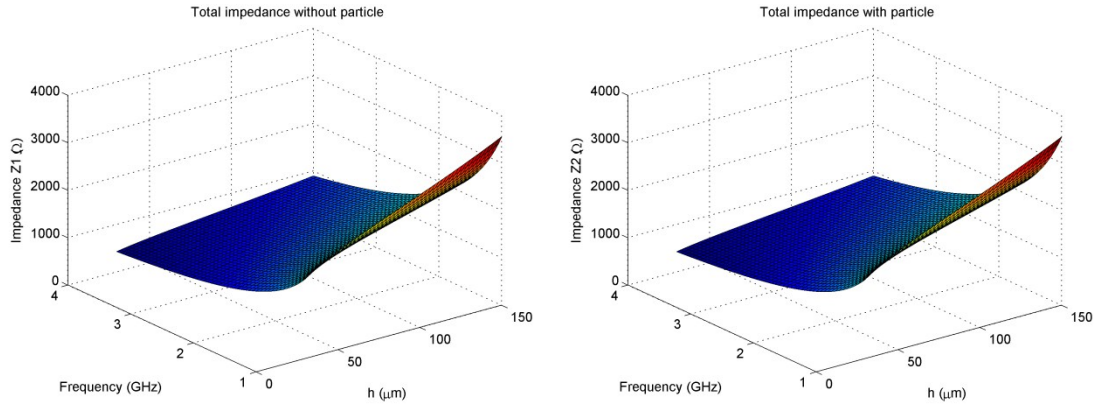


**Figure 7.29: The total impedance of overlapped parallel facing electrodes with ( $Z_1$ ) and without ( $Z_2$ ) the WBC. The cell is suspended in sucrose/dextrose**

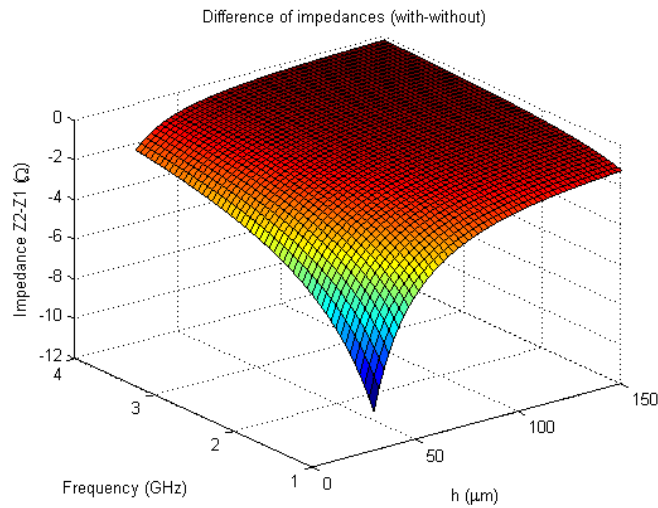


**Figure 7.30: The difference of the total impedance with and without the WBC (sucrose/dextrose)**

The impedances  $Z_1$  varies between about  $413 \Omega$  to  $875 \Omega$  at 4 GHz with the increase of channel height from 30 to 150  $\mu\text{m}$ . At 2 GHz  $Z_1$  varies between  $830 \Omega$  to  $1760 \Omega$ . The impedances  $Z_2$  varies between about  $410 \Omega$  to  $874 \Omega$  at 4 GHz with the increase of channel height from 30 to 150  $\mu\text{m}$ . At 2 GHz  $Z_2$  varies between  $825 \Omega$  to  $1759 \Omega$ . The difference between  $Z_2$  and  $Z_1$  is at its maximum  $48 \Omega$  at 30  $\mu\text{m}$  and 1 GHz. Therefore when the channel height becomes smaller, the impedance change is greater between measurements with and without the cell.

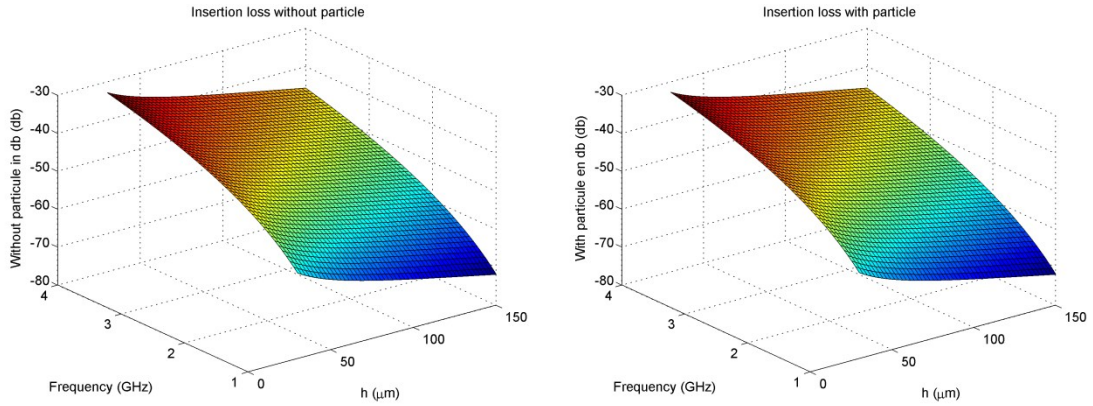


**Figure 7.31: The insertion loss of overlapped parallel facing electrodes with and without the WBC. The cell is suspended in sucrose/dextrose**

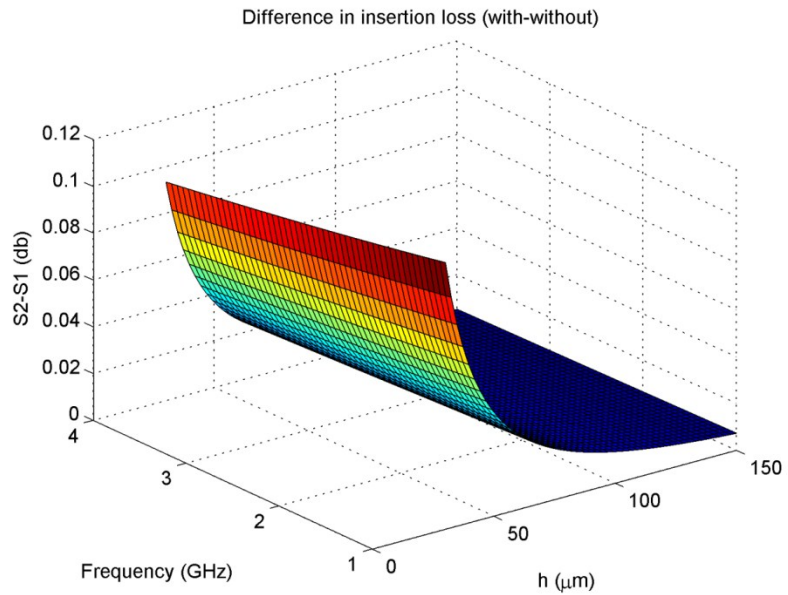


**Figure 7.32: The difference of the insertion loss with and without the OCM (sucrose/dextrose)**

The insertion loss difference is larger when the channel height is reduced. When the height is equal to 30  $\mu\text{m}$  the insertion loss difference between the measurements with and without the cell is close to about 0.1 dB for all frequencies in the range of 1 to 4 GHz.

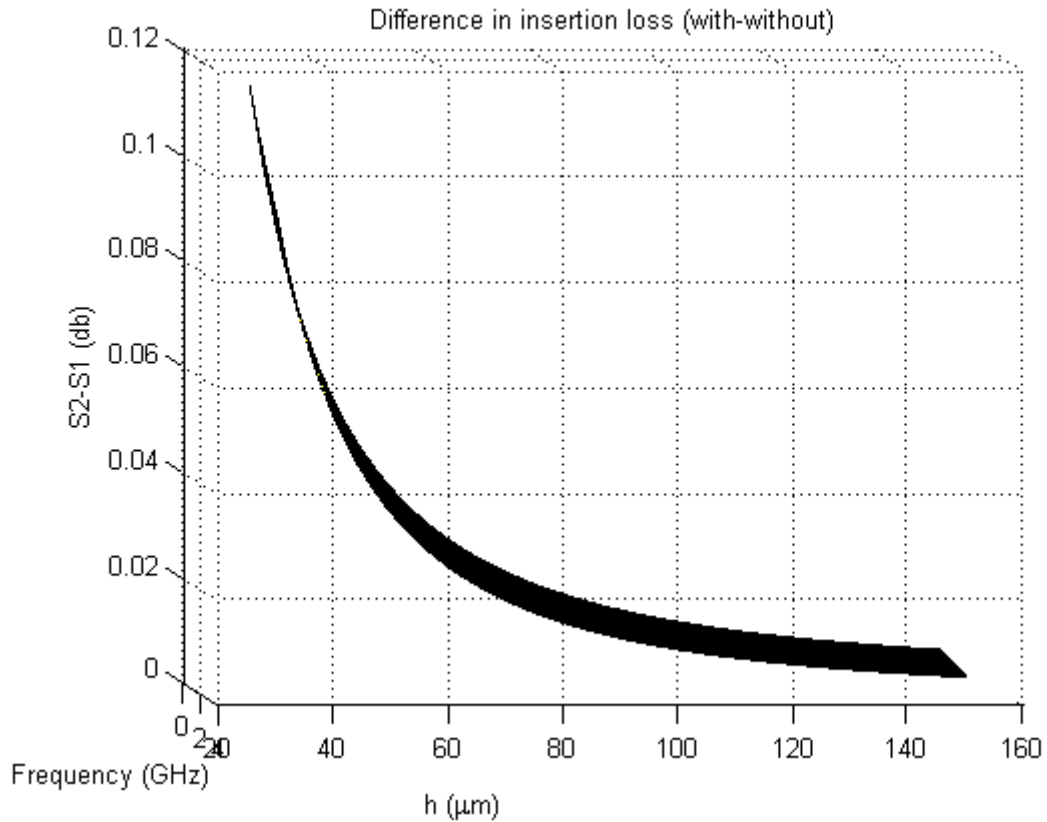


**Figure 7.33: Another view of the difference of the insertion loss with and without the WBC (sucrose/dextrose)**

All these results confirm the utility of using small channel height to increase the sensitivity of the measured insertion loss difference. It is not only the contribution of the dielectric constants of the cell and the media that needs to be considered, the dielectric losses are also important to consider in the single cell model under the overlapped parallel facing electrodes.

### **7.4.3 Single cell RF/Microwave measurements for cell characterization**

#### **7.4.3.1 Material and media preparation**

Cells need to be kept in a media for their survivability and good health within the measurement period of time. The two selected media are sucrose/dextrose and Glycerol. Sucrose/dextrose is a sugar based media having a dielectric constant close to the water at high frequencies. Glycerol, although sweet tasting, is a triglyceride based media that is soluble in water and has very low dielectric constant, close to ethanol's dielectric constant at high frequencies. Cells survive longer in sucrose/dextrose and can survive limited time only in Glycerol.

The details of the preparation of the sucrose/dextrose with different media conductivity values are already given in paragraph 7.2.2 .

For Glycerol, the material is acceptable to insure the viability of cells during the period of time required for the measurement. At high frequencies, the glycerol dielectric constant and dielectric loss are equal to about 6 and 4 respectively. The high contrast of dielectric properties between this media and cells increases the sensitivity of the insertion loss measurement. Trypsin is added to the Glycerol (Glycerol-Trypsin ratio 3.5:1) to obtain DC conductivity between 10 and 20 mS/m. This mixture gives a dielectric constant of about 18 and dielectric loss of 18. Trypsin helps also reducing the clustering of cells.

Next, cells are suspended in the prepared media and are injected through a syringe of 1ml with a flow set on the pump of about 0.5 ml/hm.

### 7.4.3.2 Single cell RF/Microwave measurement set-up

The insertion and return losses (amplitudes only) are measured with the network analyzer Agilent 8722ES given its high dynamic operating range. The power injected to any device under test (DUT) can be easily adjusted by the set-up of the network analyzer by adding internal analyzer attenuation in front of RF/Microwave internal source. Although relative measurements are performed with and without the cells in the media, the calibration of the network analyzer is required for two reasons: it helps removing the cross talks between port 1 and port 2 of the network analyzer, and it gives a good understanding of measurement results compared to the ones simulated and analytically modeled. Therefore, before starting the tests the network analyzer is calibrated for a wide frequency range from 1 to 12 GHz. The RF/Microwave power is set to less than 0 dBm. The frequency responses of insertion and return losses are saved as an Excel file through the Agilent 82357B USB/GPIB Interface.

The complete RF/Microwave measurement set-up for the first device is given in Figure 7.34.

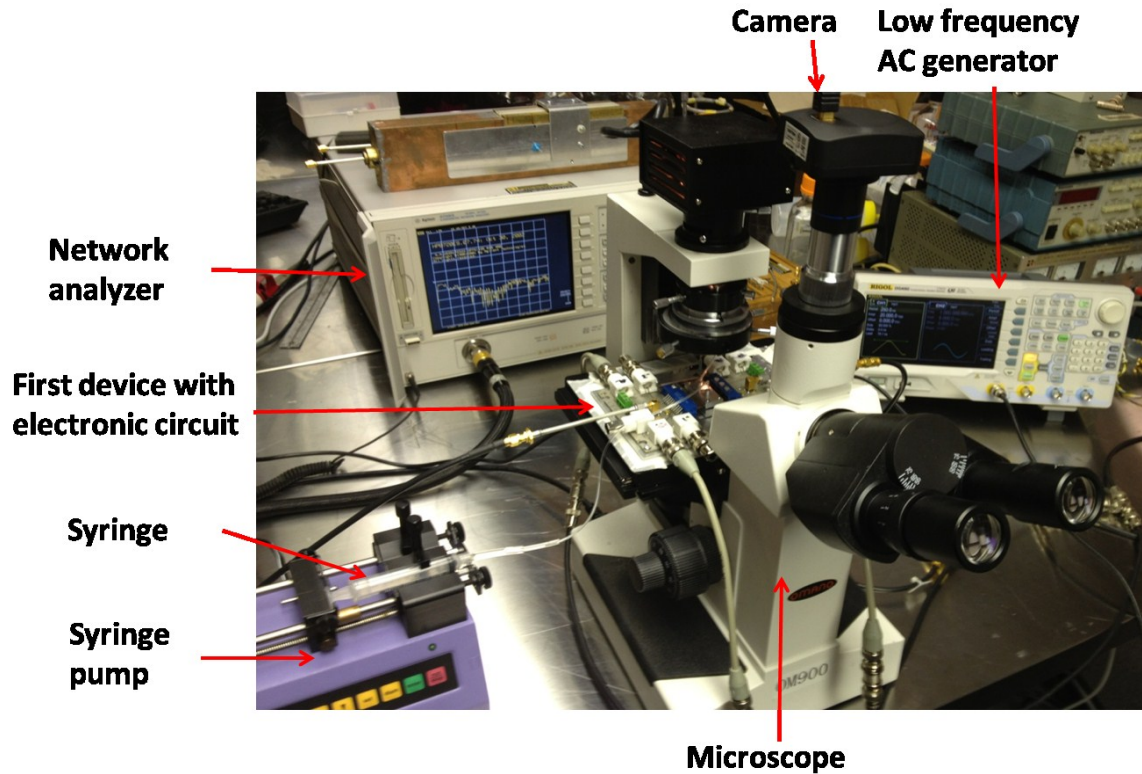


Figure 7.34: The complete RF/Microwave measurement set-up for the first device

The integrated microfluidic channel (first device) and the electronic circuit of Figure 5.13 are connected to the RF/Microwave network analyzer through the two SMA connectors. AC voltages are applied to the BNC connectors on the focusing electrodes with the appropriate amplitude and frequency determined from the cross frequency results of section 7.2. As for the second device, it is directly connected to the network analyzer.

The measurement set-up for the second device is given Figure 7.35.

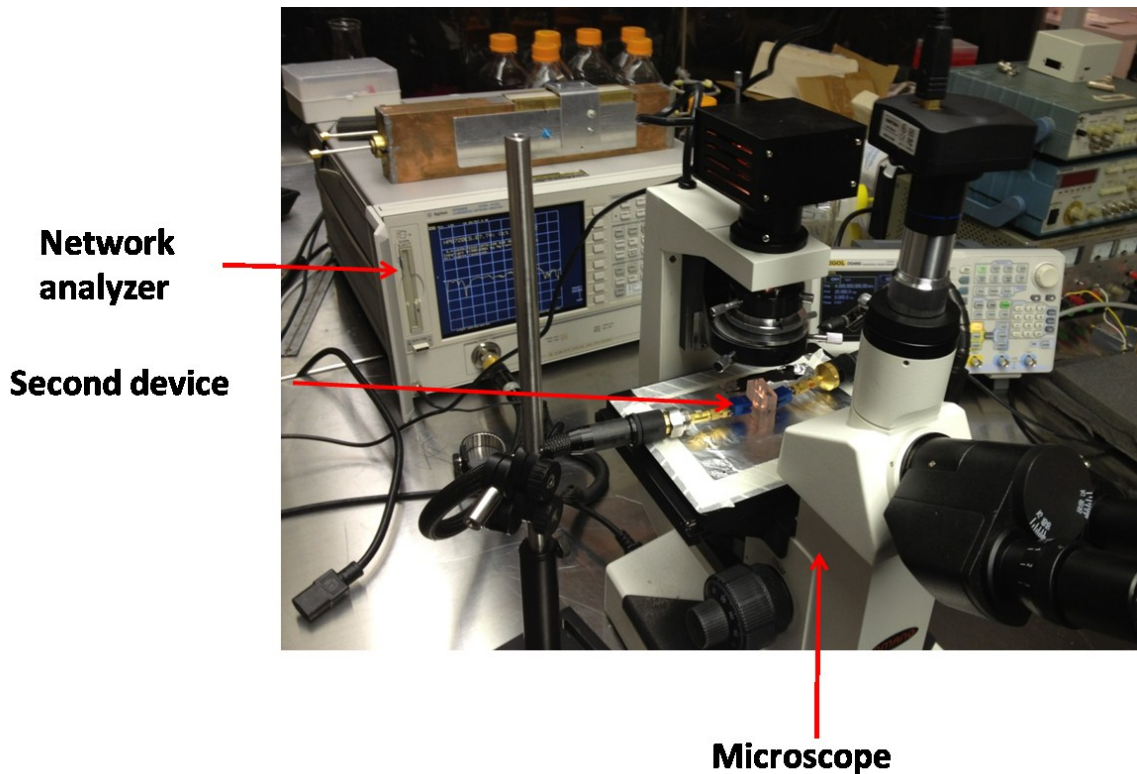


Figure 7.35: The complete RF/Microwave measurement set-up for the second device

### 7.4.3.3 Cells centering

In the first microfluidic device, when the cells are flown at very low velocity and the dielectrophoresis force dominates on the other forces, the cells are attracted or repelled from the centering electrodes. Negative DEP mechanism enables cell centering and directs the cells to the tips or RF/Microwave electrodes for high frequency measurement. These high frequency electrodes are also used simultaneously to detect and count cells passing through the microchannel.

In section 7.2 the WBCs - Jurkat, Clone E6-1 show always pDEP for all DC conductivities of the media and all low AC frequencies, whereas uveal melanoma cells (lines 92.1 and OCM) show negative and positive DEP effect determined by the applied low AC signal frequency.

Therefore with the presence of dielectrophoresis effect, when WBCs - Jurkat, Clone E6-1 arrive close to the focusing electrodes, they are attracted by these electrodes and they are not centered.

Bulk WBCs, uveal melanoma cell lines 92.1 and OCM suspended in 10 mS/m sucrose/dextrose are filled into syringes for injection into the first device microchannel and DEP measurements.

#### 7.4.3.3.1 WBC measurements

The suspended WBCs - Jurkat, Clone E6-1 are injected slowly into the microchannel and a 1 MHz AC signal at 20 Volts peak to peak is applied on the focusing electrodes. Figure 7.36 shows the pDEP effect on two types of focusing electrodes. The cells are gathered around the edges of these electrodes. Changing the frequency did not change the effect of pDEP. Nevertheless when the frequency is reduced to 10 KHz bubble creation through the water dissociation starts. Figure 7.37 shows the bubble at the center of the electrodes.

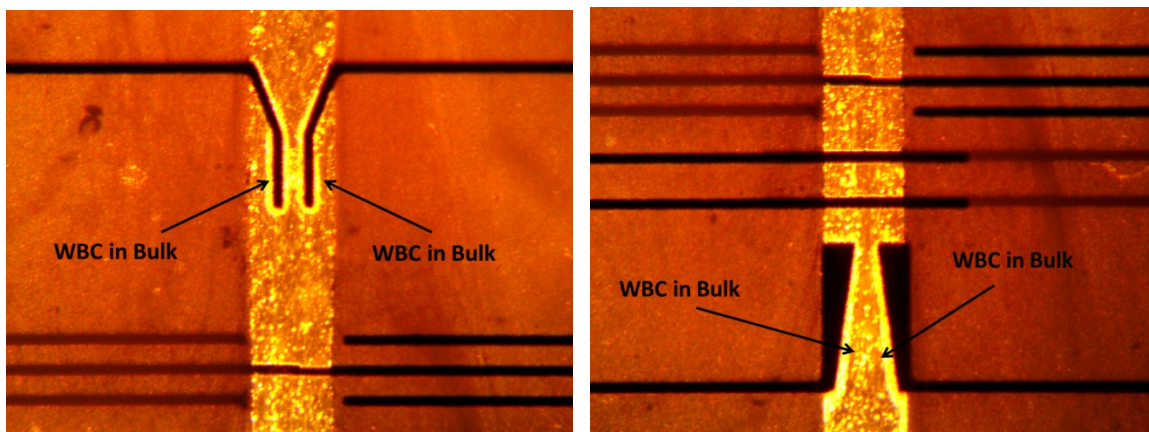


**Figure 7.36: pDEP is observed on bulk WBCs – Jurkat, Clone E6-1 attracted by the 2 types of focusing electrodes (Y shape and trapezoidal shape) within the microchannel. AC signal frequency is 1 MHz with amplitude of 20 Volts peak to peak**

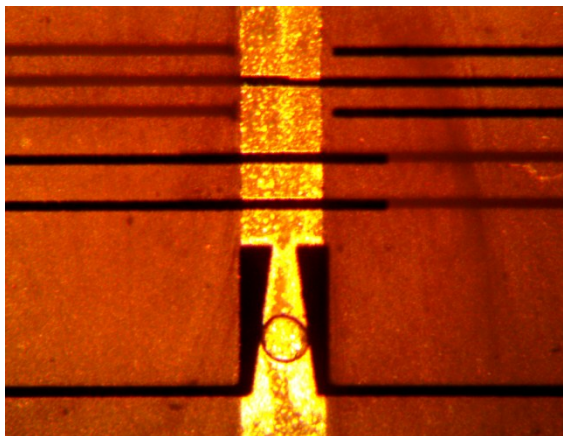


**Figure 7.37:** With a frequency of 10 KHz the WBCs – Jurkat, Clone E6-1 are still under pDEP but a bubble is created between the trapezoidal electrodes

Figure 7.38 shows the pDEP vanishing effect when the generator is turned off and cells are detached from the electrodes due to the absence of the DEP force. The cloud of WBC follows the flow direction, in this case downward. Reduction of the amplitude from 20 to 10 Volts peak to peak reduces the attraction force on the cells. With 20 Volts peak to peak, reducing the frequency from 1 MHz to 20 KHz also yields reduction in the attraction force of the cells by the electrodes.

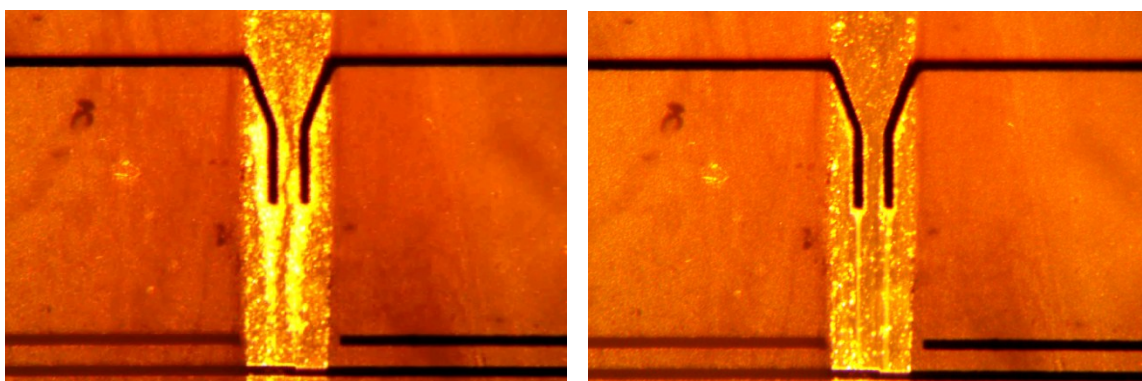


**Figure 7.38:** When the signal of the generator is turned off, WBCs – Jurkat, Clone E6-1 follow the flow of the media and the effect of pDEP is slowly vanishing. The 2 pictures show the evolution of the DEP vanishing effect with WBCs that are detached from the electrodes

#### 7.4.3.3.2 Uveal melanoma cell lines 92.1 measurements

The suspended uveal melanoma cells line 92.1 are injected slowly into the microchannel and a 1 MHz AC signal at 20 Volts peak to peak is applied on the focusing electrodes. Figure 7.39 shows the pDEP effect on the focusing electrodes. The cells are gathered around the edges of these electrodes. Figure 7.40 shows the nDEP effect when the frequency is changed from 1 MHz to 50 KHz. The four pictures show the movement evolution of the cell at the center of the channel.

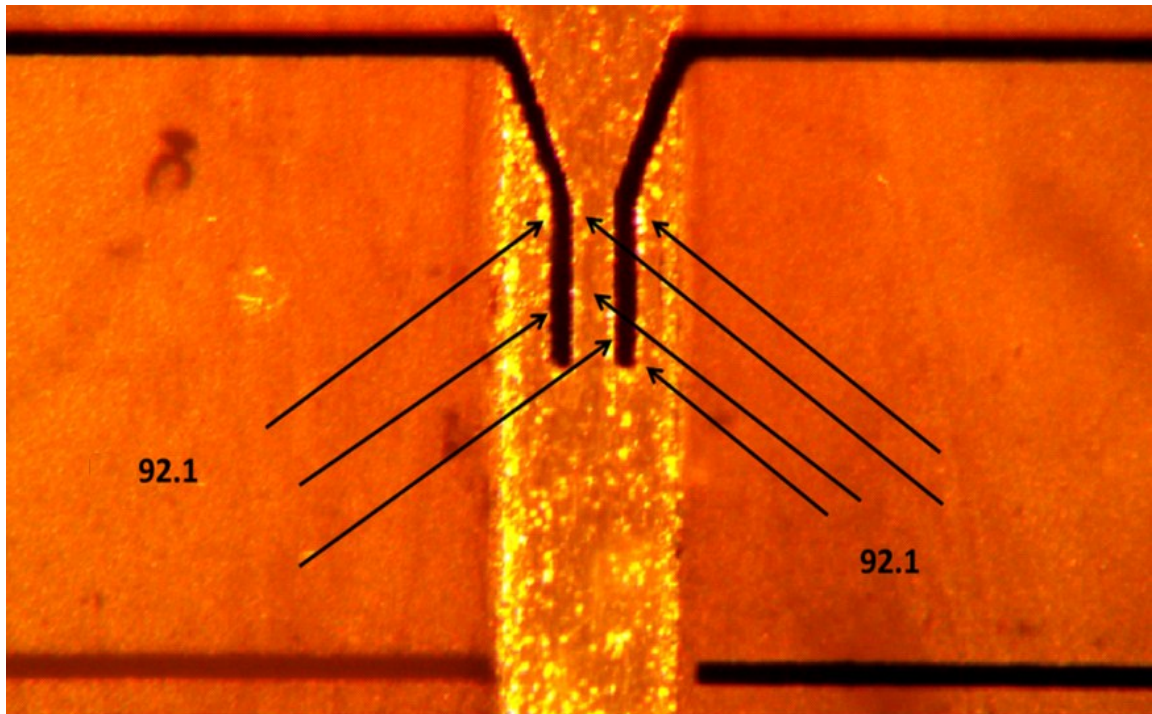


**Figure 7.39: pDEP is observed on uveal melanoma cells line 92.1 attracted by the focusing electrodes within the microchannel. AC signal frequency is 1 MHz with amplitude of 20 Volts peak to peak**

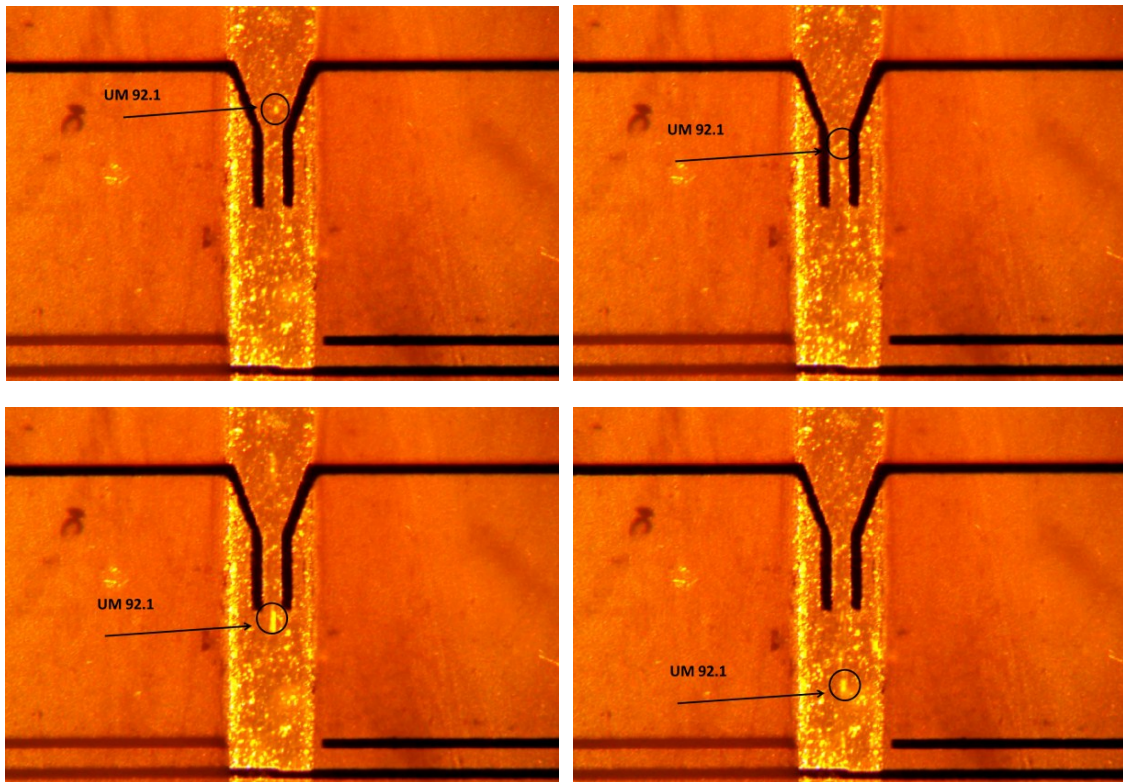


**Figure 7.40: nDEP is observed on uveal melanoma cells line 92.1 repulsed from the focusing electrodes and centered within the microchannel. AC signal frequency is 50 KHZ with amplitude of 20 Volts peak to peak. In the four pictures the movement of the 92.1 cell at the center is observed. As seen in these pictures, when the particle gets close to the center of the channel with a smaller electrodes gap, the velocity of the particle is higher and the clarity of the picture of the particle is reduced due to this higher speed effect**

### **7.4.3.3.3 Uveal melanoma cell lines OCM measurements**

The suspended uveal melanoma cells line OCM is injected slowly into the microchannel and a 1 MHz AC signal at 20 Volts peak to peak is applied on the focusing electrodes. Figure 7.41 shows the pDEP effect on the focusing electrodes. The cells are gathered around the edges of these electrodes. Figure 7.42 shows the nDEP effect when the frequency is changed from 1 MHz to 10 KHz. The two pictures show the movement evolution of the cell at the center of the channel.

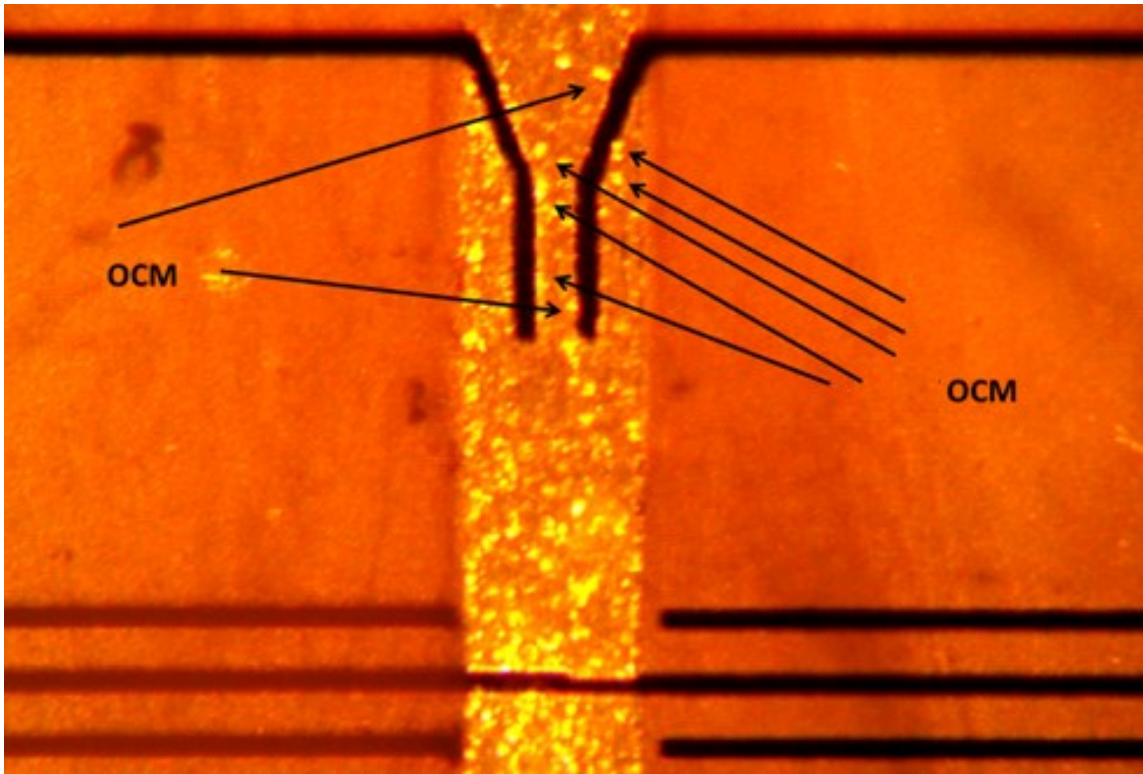


**Figure 7.41: pDEP is observed on uveal melanoma OCM cells attracted by the focusing electrodes within the microchannel. AC signal frequency is 1 MHz with amplitude of 20 Volts peak to peak**

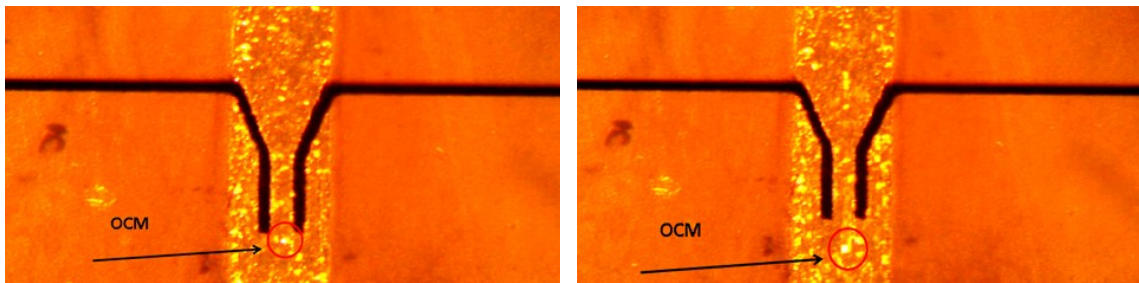


**Figure 7.42: nDEP is observed on uveal melanoma OCM cells repulsed from the focusing electrodes and centered within the microchannel. AC signal frequency is 10 KHZ with amplitude of 20 Volts peak to peak**

#### 7.4.3.4 Single cell RF/Microwave measurements

The analytical single model between two overlapped electrodes showed that for better sensitivity the height of the channel should be small. Therefore, the second device

is used to do the RF/Microwave measurements of characterization. For high frequency measurement response four parameters could be measured (insertion and return loss, amplitude and phase). Measurements show that the system is noise sensitive to the phase change even with just the movement of the media without the presence of the cell. Therefore phase variation information would be difficult to interpret at this moment and will be part of the future work. The amplitude responses of the insertion loss and the return loss are already evaluated with CPW numerical and analytical model with and without the particle. Hence, only the amplitudes of the insertion loss and return loss with and without cell are measured and are compared for differentiation.

Measurements of insertion losses and return losses are carried out with empty channel (air), with the media (Glycerol) and with the suspended single cell (92.1 and WBC - Jurkat, Clone E6-1). Since this device does not have focusing electrodes, the centering is controlled by the slow injection of cells in the channel and monitoring under the microscope the centering of cells.

Figure 7.43, Figure 7.44, Figure 7.45 and Figure 7.46 show the insertion losses of the channel response with air, with Glycerol and the suspended single cell of 92.1 and WBC - Jurkat, Clone E6-1 in Glycerol. The same measurements for the return losses are given in Figure 7.47, Figure 7.48 and Figure 7.49. These measurements are performed with a frequency swept from 1 to 12 GHz. Comparison between these curves are easier with reduced frequency range. Therefore, the curves of Figure 7.50, Figure 7.51, Figure 7.52, Figure 7.53, Figure 7.54, Figure 7.55 and Figure 7.56 are shown from 2 to 4.5 GHz.

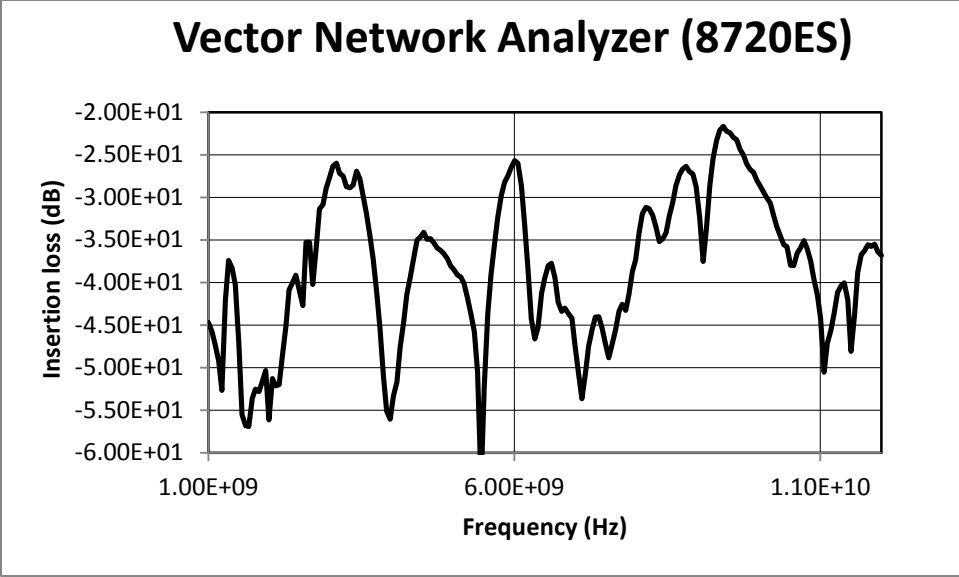


Figure 7.43: Insertion loss of the channel response filled with air (1 to 12 GHz)

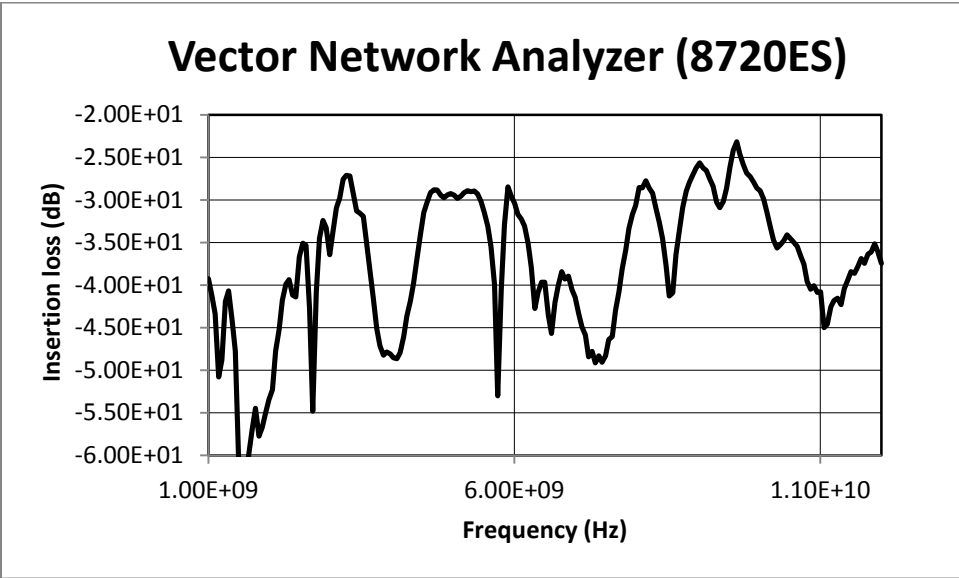
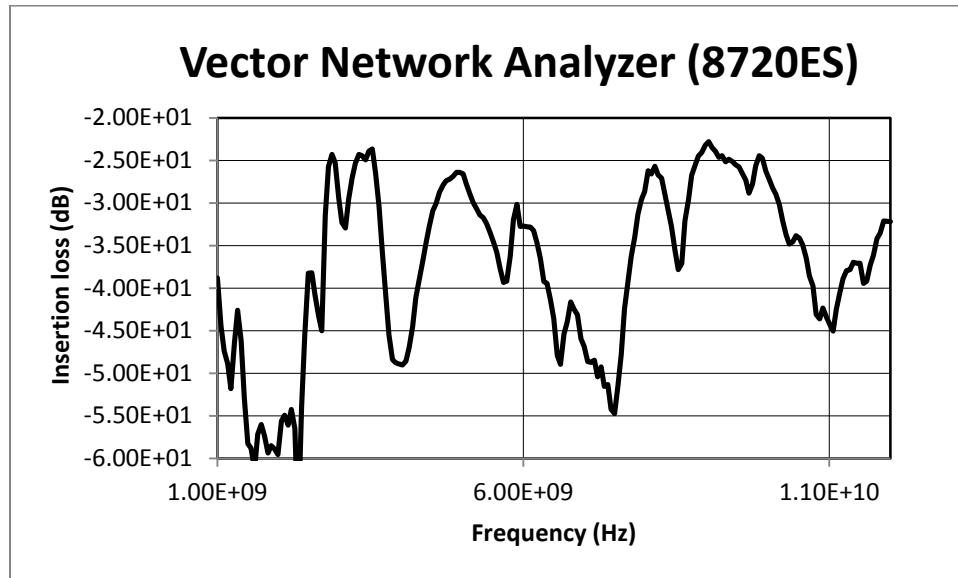


Figure 7.44: Insertion loss of the channel response filled with Glycerol (1 to 12 GHz)

The insertion loss response of the channel filled with air shows several peaks from 1 to 12 GHz. The high peaks have values between -22.5 to -25 dB. The low peaks have values as low as -60 dB. Similar behavior is observed when the channel is filled

with Glycerol, though the peak values are slightly changed. The overall response from 1 GHz to 12 GHz of these two insertion losses is different.



**Figure 7.45: Insertion loss of the channel response filled with suspended single 92.1 cell in Glycerol (1 to 12 GHz)**

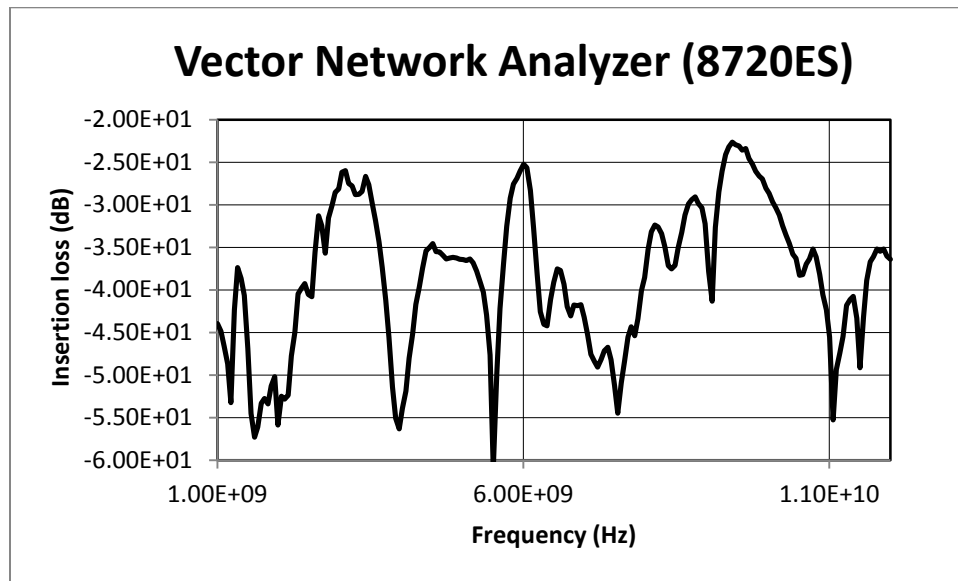


**Figure 7.46: Insertion loss of the channel response filled with suspended single WBC in Glycerol (1 to 12 GHz)**

The insertion loss response of the channel when a suspended 92.1cell passes through the interrogation point has high peaks values close to -25 dB. The low peaks

have values as low as -60 dB. Similar behavior is observed when a suspended WBC passes through the interrogation point, though the peak values are reduced by about 2 to 3 dB. This difference of 2 to 3 dB is validated when compared with the single cell analytical model of section 7.4.2 . Again, the overall response from 1 GHz to 12 GHz of these two insertion losses is different.

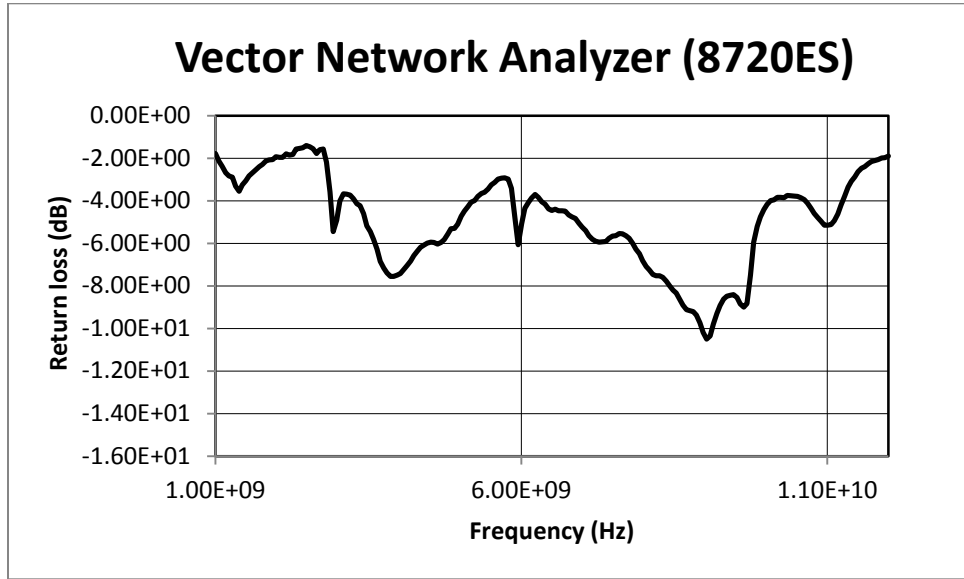


**Figure 7.47: Return loss of the channel response filled with air (1 to 12 GHz)**

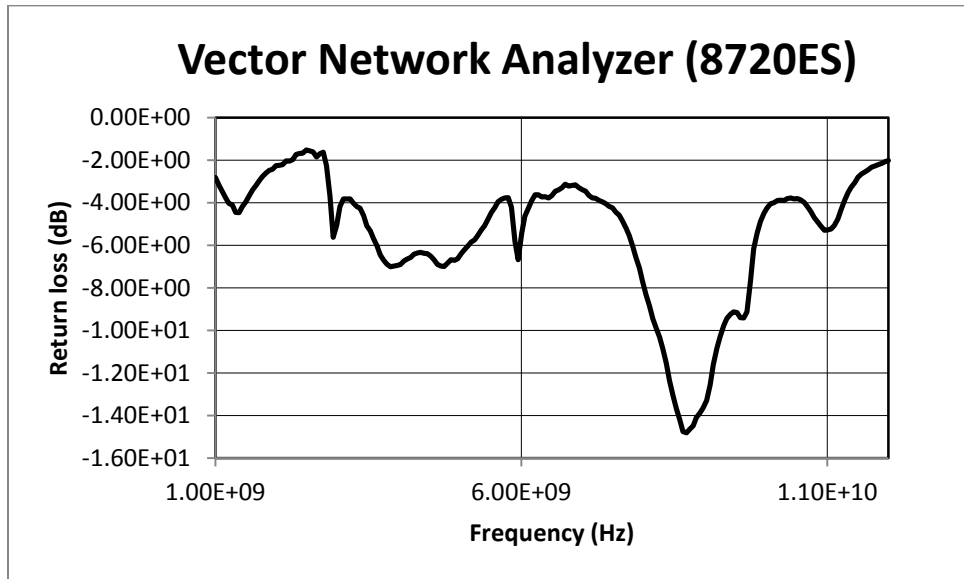


**Figure 7.48: Return loss of the channel response filled with Glycerol (1 to 12 GHz)**

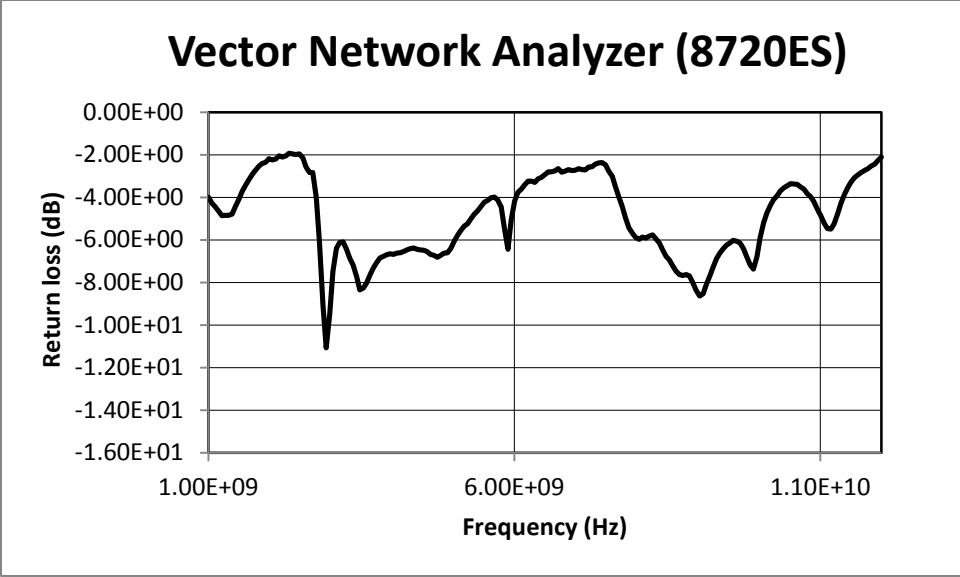


**Figure 7.49: Return loss of the channel response filled with suspended single 92.1 cell in Glycerol (1 to 12 GHz)**

The response of the return loss did not show a real appreciable change when channel is filled with air, Glycerol or suspended single cell. The observation is validated when compared with the single cell analytical model of section 7.4.2 .

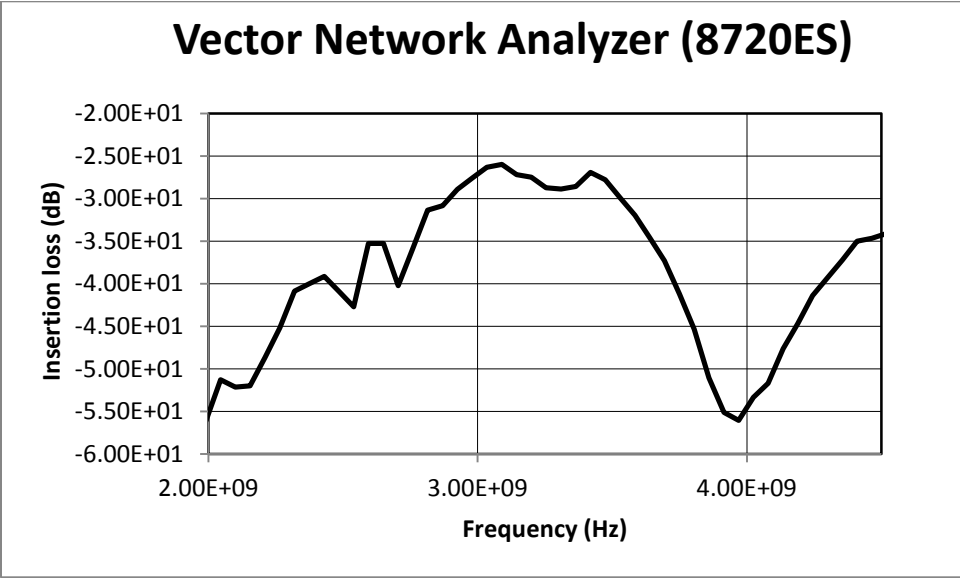


**Figure 7.50: Insertion loss of the channel response filled with air (2 to 4.5 GHz)**

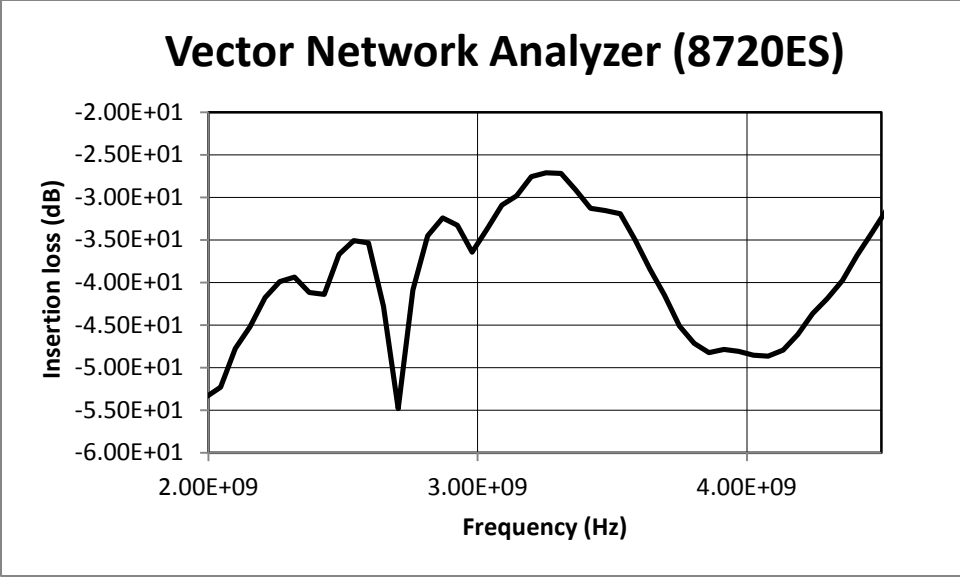


**Figure 7.51: Insertion loss of the channel response filled with Glycerol (2 to 4.5 GHz)**

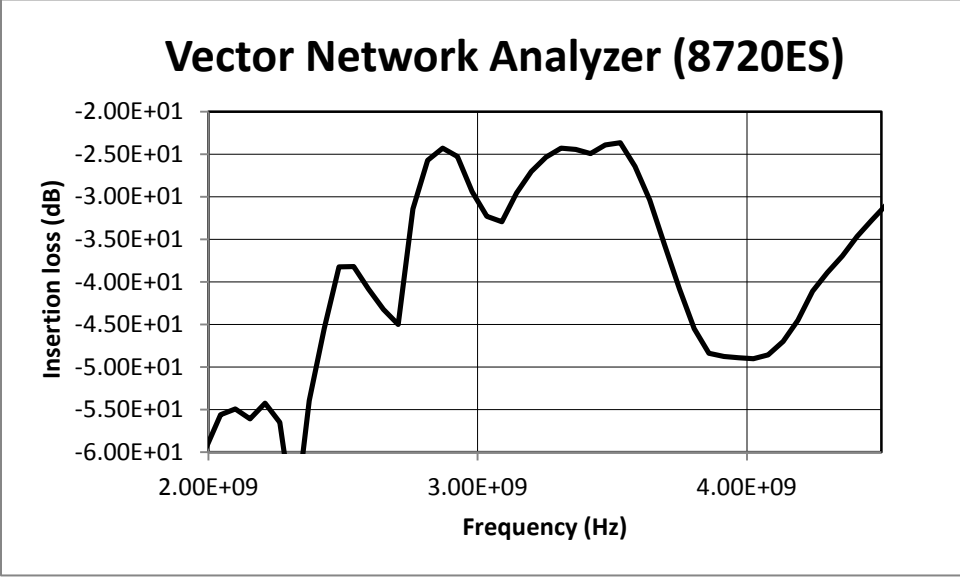


**Figure 7.52: Insertion loss of the channel response filled with suspended single 92.1 cell in Glycerol (2 to 4.5 GHz)**

When the insertion loss data are presented in much narrower frequency range between 2 to 4.5 GHz, the measurement variation is observed for each situation and the

data differences over this frequency range can be analyzed for further processing by signature comparison and differentiation.

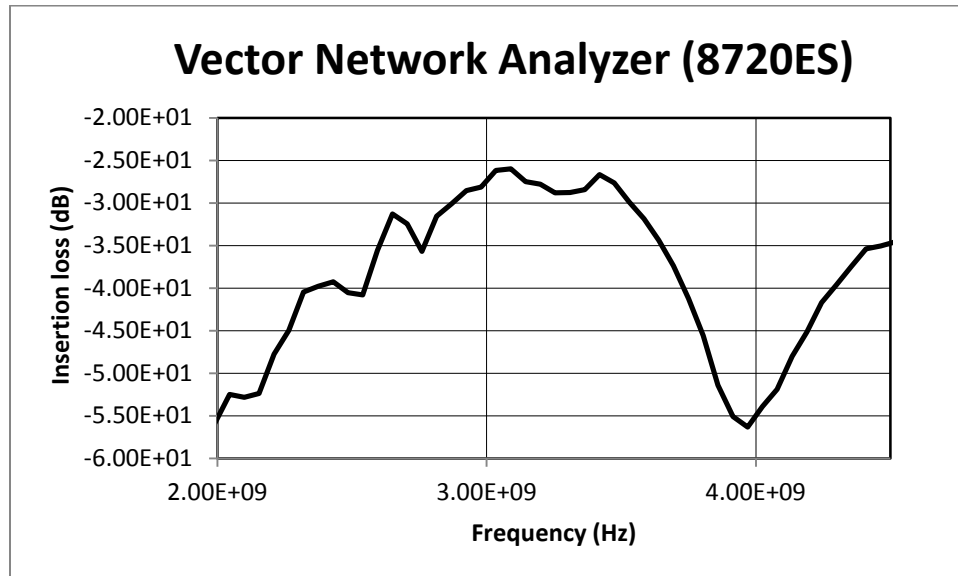


**Figure 7.53: Insertion loss of the channel response filled with suspended single WBC in Glycerol (2 to 4.5 GHz)**

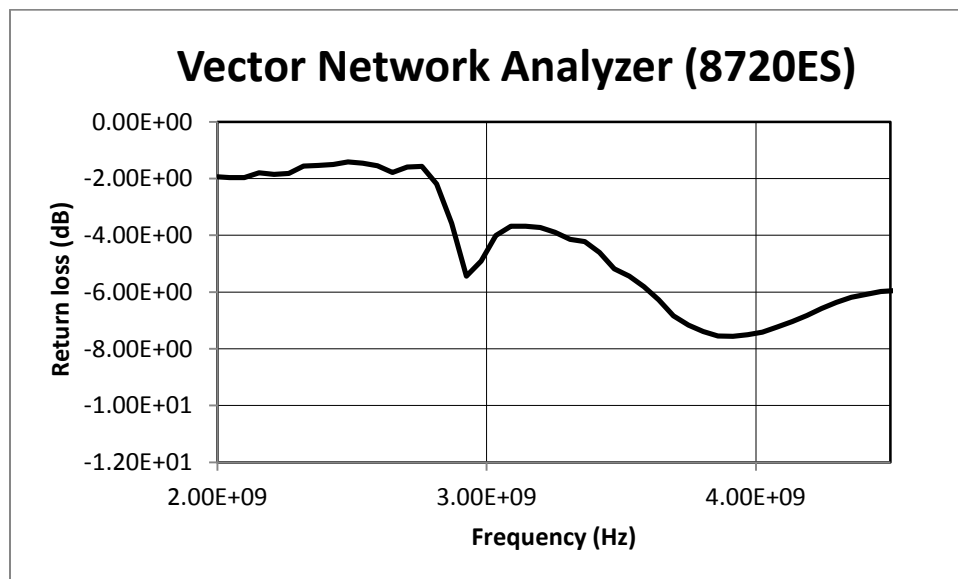


**Figure 7.54: Return loss of the channel response filled with air (2 to 4.5 GHz)**

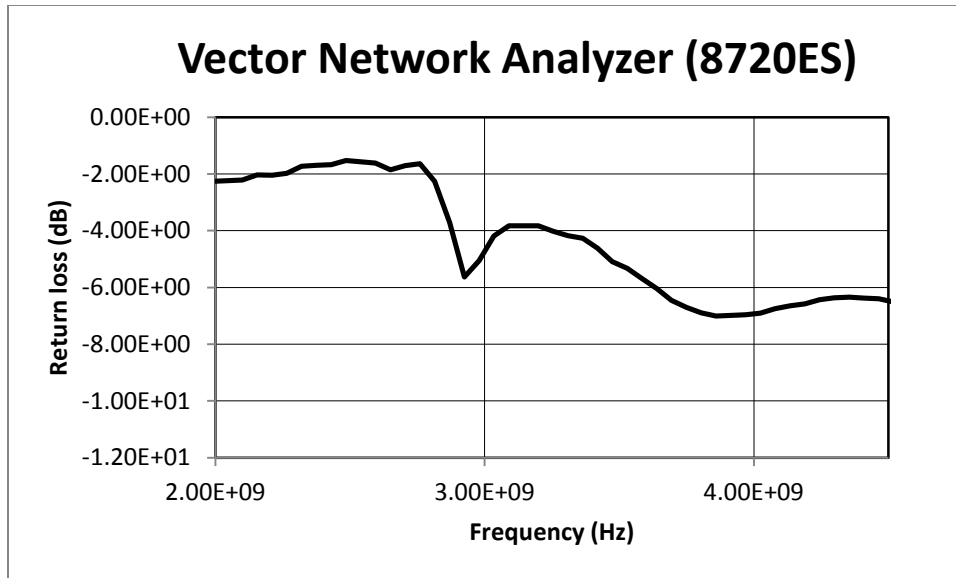


**Figure 7.55: Return loss of the channel response filled with Glycerol (2 to 4.5 GHz)**

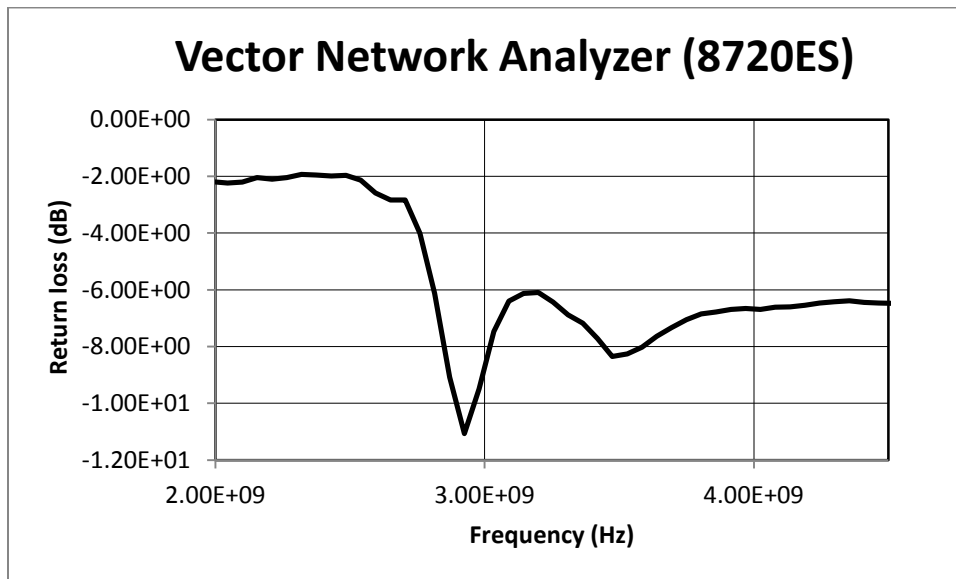
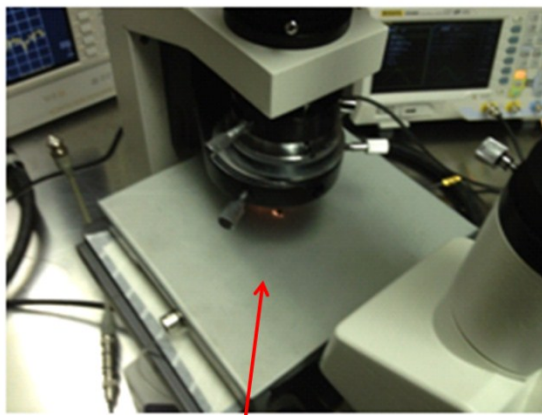


**Figure 7.56: Return loss of the channel response filled with suspended 92.1 cells in Glycerol (2 to 4.5 GHz)**

With the frequency range between 2 to 4.5 GHz, the return loss results are slightly different with the presence of the cell. This can be attributed to several reflections at different points of the microwave transmission lines.

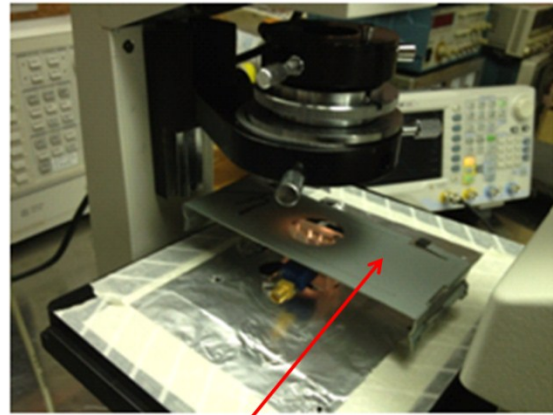
During the measurement both devices are covered with metallic enclosure to reduce the effect of noise injected from the external environment.

Figure 7.57 shows the two metallic enclosures covering the two devices. Since the second device is very fragile, its cover has a large opening to let the inlet and outlet tubing be connected with the device. For the first device only a small opening is required for microscope monitoring of the channel.



**Metallic enclosure for the first device**

(a)



**Metallic enclosure for the second device**

(b)

**Figure 7.57: The metallic enclosure for noise reduction over the first device (a) and the second device (b)**

#### 7.4.3.5 Challenges and discussion

The insertion loss responses for Glycerol media, single 92.1cell and single WBC (Figure 7.44, Figure 7.45 and Figure 7.46) show a big variation within the frequency range of 1 to 12 GHz. Insertion loss values vary from about -26 dB to as low as -60 dB. Several negative peaks suggest the presence of some type of resonance where the input RF/Microwave signal is completely blocked at these peak frequencies. The reason of

these high attenuations is difficult to interpret with the complexity of the micro device. Nevertheless at frequencies within the interested band of 2 to 4.5 GHz (cells were measured in this band of frequency for complex permittivity), the insertion loss results behave closely to the analytical models.

With the frequency range between 2 to 4.5 GHz, the return loss results are slightly different with the presence of the cell. This can be attributed to several reflections at different points of the microwave transmission lines.

Measurement results of Figure 7.55 (media) and Figure 7.56 (92.1) show that the return losses with and without cell (with cell or only with media) have the same type of response but are not identical. Similar return loss behavior is confirmed when compared to the simulated and analytical results. Nevertheless, the response does not show a smooth constant value as obtained by theoretical analysis. Drastic change of return loss value to about -10 dB is probably due to several reflections at the SMA connector interfaces, microchannel substrate interface and the impedance changes between each segment of CPW. This variation influences the insertion loss response since the insertion loss is also related to the mismatch losses.

The characterization of different cells (92.1 and WBC) enables insertion loss difference signature. Therefore to observe this differentiation signature, the insertion loss differences between media and single 92.1 cell, media and single WBC, and single 92.1 cell and single WBC are given in Figure 7.58, Figure 7.59 and Figure 7.60 respectively.

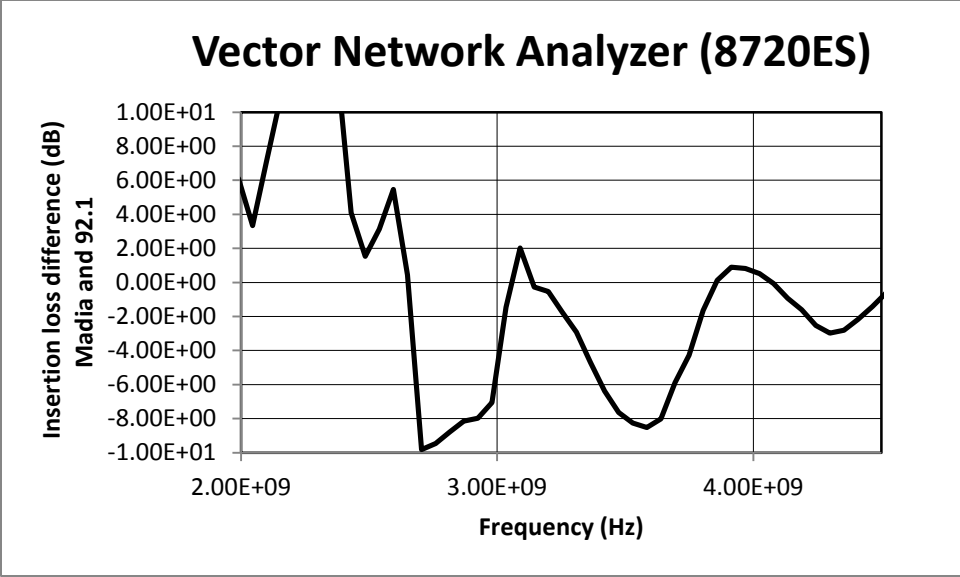


Figure 7.58: Insertion loss difference between media and single 92.1 cell (2 to 4.5 GHz)

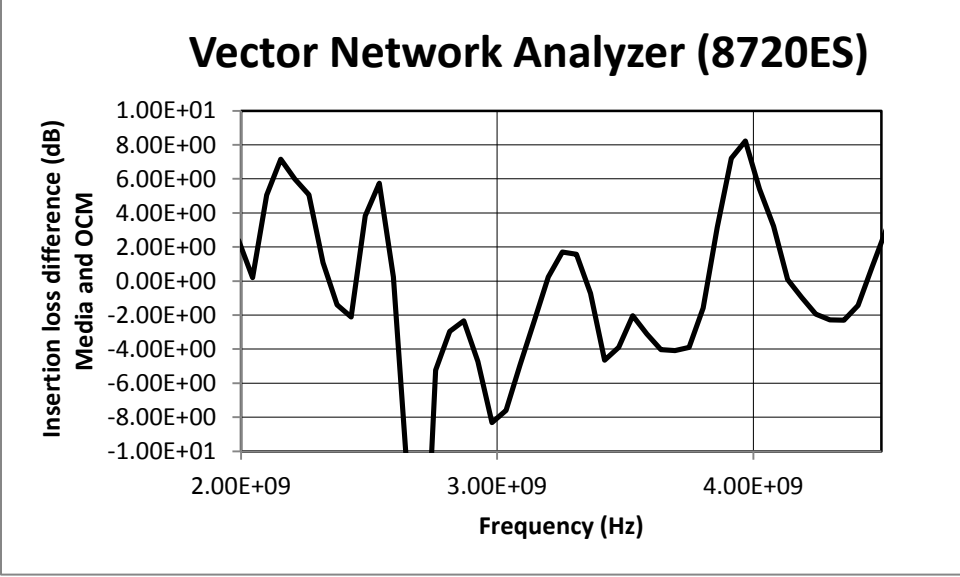
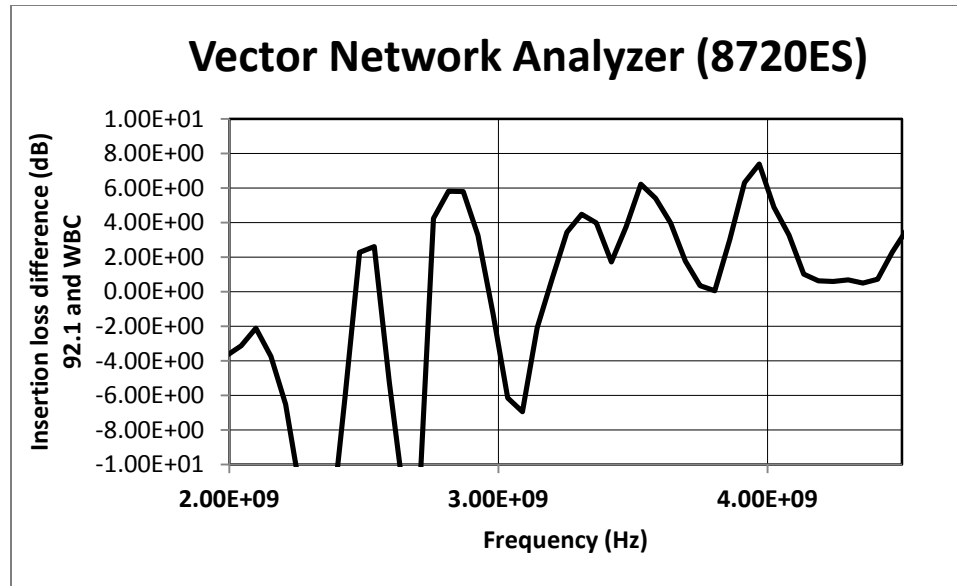


Figure 7.59: Insertion loss difference between media and single WBC (2 to 4.5 GHz)



**Figure 7.60: Insertion loss difference between single 92.1 cell and single WBC (2 to 4.5 GHz)**

These three signatures can be used to compare the type of the cell passing through the channel. For other type of cancers (MDA231, PC3 and Hela) tests can be repeated using the same technique and the associated signature differentiation can be obtained.

During the repetition of tests, variation in response was noticed. This variation is dependent with the movement of non-homogeneous fluid within the microchannel (containing micro impurities and other attached micro particles), and the presence of the unpredicted variation of the reflection response and the resonance effect of the insertion losses. Therefore, sometimes it is difficult to continuously validate one by one the signatures of all passing cells and identify the type of cancer present at the interrogation point. Moreover, after several experimentations and investigations, visual observation on the network analyzer showed a variation of insertion loss close to 1.5 dB for single 92.1 cell and close to 0.5 dB for single WBC. These observations are quite close to the analytical calculations. The analytical results and the experimental results suggest the

reduction in the channel height increasing the variation of the insertion loss with and without the cell, and hence increasing the sensitivity of the system.

## **7.5 Chapter summary**

In this chapter the cross frequency of different cancer cells suspended in sucrose/dextrose with different DC conductivities are found. The cross frequency determines the transition between nDEP to pDEP. WBC experiences only pDEP for DC conductivity of the media between 0 to 20 mS/m. For a conductivity of 10 mS/m, the lowest transition frequency from nDEP to pDEP was for the MDA231, followed by the RBC, OCM and 92.1 cells.

For cell detection and counting, an RF detection circuit is proposed and experimented. The main component of the circuit is a high frequency Schottky detector. The output of the RF/Microwave electrodes is used to detect the cells passing through the microchannel.

With the help of the dielectric property measurements (off line measurement) of different cancer cells, analytical models are created for 92.1 and WBC cells suspended in two media namely sucrose/dextrose and Glycerol. On line measurements are also performed by passing the suspended cells within the media into the center of the microchannel. Measurements of 92.1 and WBC are compared for signature identification. The signature is used to compare two different cells with different dielectric properties and different geometrical dimensions.

## **Chapter 8: General conclusions, Summary of contributions and Future Work**

### **8.1 General conclusions of the research study**

The main objective of this research is to investigate the feasibility of a new approach and of a measurement technique to characterize cancer cells through non-chemical destructive assays. Several characterization techniques using micro devices are investigated by other authors and researchers. Most of these techniques use low frequency characterization. At these frequencies it is quite difficult to discriminate between different types and sizes of bio particles and internal cell structures of the same type since the properties of individual cell is masked by internal parameters population variance. This thesis presents an investigation on a measurement technique based on RF/Microwave characterization of different cancer circulating tumor cells in-vitro. With microwave frequencies, the interferences and variability are avoided and sample preparation is simple and without the need of any tag or marker.

With RF power level of 20 dBm in the frequency range from 1 to 3 GHz injected into the test apparatus containing uveal melanoma cells, a proliferation reduction of 2 to 9 % is observed on uveal melanoma cell line 92.1 following a relatively specific signature.

When low frequency AC signals are injected on the trapezoidal and Y shaped electrodes (for the generation of non-uniform electric field) of the designed microfluidic device, DEP forces are observed on cells. The cross frequency defining the passage from nDEP to pDEP for different cancer cells is in the range of 12 to 90 KHz with media

conductivities from 5 to 20 mS/m. For WBCs only pDEP is observed preventing cells from being centered with these electrodes.

This device fabricated by simple technique of silicone serigraphy has a channel cross section of 300  $\mu\text{m}$  by 50  $\mu\text{m}$ . RF/Microwave electrodes are also built in it to characterize single cancer cell by comparing the insertion loss with and without specific cell.

Characterization of dielectric properties of different cancer cells and WBC from 2 to 4.35 GHz showed dielectric constants between 42 and 68 and dielectric losses between 12 and 22. High frequency WR284 resonant cavity is designed and fabricated to measure with precision the complex permittivity of different cancer cells. In the frequency band of this cavity, complex permittivity of five different discrete frequencies is measured from 2 to 4.3 GHz. The measurement system being automated, a continuous measurement of the complex permittivity with time gave important information about the dielectric change of cells with time.

Using the information on dielectric property and a single cell under overlapped parallel facing electrodes, single cell models (capacitance in parallel with resistance) are generated. An interesting conclusion is drawn with the models extracted regarding the sensitivity of the device: for 92.1 cell, with about 20  $\mu\text{m}$  of diameter, the sensitivity to the insertion loss variation (equivalent to the signature) increases exponentially when the height of the channel is reduced to 30  $\mu\text{m}$  and less. The fabrication of channels having height less than 30  $\mu\text{m}$  using serigraphy technique is quite challenging and clustering of cells needs to be considered to avoid channel clogging. Therefore other techniques are to be used for channel creation with hermetic characteristics such as SU-8 technique.

Some practical observation could be highlighted regarding channel cleaning. In fact, after hundred times of injecting suspended particle with different sizes and different characteristics into the microchannel, it was impossible to remove some particles deposited and adhered to the surface of the substrates and electrodes. Pressure cleaning, with high pressure flow, water and alcohol from syringes into the inlet of the microchannel, did not eliminate 100 % the traces of the remaining particles. Bleach could have been an efficient solution but with the drawback of affecting the next measurements if sub-pockets of bleach remained in the microchannel. More effective techniques and processes that would yield low cost such devices would easily overcome this inconvenience.

## **8.2 Summary of contributions**

The contribution of this research is exposed by several scientific accomplishments as:

- Analytical and numerical studies of the transmission lines and impedance of single model of particles between two parallel facing electrodes
- Design and fabrication of the required devices satisfying the experimentation needs using the available technologies
- Performing of the experimental measurements to demonstrate the validity of the proposed RF/Microwave solution and to compare it with analytical solutions and models.

A device is designed, fabricated and measurements are carried out to assess the appropriate microwave power and frequency bandwidth to be applied on the cells during the characterization step.

Cell characterization phase requires centering of cells by electrodes of appropriate geometry and the selection of the frequency to be applied on the focusing electrodes. Therefore a thorough analytical study determined the exact DEP force distribution within a channel ensuring the DEP mechanism occurrence at any point.

Different types of cancer cells were measured at low frequency and the associated cross frequencies were found.

For single cell characterization, a system for the evaluation of the complex permittivity at high frequencies in the S-band was designed, fabricated and the measurements carried out. The system consists of resonant cavity automatically controlled by an original developed program. This software tool enables the assessment of complex permittivity of cells versus time.

The complex permittivity values of cells and media gathered by the cavity measurements between 2 to 4.5 GHz are injected into the single cell models created for overlapped parallel facing electrodes with and without a particle.

Several other devices were also designed and fabricated to detect and characterize single cell in the microchannel. Measurements with these devices enabled the characterization of the cells by signature identification with and without the particles.

Finally, this investigation asserted that the cells can be characterized with RF/microwave technique using the signature obtained when the particle is present or not.

The contributions highlighted in the last section satisfied the objectives as defined at the beginning of this research. The future work identified in the next section can be continued and extended in the following directions.

### **8.3 Areas of future research work**

For future research work four subdomains could be considered:

- Signature identification of other type of cancer cells and correlations among them
- Microchannel fabrication with other substrates other gasket materials and other electrode geometric dimensions
- Integration of the microfluidic device with the measuring devices
- Automatic system design to control the measurement trigger time when cell passes under the RF/Microwave measurement electrodes, automatic acquisition of all signatures, and signal processing with different algorithm for exact identification and differentiation.

This research was concentrated on different type of cancer cell evaluation. Nevertheless, the characterization for signature identification was performed only on human uveal melanoma cell line 92.1 and WBCs - Jurkat, Clone E6-1. The next step would be the repetition of these tests for sensitivity and specificity and the experimentation on the other type of cancer cells such as prostate cancer cell line PC3, Hela human cervical cancer cell and breast cancer cell line MDA231 and others.

A new design for microfluidic device with a polymer substrate such as cyclic olefin copolymer can be a good alternative that will enable machining of the microfluidic

chip and shape the substrate to the desired dimension and geometry. The microchannel might be made from SU-8 modified material or polyimide. The sealing of the two substrates is challenging to ensure hermetic sealing of the microchannel. Different dimensions and shapes for the parallel facing electrodes could be used for modeling study of the length and the width of the overlapping electrodes.

Complex permittivity measurement at X-band (from about 6.5 to 12 GHz) and higher bands could be carried out to model the single cell between parallel facing electrodes at higher frequencies. These measurements could suggest creating micro devices for much higher frequencies close to the millimeter waves.

Another technology using non-transparent substrate material can be used to create micro channels. The Low Temperature Co-fired Ceramic (LTTC) process is a serigraphy process that is used for high frequency applications. The advantage of this process is its capability to create several layers of ceramic where micro channels with different cross section areas can be made and each could be used for different cell size sorting and characterization. The same RF/Microwave electrodes for characterization can be used for different micro channels using multiplexing techniques through MEMS RF switches. The process of LTTC reduces the microfluidic device size and cost for high volume production, although Bio-compatibility remains an issue. Moreover, the integration of RF/Microwave components is easy to be carried out along with via holes connection from one layer to another. The drawback of this process is the non-transparent ceramic material that could not allow the visual observation of the microchannel under the microscope. In the research stage of such a project, visualization of the cells in the channel is essential. Therefore LTTC can be used once the cell characterization

technique, measurement protocols and the signature results are well established. It is also imperative to have a reliable and robust LTTC process available.

The microfluidic device is surrounded by different RF/Microwave equipment and components. For example the network analyzer is costly equipment and a good approach is to integrate all possible components and equipment together. The technology of Microwave Monolithic Integrated Circuits (MMIC) enables the integration of several components. High frequency voltage controlled oscillator, couplers, attenuators, switches and other components can be integrated in MMIC yielding a chip of very small size. This chip could be easily integrated to the microchannel made by LTTC or another process such as polymer material. Once the frequencies, the power, the detection range and the data processing algorithm established, an integrated chip could be created to perform the above detection and the large pieces of equipment would not be any more necessary at that stage. Moreover, the integration of the chip will improve the return loss and insertion loss responses, increase the robustness of the device and the reliability of the tests by removing noise sources from the system.

The acquisition of measurement results carried out manually during this research. The output signal obtained from the output RF/Microwave detector can be processed, amplified, digitized and sent to the triggering input of the network analyzer. Therefore when a cell is detected, the triggering mechanism control initiates the measurement of the network analyzer. The results for each measurement can be massaged and processed for signature identification and differentiation through an algorithm that can identify and differentiate the cell type from another.

# Appendix A

## License agreement between Vahé Nerguizian and the editors or authors to use figures in the thesis.

- **For Figures 2.1 and 2.2**

This is a License Agreement between Vahe Nerguizian ("You") and Elsevier ("Elsevier") provided by Copyright Clearance Center ("CCC"). The license consists of your order details, the terms and conditions provided by Elsevier, and the payment terms and conditions.

All payments must be made in full to CCC. For payment instructions, please see information listed at the bottom of this form.

Supplier Elsevier Limited

The Boulevard, Langford Lane

Kidlington, Oxford, OX5 1GB, UK

Registered Company

Number 1982084

Customer name Vahe Nerguizian

Customer address 1100 Notre Dame West

Montreal, QC H3C1K3

License number 2826080740319

License date Jan 11, 2012

Licensed content publisher Elsevier

Licensed content publication Biosensors and Bioelectronics

Licensed content title High throughput particle analysis: Combining dielectrophoretic particle focussing with confocal optical detection

Licensed content author David Holmes, Hywel Morgan, Nicolas G. Green

Licensed content date 15 February 2006

Licensed content volume Number 21

Licensed content issue Number 8

Number of pages 10

Start Page 1621

End Page 1630

Type of Use reuse in a thesis/dissertation

Portion figures/tables/illustrations

Number of figures/tables/illustrations 2

Format both print and electronic

Are you the author of this Elsevier article? No

Will you be translating? No

Order reference number

Title of your thesis/dissertation Non-Destructive Bio-Assay of Single Living Cell

Expected completion date Apr 2012

Estimated size (number of pages) 200

Elsevier VAT number GB 494 6272 12

Permissions price 0.00 USD

VAT/Local Sales Tax 0.0 USD / 0.0 GBP

Total 0.00 USD

- **For Figures 2.3 and 2.4**

This is a License Agreement between Vahe Nerguizian ("You") and John Wiley and Sons ("John Wiley and Sons"). The license consists of your order details, the terms and conditions provided by John Wiley and Sons, and the payment terms and conditions.

Get the printable license.

License Number 2826090136970

License date Jan 11, 2012

Licensed content publisher John Wiley and Sons

Licensed content publication Cytometry Part A

Licensed content title Impedance spectroscopy flow cytometry: On-chip label-free cell differentiation

Licensed content author Karen Cheung,Shady Gawad,Philippe Renaud  
Licensed content date Jun 1, 2005  
Start page 124  
End page 132  
Type of use Dissertation/Thesis  
Requestor type University/Academic  
Format Print and electronic  
Portion Figure/table  
Number of  
figures/tables 1  
Original Wiley  
figure/table number(s) Figure 2  
Will you be translating? No  
Order reference number  
Total 0.00 USD

- **For Figure 2.5**

This is a License Agreement between Vahe Nerguizian ("You") and Springer ("Springer"). The license consists of your order details, the terms and conditions provided by Springer, and the payment terms and conditions.

Get the printable license.

License Number 2826081269629

License date Jan 11, 2012

Licensed content publisher Springer

Licensed content publication Biomedical Microdevices

Licensed content title Microfluidic device for cell capture and impedance measurement

Licensed content author Ling-Sheng Jang

Licensed content date Oct 1, 2007

Volume number 9

Issue number 5

Type of Use Thesis/Dissertation

Portion Figures

Author of this Springer article No

Title of your thesis / dissertation Non-Destructive Bio-Assay of Single Living Cell

Expected completion date Apr 2012

Estimated size(pages) 200

Total 0.00 USD

- **For Figure 3.1**

This is a License Agreement between Vahe Nerguizian ("You") and Springer ("Springer"). The license consists of your order details, the terms and conditions provided by Springer, and the payment terms and conditions.

Get the printable license.

License Number 2826100033289

License date Jan 11, 2012

Licensed content publisher Springer

Licensed content publication Springer eBook

Licensed content title Dielectrophoretic Traps for Cell Manipulation

Licensed content author Joel Voldman

Licensed content date Jan 1, 2007

Type of Use Thesis/Dissertation

Portion Figures

Author of this Springer article No

Title of your thesis /dissertation Non-Destructive Bio-Assay of Single Living Cell

Expected completion date Apr 2012

Estimated size(pages) 200

Total 0.00 USD

- **For Figure 3.2**

This is a License Agreement between Vahe Nerguizian ("You") and Elsevier ("Elsevier"). The license consists of your order details, the terms and conditions provided by Elsevier, and the payment terms

and conditions.  
Get the printable license.  
License Number 2826250841748  
License date Jan 11, 2012  
Licensed content publisher Elsevier  
Licensed content publication Sensors and Actuators A: Physical  
Licensed content title A continuous cell separation chip using hydrodynamic dielectrophoresis (DEP) process  
Licensed content author Il Doh,Young-Ho Cho  
Licensed content date 31 May 2005  
Licensed content volume number 121  
Licensed content issue number 1  
Number of pages 7  
Type of Use reuse in a thesis/dissertation  
Portion figures/tables/illustrations  
Number of figures/tables/illustrations 1  
Format both print and electronic  
Are you the author of this Elsevier article? No  
Will you be translating? No  
Order reference number  
Title of your thesis/dissertation Non-Destructive Bio-Assay of Single Living Cell  
Expected completion date Apr 2012  
Estimated size (number of pages) 200  
Elsevier VAT number GB 494 6272 12  
Permissions price 0.00 USD  
VAT/Local Sales Tax 0.0 USD / 0.0 GBP  
Total 0.00 USD

- **For Figure 3.3**

Adapted from Kua et al 2005 [130]

- **For Figures 3.4 and 3.6**

Bonjour,  
oui vous pouvez utiliser les figures 2.1 et 2.2 de ma thèse.  
bien sûr qu'une référence appropriée à ce travail serait appréciée.  
je vous souhaite bon plaisir pour la finalisation de votre thèse.  
cordialement  
nicolas

Bonjour,  
Je vous envoie ce courriel afin de pouvoir prendre la permission de pouvoir utiliser les figures 2.1 et 2.2 de votre thèse (THÈSE NO 4099 (2008)).  
En fait j'aimerais pouvoir les utiliser dans ma thèse. Je complète dans 2 mois mon PhD à temps partiel à l'Université Concordia à Montréal et le titre de ma thèse est ' Non-Destructive Bio-Assay of Single Living Cell'.  
Dans l'attente de votre réponse, mes salutations.  
Professeur Vahé Nerguizian

- **For Figure 3.5**

Good morning Dr. Alazzam,

I am sending you this e-mail in order to get the permission to use the figure 1.3 of your thesis titled Hybrid Flow through Microchannels for Blood Cell Separation.  
In fact I am going to use it in my thesis titled Non-Destructive Bio-Assay of Single Living Cell  
Waiting for your positive response,  
Good day.  
Professor Vahé Nerguizian

Dear Vahé

You have my permission to use the figure in your thesis. Please add my reference at the end of your thesis.

Sincerely,  
Anas Alazzam

- **For Figure 3.13**

Licensed content  
publisher  
Elsevier  
Licensed content  
publication  
Measurement  
Licensed content title Measurements of microwave dielectric properties by an amended cavity perturbation technique  
Licensed content author Jyh Sheen  
Licensed content date January 2009  
Licensed content volume  
number  
42  
Licensed content issue  
number  
1  
Number of pages 5  
Type of Use reuse in a thesis/dissertation  
Portion figures/tables/illustrations  
Number of  
figures/tables/illustrations  
1  
Format both print and electronic  
Are you the author of this  
Elsevier article?  
No  
Will you be translating? No  
Order reference number  
Title of your  
thesis/dissertation  
Non-Destructive Bio-Assay of Single Living Cell  
Expected completion date Apr 2012  
Estimated size (number  
of pages)  
200  
Elsevier VAT number GB 494 6272 12  
Permissions price 0.00 USD  
VAT/Local Sales Tax 0.00 USD / 0.00 GBP  
Total 0.00 USD

## **Appendix B**

### **The manuscripts of accepted and to be submitted articles and a summary description of these articles**

The candidate presented a poster in May 2009 at the ARVO (The Association for Research in Vision and Ophthalmology) conference in Fort Lauderdale, showing in vitro the effect of RF/Microwave energy on uveal melanoma cells. Measurements were completed to evaluate the proliferation of the cancer cells after the exposure to RF signal.

The candidate presented another paper as an extension on the same subject in July 2009 in New York City at the AMWC (Armenian Medical World Congress) congress. New results were presented in this paper.

The candidate presented a poster in June 2008 at the ASME Summer Bioengineering Conference (SBC) in Marco Island, Florida. The poster investigated the evaporation cycle and duration of the small size liquid bridges. During experimentation, the evaporation is arrested and the thermodynamic equilibrium is maintained during the reaction between the biochemical marker and its analyte.

A paper was presented at the Microsystems and Nanoelectronics Research Conference (MNRC) in October 2008 in Ottawa. It described a real-time continuous dielectrophoretic separation of malignant cells.

In October 2009, a paper on the finite element analysis (simulation) on RF radiation structure on uveal melanoma cells was presented at COMSOL conference in Boston.

The summary of the titles of all these 5 conference papers and posters are:

- a. V. Nerguizian, A. Dulipovici, D. Abourbih, S. Maloney, S. Bakalian, I. Stiharu and M.N. Burnier, Jr., "The Effect of Non Thermal radio Frequency Radiation on Uveal Melanoma Cells". ARVO2009: E-Abstract 3375, May 3-7, 2009, Fort Lauderdale, Florida, USA.
- b. V. Nerguizian, S. Bakalian, I. Stiharu and M.N. Burnier, Jr., "The Effect of Low Power Microwave Frequencies on Uveal Melanoma Cells", AAHPO-AMWC 2009, 1-4 July 2009, New York, NY, USA.
- c. Dacian Roman, Vahé Nerguizian and Ion Stiharu, "Droplet evaporation in capillary bridges", Proceedings of the ASME 2008 Summer Bioengineering Conference (SBC2008), June 25-29, 2008, Marco Island, Florida, USA.
- d. Anas Alazzam, Dacian Roman, Vahé Nerguizian, Ion Stiharu, Rama Bhat, Amber Yasmeen and Ala-Eddin Al Moustafa, "Real-time continuous dielectrophoretic separation of malignant cells", 1st Microsystems and Nanoelectronics Research Conference, MNRC 2008, October 14-15, 2008, Ottawa, Canada.
- e. Andrei Dulipovici, Dacian Roman, Ion Stiharu, Vahé Nerguizian and Nicolas Constantin, "An Efficient FEA on an RF Structure Used to Evaluate the Effect of Microwave Radiation on Uveal Melanoma Cells", Proceedings of the COMSOL Conference, 8-10 October 2009, Boston, USA.

A journal paper is accepted and published in the Journal of Electrophoresis in January 2012. The candidate is the first author of this paper and the paper presents the analytical solution of a microfluidic device with parallel facing electrodes using Fourier series approach. A second journal paper is accepted and published in the journal of Microfluidic and Nano Fluidics in May 2010 where the candidate is the co-author. The

paper presents the DEP for analytical solution of a microfluidic structure. A third paper is ready for submitting (on hold for confidentiality purposes). I am the first author of this paper. The paper presents the characteristic of different standard and biological solutions in the S-band frequency range. Different cancer cell's dielectric properties are measured using the resonant cavity perturbation method.

The summary of the titles of all these 3 journal papers are:

- a. Vahé Nerguizian, Anas Alazzam, Dacian Roman, Ion Stiharu and Miguel Jr. Burnier, “Analytical Solutions and Validation of Electric Field and Dielectrophoretic Force in a Bio-microfluidic Channel”, *Journal of Electrophoresis*, 2012, Volume 33, Issue 3, p 426-435.
- b. Anas Alazzam, Dacian Roman, Vahé Nerguizian, Ion Stiharu and Rama Bhat, “Analytical formulation of electric field and dielectrophoretic force for moving dielectrophoresis using Fourier series”, *Journal of Microfluidics and Nanofluidics*, 2010, Volume 9, Issue 6, p 1115-1124.
- c. Vahé Nerguizian, Anas Alazzam, Sylvain Brisebois, Dacian Roman, Ion Stiharu and Miguel Jr. Burnier, “Dielectric Characterization of Biological Cells at Microwave Frequencies”, (on hold for confidentiality purposes).

## References:

1. Keeney, M., I. Chin-Yee, K. Weir, J. Popma, R. Nayar, and D.R. Sutherland, *Single platform flow cytometric absolute CD34+ cell counts based on the ISHAGE guidelines*. Cytometry, 1998. **34**(2).
2. Reyes, D.R., D. Iossifidis, P.A. Auroux, and A. Manz, *Micro Total Analysis Systems. 1. Introduction, Theory, and Technology*. ANALYTICAL CHEMISTRY-WASHINGTON DC-, 2002. **74**(12): p. 2623-2636.
3. Lee, G.B., C.H. Lin, and G.L. Chang, *Micro flow cytometers with buried SU-8/SOG optical waveguides*. Sensors & Actuators: A. Physical, 2003. **103**(1-2): p. 165-170.
4. Huh, D., W. Gu, Y. Kamotani, J.B. Grotberg, and S. Takayama, *Microfluidics for flow cytometric analysis of cells and particles*. PHYSIOLOGICAL MEASUREMENT, 2005. **26**(3): p. 73.
5. Koch, M., A.G.R. Evans, and A. Brunnschweiler, *Design and fabrication of a micromachined Coulter counter*. Journal of Micromechanics and Microengineering, 1999. **9**: p. 159-161.
6. Kim, E., W. Kim, S.G. Lee, and S. Park, *Flow cell detection with an optical fiber*.
7. Suehiro, J., M. Shutou, T. Hatano, and M. Hara, *High sensitive detection of biological cells using dielectrophoretic impedance measurement method combined with electropermeabilization*. Sensors & Actuators: B. Chemical, 2003. **96**(1-2): p. 144-151.
8. Cheung, K., S. Gawad, and P. Renaud, *Impedance Spectroscopy Flow Cytometry: On-Chip Label-Free Cell Differentiation*. CYTOMETRY PART A, 2005. **65**(2): p. 124.
9. Dario, P., M.C. Carrozza, A. Benvenuto, and A. Menciassi, *Micro-systems in biomedical applications*. Journal of Micromechanics and Microengineering, 2000. **10**(2): p. 235-244.
10. Lee, S.J. and S.Y. Lee, *Micro total analysis system ( $\mu$ -TAS) in biotechnology*. Applied Microbiology and Biotechnology, 2004. **64**(3): p. 289-299.
11. Gao, Y., *MICROFABRICATED DEVICES FOR SINGLE CELL ANALYSIS*, 2006, University of Missouri.
12. Byun, I., J. Yang, and S. Park, *Fabrication of a new micro bio chip and flow cell cytometry system using Bio-MEMS technology*. Microelectronics Journal, 2008.
13. Ateya, D.A., J.S. Erickson, P.B. Howell, L.R. Hilliard, J.P. Golden, and F.S. Ligler, *The good, the bad, and the tiny: a review of microflow cytometry*. Analytical and Bioanalytical Chemistry, 2008. **391**(5): p. 1485-1498.
14. Saliterman, S., *Fundamentals of BioMEMS and Medical Microdevices* 2006: SPIE Press.
15. Cools-Lartigue, J.J., C.S. McCauley, J.C.A. Marshall, S. Di Cesare, F. Gregoire, E. Anteck, P. Logan, and M.N. Burnier Jr, *Immunomagnetic isolation and in vitro expansion of human uveal melanoma cell lines*. Molecular Vision, 2008. **14**: p. 50.
16. Altendorf, E., D. Zebert, M. Holl, and P. Yager, *Differential blood cell counts obtained using a microchannel based flow cytometer*. 1997.
17. Lin, C.H., G.B. Lee, and B.H. Hwei, *A novel micro flow cytometer with 3-dimensional focusing utilizing dielectrophoretic and hydrodynamic forces*. 2003.
18. Wolff, A., I.R. Perch-Nielsen, U.D. Larsen, P. Friis, G. Goranovic, C.R. Poulsen, J.P. Kutter, and P. Telleman, *Integrating advanced functionality in a microfabricated high-throughput fluorescent-activated cell sorter*. Lab on a Chip, 2003. **3**(1): p. 22-27.
19. Lin, C.H., G.B. Lee, L.M. Fu, and S.H. Chen, *Integrated optical-fiber capillary electrophoresis microchips with novel spin-on-glass surface modification*. Biosensors and Bioelectronics, 2004. **20**(1): p. 83-90.
20. Fu, L.M., R.J. Yang, C.H. Lin, Y.J. Pan, and G.B. Lee, *Electrokinetically driven micro flow cytometers with integrated fiber optics for on-line cell/particle detection*. Analytica Chimica Acta, 2004. **507**(1): p. 163-169.
21. Erickson, D. and D. Li, *Integrated microfluidic devices*. Analytica Chimica Acta, 2004. **507**(1): p. 11-26.
22. Bernini, R., E. De Nuccio, F. Brescia, A. Minardo, L. Zeni, P.M. Sarro, R. Palumbo, and M.R. Scarfi, *Development and characterization of an integrated silicon micro flow cytometer*. Analytical and Bioanalytical Chemistry, 2006. **386**(5): p. 1267-1272.
23. Simonnet, C. and A. Groisman, *High-throughput and high-resolution flow cytometry in molded microfluidic devices*. Anal. Chem, 2006. **78**(16): p. 5653-5663.

24. Wheeler, A.R., W.R. Thronset, R.J. Whelan, A.M. Leach, R.N. Zare, Y.H. Liao, K. Farrell, I.D. Manger, and A. Daridon, *Microfluidic device for single-cell analysis*. *Electrophoresis*, 2001. **22**: p. 283-288.
25. McClain, M.A., C.T. Culbertson, S.C. Jacobson, N.L. Allbritton, C.E. Sims, and J.M. Ramsey, *Microfluidic Devices for the High-Throughput Chemical Analysis of Cells*. ANALYTICAL CHEMISTRY-WASHINGTON DC-, 2003. **75**(21): p. 5646-5655.
26. Yi, C., C.W. Li, S. Ji, and M. Yang, *Microfluidics technology for manipulation and analysis of biological cells*. *Analytica Chimica Acta*, 2006. **560**(1-2): p. 1-23.
27. Ferrier, G.A., A.N. Hladio, D.J. Thomson, G.E. Bridges, M. Hedayatipoor, S. Olson, and M.R. Freeman, *Microfluidic electromanipulation with capacitive detection for the mechanical analysis of cells*. *Biomicrofluidics*, 2008. **2**: p. 044102.
28. Ferrier, G., S. Romanuik, D. Thomson, G. Bridges, and M. Freeman, *A microwave interferometric system for simultaneous actuation and detection of single biological cells*. *Lab on a Chip*, 2009. **9**(23): p. 3406-3412.
29. Romanuik, S., S. Grist, B. Gray, N. Gulzar, J. Scott, D. Hohertz, K. Kavanagh, R. Nirwan, C. Hui, and A. Brolo. *The detection of antibodies secreted by microfluidically trapped biological cells via extraordinary optical detection-based nanoscale immunobiosensing arrays*. 2010.
30. Larsen, L.E. and J.H. Jacobi, *Electromagnetic method for the noninvasive analysis of cell membrane physiology and pharmacology*, 1980, Google Patents.
31. Alazzam, A.Z., *Hybrid Flow through Microchannels for Blood Cell Separation*, 2011, CONCORDIA UNIVERSITY.
32. Veridex, L., *CellSearch circulating tumor cell kit premarket notification-expanded indications for use—metastatic prostate cancer*. K073338. pdf (February, 2008)(accessed March 18, 2010).
33. Nguyen, L.K., *High-throughput image cytometer for detection of circulating tumor cells and contrast-enhancement filtering for automated 3D image segmentation of cartilage tissue explants*, 2007, University of California, San Diego.
34. Cheng, I., V. Froude, Y. Zhu, H. Chang, and H. Chang, *A continuous high-throughput bioparticle sorter based on 3D traveling-wave dielectrophoresis*. *Lab on a Chip*, 2009. **9**(22): p. 3193-3201.
35. Choi, S. and J.K. Park, *Microfluidic system for dielectrophoretic separation based on a trapezoidal electrode array*. *Lab on a Chip*, 2005. **5**(10): p. 1161-1167.
36. Collins, J. and A.P. Lee, *Microfluidic flow transducer based on the measurement of electrical admittance*. *Lab on a Chip*, 2004. **4**(1): p. 7-10.
37. Gawad, S., K. Cheung, U. Seger, A. Bertsch, and P. Renaud, *Dielectric spectroscopy in a micromachined flow cytometer: theoretical and practical considerations*. *Lab on a Chip*, 2004. **4**(3): p. 241-251.
38. Gawad, S., L. Schild, and P. Renaud, *Micromachined impedance spectroscopy flow cytometer for cell analysis and particle sizing*. *Lab on a Chip*, 2001. **1**(1): p. 76-82.
39. Pamme, N., *Continuous flow separations in microfluidic devices*. *Lab on a Chip*, 2007. **7**(12): p. 1644-1659.
40. Pamme, N., R. Koyama, and A. Manz, *Counting and sizing of particles and particle agglomerates in a microfluidic device using laser light scattering: application to a particle-enhanced immunoassay*. *Lab on a Chip*, 2003. **3**(3): p. 187-192.
41. Revzin, A., K. Sekine, A. Sin, R.G. Tompkins, and M. Toner, *Development of a microfabricated cytometry platform for characterization and sorting of individual leukocytes*. *Lab on a Chip*, 2005. **5**(1): p. 30-37.
42. Schwarz, M.A. and P.C. Hauser, *Recent developments in detection methods for microfabricated analytical devices*. *Lab on a Chip*, 2001. **1**(1): p. 1-6.
43. Thomas, R.S., H. Morgan, and N.G. Green, *Negative DEP traps for single cell immobilisation*. *Lab on a Chip*, 2009. **9**(11): p. 1534-1540.
44. Vulto, P., N. Glade, L. Altomare, J. Bablet, L. Tin, G. Medoro, I. Chartier, N. Manaresi, M. Tartagni, and R. Guerrieri, *Microfluidic channel fabrication in dry film resist for production and prototyping of hybrid chips*. *Lab on a Chip*, 2005. **5**(2): p. 158-162.
45. Wang, Z., J. El-Ali, M. Engelund, T. Gotsæd, I.R. Perch-Nielsen, K.B. Mogensen, D. Snakenborg, J.P. Kutter, and A. Wolff, *Measurements of scattered light on a microchip flow cytometer with integrated polymer based optical elements*. *Lab on a Chip*, 2004. **4**(4): p. 372-377.

46. Xu, G., J. Wang, Y. Chen, L. Zhang, D. Wang, and G. Chen, *Fabrication of poly (methyl methacrylate) capillary electrophoresis microchips by in situ surface polymerization*. *Lab on a Chip*, 2006. **6**(1): p. 145-148.
47. Soeth, E., *Comparative analysis of bone marrow and venous blood isolates from gastrointestinal cancer patients for the detection of disseminated tumor cells using reverse transcription PCR*. *Cancer Research*, 1997. **57**(15): p. 3106-3110.
48. Weitz, J., P. Kienle, A. Magener, M. Koch, A. Schrodell, F. Willeke, F. Autschbach, J. Lacroix, T. Lehnert, and C. Herfarth, *Detection of Disseminated Colorectal Cancer Cells in Lymph Nodes, Blood and Bone Marrow*. *Clinical Cancer Research*, 1999. **5**(7): p. 1830.
49. Evron, E., W.C. Dooley, C.B. Umbricht, D. Rosenthal, N. Sacchi, E. Gabrielson, A.B. Soito, D.T. Hung, B.M. Ljung, and N.E. Davidson, *Detection of breast cancer cells in ductal lavage fluid by methylation-specific PCR*. *The Lancet*, 2001. **357**(9265): p. 1335-1336.
50. Naoe, M., Y. Ogawa, J. Morita, K. Omori, K. Takeshita, T. Shichijyo, T. Okumura, A. Igarashi, A. Yanaihara, and S. Iwamoto, *Detection of circulating urothelial cancer cells in the blood using the CellSearch™ System*. *Cancer*, 2007. **109**(7): p. 1439-1445.
51. Lacombe, F. and F. Belloc, *Flow cytometry study of cell cycle, apoptosis and drug resistance in acute leukemia*. *Hematology and Cell Therapy*, 1997. **38**(6): p. 495-504.
52. Redkar, A.A. and A. Krishan, *Flow Cytometric Analysis of Estrogen, Progesterone Receptor Expression and DNA Content in Formalin-Fixed, Paraffin-Embedded Human Breast Tumors*. *Cytometry (Communications in Clinical Cytometry)*, 1999. **38**: p. 61-69.
53. Veal, D.A., D. Deere, B. Ferrari, J. Piper, and P.V. Attfield, *Fluorescence staining and flow cytometry for monitoring microbial cells*. *J Immunol Methods*, 2000. **243**(1-2): p. 191-210.
54. Cualing, H.D., *Automated Analysis in Flow Cytometry*. *Cytometry (Communications in Clinical Cytometry)*, 2000. **42**: p. 110-113.
55. Ashcroft, R.G. and P.A. Lopez, *Commercial high speed machines open new opportunities in high throughput flow cytometry (HTFC)*. *Journal of Immunological Methods*, 2000. **243**(1-2): p. 13-24.
56. De Rosa, S.C., L.A. Herzenberg, and M. Roederer, *11-color, 13-parameter flow cytometry: Identification of human naive T cells by phenotype, function, and T-cell receptor diversity*. *NATURE MEDICINE*, 2001. **7**(2): p. 245-248.
57. Herzenberg, L.A., D. Parks, B. Sahaf, O. Perez, and M. Roederer, *The History and Future of the Fluorescence Activated Cell Sorter and Flow Cytometry: A View from Stanford*, 2002, *Am Assoc Clin Chem*. p. 1819-1827.
58. Kapoor, V., V. Karpov, C. Linton, F.V. Subach, V.V. Verkhusha, and W.G. Telford, *Solid state yellow and orange lasers for flow cytometry*. *Cytometry. Part A: the journal of the International Society for Analytical Cytology*, 2008.
59. Jeffries, D., I. Zaidi, B. de Jong, M.J. Holland, and D.J. Miles, *Analysis of flow cytometry data using an automatic processing tool*. *Cytometry A*, 2008.
60. Darzynkiewicz, Z., D. Galkowski, and H. Zhao, *Analysis of apoptosis by cytometry using TUNEL assay*. *Methods*, 2008. **44**(3): p. 250-4.
61. Davey, H.M. and D.B. Kell, *Flow cytometry and cell sorting of heterogeneous microbial populations: the importance of single-cell analyses*. *Microbiology and Molecular Biology Reviews*, 1996. **60**(4): p. 641-696.
62. Sack, U., A. Tárnok, and G. Rothe, *Cellular diagnostics: basic principles, methods and clinical applications of flow cytometry* 2009: S Karger Ag.
63. Krishnamurthy, H. and L.S. Cram, *BASICS OF FLOW CYTOMETRY. Applications of Flow Cytometry in Stem Cell Research and Tissue Regeneration*, 2010: p. 1.
64. Hurley, J., *Sizing Particles with a Coulter Counter*. *Biophysical Journal*, 1970. **10**(1): p. 74.
65. Kubitschek, H.E. and J.A. Friske, *Determination of bacterial cell volume with the Coulter Counter*. *Journal of Bacteriology*, 1986. **168**(3): p. 1466-1467.
66. Rouzair-Dubois, B. and J.M. Dubois, *K<sup>+</sup> channel block-induced mammalian neuroblastoma cell swelling: a possible mechanism to influence proliferation*. *The Journal of Physiology*, 1998. **510**(1): p. 93-102.
67. Wu, W.K., C.K. Liang, and J.Z. Huang. *MEMS-based flow cytometry: microfluidics-based cell identification system by fluorescent imaging*. 2004.
68. Jang, L.S. and M.H. Wang, *Microfluidic device for cell capture and impedance measurement*. *Biomedical Microdevices*, 2007. **9**(5): p. 737-743.

69. Sun, T., D. Holmes, S. Gawad, N.G. Green, and H. Morgan, *High speed multi-frequency impedance analysis of single particles in a microfluidic cytometer using maximum length sequences*. Lab Chip, 2007. **7**(8): p. 1034-40.
70. Zheng, S., M. Liu, and Y.C. Tai, *Micro coulter counters with platinum black electroplated electrodes for human blood cell sensing*. Biomed Microdevices, 2008. **10**(2): p. 221-31.
71. Wu, Y., J. Benson, J. Critser, and M. Almasri, *MEMS-based Coulter counter for cell counting and sizing using multiple electrodes*. Journal of Micromechanics and Microengineering, 2010. **20**: p. 085035.
72. Oh, S.H., D.K. Wood, S.H. Lee, K.Y. Dane, P.S. Daugherty, H.T. Soh, and A.N. Cleland, *MICROMACHINED BROADBAND RF CYTOMETER FOR HIGH-THROUGHPUT ANALYSIS OF MAMMALIAN CELLS*.
73. Holmes, D., H. Morgan, and N.G. Green, *High throughput particle analysis: Combining dielectrophoretic particle focussing with confocal optical detection*. Biosensors and Bioelectronics, 2006. **21**(8): p. 1621-1630.
74. Wood, D., M. Requa, and A. Cleland, *Microfabricated high-throughput electronic particle detector*. Review of Scientific Instruments, 2007. **78**: p. 104301.
75. Rodriguez-Trujillo, R., O. Castillo-Fernandez, M. Garrido, M. Arundell, A. Valencia, and G. Gomila, *High-speed particle detection in a micro-Coulter counter with two-dimensional adjustable aperture*. Biosensors and Bioelectronics, 2008. **24**(2): p. 290-296.
76. Cheung, K.C., M. Di Berardino, G. Schade Kampmann, M. Hebeisen, A. Pierzchalski, J. Bocsi, A. Mittag, and A. Tárnok, *Microfluidic impedance based flow cytometry*. Cytometry Part A, 2010. **77**(7): p. 648-666.
77. Venkatesh, M., *Optimization of the Mini-Flo flow cytometer*, 1996, UCRL-ID--124076, Lawrence Livermore National Lab., CA (United States).
78. Lin, C.H. and G.B. Lee, *Micromachined flow cytometers with embedded etched optic fibers for optical detection*. Journal of Micromechanics and Microengineering, 2003. **13**(3): p. 447-453.
79. Hunt, H.C. and J.S. Wilkinson, *Optofluidic integration for microanalysis*. Microfluidics and Nanofluidics, 2008. **4**(1): p. 53-79.
80. Altendorf, E.H. and P. Yager, *Silicon microchannel optical flow cytometer*, 1998, US Patent 5,726,751.
81. Dittrich, P.S. and P. Schuille, *An Integrated Microfluidic System for Reaction, High-Sensitivity Detection, and Sorting of Fluorescent Cells and Particles*. ANALYTICAL CHEMISTRY- WASHINGTON DC-, 2003. **75**(21): p. 5767-5774.
82. Gruden, C., S. Skerlos, and P. Adriaens, *Flow cytometry for microbial sensing in environmental sustainability applications: current status and future prospects*. FEMS Microbiology Ecology, 2004. **49**(1): p. 37-49.
83. Kurabayashi, K., S. Takayama, S.J. Skerlos, D. Huh, J.B. Grothberg, and Y.C. Tung, *Flow cytometers and detection system of lesser size*, 2006, Google Patents.
84. Wood, D.K., S.H. Oh, S.H. Lee, H.T. Soh, and A.N. Cleland, *High-bandwidth radio frequency Coulter counter*. Applied Physics Letters, 2005. **87**: p. 184106.
85. Korampally, M., *A MEMS BASED COULTER COUNTER FOR CELL SIZING*, 2007, University of Missouri.
86. Bao, N., J. Wang, and C. Lu, *Recent advances in electric analysis of cells in microfluidic systems*. Analytical and Bioanalytical Chemistry, 2008. **391**(3): p. 933-942.
87. Prasad, B. and R. Lal, *A capacitive immunosensor measurement system with a lock-in amplifier and potentiostatic control by software*. Measurement Science and Technology, 1999. **10**(11): p. 1097-1104.
88. Allsopp, D.W.E., K.R. Milner, A.P. Brown, and W.B. Betts, *Impedance technique for measuring dielectrophoretic collection of microbiological particles*. JOURNAL OF PHYSICS-LONDON-D APPLIED PHYSICS, 1999. **32**: p. 1066-1074.
89. Sohn, L.L., O.A. Saleh, G.R. Facer, A.J. Beavis, R.S. Allan, and D.A. Notterman, *Capacitance cytometry: Measuring biological cells one by one*. Proceedings of the National Academy of Sciences, 2000. **97**(20): p. 10687.
90. De Bisschop, F., J. Vierendeels, and C. De Langhe, *Electronic gate detection for cell or particle counting and sizing in liquids: front-end characteristics, flow-dependent gate impedance, and its*

- remediation*. Instrumentation and Measurement, IEEE Transactions on, 2006. **55**(4): p. 1160-1168.
91. Choi, J.W., K.W. Oh, A. Han, C.A. Wijayawardhana, C. Lannes, S. Bhansali, K.T. Schlueter, W.R. Heineman, H.B. Halsall, and J.H. Nevin, *Development and Characterization of Microfluidic Devices and Systems for Magnetic Bead-Based Biochemical Detection*. Biomedical Microdevices, 2001. **3**(3): p. 191-200.
  92. Watarai, H., M. Suwa, and Y. Iiguni, *Magnetophoresis and electromagnetophoresis of microparticles in liquids*. Analytical and Bioanalytical Chemistry, 2004. **378**(7): p. 1693-1699.
  93. Yang, S.Y., K.Y. Lien, K.J. Huang, H.Y. Lei, and G.B. Lee, *Micro flow cytometry utilizing a magnetic bead-based immunoassay for rapid virus detection*. Biosens Bioelectron, 2008.
  94. Larsen, L.E. and J.H. Jacobi, *Microwave time delay spectroscopic methods and apparatus for remote interrogation of biological targets*, 1979, Google Patents.
  95. Larsen, L.E., *Millimeter wave flow cytometer*, 1992, Google Patents.
  96. Dittrich, P., F. Malik, and P. Schuille, *Cytometry on Microfluidic Chips*. Microfluidic Technologies for Miniaturized Analysis Systems, 2007: p. 569-605.
  97. Lee, G.B., C.I. Hung, B.J. Ke, G.R. Huang, B.H. Hwei, and H.F. Lai, *Hydrodynamic Focusing for a Micromachined Flow Cytometer*. TRANSACTIONS-AMERICAN SOCIETY OF MECHANICAL ENGINEERS JOURNAL OF FLUIDS ENGINEERING, 2001. **123**(3): p. 672-679.
  98. Chung, S., S.J. Park, J.K. Kim, C. Chung, D.C. Han, and J.K. Chang, *Plastic microchip flow cytometer based on 2-and 3-dimensional hydrodynamic flow focusing*. Microsystem Technologies, 2003. **9**(8): p. 525-533.
  99. Lee, G., C. Chang, S. Huang, and R. Yang, *The hydrodynamic focusing effect inside rectangular microchannels*. Journal of Micromechanics and Microengineering, 2006. **16**(5): p. 1024.
  100. Chang, C., Z. Huang, and R. Yang, *Three-dimensional hydrodynamic focusing in two-layer polydimethylsiloxane (PDMS) microchannels*. Journal of Micromechanics and Microengineering, 2007. **17**(8): p. 1479.
  101. Jr, P.B.H., J.P. Golden, L.R. Hilliard, J.S. Erickson, D.R. Mott, and F.S. Ligler, *Two simple and rugged designs for creating microfluidic sheath flow*. Lab on a Chip, 2008. **8**(7): p. 1097-1103.
  102. Fiedler, S., S.G. Shirley, T. Schnelle, and G. Fuhr, *Dielectrophoretic Sorting of Particles and Cells in a Microsystem*. ANALYTICAL CHEMISTRY-WASHINGTON DC-, 1998. **70**: p. 1909-1915.
  103. Morgan, H., M.P. Hughes, and N.G. Green, *Separation of Submicron Bioparticles by Dielectrophoresis*. Biophysical Journal, 1999. **77**(1): p. 516-525.
  104. Morgan, H., D. Holmes, and N.G. Green. *3D focusing of nanoparticles in microfluidic channels*. 2003.
  105. Chou, C.F. and F. Zenhausern, *Electrodeless dielectrophoresis for micro total analysis systems*. Engineering in Medicine and Biology Magazine, IEEE, 2003. **22**(6): p. 62-67.
  106. Holmes, D., N.G. Green, and H. Morgan, *Microdevices for dielectrophoretic flow-through cell separation*. Engineering in Medicine and Biology Magazine, IEEE, 2003. **22**(6): p. 85-90.
  107. Lin, C.H., G.B. Lee, L.M. Fu, and B.H. Hwey, *Vertical focusing device utilizing dielectrophoretic force and its application on microflow cytometer*. Microelectromechanical Systems, Journal of, 2004. **13**(6): p. 923-932.
  108. Yu, C., J. Vykoukal, D.M. Vykoukal, J.A. Schwartz, L. Shi, and P.R.C. Gascoyne, *A three-dimensional dielectrophoretic particle focusing channel for microcytometry applications*. Microelectromechanical Systems, Journal of, 2005. **14**(3): p. 480-487.
  109. Doh, I. and Y.H. Cho, *A continuous cell separation chip using hydrodynamic dielectrophoresis (DEP) process*. Sensors & Actuators: A. Physical, 2005. **121**(1): p. 59-65.
  110. Goddard, G., J.C. Martin, S.W. Graves, and G. Kaduchak, *Ultrasonic particle-concentration for sheathless focusing of particles for analysis in a flow cytometer*. CYTOMETRY PART A, 2006. **69**(2): p. 66.
  111. Demierre, N., T. Braschler, R. Muller, and P. Renaud, *Focusing and continuous separation of cells in a microfluidic device using lateral dielectrophoresis*. Sensors & Actuators: B. Chemical, 2007.
  112. Jacobson, S.C. and J.M. Ramsey, *Electrokinetic Focusing in Microfabricated Channel Structures*. ANALYTICAL CHEMISTRY-WASHINGTON DC-, 1997. **69**: p. 3212-3217.

113. Morgan, H., D. Holmes, and N.G. Green, *High speed simultaneous single particle impedance and fluorescence analysis on a chip*. Current Applied Physics, 2006. **6**(3): p. 367-370.
114. Sun, T., N.G. Green, S. Gawad, and H. Morgan, *Analytical electric field and sensitivity analysis for two microfluidic impedance cytometer designs*. Nanobiotechnology, IET, 2007. **1**(5): p. 69-79.
115. Han, A., *Microfabricated multi-analysis system for electrophysiological studies of single cells*, 2005, Georgia Institute of Technology: United States -- Georgia.
116. Rodriguez-Trujillo, R., C.A. Mills, J. Samitier, and G. Gomila, *Low cost micro-Coulter counter with hydrodynamic focusing*. Microfluidics and Nanofluidics, 2007. **3**(2): p. 171-176.
117. Larsen, U.D., G. Blankenstein, and J. Branebjerg, *Microchip Coulter particle counter*, in *Solid State Sensors and Actuators, 1997. TRANSDUCERS '97 Chicago., 1997 International Conference on 1997*. p. 1319-1322 vol.2.
118. Son, S.U., Y.H. Choi, and S.S. Lee, *Micro-cell counter using photoconductance of boron diffused resistor (BDR)*. Sensors & Actuators: A. Physical, 2004. **111**(1): p. 100-106.
119. De Bisschop, F.R.E. *Electronic Gating for Particle/Cell Counting and Sizing, DSP-operated*. 2006.
120. Romani, A., N. Manaresi, L. Marzocchi, G. Medoro, A. Leonardi, L. Altomare, M. Tartagni, and R. Guerrieri. *Capacitive sensor array for localization of bioparticles in CMOS lab-on-a-chip*. 2004.
121. Burchill, S.A., M.F. Bradbury, K. Pittman, J. Southgate, B. Smith, and P. Selby, *Detection of epithelial cancer cells in peripheral blood by reverse transcriptase-polymerase chain reaction*. Br J Cancer, 1995. **71**(2): p. 278-81.
122. Kubista, M., J.M. Andrade, M. Bengtsson, A. Forootan, J. Jonák, K. Lind, R. Sindelka, R. Sjöback, B. Sjögreen, and L. Strömbom, *The real-time polymerase chain reaction*. Molecular aspects of medicine, 2006. **27**(2-3): p. 95-125.
123. Cho, Y.H., T. Yamamoto, Y. Sakai, T. Fujii, and B. Kim, *Development of Microfluidic Device for Electrical/Physical Characterization of Single Cell*.
124. Facer, G.R., L.L. Sohn, and D.A. Notterman, *Method and apparatus for dielectric spectroscopy of biological solutions*, 2002, Google Patents.
125. Suehiro, J., R. Hamada, D. Noutomi, M. Shutou, and M. Hara, *Selective detection of viable bacteria using dielectrophoretic impedance measurement method*. Journal of Electrostatics, 2003. **57**(2): p. 157-168.
126. Bernini, R., S. Campopiano, L. Zeni, and P.M. Sarro, *ARROW optical waveguides based sensors*. Sensors & Actuators: B. Chemical, 2004. **100**(1-2): p. 143-146.
127. Bogomolny, E., S. Argov, S. Mordechai, and M. Huleihel, *Monitoring of viral cancer progression using FTIR microscopy: A comparative study of intact cells and tissues*. Biochim Biophys Acta, 2008.
128. Voldman, J., *Dielectrophoretic traps for cell manipulation*. BioMEMS and Biomedical Nanotechnology, 2007: p. 159-186.
129. Voldman, J., *Dielectrophoretic Traps for Cell Manipulation*. BioMEMS and Biomedical Nanotechnology Volume IV: Biomolecular Sensing, Processing and Analysis: p. 159-186.
130. Kua, C.H., Y.C. Lam, C. Yang, and K. Youcef-Toumi, *Review of bio-particle manipulation using dielectrophoresis*. 2005.
131. Hardt, S. and F. Schönfeld, *Microfluidic Technologies for Miniaturized Analysis Systems 2007*: Not Avail.
132. Demierre, N., *Continuous-Flow Separation of Cells in a Lab-on-a-Chip using "Liquid Electrodes" and Multiple-Frequency Dielectrophoresis*. Ph D thesis, 2008.
133. Davey, H.M., *Flow cytometry of microorganisms* 1994: University of Wales. Aberystwyth.
134. Spiller, E., A. Schöll, R. Alexy, K. Kümmerer, and G.A. Urban, *A sensitive microsystem as biosensor for cell growth monitoring and antibiotic testing*. Sensors & Actuators: A. Physical, 2006. **130**: p. 312-321.
135. Marx, G.H. and C.L. Davey, *The dielectric properties of biological cells at radiofrequencies: applications in biotechnology*. Enzyme and Microbial Technology, 1999. **25**(3-5): p. 161-171.
136. Jones, T.B., *Electromechanics of particles* 1995: Cambridge University Press.
137. Dukhin, S.S., V.N. Shilov, and J.J. Bikerman, *Dielectric Phenomena and Double Layer in Disperse Systems and Polyelectrolytes*. Journal of The Electrochemical Society, 1974. **121**: p. 154C.

138. Russel, W.B., D.A. Saville, and W.R. Schowalter, *Colloidal dispersions* 1989: Cambridge University Press.
139. Morgan, H., T. Sun, D. Holmes, S. Gawad, and N.G. Green, *Single cell dielectric spectroscopy*. JOURNAL OF PHYSICS-LONDON-D APPLIED PHYSICS, 2007. **40**(1): p. 61.
140. Das, C.M., F. Becker, S. Vernon, J. Noshari, C. Joyce, and P.R.C. Gascoyne, *Dielectrophoretic segregation of different human cell types on microscope slides*. Analytical chemistry, 2005. **77**(9): p. 2708.
141. Simons, R.N. and G.E. Ponchak, *Modeling of some coplanar waveguide discontinuities*. Microwave Theory and Techniques, IEEE Transactions on, 1988. **36**(12): p. 1796-1803.
142. Chen, E. and S.Y. Chou, *Characteristics of coplanar transmission lines on multilayer substrates: Modeling and experiments*. Microwave Theory and Techniques, IEEE Transactions on, 1997. **45**(6): p. 939-945.
143. Pozar, D.M., *Microwave Engineering, 3rd*, 2005, John Wiley & Sons, Hoboken, NJ, USA.
144. Pozar, D.M., *Microwave engineering*. Reading, MA, 1993.
145. Frickey, D.A., *Conversions between S, Z, Y, h, ABCD, and T parameters which are valid for complex source and load impedances*. Microwave Theory and Techniques, IEEE Transactions on, 1994. **42**(2): p. 205-211.
146. Hosseini, M., G. Zhu, and Y.A. Peter, *A new formulation of fringing capacitance and its application to the control of parallel-plate electrostatic micro actuators*. Analog Integrated Circuits and Signal Processing, 2007. **53**(2): p. 119-128.
147. Lonappan, A., V.O. Timothy, C. Rajasekaran, V. Thomas, J. Jacob, and K.T. Mathew, *A novel method of detecting cervical cancer using microwaves*. Microwave and Optical Technology Letters, 2008. **50**(6).
148. Waldron, R., *Perturbation theory of resonant cavities*. Proceedings of the IEE-Part C: Monographs, 1960. **107**(12): p. 272-274.
149. Krupka, J., *Frequency domain complex permittivity measurements at microwave frequencies*. Measurement Science and Technology, 2006. **17**: p. R55.
150. Paz, A.M., *The dielectric properties of solid biofuels*. 2010.
151. Sheen, J., *Measurements of microwave dielectric properties by an amended cavity perturbation technique*. Measurement, 2009. **42**(1): p. 57-61.
152. Mathew, K., *Perturbation theory*. Encyclopedia of RF and microwave engineering, 2005.
153. Lin, M., M.H. Duane, and M.N. Afsar, *Cavity-perturbation measurement of complex permittivity and permeability of common ferrimagnetics in microwave-frequency range*. Magnetics, IEEE Transactions on, 2006. **42**(10): p. 2885-2887.
154. Kumar, S.B., H. Hohn, R. Joseph, M. Hajian, L. Ligthart, and K. Mathew, *Complex permittivity and conductivity of poly aniline at microwave frequencies*. Journal of the European Ceramic Society, 2001. **21**(15): p. 2677-2680.
155. Kumar, A. and G. Singh, *Measurement of dielectric constant and loss factor of the dielectric material at microwave frequencies*. Progress In Electromagnetics Research, 2007. **69**: p. 47-54.
156. Chen, L., C. Ong, and B. Tan, *Cavity perturbation technique for the measurement of permittivity tensor of uniaxially anisotropic dielectrics*. Instrumentation and Measurement, IEEE Transactions on, 1999. **48**(6): p. 1023-1030.
157. Champlin, K. and R. Krongard, *The measurement of conductivity and permittivity of semiconductor spheres by an extension of the cavity perturbation method*. Microwave Theory and Techniques, IRE Transactions on, 1961. **9**(6): p. 545-551.
158. Chao, S.H., *Measurements of microwave conductivity and dielectric constant by the cavity perturbation method and their errors*. Microwave Theory and Techniques, IEEE Transactions on, 1985. **33**(6): p. 519-526.
159. Kraszewski, A.W. and S.O. Nelson, *Observations on resonant cavity perturbation by dielectric objects*. Microwave Theory and Techniques, IEEE Transactions on, 1992. **40**(1): p. 151-155.
160. Penirschke, A., S. Mueller, F. Goelden, A. Lapanik, V. Lapanik, V. Bezborodov, W. Haase, and R. Jakoby. *Cavity Perturbation Method for Temperature Controlled Characterization of Liquid Crystals at 38 GHz*. 2006.
161. Gaebler, A., F. Goelden, S. Mueller, and R. Jakoby. *Triple-Mode Cavity Perturbation Method for the Characterization of Anisotropic Media*. IEEE.

162. Yohannan, J., J. Jacob, A. Lonappan, and K. Mathew, *Dielectric properties of strontium sodium niobate ceramics using the microwave cavity perturbation technique*. Microwave and optical technology letters, 2003. **39**(2): p. 112-115.
163. Parkash, A., J. Vaid, and A. Mansingh, *Measurement of dielectric parameters at microwave frequencies by cavity-perturbation technique*. Microwave Theory and Techniques, IEEE Transactions on, 1979. **27**(9): p. 791-795.
164. Harrington, R.F., *Time-Harmonic Fields* 1961: McGraw-Hill, New York, NY.
165. Rubinger, C. and L. Costa, *Building a resonant cavity for the measurement of microwave dielectric permittivity of high loss materials*. Microwave and Optical Technology Letters, 2007. **49**(7): p. 1687-1690.
166. Abbas, S., M. Chandra, A. Verma, R. Chatterjee, and T. Goel, *Complex permittivity and microwave absorption properties of a composite dielectric absorber*. Composites Part A: Applied Science and Manufacturing, 2006. **37**(11): p. 2148-2154.
167. Krivenko, E., A. Kirichenko, V. Lutsenko, and G. Golubnichaya. *Resonant method for measurement of a complex permittivity of wine*. 2009. IEEE.
168. Verma, A. and D.C. Dube, *Measurement of dielectric parameters of small samples at X-band frequencies by cavity perturbation technique*. Instrumentation and Measurement, IEEE Transactions on, 2005. **54**(5): p. 2120-2123.
169. Venkatesh, M. and G. Raghavan, *An overview of dielectric properties measuring techniques*. vol, 2005. **47**: p. 7.15-7.30.
170. NPL, I.a., "*A Guide to the characterization of dielectric materials at RF and microwave Frequencies*" The Institute of Measurement and Control (IMC) and The National Physical Laboratory (NPL), London, 2003.
171. Munson, B.R., D.F. Young, and T.H. Okiishi, *Fundamentals of fluid mechanics 4 th edition*, 2002, New York: John Wiley & Sons, Inc. Table.
172. Ling, S.H., Y.C. Lam, and C.H. Kua, *Particle streaming and separation using dielectrophoresis through discrete periodic microelectrode array*. Microfluidics and Nanofluidics: p. 1-13.
173. Weier, T. and G. Gerbeth, *Control of separated flows by time periodic Lorentz forces*. European Journal of Mechanics-B/Fluids, 2004. **23**(6): p. 835-849.
174. Wang, X., *Selective dielectrophoretic confinement of bioparticles in potential energy wells*. Journal of Physics D: Applied Physics, 1993. **26**: p. 1278.
175. Wang, X., X. Wang, F. Becker, and P. Gascoyne, *A theoretical method of electrical field analysis for dielectrophoretic electrode arrays using Green's theorem*. Journal of Physics D: Applied Physics, 1996. **29**: p. 1649.
176. Garcia, M. and D. Clague, *The 2D electric field above a planar sequence of independent strip electrodes*. Journal of Physics D: Applied Physics, 2000. **33**: p. 1747.
177. Clague, D. and E. Wheeler, *Dielectrophoretic manipulation of macromolecules: The electric field*. Physical review E, 2001. **64**(2): p. 026605.
178. Morgan, H., A.G. Izquierdo, D. Bakewell, N.G. Green, and A. Ramos, *The dielectrophoretic and travelling wave forces generated by interdigitated electrode arrays: analytical solution using Fourier series*. JOURNAL OF PHYSICS-LONDON-D APPLIED PHYSICS, 2001. **34**(10): p. 1553-1561.
179. Morgan, H., D. Holmes, and N.G. Green. *3D focusing of nanoparticles in microfluidic channels*. in *IEE proceeding Nanobiotechnology*. 2003.
180. Sun, T., N.G. Green, and H. Morgan, *Analytical solutions for the electric field and dielectrophoretic force in a dielectrophoretic focusing electrode structure*. Applied Physics Letters, 2008. **92**: p. 173901.
181. Alazzam, A., D. Roman, V. Nerguizian, I. Stiharu, and R. Bhat, *Analytical formulation of electric field and dielectrophoretic force for moving dielectrophoresis using Fourier series*. Microfluidics and Nanofluidics, 2010. **9**(6): p. 1115-1124.
182. Pohl, H.A., K. Pollock, and J.S. Crane, *Dielectrophoretic force: A comparison of theory and experiment*. Journal of Biological Physics, 1978. **6**(3): p. 133-160.
183. Kua, C., Y. Lam, I. Rodriguez, C. Yang, and K. Youcef-Toumi, *Cell motion model for moving dielectrophoresis*. Analytical chemistry, 2008. **80**(14): p. 5454-5461.
184. Wakizaka, Y., M. Hakoda, and N. Shiragami, *Effect of electrode geometry on dielectrophoretic separation of cells*. Biochemical engineering journal, 2004. **20**(1): p. 13-19.

185. Alazzam, A., I. Stiharu, R. Bhat, and A.N. Meguerditchian, *Interdigitated comb like electrodes for continuous separation of malignant cells from blood using dielectrophoresis*. *Electrophoresis*, 2010. **32**: p. 1327–1336.
186. Becker, F., X. Wang, Y. Huang, R. Pethig, J. Vykoukal, and P. Gascoyne, *Separation of human breast cancer cells from blood by differential dielectric affinity*. *Proceedings of the National Academy of Sciences of the United States of America*, 1995. **92**(3): p. 860.
187. Bhusari, D., H. Reed, M. Wedlake, A. Padovani, S. Allen, and P. Kohl, *Fabrication of air-channel structures for microfluidic, microelectromechanical, and microelectronic applications*. *Microelectromechanical Systems, Journal of*, 2002. **10**(3): p. 400-408.
188. Hunt, T. and R. Westervelt, *Dielectrophoresis tweezers for single cell manipulation*. *Biomedical Microdevices*, 2006. **8**(3): p. 227-230.
189. Nordström, M., R. Marie, M. Calleja, and A. Boisen, *Rendering SU-8 hydrophilic to facilitate use in micro channel fabrication*. *Journal of Micromechanics and Microengineering*, 2004. **14**: p. 1614.
190. Hsieh, S., C. Lin, C. Huang, and H. Tsai, *Liquid flow in a micro-channel*. *Journal of Micromechanics and Microengineering*, 2004. **14**: p. 436.
191. Morgan, H., D. Holmes, and N.G. Green. *3D focusing of nanoparticles in microfluidic channels*. 2003. IET.
192. Mata, A., A.J. Fleischman, and S. Roy, *Characterization of polydimethylsiloxane (PDMS) properties for biomedical micro/nanosystems*. *Biomedical Microdevices*, 2005. **7**(4): p. 281-293.
193. Chang-Yen, D., D. Myszka, and B. Gale, *A novel PDMS microfluidic spotter for fabrication of protein chips and microarrays*. *Microelectromechanical Systems, Journal of*, 2006. **15**(5): p. 1145-1151.
194. Xu, J., L. Locascio, M. Gaitan, and C.S. Lee, *Room-temperature imprinting method for plastic microchannel fabrication*. *Anal. Chem*, 2000. **72**(8): p. 1930-1933.
195. Leclerc, E., Y. Sakai, and T. Fujii, *Cell culture in 3-dimensional microfluidic structure of PDMS (polydimethylsiloxane)*. *Biomedical Microdevices*, 2003. **5**(2): p. 109-114.
196. Fiorini, G. and D. Chiu, *Disposable microfluidic devices: fabrication, function, and application*. *Biotechniques*, 2005. **38**(3): p. 429-446.
197. De Iuliis, G.N., R.J. Newey, B.V. King, and R.J. Aitken, *Mobile phone radiation induces reactive oxygen species production and DNA damage in human spermatozoa in vitro*. *PLoS One*, 2009. **4**(7): p. e6446.
198. Schwarz, C., E. Kratochvil, A. Pilger, N. Kuster, F. Adlkofer, and H.W. Rüdiger, *Radiofrequency electromagnetic fields (UMTS, 1,950 MHz) induce genotoxic effects in vitro in human fibroblasts but not in lymphocytes*. *International archives of occupational and environmental health*, 2008. **81**(6): p. 755-767.
199. Leal, B.Z., M. Szilagyi, T.J. Prihoda, and M.L. Meltz, *Primary DNA damage in human blood lymphocytes exposed in vitro to 2450 MHz radiofrequency radiation*. 2009.
200. Agarwal, A., N.R. Desai, K. Makker, A. Varghese, R. Mouradi, E. Sabanegh, and R. Sharma, *Effects of radiofrequency electromagnetic waves (RF-EMW) from cellular phones on human ejaculated semen: an in vitro pilot study*. *Fertility and sterility*, 2009. **92**(4): p. 1318-1325.
201. Capri, M., E. Scarcella, C. Fumelli, E. Bianchi, S. Salvioli, P. Mesirca, C. Agostini, A. Antolini, A. Schiavoni, and G. Castellani, *In vitro exposure of human lymphocytes to 900 MHz CW and GSM modulated radiofrequency: studies of proliferation, apoptosis and mitochondrial membrane potential*. 2009.
202. Xu, L., M.Q.H. Meng, and C. Hu, *Effects of dielectric values of human body on specific absorption rate following 430, 800, and 1200 MHz RF exposure to ingestible wireless device*. *Information Technology in Biomedicine, IEEE Transactions on*, 2010. **14**(1): p. 52-59.
203. Cameron, T., M. Okoniewski, E. Fear, D. Mew, B. Banks, and T. Ogilvie. *A preliminary study of the electrical properties of healthy and diseased lymph nodes*. 2010. IEEE.
204. Fahland, M., P. Karlsson, and C. Charton, *Low resistivity transparent electrodes for displays on polymer substrates*. *Thin Solid Films*, 2001. **392**(2): p. 334-337.
205. Leung, G.W., F.T. Lau, S.L. Leung, and W.J. Li. *Formation of au colloidal crystals for optical sensing by DEP-based nano-assembly*. 2007. IEEE.

206. Kim, U., C.W. Shu, K.Y. Dane, P.S. Daugherty, J.Y.J. Wang, and H. Soh, *Selection of mammalian cells based on their cell-cycle phase using dielectrophoresis*. Proceedings of the National Academy of Sciences, 2007. **104**(52): p. 20708.
207. Pohl, H.A., *Dielectrophoresis: the behavior of neutral matter in nonuniform electric fields* 1978: Cambridge University Press Cambridge:.
208. Gordon, J.E., Z. Gagnon, and H.C. Chang, *Dielectrophoretic discrimination of bovine red blood cell starvation age by buffer selection and membrane cross-linking*. Biomicrofluidics, 2007. **1**: p. 044102.
209. Chen, D., H. Du, and W. Li, *Bioparticle separation and manipulation using dielectrophoresis*. Sensors and Actuators A: Physical, 2007. **133**(2): p. 329-334.
210. Feeley, C. and F. McGovern, *Dielectrophoresis of bubbles in isomotive electric fields*. Journal of Physics D: Applied Physics, 1988. **21**: p. 1251.
211. Choi, J.W., A. Pu, and D. Psaltis, *Optical detection of asymmetric bacteria utilizing electro orientation*. Opt. Express, 2006. **14**(21): p. 9780–9785.
212. Cummings, E.B. and A.K. Singh, *Dielectrophoresis in microchips containing arrays of insulating posts: theoretical and experimental results*. Analytical chemistry, 2003. **75**(18): p. 4724-4731.
213. Campbell, A. and D. Land, *Dielectric properties of female human breast tissue measured in vitro at 3.2 GHz*. Physics in medicine and biology, 1992. **37**: p. 193.
214. Mathew, K.T. and U. Raveendranath, *Cavity Perturbation Techniques for Measuring Dielectric Parameters of Water and Other Allied Liquids*. Sensors Update, 2000. **7**(1).
215. Yang, J., Y. Huang, X. Wang, X.B. Wang, F.F. Becker, and P.R.C. Gascoyne, *Dielectric properties of human leukocyte subpopulations determined by electrorotation as a cell separation criterion*. Biophysical Journal, 1999. **76**(6): p. 3307-3314.
216. Chaudhary, S.S., R.K. Mishra, A. Swarup, and J.M. Thomas, *Dielectric properties of normal & malignant human breast tissues at radiowave & microwave frequencies*. Indian journal of biochemistry & biophysics, 1984. **21**(1): p. 76.
217. Foster, K.R. and H.P. Schwan, *Dielectric properties of tissues and biological materials: a critical review*. Critical Reviews in Biomedical Engineering, 1989. **17**(1): p. 25.
218. Stoy, R., K. Foster, and H. Schwan, *Dielectric properties of mammalian tissues from 0.1 to 100 MHz; a summary of recent data*. Physics in medicine and biology, 1982. **27**: p. 501.
219. Schwan, H.P. and K.R. Foster, *RF-field interactions with biological systems: Electrical properties and biophysical mechanisms*. Proceedings of the IEEE, 1980. **68**(1): p. 104-113.
220. Gabriel, C., S. Gabriel, and E. Corthout, *The dielectric properties of biological tissues: I. Literature survey*. Physics in medicine and biology, 1996. **41**: p. 2231.
221. Gabriel, S., R. Lau, and C. Gabriel, *The dielectric properties of biological tissues: II. Measurements in the frequency range 10 Hz to 20 GHz*. Physics in medicine and biology, 1996. **41**: p. 2251.
222. Gabriel, S., R. Lau, and C. Gabriel, *The dielectric properties of biological tissues: III. Parametric models for the dielectric spectrum of tissues*. Physics in medicine and biology, 1996. **41**: p. 2271.
223. Tran, V., M. Afsar, and T. Vo. *Microwave complex permittivity measurement of biological medium for stem cell culture*. 2009. IEEE.
224. Nikawa, Y. and T. Michiyama. *Non-invasive measurement of blood-sugar level by reflection of millimeter-waves*. 2008. IEEE.
225. Afsar, M., N. Suwanvisan, and Y. Wang, *Permittivity measurement of low and high loss liquids in the frequency range of 8 to 40 GHz using waveguide transmission line technique*. Microwave and optical technology letters, 2006. **48**(2): p. 275-281.
226. Sun, T., S. Gawad, C. Bernabini, N.G. Green, and H. Morgan, *Broadband single cell impedance spectroscopy using maximum length sequences: theoretical analysis and practical considerations*. Measurement Science and Technology, 2007. **18**(9): p. 2859-2868.
227. Sun, T., S. Gawad, N.G. Green, and H. Morgan, *Dielectric spectroscopy of single cells: time domain analysis using Maxwell's mixture equation*. JOURNAL OF PHYSICS-LONDON-D APPLIED PHYSICS, 2007. **40**(1): p. 1.
228. Sun, T. and H. Morgan, *Single-cell microfluidic impedance cytometry: A review*. Microfluidics and Nanofluidics, 2010. **8**(4): p. 423-443.
229. Kao, M., *The study of impedance spectroscopy for single cell analysis*. 2007.
230. Pommer, M., *Fluid mechanic manipulations on cells*. 2007.

231. Karkkainen, K., A. Sihvola, and K. Nikoskinen, *Analysis of a three-dimensional dielectric mixture with finite difference method*. Geoscience and Remote Sensing, IEEE Transactions on, 2002. **39**(5): p. 1013-1018.
232. Sun, T., N. Green, and H. Morgan, *Analytical solutions for the electric field and dielectrophoretic force in a dielectrophoretic focusing electrode structure*. Applied Physics Letters, 2008. **92**: p. 173901.
233. Sun, T., N.G. Green, and H. Morgan, *Analytical and numerical modeling methods for impedance analysis of single cells on-chip*. Nano, 2008. **3**(1): p. 55-63.
234. Sanghyun, S., T. Stintzing, I. Block, D. Pavlidis, M. Rieke, and P.G. Layer. *High frequency wideband permittivity measurements of biological substances using coplanar waveguides and application to cell suspensions*. in *Microwave Symposium Digest, 2008 IEEE MTT-S International*. 2008.
235. Trabelsi, S. and S. Nelson, *Nondestructive sensing of physical properties of granular materials by microwave permittivity measurement*. IEEE Transactions on Instrumentation and Measurement, 2006. **55**(3): p. 953-963.
236. Hackl, E., S. Gatash, and O. Nikolov, *Using UHF-dielectrometry to study protein structural transitions*. Journal of biochemical and biophysical methods, 2005. **63**(2): p. 137-148.
237. Pethig, R. and D.B. Kell, *The passive electrical properties of biological systems: their significance in physiology, biophysics and biotechnology*. Physics in medicine and biology, 1987. **32**: p. 933.
238. Bao, J., C. Davis, and M. Swicord, *Microwave dielectric measurements of erythrocyte suspensions*. Biophysical Journal, 1994. **66**(6): p. 2173-2180.
239. Nyfors, E., *Industrial microwave sensors—A review*. Subsurface Sensing Technologies and Applications, 2000. **1**(1): p. 23-43.
240. Bagnaninchi, P., M. Dikeakos, T. Veres, and M. Tabrizian, *Towards on line monitoring of cell growth in microporous scaffolds: Utilization and interpretation of complex permittivity measurements*. Biotechnology and bioengineering, 2003. **84**(3): p. 343-350.
241. Padmanabhan, S., *Dielectric Relaxation Spectroscopy of Proteins in Solution: Insight into Protein-Water Interactions, Protein Folding Phenomena and Self-Association of Proteins*. Ph D Thesis, 2007.
242. Liu, N. and J. Mitchell, *Modelling electromagnetic properties of saturated sand and clay*. Geomechanics and Geoengineering, 2009. **4**(4): p. 253-269.
243. Williams, G. and D. Thomas, *Phenomenological and molecular theories of dielectric and electrical relaxation of materials*. Novocontrol Applications Note—Dielectrics, 1998.
244. Haltiwanger, S. *The electrical properties of cancer cells*. 2003.
245. Stuchly, M., *Interaction of radiofrequency and microwave radiation with living systems*. Radiation and environmental biophysics, 1979. **16**(1): p. 1-14.
246. Bagnaninchi, P., M. Dikeakos, T. Veres, and M. Tabrizian, *Complex permittivity measurement as a new noninvasive tool for monitoring in vitro tissue engineering and cell signature through the detection of cell proliferation, differentiation, and pretissue formation*. IEEE transactions on nanobioscience, 2004. **3**(4): p. 243.
247. Kaatz, U., *Complex permittivity of water as a function of frequency and temperature*. Journal of Chemical and Engineering Data, 1989. **34**(4): p. 371-374.
248. Fam, M. and M. Dusseault, *High-frequency complex permittivity of shales (0.02-1.30 GHz)*. Canadian Geotechnical Journal, 1998. **35**(3): p. 524-531.
249. Esselle, K.P.A.P. and S. Stuchly, *Capacitive sensors for in-vivo measurements of the dielectric properties of biological materials*. Instrumentation and Measurement, IEEE Transactions on, 2002. **37**(1): p. 101-105.
250. Stefanski, A. and J. Krupka. *Complex permittivity measurements of lossy liquids at microwave frequencies*. 2008. IEEE.
251. Sarabandi, K., *A technique for dielectric measurement of cylindrical objects in a rectangular waveguide*. Instrumentation and Measurement, IEEE Transactions on, 2002. **43**(6): p. 793-798.
252. Faircloth, D.L., M.E. Baginski, and S.M. Wentworth, *Complex permittivity and permeability extraction for multilayered samples using S-parameter waveguide measurements*. Microwave Theory and Techniques, IEEE Transactions on, 2006. **54**(3): p. 1201-1209.
253. Wolfson, B. and S. Wentworth, *Complex permittivity and permeability measurement using a rectangular waveguide*. Microwave and Optical Technology Letters, 2000. **27**(3): p. 180-182.

254. Haigh, A.D., F. Thompson, A.A.P. Gibson, G.M. Campbell, and C. Fang, *Complex permittivity of liquid and granular materials using waveguide cells*. Subsurface Sensing Technologies and Applications, 2001. **2**(4): p. 425-434.
255. Khan, U., N. Al-Moayed, N. Nguyen, M. Obol, K. Korolev, M. Afsar, and S. Naber. *High Frequency Dielectric Characteristics of Tumorous and Non-tumorous Breast Tissues*. in *Microwave Symposium, 2007. IEEE/MTT-S International*. 2007.
256. Ebara, H., T. Inoue, and O. Hashimoto, *Measurement method of complex permittivity and permeability for a powdered material using a waveguide in microwave band*. Science and Technology of Advanced Materials, 2006. **7**(1): p. 77-83.
257. Saito, H., Y. Suzuki, and M. Taki, *Measurement of complex permittivity for biological cells at 1.7-2.6 GHz by waveguide penetration method*.
258. Wang, Y. and M.N. Afsar, *Measurement of complex permittivity of liquid dielectrics*. Microwave and optical technology letters, 2002. **34**(4): p. 240-243.
259. Afsar, Y.W., *Measurement of complex permittivity of liquids using waveguide techniques*. Progress In Electromagnetics Research, 2003. **42**: p. 131-142.
260. Henry, F., C. Pichot, A. Kamel, and M. El Aasser, *Dielectric properties of cleaned and monodisperse polystyrene latexes in microwaves*. Colloid & Polymer Science, 1989. **267**(1): p. 48-58.
261. Gregory, A.P. and R.N. Clarke, *A review of RF and microwave techniques for dielectric measurements on polar liquids*. Dielectrics and Electrical Insulation, IEEE Transactions on, 2006. **13**(4): p. 727-743.
262. Sheen, J., *Comparisons of microwave dielectric property measurements by transmission/reflection techniques and resonance techniques*. Measurement Science and Technology, 2009. **20**: p. 042001.
263. Jylhä, L., *Modeling of Electrical Properties of Composites*, 2008, Helsinki University of Technology.
264. Hanai, T., K. Asami, and N. Koizumi, *Dielectric theory of concentrated suspensions of shell-spheres in particular reference to the analysis of biological cell suspensions*. Bull. Inst. Chem. Res. Kyoto Univ, 1979. **57**: p. 297-305.
265. Rogers, C.A., *The Packing of Equal Spheres*. Proc. London Math. Soc., 1958. **8**: p. 609-620.
266. Jao, J.Y., C.F. Liu, M.K. Chen, Y.C. Chuang, and L.S. Jang, *Electrical characterization of single cell in microfluidic device*. Microelectronics Reliability, 2011.
267. Bone, S., P. Gascoyne, and R. Pethig, *Dielectric properties of hydrated proteins at 9.9 GHz*. Journal of the Chemical Society, Faraday Transactions 1, 1977. **73**: p. 1605-1611.
268. Kouzai, M., A. Nishikata, K. Fukunaga, and S. Miyaoka, *Complex permittivity measurement at millimetre-wave frequencies during the fermentation process of Japanese sake*. Journal of Physics D: Applied Physics, 2007. **40**: p. 54.
269. Bianco, B., G.P. Drago, M. Marchesi, C. Martini, G.S. Mela, and S. Ridella, *Measurements of Complex Dielectric Constant of Human Sera and Erythrocytes*. Instrumentation and Measurement, IEEE Transactions on, 1979. **28**(4): p. 290-295.
270. Wei, M.T., J. Junio, and H.D. Ou-Yang, *Direct measurements of the frequency-dependent dielectrophoresis force*. Biomicrofluidics, 2009. **3**: p. 012003.
271. Urdaneta, M. and E. Smela, *Multiple frequency dielectrophoresis*. Electrophoresis, 2007. **28**(18): p. 3145-3155.
272. Kempainen, E., *Effective permittivity and attenuation coefficient of microstrip transmission line determined by 1-port and 2-port measuring methods*. Measurement Science and Technology, 2000. **11**: p. 38.